INRES/ Forschungszentrum Jülich IBG-2: Institute for Bio- and Geosciences

Retrieval of information and data products for calibration, validation and spatial-temporal analyses from automated field spectrometers

DISSERTATION

Zur Erlangung des Grades

Doktor der Agrarwissenschaften (Dr. agr.)

Der Landwirtschaftlichen Fakultät

Der Rheinischen Friedrich-Wilhelm-Universität zu Bonn

Vorgelegt von

Paul Näthe

aus

Eisenach

Bonn, 2024

Referent: Prof. Dr. Uwe Rascher

Koreferent: Prof. Dr. Jan-Henrik Haunert

Tag der mündlichen Prüfung: 08.11.2024

Angefertigt mit Genehmigung der Landwirtschaftlichen Fakultät der Universität Bonn

Table of Contents

“The prerequisite for knowledge is curiosity” - Jacques-Yves Cousteau

Table of Abbreviations

aC	after Corona
AERONET	aerosol robotic network
AMLS	Fraunhofer Anwendungszentrum für multimodale und luftgestützte Sensorik
bC	before Corona
BMVI	ehem. Bundesministerium für Verkehr und digitale Infrastruktur (inzw. Bundesministerium für Digitales und Verkehr)
BOA	bottom of atmosphere
BRDF	bi-directional reflectance distribution function
CForest	conditional inference forest
CIC	continuous irradiance correction
COST	European cooperation in science and technology
CV	cross validation
DLS	down-welling light sensor
DN	digital numbers
ELC	empirical line correction
Enet	elastic net
ESA	European space agency
EVI	enhanced vegetation index
FLD	Fraunhofer line discrimination
FLEX	fluorescence explorer
FloX	fluorescence box
FMS	flight management system
FOV	field of view
FWHM	full width at half-maximum spectral resolution

GNSS	global navigation satellite system
GPP	gross primary production
GPR	Gaussian process regression
GPS	global positioning system
GSD	ground sampling distance
GSP	ground sampling points
ICOS	integrated carbon observation system
iFLD	improved Fraunhofer line discrimination
IQR	inter-quartile range
ISRF	instrumental spectral response function
IT	integration time
L	radiance
LANUV NRW	State Department for Nature, Environment and Consumer Protection North-Rhine Westphalia
LM	linear model
ML	machine learning
MLA	machine learning algorithm
NDVI	normalized difference vegetation index
NedL	noise-equivalent delta radiance
NEON	National ecological observatory network
NIR	near infrared
NN	neural network
NOx	nitrous oxides
O2	oxygen
OHP	Observatoire de Haute-Provence

PC	principle component
PCA	principle component analysis
PLS	partial least squares
PPK	post-processed kinematics
R	reflectance
RadCalNet	radiometric calibration network
RMSE	root mean square error
RMSEP	root mean square error of prediction
ROI	region of interest
RoX	reflectance box
RRMSE	relative root mean square error
RTK	real-time kinematics
RTM	radiative transfer model
S-2	Sentinel 2
SCOPE	soil canopy observation, photochemistry and energy fluxes
sd	standard deviation
SFL	solar Fraunhofer lines
SFM	spectral fitting method
sfm	structure for motion
SI	Système international d'unités
SIF	sun-induced chlorophyll fluorescence
SMS	sensor management system
SNR	signal to noise ratio
SpecNet	spectral network
SVD	singular vector decomposition

SVM	support vector machine
SZA	solar zenith angle
TCARI	transformed chlorophyll absorption in reflectance index
TOC	top of canopy
UAV	unmanned aerial vehicles
VI	vegetation indices
VIS	visible
VIS-NIR	visible-near-infrared

Acknowledgment

Nach Allem ist es nun an der Zeit, Danke zu sagen.

Mein erster Dank gilt meinen Doktorvater Prof. Dr. Uwe Rascher. Du hast mir im Laufe der Zeit viel beigebracht und mich inspiriert. Du hast an mich geglaubt und mir auf diesem Abenteuer stets mit Deinem Blick fürs Größere aufzeigen können, in welche Richtung ich selbstbestimmt nach vorn gehen konnte. Ich bin sehr dankbar und stolz darauf, mit Dir diesen Weg gemacht haben zu dürfen.

Mein weiterer Dank gilt Dr. Tommaso Julitta und Dr. Andreas Burkart, die mir bei JB Hyperspectral Devices während dieses Abenteuers ein Zuhause gegeben haben. Nicht nur, dass Ihr mir bei JB die Arbeit an spannenden Projekten ermöglicht habt. Ihr habt auch aktiv meine Promotion unterstützt und ward stets als direkte Betreuer ansprechbar, konntet mit Rat und Tat bei vielen kleinen und großen Unwägbarkeiten helfen. Danke auch an Mitch, Miro, Mike, Jenny, Mark, Andre, Isabell und Rimmi für eure Anteilnahme, Unterstützung und unvorhersehbaren Anregungen.

Darüber hinaus möchte ich allen Weggefährten, Kollegen und Freunden aus der FLEX Community, dem Forschungszentrum Jülich und der großen SIF-Familie danken. Ihr habt mich stets inspiriert und wisst, wer ihr seid. Das eine oder andere Gespräch mit euch wird mir noch lange in Erinnerung bleiben.

Ich danke auch Prof. Dr. Daniela Lud für die Unterstützung, dass ich zwei Bachelorarbeiten betreuen und in dieser neuen Rolle viel hinzulernen durfte.

Mein besonderer Dank gilt auch meiner Familie, meiner Mutter Gisela und meinem Vater Wolfgang. Ihr habt mich stets unterstützt und ermutigt. Christiane, Du hast mich gehalten und geerdet, wir sind zusammen durch diese Zeit gepurzelt. Felix und Tim, ihr verbreitet viel Frohsinn in meinem Leben und ich bin dankbar, dass es euch gibt. Ich wünsche mir, dass Ihr in einer gerechten und friedlichen Welt aufwachsen, leben und euch frei entfalten dürft. Mein Dank gilt auch Ricki, Bernd, Norbert, Gitti, Jutta und Dieter.

Danke weiterhin an alle, die diese unglaubliche Reise, dieses Abenteuer ermöglicht und begleitet haben. Ohne Euch wäre das Alles nicht gegangen. Mit euch bin ich so weit gekommen. Zusammen geht es weiter.

„***Es ist nichts als die Tätigkeit nach einem bestimmten Ziel, was das Leben erträglich macht.***“ - Friedrich von Schiller, Briefe. An Christian Gottfried Körner, 27. April 1801.

Abstract

Intact ecosystems are the basis of human food security, air quality and provide naturally re-growing resources. Adaptive ecosystem management in the face of climate change requires detailed and continuous data about the ecosystems' status. Optical remote sensing allows the non-invasive acquisition of information from terrestrial ecosystems and produces very large amounts of multi-dimensional data. However, it poses the following challenges at the same time: (1) Many different optical sensors use different measurement protocols, yet a joint exploitation of their data would improve temporal, spatial and spectral details available for further analyses. (2) Standardizing data products eases comparing and interpreting optical, remote-sensed data, but requires a specific processing chain, which also includes the propagation of uncertainties. (3) The retrieval of data-products is affected by systematic influences, e.g. from the atmosphere or the surface-properties, which bias the retrieved signal and require a correction approach.

The use of standardized, automated field spectrometers enables the continuous, unattended acquisition of hyperspectral data at very high temporal resolution in proximity sensing on the ground. The high dimensionality of hyperspectral down-welling and up-welling radiance recorded in the visible-near infrared (VIS-NIR) spectral range enables the retrieval of detailed atmosphere and vegetation properties. The application of Machine Learning (ML) algorithms is promising to disentangle multiple-redundant spectral information, isolate irrelevant or disturbing spectral information and find relevant, correlating spectral information, while offering detailed investigation of uncertainties and levels of confidence around the data products. Thus in the first study, Solar Induced chlorophyll Fluorescence (SIF), a proxy for photosynthesis in vegetation, is retrieved from hyperspectral field-measurements using a novel, ML-driven approach and avoiding atmospheric reabsorption. The second study in this thesis demonstrates farther the potential of exploiting continuous, hyperspectral VIS-NIR measurements using ML for the investigation of NOx concentration in the atmosphere. Furthermore, high-resolution field spectrometer measurements allow the convolution of multispectral sensor characteristic at overlapping spectral ranges. In consequence, the third study of this thesis harmonizes a network of standardized, automated field spectrometers in ten different locations around the world in comparison to Sentinel-2 bottom of atmosphere reflectance, and investigates effects of variable temporal-spatial heterogeneity. In the final study, automated field spectrometers were used as central transfer instruments inter-calibrating satellite and two airborne multispectral sensors, while correcting for continuous changes of down-welling radiance over time. Addressing the above stated challenges facilitated recommendations for the standardization of optical proximity sensing data and for using automated field spectrometers as a centerpiece of data fusion enabling a more holistic and more detailed ecosystem monitoring.

Zusammenfassung

Intakte Ökosysteme sind die Grundlage für Ernährungssicherheit, Luftqualität und natürlich nachwachsende Rohstoffe. Ein adaptives Ökosystemmanagement erfordert detaillierte und kontinuierliche Daten über den Zustand der Ökosysteme angesichts des Klimawandels. Die optische Fernerkundung ermöglicht nichtinvasive Erfassung von Informationen terrestrischer Ökosysteme und erzeugt gleichzeitig sehr große Mengen mehrdimensionaler Daten. Es stellen sich die folgenden Herausforderungen: (1) Viele verschiedene optische Sensoren verwenden unterschiedliche Messprotokolle. Eine gemeinsame Nutzung ihrer Daten würde jedoch die verfügbaren zeitlichen, räumlichen und spektralen Details für weitere Analysen verbessern. (2) Standardisierte Datenprodukte erleichtern den Vergleich und die Interpretation optischer Fernerkundungsdaten, erfordern jedoch eine spezifische Verarbeitungskette, welche auch die Messunsicherheiten berücksichtigt. (3) Die Ableitungen von Datenprodukten werden durch Einflüsse aus der Atmosphäre oder den Oberflächeneigenschaften beeinflusst, welche das abgeleitete Signal verzerren und einen Korrekturansatz erfordern.

Der Einsatz standardisierter, automatisierter Feldspektrometer ermöglicht die kontinuierliche, unbeaufsichtigte Erfassung hyperspektraler Daten mit sehr hoher zeitlicher Auflösung in unmittelbarer Nähe am Boden. Die hohe Dimensionalität der hyperspektralen Messung einfallender und reflektierter Strahlung im sichtbaren und nahinfraroten Spektralbereich (VIS-NIR) ermöglicht die Ableitung detaillierter Atmosphären- und Vegetationseigenschaften. Besonders vielversprechend ist die Anwendung von maschinellem Lernen (ML), um mehrfach redundante Spektralinformationen zu reduzieren, irrelevante oder störende Spektralinformationen zu isolieren und relevante, korrelierende Spektralinformationen zu identifizieren. Gleichzeitig wird eine detaillierte Untersuchung von Vorhersagesicherheiten und Fehlerfortpflanzung ermöglicht. In der ersten Studie dieser Dissertation wird die sonneninduzierte Chlorophyllfluoreszenz (SIF), ein Zeigerwert für die Photosynthese, aus hyperspektralen Feldmessungen mithilfe eines neuartigen, datengestützten ML-Ansatzes und unter Vermeidung atmosphärischer Verzerrung ermittelt. Die zweite Studie dieser Dissertation demonstriert darüber hinaus die Nutzung hyperspektraler VIS-NIR-Daten mittels verschiedener ML Algorithmen zur Untersuchung von der NOx-Konzentration in der Atmosphäre. Weiterhin ermöglicht die hohe hyperspektrale Auflösung von Feldspektrometermessungen die Simulation anderer multispektraler Sensoren mit überlappenden Spektralbereichen. Daher harmonisiert die dritte Studie dieser Arbeit ein Netzwerk standardisierter, automatisierter Feldspektrometer an zehn verschiedenen Standorten auf der Welt im Abgleich mit Sentinel-2 und untersucht Auswirkungen der zeitlich-räumlichen Heterogenität. In der vierten Studie werden schließlich automatisierte Feldspektrometer als Übertragungsinstrumente genutzt, um zwei luftgestützte Multispektralsensoren in Bezug auf einen

Satelliten miteinander zu interkalibrieren und Auswirkungen von kontinuierlichen Änderungen der einfallenden Strahlung zu korrigieren. Aus der Bearbeitung der oben genannten Herausforderungen leiten sich Empfehlungen für die Standardisierung und Fusion optischer Fernerkundungsdaten automatisierter Feldspektrometersysteme ab, um eine ganzheitlichere und detailliertere Ökosystemüberwachung zu ermöglichen.

1 Introduction

1.1 Background

Intact ecosystems are at the basis of human well-being, provide naturally re-growing resources, affect air quality and enable food security. The carbon cycle in ecosystems interlinks atmosphere and biosphere, describes the fixation of atmospheric carbon into biomass by photosynthesis and the release of carbon into the atmosphere by oxidative processes, e.g. combustion and respiration (Baldocchi, 2014; Beer et al., 2010; Humphrey et al., 2021; Schlesinger et al., 2013). Terrestrial ecosystem services are resources naturally available to humankind and regimented by both the floral composition and the vegetation phenology. Climate change directly affects and alters the composition and phenology of terrestrial ecosystems, which places ecosystem services at risk (Blair et al., 2014; L. He et al., 2019; Seidl et al., 2017). While the climate of the earth changes globally and locally, extreme weather events increase vegetation stressors, e.g. by heat and drought, directly affecting plant health, and affect air quality, e.g. by natural aerosol release and anthropogenic pollution (Ehn et al., 2014; Gu et al., 2016; Jansen et al., 2009; Niinemets, 2010). Established routines and conventions of agriculture and forestry outdate with increasing pace and require comprehensive environmental data to adjust ecosystem management quickly and appropriately (Peine et al., 2011; Soudani and François, 2014). Remote sensing, in the strict sense, has been an emerging discipline in earth observation over decades and enables environmental monitoring by non-invasive data acquisition from a distance for scientific purposes (Cracknell, 2018). Dedicated optical sensors investigate in this context the visible (VIS) and non-visible electromagnetic spectrum, e.g. in the Near Infrared (NIR), of received, reflected and absorbed solar radiation and derive insights into properties of the Earth's surface (Burnett et al., 2021; Green et al., 1998; Peddle et al., 2001; Pinter et al., 1983; Smith et al., 2003; Spyrakos et al., 2018; Viscarra Rossel et al., 2016) and atmosphere (Ehn et al., 2014; Gao et al., 1993; Giles et al., 2019; Sirignano et al., 2010). Spectroscopy covers multiple scales in terrestrial surface monitoring, which requires the differentiation of proximal sensing at a close distance on the ground and remote sensing at a larger distance from aircraft or satellites (Gamon et al., 2019). Thus, following the term "proximity sensing" will relate to spectroscopy on the ground in relatively close distance to the target. The term "remote sensing" will be used to distinguish airborne or spaceborne use cases, to ease the differentiation of spatial scales in this thesis.

The airborne use of optical sensors on drones and aircraft enables the quantitative observations of vegetation in limited areas with a very high spatial resolution (Aasen et al., 2018; Chapman et al., 2019; Frankenberg et al., 2018; Gao et al., 1993; Green et al., 1998; Middleton et al., 2017; Siegmann et al., 2019; Vanderbilt et al., 1998). In theory, a higher photon flux density is available from a single point at

a shorter distance according to the inverse-square law (Kepler, 1604). However neglecting atmospheric influences such as path transmittance and diffuse scattering (Richter and Schläpfer, 2002), distance is irrelevant for the amount of light collected by the optical sensor, because the ground projected area of each pixel increases at the same ratio as photon flux density of each integral point decreases with increasing distance to target (Schaepman-Strub et al., 2008). The specific excitation energy of the detector required for sufficient differentiation of the signal from the baseline of noise determines the minimal amount of measurable light in a spatial and spectral pixel within a reasonable integration time. Thus, a tradeoff is required between achieving high spatial resolution with a sufficient pixel size for a given distance to target and achieving a high spectral resolution, both limited by the amount of available light at the detector for a given integration time. Large optics are capable of collecting more light, while they are heavy and expensive at the same time. Equally, longer integration time allows collecting more light at the detector, but is critical for moving targets and sensors in motion. Satellites typically use those large optics to provide observations on a global scale, yet at a larger spatial resolution due to the immense distance to target (Gamon et al., 2019; Slater et al., 1987). In contrast to airborne missions, satellites offer more frequent revisit rates thus allowing the analysis of time-series with regular intervals (Guyet and Nicolas, 2016; Oxoli et al., 2020; Petitjean and Weber, 2014). For example, the Sentinel-2 mission offers a single/dual satellite revisit-rate of 5/10 days and supports vegetation monitoring with good temporal resolution (Debella-Gilo and Gjertsen, 2021; Drusch et al., 2012). Furthermore, Sentinel-2 provides very stable, vigorously calibrated and stable data products (Origo et al., 2020). However, this temporal resolution could be significantly improved by combining other satellite instruments, airborne data and continuous records from automated sensors on the ground (Wen et al., 2020). On the ground, imaging sensors allow the most detailed reconstruction of spatial information due to the very short distance to target, while non-imaging sensors integrate high-resolution, spectral information according to the Field of View (FOV) into one, well characterized point (Alberton et al., 2017; Gamon, 2015; Harris et al., 2014; Kuester et al., 2001; Mac Arthur et al., 2007a; Milton et al., 2009; Wingate et al., 2015). Due to their stationary use, ground-based sensors typically allow higher integration times and achieve a higher spectral and spatial resolution even when using inexpensive optics and detectors at the same time. Therefore, proximal sensing on the ground allows optical measurements at the highest spectral and spatial resolution devoid of atmospheric distortion (Galvagno and Gamon, 2017; Gamon and Surfus, 1999; Milton et al., 2009), and continuous repeat rates at very high temporal resolution over long periods of time using automated spectroscopy systems (Cogliati et al., 2015a; Drolet et al., 2014; Pacheco-Labrador and Martín, 2015; Painter and Dozier, 2004).

The degree of differentiation of the electromagnetic spectrum distinguishes between multispectral (a few spectral bands) and hyperspectral (hundreds of continuous spectral bands) sensors. The study of

multispectral reflectance of vegetation is very suitable for change-detection, mapping and classification for example (Berni et al., 2009; Feilhauer et al., 2012; Oxoli et al., 2020; Roberts et al., 2002; Ustin et al., 2004; Wang et al., 2018). At the same time, hyperspectral reflectance of vegetation increases in complexity but enables the retrieval of more detailed information (Aasen and Bolten, 2018; Malenovský et al., 2006; Rahman et al., 2001; Ustin et al., 2004). Recent advancements in computer technology, data science and algorithms provide new and powerful tools for the exploitation of large and complex, hyperspectral datasets in earth observation (Hank et al., 2019; Jung et al., 2019; Mateo-Sanchis et al., 2021; Rivera-Caicedo et al., 2014; Rommel et al., 2022; Viscarra Rossel et al., 2016). This presents the following challenges:

- Many differently specified optical sensors across different instrument-platforms use differing measurement protocols and acquire optical data, which could be suitable for the combined observation of ecosystems. However, they require a way to unify the data and validate the information across those different optical sensors.
- The high dimensionality of hyperspectral data is multi-redundant and requires dedicated processing pipelines for the retrieval of the relevant information into standardized data products, including assigned uncertainties.
- Remote sensing data products are affected by interfering optical influences, distortion from the atmosphere or surface properties, which alter the measured signal and require a correction.

1.2 Thesis aims and structure

This thesis aims to address the three above stated challenges to support the retrieval of information relevant for the investigation of ecosystems across multiple sensors scales, and domains using automated field spectrometer systems as a centerpiece. The details of using continuous, automated, hyperspectral point measurements of up-welling and down-welling light on the ground are described with the aim to achieve standardized and comparable results, to support the generation of holistic, standardized datasets including associated uncertainties and quality control. The hyperspectral analysis of field-measured data is studied with respect to deriving higher data products for the investigation of air-quality and vegetation photosynthesis. Furthermore, this thesis aims to demonstrate the combination of data from vigorously standardized, automated spectrometers on the ground and satellite data facilitating the integration of information across temporal and spatial scales. Finally, the standardized, automated field spectrometers are used as a reference for the integration of remote sensing data across multiple, optical sensors on different platforms, to serve as the central transfer instrument.

The thesis presents first an overarching framework of applying automated field spectrometers in proximity sensing, introduces hyperspectral analysis and retrieval of higher data products and machine learning, radiometric noise, the propagation of uncertainties, the validation and calibration of optical data across different sensors. Furthermore, the knowledge gain and scientific contribution is shown. Four studies follow. Studies 1 and 2 are centered on the exploitation of the hyperspectral data using ML. Studies 3 and 4 are focused on the use of proximal sensing for the purpose of sensor calibration and validation in the field. Regarding the studies inside the pairs, the first one is an enabling study, the second one is a subsequent case study. 1) A data-driven retrieval method of Sun Induced chlorophyll Fluorescence unaffected by atmospheric reabsorption was developed. 2) Furthermore, a case study employed ML farther for the hyperspectral analyses of down-welling radiance to relate to changes of NOx in urban air during the coronavirus pandemic. 3) Harmonizing time-series from a standardized network of autonomous field spectrometers using data from Sentinel-2 as reference was enabled. 4) Finally, the inter-calibration and validation of time-synchronous field spectroscopy, drone, aircraft and Sentinel-2 imaging was examined in a case study. At last, an overarching conclusion is provided.

2 Overarching framework and implications

2.1 Fundamentals of applying automated field spectrometers

Automated field spectrometer systems are introduced and current applications in environmental monitoring are outlined in this section. Furthermore, the exploitation of the hyperspectral data for vegetation monitoring using VI and SIF as proxies for plant physiology are briefly introduced. Following, the potential of machine learning in hyperspectral SIF retrieval and analysis of the atmosphere are outlined. Specific pipelines have been developed for example for SIF retrieval and atmospheric NOx investigation, which are examined in detail in Study 1 and 2 in this thesis.

2.1.1 Automated field spectrometers

Field spectroscopy stems from the use of spectro-radiometers outdoors which were, in their origin, pure laboratory instruments and enabled investigating optical characteristics of the environment in-situ and in-vivo (Milton, 1987; Milton et al., 2009). Within the field of optical proximity sensing, field spectrometers allow the non-invasive and non-destructive collection of information about an object from a distance by measuring unique details of the electromagnetic spectrum of received, absorbed and reflected radiation (Kuester et al., 2001; Mac Arthur et al., 2007b; Peddle et al., 2001). Early systems were bulky, heavy, and demanding in the handling, requiring an operator at all times (Milton, 1987; Milton et al., 2009). Especially, the ASD FieldSpec (today marketed by Malvern Panalytical,

United Kingdom, Almelo, The Netherlands) has been used for over 25 years as a portable and reliable field spectro-radiometer (Kuester et al., 2001; Milton et al., 2009). Nevertheless, rapid advancements in technology enabled developing automated field spectrometer systems, which are applied in continuous vegetation monitoring (Burkart et al., 2014; Cogliati et al., 2015a; Drolet et al., 2014; Grossmann et al., 2018; Mac Arthur et al., 2014; Meroni et al., 2011; Rossini et al., 2010; X. Yang et al., 2018), examination of water quality (Keller et al., 2018; Maier et al., 2021) or air quality monitoring (Hundt et al., 2018; Naethe et al., 2020; Viana et al., 2015). Regardless of the specific field of application, automated field spectrometers continuously record time-series of optical data at very high spectral resolution and rapid repeat rates, enabling unprecedented insights into temporal dynamics. Continuous data of very high temporal and spectral resolution allow insights into short-term phenology and vegetation stress responses using plant physiological proxies, e.g. Vegetation Indices (VIs) and Sun-Induced chlorophyll Fluorescence (SIF) (Alonso et al., 2017; Bertolli et al., 2013; Burkart et al., 2015b; Campbell et al., 2014; Damm et al., 2010a; Rascher and Pieruschka, 2008; Roth et al., 2018; Wieneke et al., 2018). The SIF signal is especially promising for early stress detection, but requires a complex interpretation of canopy structure, physiology, retrieval method, instrument and atmospheric distortion with respect to a direct reference in the field (Chang et al., 2021; Martini et al., 2022; Sabater et al., 2018). Since SIF contributes only 2% - 5% to the total up-welling radiance, sophisticated retrieval methods need to carefully decouple the SIF signal with little uncertainty to allow the meaningful investigation of stress events (Mohammed et al., 2019). Furthermore, applied to record surface reflectance in close proximity on the ground, field spectrometer data serve as a reference for validating airborne or spaceborne optical remote sensing (Buman et al., 2022; Hueni et al., 2017; Mihai et al., 2018; Naethe et al., 2023; Olsson et al., 2021). Used as a ground reference, field spectrometer data inform mapping and classification of vegetation and land-surface cover (Debella-Gilo and Gjertsen, 2021; Rommel et al., 2022; Sefrin et al., 2021; Serbin and Townsend, 2020; Smith et al., 2003).

The automated field spectrometer system FloX, JB-Hyperspectral Devices, Düsseldorf, Germany, was developed specifically for the continuous long-term observation of vegetation reflectance and SIF, and is specified with optical characteristics similar to the upcoming Fluorescence Explorer (FLEX) Satellite mission of the European Space Agency (ESA) (Drusch et al., 2017; Middleton et al., 2017; Rascher et al., 2015). The FloX is a dual spectrometer system, which includes a full-range VIS/NIR spectrometer for monitoring reflectance and VI of vegetation between 400 nm and 950 nm in combination with a high-performance red/NIR spectrometer dedicated to retrieving SIF between 650 nm and 800 nm (Burkart et al., 2015b; Julitta et al., 2016). Multiplexing each spectrometer into a hemispherical channel and a conical channel allows near-time-synchronous recordings of down-welling and up-welling light and enables internal quality checks by recording stability of illumination, sensor saturation, integration time and optimization level, GPS coordinates, time-stamp, Solar Zenith Angle (SZA) and dark-currents

for each measurement cycle (Cogliati et al., 2015a). The RoX, JB-Hyperspectral Devices, Düsseldorf, Germany, is a smaller version of the FloX including only full-range VIS/NIR spectrometer from the FloX for reflectance monitoring. FloX and RoX both are designed as stationary, automated spectrometer systems capable of continuously monitoring vegetation as they measure up-welling and down-welling light at the top of canopy (TOC) with identical optical characteristics. Due to identical radiometric and spectral calibration routines, as well as identical specifications of the optical path and spectrometers, the FloX and RoX systems provide highly standardized reflectance, up-welling radiance, down-welling radiance, VIs and quality flags suitable for synergistic, integrated use. In addition, the FloX's red/NIR spectrometer enables advanced retrievals of the SIF signal (Burkart et al., 2015b), as well as further investigation of SIF retrievals by the use of ML (Naethe et al., 2022; Scodellaro et al., 2022). The RoX can be used also as a portable device, which is furthermore interesting for the in-situ validation of cross-calibration of airborne and satellite remote sensing products (Naethe et al., 2023). The totality of recorded data from all those instruments already covers many different ecosystems and climate conditions, determined by the use-case of the owners respectively, but also represent a very large source of secondary information in standby for further analyses beyond the originally intended use-case. Another, secondary use-case of the data is the application for validation and calibration against satellite reflectance data worldwide (Naethe et al., 2024). Furthermore, the retrieval of atmospheric properties from exploiting the continuous readings of down-welling light is possible (Naethe et al., 2020), as each recoded spectrum of down-welling radiance on the ground contains information of the atmospheric transmission affected by gases and aerosols absorbing light at specific wavelengths (Green et al., 1998). With the increasing, synergistic use of multiple environmental sensors from different scientific communities and networks in mind (Cheng et al., 2006; Joiner et al., 2018; Jung et al., 2019; Musavi et al., 2016; Peltoniemi et al., 2018; Sirignano et al., 2010), a better and deeper understanding of the interactions of the earth's systems and processes could be enabled from harmonizing existing and future proximity sensing products from a network of automated field spectrometers and combine them with remote sensing products from other optical sensors. A standardized network of automated field spectrometers on the ground is furthermore interesting for calibrating spaceborne and airborne optical sensors (Bouvet et al., 2019). However, this proposes the challenge of integrating increasing dimensionality and high complexity of measured variables in a meaningful way (Bioucas-Dias et al., 2013). For hyperspectral data, synergistic integration is only possible for multiple times and sites, which are standardized and as similar as possible in terms of instrumentation specifications, calibrated data output, quality flags, uncertainty tracing and associated meta-data (Graf et al., 2023; Hueni et al., 2023).

2.1.2 Hyperspectral analysis in field spectroscopy for vegetation monitoring

The high dimensionality of hyperspectral data recorded by automated field spectrometer systems is a challenge but presents a large source of information at the same time. FloX and RoX provide hyperspectral data in over 1000 spectral bands per integrated spectrometer, each. To the hyperspectral domain adds the temporal domain of continuous time-series and, if applicable, the spatial domain of various sites and locations. Investigating hyperspectral reflectance of vegetation within this order of dimensionality is beyond the capacity of human perception. However, extracting relevant information from hyperspectral reflectance requires to investigate only a fraction of the hyperspectral domain relevant for the study of plant physiological processes and phenology (Gitelson et al., 2006; Linkosalmi et al., 2022; Yang et al., 2019). VIs are used as widespread proxies for vegetation, originating from multispectral sensors and combining fractions of the reflectance spectrum susceptible to plant density (Tucker, 1979), chlorophyll content (Dash et al., 2004), pigment regulation (Gamon et al., 1992), or Gross Primary Production (GPP) (Dechant et al., 2020) in singular values. Furthermore, SIF is used as a proxy for photosynthesis, but requires a higher amount of spectral information and additional considerations to reconstruct the signal from hyperspectral measurements (Frankenberg and Berry, 2018; Mohammed et al., 2019; Porcar-Castell et al., 2014). It must be noted that SIF is measured at the top of the canopy and the distribution of the signal inside the canopy is much more complex due to scattering, reabsorption and anisotropic distribution, which complicates the interpretation of signal (Liu et al., 2019a; Siegmann et al., 2021; Van Wittenberghe et al., 2021, 2015). Several different mechanistic retrieval methods exploit the overlapping spectral signature of the SIF signal with the telluric oxygen absorption bands (Alonso et al., 2008; Cendrero-Mateo et al., 2019; Cogliati et al., 2015b; Meroni et al., 2010) and even reconstruct the full spectral shape of SIF (Cogliati et al., 2019; X. Liu et al., 2015). However, SIF retrievals based on telluric oxygen are sensitive to atmospheric distortion and require challenging signal corrections for increasing distance between sensor and canopy (Liu et al., 2019b; Sabater et al., 2018; van der Tol et al., 2023; Yang et al., 2020, 2015). In contrast, SIF retrieval methods based on Solar Fraunhofer Lines (SFL) are in principle unaffected by atmospheric reabsorption of the SIF signal (Grossmann et al., 2018; Guanter et al., 2013; Joiner et al., 2016; Köhler et al., 2020; Sun et al., 2018). The FloX instruments and retrieval methods need to comply with the FLEX satellite mission requiring an error in SIF not exceeding 0.2 mW m^{-2} sr^{-1} nm^{-1} as candidate ground reference in the satellite validation plan (Vicent et al., 2016). This value is also equivalent to the lowest differentiable signal quantity and relevant for SIF being used to identify early stress in vegetation, which is typically apparent with low signal intensities (Chang et al., 2021; Martini et al., 2022; Siegmann et al., 2021; Wohlfahrt et al., 2018). Also from the perspective of standardization, data quality and uncertainty tracing are important.

2.1.3 Fundamentals of machine-learning for hyperspectral analyses and retrievals

More recently, advancements in computer technology, scientific computing and Machine Learning (ML) provide very powerful tools for the fast processing and analysis of high-dimensional, hyperspectral data (Boyle, 2013; Madin et al., 2007; Mardia et al., 1979; Matheron, 1963; Pompilio et al., 2014; Verrelst et al., 2012; Wilson et al., 2014). Fundamentally, supervised and unsupervised methods are distinguished by whether or not training datasets are used (Eick et al., 2004; Hosseiny et al., 2024). Unsupervised methods investigate the variance in the input data and find connected groups based on the distance of measurement, commonly applied in dimensionality reduction and clustering, change detection and gap filling (Banerjee et al., 2005; Dray, 2008; Mardia et al., 1979; Murphy and Maggioni, 2019; Pompilio et al., 2014; Wallace and Dale, 2005). Based on the principles of curve fitting, maximum likelihood and correlation, supervised ML algorithms exploit relevant spectral features from the predictor space with respect to the predicted variable space and are suitable for the retrieval of higher products, classification, spectral unmixing and feature extraction (Benoudjit et al., 2009; Biancolillo and Marini, 2018; Dayal and Macgregor, 1997; Mou et al., 2017; Pompilio et al., 2014; Roberts et al., 2002; Schmidtlein et al., 2007; Serbin et al., 2012; Siegmann and Jarmer, 2015; Verrelst et al., 2012). However, supervised ML are also susceptible to overfitting and to accidentally exploiting surrogate relationships inside the data, which get increasingly problematic when transferring and scaling the obtained ML models (Hosseiny et al., 2024). While overfitting and underfitting can be effectively addressed by optimizing the training routines of the algorithms using segmentation, bootstrapping, random permutations and k-fold cross-validation (CV) (Rommel et al., 2022; Siegmann and Jarmer, 2015), surrogate relationships are more difficult to overcome as they exploit correlated co-variances by chance which have no real, mechanistic link to the aimed variable of interest. Cross-validation with a second testing dataset can address this issue, but proposes the requirement that the dataset used for secondary cross-validation is not repeating misleading surrogate dependencies (Rommel et al., 2022; Wagner et al., 2018). Popular supervised ML algorithms in vegetation monitoring and phenotyping are Neural Network (NN), Partial Least Squares regression (PLS), Gaussian Process Regression (GPR), Elastic Net regression (ENet), Random Forest and Support Vector Machine (SVM), which tread the input data each in a specific way to facilitate the optimization of regression between predictor space and predicted variable space (Berger et al., 2022; Mou et al., 2017; Rivera-Caicedo et al., 2014; Sefrin et al., 2021; Serbin and Townsend, 2020; Siegmann and Jarmer, 2015; Verrelst et al., 2012). Furthermore, it must be noted that each of those algorithms calculates differently uncertainty estimates of their predictions, e.g. during training, CV or even when applying the final model to unknown measurements. All ML predicted results and uncertainty estimates are fundamentally constrained by the generalization of the systematic contingent of information in the variables exploited during the training. The results of ML approaches fully depend on the input data used for

training and validation (Berger et al., 2020). Constraints of the training data and CV routines influence the limitations of transferability and of scalability for the specific ML application even over the impact of the actual algorithm choice (Siegmann and Jarmer, 2015; Ustin et al., 2004). One way to address this issue is to use self-similar field measurements during the training, which cover the expected variability of the predicted vegetation parameter and resemble the experimental conditions precisely. However, this approach is likely to result in overfitting, suffers from poor generalization, and requires precise a-priori knowledge about the expected conditions, which is rarely achieved during field experiments. The use of modelled training data is an alternative to the previous approach and benefits from precisely controlling the influencing parameters to create very determined ML models (Gamon et al., 2019; Rivera-Caicedo et al., 2014; Verrelst et al., 2012). For example, the Soil Canopy Observation, Photochemistry and Energy fluxes (SCOPE) model can calculate specific vegetation spectra including SIF for various plant physiological parameters (van der Tol et al., 2009; Verrelst et al., 2015). However, the modelled training data still needs to be representative for the real measurements to exploit and requires to include also a simulation of the instrument and surrounding atmosphere. Furthermore, SCOPE and other mechanistic Radiative Transfer Models (RTMs) are complex and require excessive computation, which can expand quickly over several days and more depending on the size of datasets and number of repetitions (Berk et al., 1998; Damm et al., 2015; Rivera et al., 2015; Serbin and Townsend, 2020). Inverting RTMs for the retrieval of parameters from spectral data requires even farther enhanced computational effort (Sabater et al., 2017; Ustin et al., 2004). Thus, the use of computationally fast ML algorithms is promising for creating data-driven emulations for complex radiative transfer code, especially, when used for speeding up the computationally costly RTM inversion (Pacheco-Labrador et al., 2019b; Rivera et al., 2015; Verrelst et al., 2017, 2016a). At the same time, modelling large, RTM-based look-up-tables of SIF and true reflectance enables supervised training of advanced, ML-based SIF retrieval approaches in general (Aasen et al., 2019; Rivera-Caicedo et al., 2014) and in particular with automated field spectrometers (Naethe et al., 2022; Scodellaro et al., 2022). The challenges of ML-based SIF retrievals emerge in combining thousands of instances into a realistic, yet synthetic dataset including canopy radiances, atmosphere and known SIF contribution for training the algorithm properly. Furthermore, integrating the real sensor characteristics and combined uncertainties into the training dataset is mandatory for the transfer of the model from synthetic data into real field measurements. Harnessing high dimensionality and high complexity of interacting, in parts redundant and in parts unique variables in hyperspectral data remains another challenge. Those challenges are further examined in Study 1 of this thesis (Naethe et al., 2022).

ML and statistical dimensionality reduction identify and eliminate redundant variables and extract relevant spectral features, but on the contrary, they can uncontrollably lose information (Dray, 2008; Nock et al., 2013; Wiklund, 2007). Especially, Singular Vector Decomposition (SVD) or Principal

Component Analysis (PCA), which are mathematically very similar unsupervised methods, reduce dimensionality of the input data by calculating replacement dimensions according to the fraction of total variance explained. In contrast, PLS regression involves matrix deflation and sequential regression optimization to obtain latent components according to the covariance between the predicted variable and the deflated predictor (Abdi, 2010; Burnett et al., 2021; Dayal and Macgregor, 1997; De Jong and Ter Braak, 1994). Due to its nearly mechanistic behavior and transparent data transformation based on optimizing for covariance in the predictor space, PLS allows the thorough analysis of the obtained models similar to PCA or SVD and does not resemble a black box. Thus, PLS is very widely used when dealing with hyperspectral data for example in chemometrics (Biagioni et al., 2011; Biancolillo and Marini, 2018; De Jong, 1993), vegetation monitoring (Jin and Wang, 2019; Meacham-Hensold et al., 2019; Singh et al., 2015), spatial scaling of vegetation functional traits (Gamon et al., 2019; Serbin and Townsend, 2020), analysis of water quality (Keller et al., 2018; Wagner et al., 2018) and analysis of air quality (Ismael and Duleba, 2021; Kim et al., 2012). Continuous down-welling light measurements have the potential of revealing atmospheric properties. For example, atmospheric NOx concentration interacts with the solar radiation along its path through the atmosphere and affects measurements of down-welling radiance on ground (Hundt et al., 2018; Ogen, 2020; Park et al., 2019). The Coronavirus pandemic reduced the anthropogenic emissions of those pollutants significantly (Gkatzelis et al., 2021; Lipfert and Wyzga, 2021; Wang et al., 2020) and enabled linking a statistically relevant difference of NO2 concentration with spectral features in continuous measurements of down-welling radiance (Naethe et al., 2020). Study 2 in this thesis details the steps of hyperspectral analyses.

2.2 From instrumental noise and propagated uncertainties

This section discusses the propagation of uncertainties in automated field spectrometer systems to support high data quality, enable traceability throughout the processing chain and standardization of protocols.

2.2.1 Fundamentals of propagating uncertainties in field spectroscopy

Converting spectrometer data from raw DN into radiance in SI units is important to allow for comparing and interpreting measurements in a meaningful way, but propagates uncertainties into the spectral radiance at the same time (Barnes et al., 2000; Milton et al., 2009; Schaepman-Strub et al., 2008; Schaepman and Dangel, 2000). Calibration coefficients are used to convert raw DN with respect to integration time into spectral radiance. However, during the calibration process radiometric and spectral uncertainties arise and require consideration. Spectral uncertainties arise around the determination of the Instrumental Spectral Response Function (ISRF), the central wavelengths for each waveband and the FWHM, which were beyond the scope of this work. Other studies investigated spectral uncertainties related to different ISRF shapes (Trim et al., 2021) and optimized spectral

calibration procedures (Hueni and Bialek, 2017; Mihai et al., 2018). Only a minor impact from uncertainties related to spectral shifts was recognized in radiance products and in the retrieved SIF, while Signal to Noise Ratio (SNR) related to radiometric uncertainties was of significantly greater impact (Damm et al., 2011). Therefore, the propagation of radiometric uncertainties and SNR has to be considered more closely when using radiance measured by field spectrometers to derive higher data products. Moreover, the hyperspectral database SPECCIO (Hueni et al., 2009) just received an update to include automated uncertainty propagation from the radiometric and spectral branch (Hueni et al., 2023), yet it requires the input of initial uncertainties to propagate.

Furthermore, systematic errors affect the data products in addition to the random uncertainties (Csavina et al., 2017). Systematic effects contribute offsets, which are attributed to specific sources, e.g. by electrical and optical components, measuring principles or retrieval approaches, setup and handling of the instrument, study design, sampling strategies and spatial representativeness, (Barnes et al., 2000; Biggar et al., 2003; Buman et al., 2022; Burkart et al., 2015b; Cendrero-Mateo et al., 2019; Graf et al., 2023; Kuester et al., 2001; Milton, 1987). Also, dependent uncertainties around the cosine correction of the down-welling radiance reference are important (Burkart et al., 2022; Rollin et al., 2000). In contrast to random uncertainties, systematic errors have a specific contribution and can be corrected if their magnitude is known. It is generally understood that cross-calibration can reduce systematic offsets at the cost of propagating random uncertainties from the validated reference (Hueni et al., 2017). In consequence, the pursuit of tracing random, radiometric uncertainties in hyperspectral radiance measured by FloX/RoX will be discussed in detail in the following. The correction of systematic errors and offsets between multiple sensors will be discussed in detail in section 2.4

2.2.2 Radiometric noise and instrument uncertainties

In physics, the propagation of uncertainties is an essential consideration for quantities, which cannot be measured directly. In this context, radiometric uncertainties express the random and not correctable aspect of an indirect radiance measurement and trace back to their precision during instrument calibration (Schaepman and Dangel, 2000). While the systematic offset in radiance, the accuracy, can be corrected for a spectro-radiometer using calibration coefficients with respect to a stable reference (e.g. stable halogen lamp), the precision of this correction will enter into the propagation of the radiometric uncertainty, which stems from the fluctuations of the initial measurement repetitions during calibration (Białek et al., 2020). In the case of a directly measured quantity, this uncertainty relates only to the random component of the calibrated instrument (spectrometer vs. stable halogen lamp with negligible random deviation). However, if the random deviation of the reference is significant, it has to be considered in the propagation of uncertainties as well (JCGM, 2008). For example, this is the case when cross-comparing two independent spectrometer

systems, which have random noise in their measured signals each, using a second calibration coefficient to calculate the referencing radiance. Mathematical rules determine the calculation of uncertainty for functional relationships (Farrance and Frenkel, 2012).

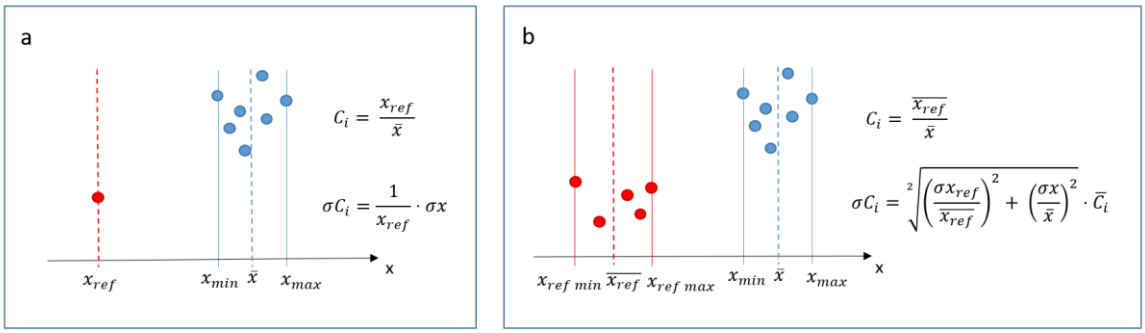

Figure 1: Random errors during calibration propagate as uncertainties of the calibration coefficients C, which are mathematically expressed as the standard deviations of the random scattering of the measured X values with respect to a stable reference in a). If the reference includes also uncertainties, the propagation of the uncertainties from both sources into the radiometric calibration coefficients C becomes more complex in b). Drawn after (Csavina et al., 2017).

Precision and accuracy are reported during calibration ideally with respect to a single, direct reference (Figure 1a), or more realistically with respect to a noisy reference (Figure 1b). For a cross-calibration, this implies mathematically that the standard deviation of the measurements from the calibrated instrument and the standard deviation of the reference instrument interact in the partial derivative of the measurement equation (Csavina et al., 2017). Given that the noise-equivalent radiance change for the calibrated instrument and for the reference are both known per wavelength and measurement, the calibration coefficients include the uncertainty associated to the calibrated radiance. The uncertainty of the calculated down-welling or up-welling radiance L for a certain waveband number i is computed according to equation 1 from the multiplication of the calibration coefficient C_i, which includes the radiometric uncertainty σC_i from the reference, and the raw spectrometer output X_i in DN including the uncertainty σX_i with respect to the central wavelength λ of the waveband:

$$\sigma L_{i,\lambda} = \sqrt{\left(\frac{\sigma C_{i,\lambda}}{\overline{C_{\iota,\lambda}}}\right)^2 + \left(\frac{\sigma X_{i,\lambda}}{\overline{X_{\iota,\lambda}}}\right)^2} \cdot \overline{L_{\iota,\lambda}} \qquad (1).$$

In consequence, the uncertainty of the radiometric calibration propagates according to Equation 1 from the calibration coefficients and initial measurements into the calibrated radiance.

As opposed to the laboratory, in field spectroscopy purely mathematical propagation of uncertainties is not always practical due to additional uncertainties introduced by a complex, dynamic, living environment, which often requires an in-situ uncertainty assessment using rapidly repeated measurements (Hueni et al., 2017). Even though mathematical rules describe the propagation of

uncertainties for measured data theoretically, it can be complex and challenging to consider all possible contributing sources appropriately. Furthermore, the complete propagation involves a comprehensive model of the sensor and requires a precise knowledge of all uncertainties related to the calibration process, coefficients used, instrumental configurations and signal gain settings (Milton et al., 2009; Peddle et al., 2001; Schaepman and Dangel, 2000). This information is not always available and can be difficult to obtain. The design of the automated field spectrometers FloX and RoX eliminates some systematic uncertainties related to temperature drift, dark current, non-linearity, channel mismatch or erroneous cosine response to allow unattended use (Pacheco-Labrador and Martín, 2015). A limiting factor for high data quality remains the amount of available light at the detector. Obviously, a higher signal level at detector results in higher SNR for a static amount of radiometric noise. FloX and RoX both optimize the integration time for each measurement with respect to the amount of available light and ensure an optimal detector gain around 80% of the maximal dynamic range while minimizing the risk of saturated spectra at the same time (Pacheco-Labrador and Martin, 2014). Thus, SNR can be theoretically 80% of the specified maximum during field conditions. However, 80% detector gain cannot be reached under all circumstances, e.g. if the available light pushes the integration time to the limits or due to the specific spectral shape of measured signal including very high and very low intensities. For example, signal levels in the NIR are much higher in comparison to the blue or the green in reflected radiance from vegetation. This leads to a variable risk of misinterpreting mathematically propagated uncertainties in measured up-welling and down-welling radiance at different wavelengths, when resorting to a singular value of SNR for the entire detector. Furthermore, mathematical propagation of radiometric uncertainties could be misleading and will eventually fail in cases when full traceability back to the national or international standard is not possible, e.g. when the actual uncertainties around the reference are unknown, when instrumental properties are not fully characterized, or when setup and complex environmental dynamics interact with the measurements. Nevertheless, it remains important to quantify the amount of random, radiometric noise in field measurements for further consideration and propagation of uncertainties into higher data products. With respect to the traceability of radiometric uncertainties from FloX and RoX, the lack of SNR values associated to measured radiance data presents a significant deficiency towards standardizing protocols. This deficiency proposes the need of quantitatively determining radiometric noise of field measured radiance spectra from FloX and RoX with an empirical approach. We addressed this issue in the following sub-section in this thesis.

2.2.3 Radiometric noise and field-measurement uncertainties

The noise of each radiance measured with a field spectrometer depends on internal factors (e.g. integration time and optical configuration for example) and external factor (e.g. available amount of light and surface brightness of the target for example). The SNR can be estimated by extracting the

standard deviation of the random contribution of the measurements and mean signal when comparing them on a stable target (Schaepman and Dangel, 2000). Since a systematic change in illumination must be expected over time (Milton et al., 2009), it is advisable to investigate multiple, consecutive radiance spectra at a time to eliminate the systematic changes. Hence, even with no direct information about the dynamic range of the detector at hand, it is still possible to extract the random noise from a series of consecutive radiance spectra measured with rapid repeat rate by FloX/ RoX and calculate the SNR with respect to the recorded signal intensity under the following assumptions:

1. The time interval between consecutive measurements is short, e.g. < 60 seconds.
2. The optical characteristics of the instrument did not change from one measurement to another.
3. The target was not significantly altered and can be assumed as stable during a period of 2 minutes, which is approximately required for 3 full measurement cycles of a FloX.
4. The recorded measurements can be directly compared with each other. Thus, one spectrum can be expressed mathematically as a function of its neighboring spectrum.
5. The spectrum is not smoothed.

Implementing in-field approximation of operational SNR with the FLoX, we selected three consecutively measured down-welling radiance to compare the one in the middle to the one before and the one after (Figure 2). Systematic changes would affect the preceding and succeeding measured spectrum similarly, assuming a steady change over the 2-minute interval.

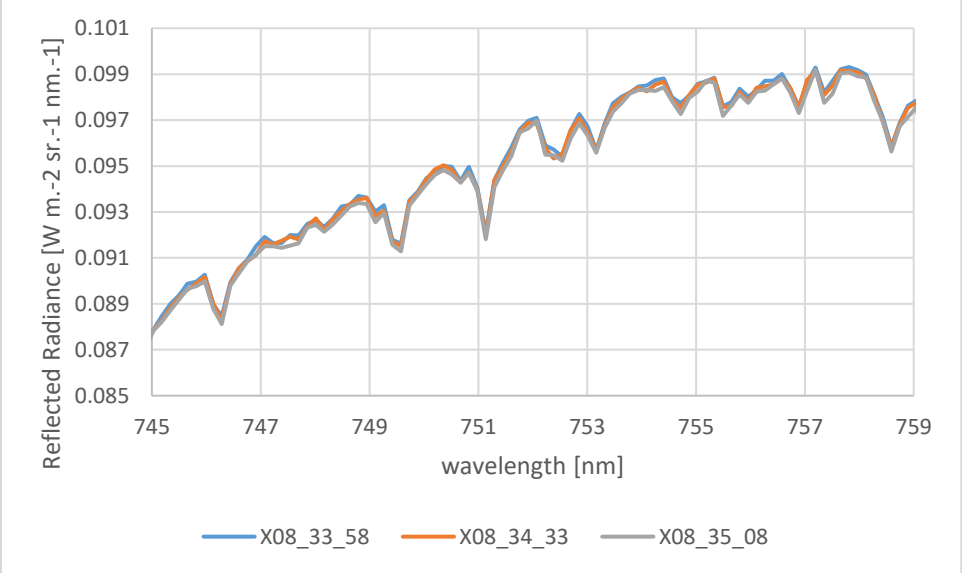

Figure 2: Three temporally neighboring radiance spectra measured by a FloX field spectrometer. The different colors indicate the times of recording given in XHH_MM_SS.

The noise is calculated using the standard deviation of the residual from approximating the middle measurement n by a linear combination of a 3rd order polynomial using the spectrum before (n-1) and

the spectrum after (n+1). Thus, the noise N is calculated according to equation 2 as the standard deviation of the two intervals *i* before and after the central spectrum n for the wavelengths between 745 nm and 759 nm as:

$$\sigma N_{i\in\{n-1;n+1\}} = \sqrt{\sum_{\lambda=745}^{759} \frac{((L_{n,\lambda}-L_{i,\lambda})-\mu(L_{n,\lambda}))^2}{\Delta(\lambda-1)}} \quad (2)$$

with L_i being the approximated intensity for example of L_2, using the spectrum with index 1 or 3 to optimize a, b, c and d in a linear, 3rd order polynomial with respect to the central wavelengths vector *wl*, scaling the spectrum L_n to overlap with L_i according to equation 3:

$$L_i \approx d \cdot wl_\lambda^3 \cdot L_{n,\lambda} + c \cdot wl^2 \cdot L_{n,\lambda} + b \cdot wl \cdot L_{n,\lambda} + a \quad (3).$$

The signal is calculated as the mean intensity of the spectra L_i in the given spectral range between 745 nm and 759 nm in equation 4:

$$S_{i\in\{n-1;n+1\}} = \frac{\sum_{\lambda=745}^{759} L_{i,\lambda}}{\Delta(\lambda-1)} \quad (4).$$

Finally, the SNR of a measured radiance spectrum *n* is calculated with respect to the two neighboring intervals *i* accordingly in equation 5:

$$SNR = \frac{\sum S_i/2}{\sum \sigma N_i/2} \quad (5).$$

Hence, systematic changes are reduced and only random changes are reported for one spectrum with respect to the preceding and succeeding measurements. Systematic changes cancel out due to the two interval steps, approximating the central measurement in terms of the previous and latter one. Thus, the residual according to equation 4 of the linear approximation of the spectra according to equation 3 marks the almost purely random noise. Finally, the SNR is the mean signal of the two approximated spectra with respect to the isolated, mean random noise from the two neighboring measurements. Approximating SNR using a ~15 nm wide spectral window moving across all bands of the detector in a diurnal series of up-welling and down-welling radiance spectra measured by a FloX on November 6th 2020 in Selhausen revealed successfully the variable SNR across the spectral domain and across the temporal domain (Figure 3). Lower signals due to the typical reflectance shape of vegetation and the telluric absorption features as well as limiting low light conditions during late afternoon clearly affect the SNR in the field. For high signal levels, both channels of the FloX exhibit very similar, maximal operational SNR around 800 due to the automatic signal optimization of the FloX spectrometer system.

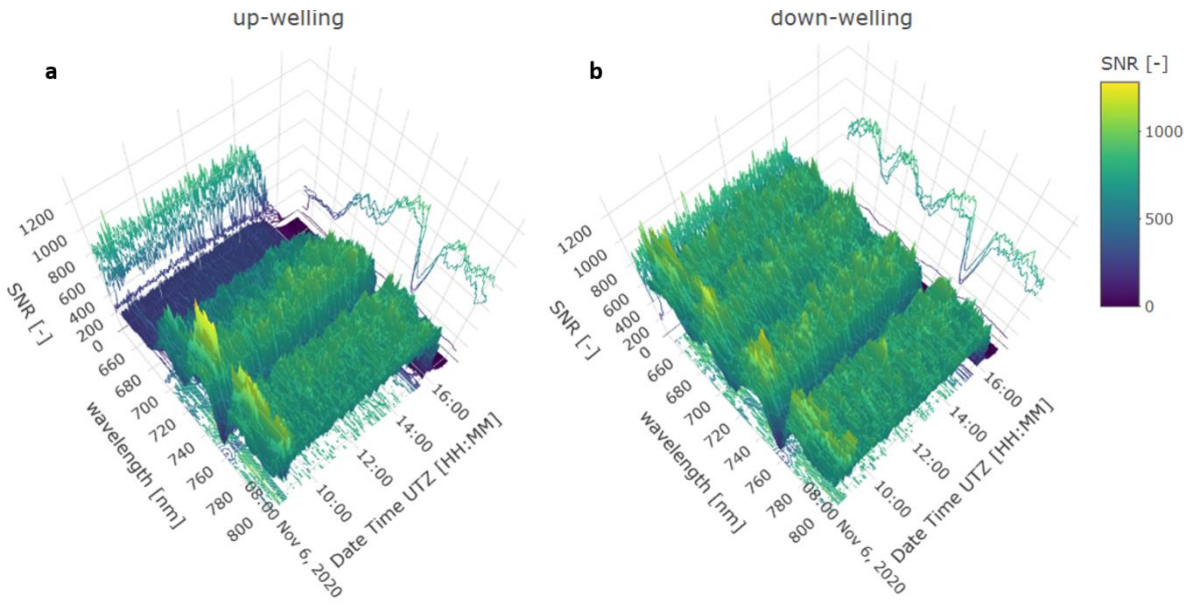

Figure 3: Spectral Signal to Noise Ratio (SNR) plotted for a diurnal series of measured up-welling radiance (a) and down-welling radiance (b) using a FloX in Selhausen, Germany, on November 6, 2020. SNR was approximated using a ~15 nm wide spectral window moving across all bands of the detector with respect to the central wavelength of each window position. The upright panels show cross-sections selected for each full hour step on the time axis (right) and for each 20 nm step labeled on the wavelength axis (left)

The observation is supported by the fact that both channels are automatically optimized in integration time to reach maximum raw DN values around 80% of the total dynamic range of the detector, unless available light is fading too much. The investigated instrument reached 80% of the nominal SNR around 1000 using automatically optimized integration times and subtracting the dark-current in the signal processing (Julitta et al., 2016). Thus, reported peak SNR values around 800 suggest that the results of the presented empirical approximation of operational SNR from field-measurements are plausible. Consequently, this approach was applied to consistently monitor operational SNR across measured and simulated up-welling radiance data during the study of a data-driven SIF-retrieval method (Naethe et al., 2022), presented in Study 1 of this thesis. Finally, SNR is important to trace the quality of field spectrometer measurements but covers only the random radiometric contribution to the total uncertainty budget. The inherited uncertainties and accuracy of the radiance calibration itself are not reflected in this consideration assuming the radiometric noise of the measured radiance as an instantaneous uncertainty. However, even without full traceability to a national standard, propagating operational noise can be considered a significant improvement to characterize better the uncertainty budget of the final data products from the FloX/RoX systems.

2.2.4 Field-measurement and retrieval uncertainties

The propagation of the radiometric uncertainty from calibrated radiance continues through further processing and corrections steps into the higher data products (Graf et al., 2023; Hueni et al., 2023). A very simple example for this cascading propagation would be calculating the NDVI (Tucker, 1979) based

on hyperspectral reflectance calculated from up-welling and down-welling radiance measured with the field spectrometer (Table 1).

Table 1: Reflectance (R), the NDVI (Tucker, 1979) *and iFLD* (Alonso et al., 2008) *far-red SIF as data products calculated from calibrated radiance measured by field spectrometers. The radiometric uncertainties of the calibrated radiance are propagate through the calculation of the partial derivative of the product equations. Uncertainty equations calculated after* (Farrance and Frenkel, 2012).

Data product	Associated radiometric uncertainty propagated
$\boldsymbol{R_{656} = \frac{L\uparrow_{656}}{L\downarrow_{656}}}$	$\sigma R_{656} = \sqrt{\left(\frac{\sigma L\uparrow_{656}}{\overline{L\uparrow_{656}}}\right)^2 + \left(\frac{\sigma L\downarrow_{656}}{\overline{L\downarrow_{656}}}\right)^2} \cdot \overline{R_{656}}$
$\boldsymbol{R_{800} = \frac{L\uparrow_{800}}{L\downarrow_{800}}}$	$\sigma R_{833} = \sqrt{\left(\frac{\sigma L\uparrow_{800}}{\overline{L\uparrow_{800}}}\right)^2 + \left(\frac{\sigma L\downarrow_{800}}{\overline{L\downarrow_{800}}}\right)^2} \cdot \overline{R_{800}}$
$\boldsymbol{NDVI = \frac{(R_{800} - R_{656})}{(R_{800} + R_{656})}}$	$\sigma NDVI = \sqrt{\left(\frac{\sqrt{\sigma R_{800}{}^2 + \sigma R_{656}{}^2}}{\overline{(R_{800} - R_{656})}}\right)^2 + \left(\frac{\sqrt{\sigma R_{800}{}^2 + \sigma R_{656}{}^2}}{\overline{(R_{800} + R_{656})}}\right)^2} \cdot \overline{NDVI}$
$\boldsymbol{SIF_{iFLD} = \frac{\alpha_R \cdot L\downarrow_{754} \cdot L\uparrow_{761}}{\alpha_R \cdot L\downarrow_{754} - \alpha_F \cdot L\downarrow_{761}} - \frac{L\downarrow_{761} \cdot L\uparrow_{754}}{\alpha_R \cdot L\downarrow_{754} - \alpha_F \cdot L\downarrow_{761}}}$	
$\sigma SIF_{iFLD} = \left(\left(\frac{\overline{\alpha_R \cdot L\downarrow_{754} \cdot L\uparrow_{761}}}{\alpha_R \cdot L\downarrow_{754} \cdot L\uparrow_{761} - L\downarrow_{761} \cdot L\uparrow_{754}} \right. \right. \cdot \sqrt{\left(\frac{\sigma L\downarrow_{754}}{\overline{L\downarrow_{754}}}\right)^2 + \left(\frac{\sigma L\uparrow_{761}}{\overline{L\uparrow_{761}}}\right)^2 + \left(\frac{\sqrt{(\alpha_R \cdot \sigma L\downarrow_{754})^2 + (\alpha_F \cdot \sigma L\downarrow_{761})^2}}{\overline{\alpha_R \cdot L\downarrow_{754} - \alpha_F \cdot L\downarrow_{761}}}\right)^2} \Bigg)^2 + \left(\frac{\overline{L\downarrow_{761} \cdot L\uparrow_{754}}}{\alpha_R \cdot L\downarrow_{754} \cdot L\uparrow_{761} - L\downarrow_{761} \cdot L\uparrow_{754}} \right. \cdot \sqrt{\left(\frac{\sigma L\downarrow_{761}}{\overline{L\downarrow_{761}}}\right)^2 + \left(\frac{\sigma L\uparrow_{754}}{\overline{L\uparrow_{754}}}\right)^2 + \left(\frac{\sqrt{(\alpha_R \cdot \sigma L\downarrow_{754})^2 + (\alpha_F \cdot \sigma L\downarrow_{761})^2}}{\overline{\alpha_R \cdot L\downarrow_{754} - \alpha_F \cdot L\downarrow_{761}}}\right)^2} \Bigg)^2 \Bigg)^{1/2}$	

The basis for this calculation is the inherent (fully traceable) or instantaneous (operational), radiometric uncertainty of the calibrated radiance data. The signal noise is mathematically derived in the inherent case above using equation 1. Conversely, noise is empirically approximated in the instantaneous case. The propagation of the radiometric uncertainty is calculated from partial derivatives of the data product equation in Table 1 (Farrance and Frenkel, 2012; JCGM, 2008). Thus, the up-welling und down-welling radiance $L\uparrow$ and $L\downarrow$ require each the associated radiometric

uncertainty $\sigma L\uparrow$ and $\sigma L\downarrow$ with respect to the central wavelengths at 656 nm and 800 nm computing reflectance and NDVI. The purely radiometric uncertainty of the measured up-welling and down-welling radiance propagates first into the calculated reflectance R at 656 nm and at 800 nm, which are further used to calculate the NDVI (Table 1). Taking experimental radiance data the from red/NIR spectrometer of the FloX in Selhausen, Germany, on November 18th 2020 for example with $L\downarrow_{656}= 82.71, L\uparrow_{656}= 4.44, L\downarrow_{800}= 86.41, L\uparrow_{800}= 42.72$, all given in *mW m^{-2} sr^{-1} nm^{-1}* results in $R_{656} = 0.054$ and $R_{800} = 0.494$, furthermore $NDVI = 0.80$ respectively. Propagating the instantaneous radiometric uncertainties $\sigma L\downarrow_{656}= 0.151, \sigma L\uparrow_{656}= 0.024, \sigma L\downarrow_{800}= 0.108, \sigma L\uparrow_{800}= 0.061$, all given in *mW m^{-2} sr^{-1} nm^{-1}* yields a radiometric uncertainty for the reflectance products of $\sigma R_{656} = 0.0004$ and $\sigma R_{800} = 0.0009$. This radiometric uncertainty propagates into $\sigma NDVI = 0.0014$ (Table 1). These radiometric noise uncertainties are negligibly small with respect to the observed values, which equate to 0.2% relative uncertainty for NDVI, 0.7% for R_{656} and 0.1% for R_{800} respectively. For comparison, study 4 demonstrated an average relative uncertainty around 10% - 20% in between the airborne multispectral products and the ground reference due to added influences from e.g. instrument handling, spatial representativeness, BRDF, sensor alignment and atmosphere under field conditions in Figure 42 (Naethe et al., 2023).

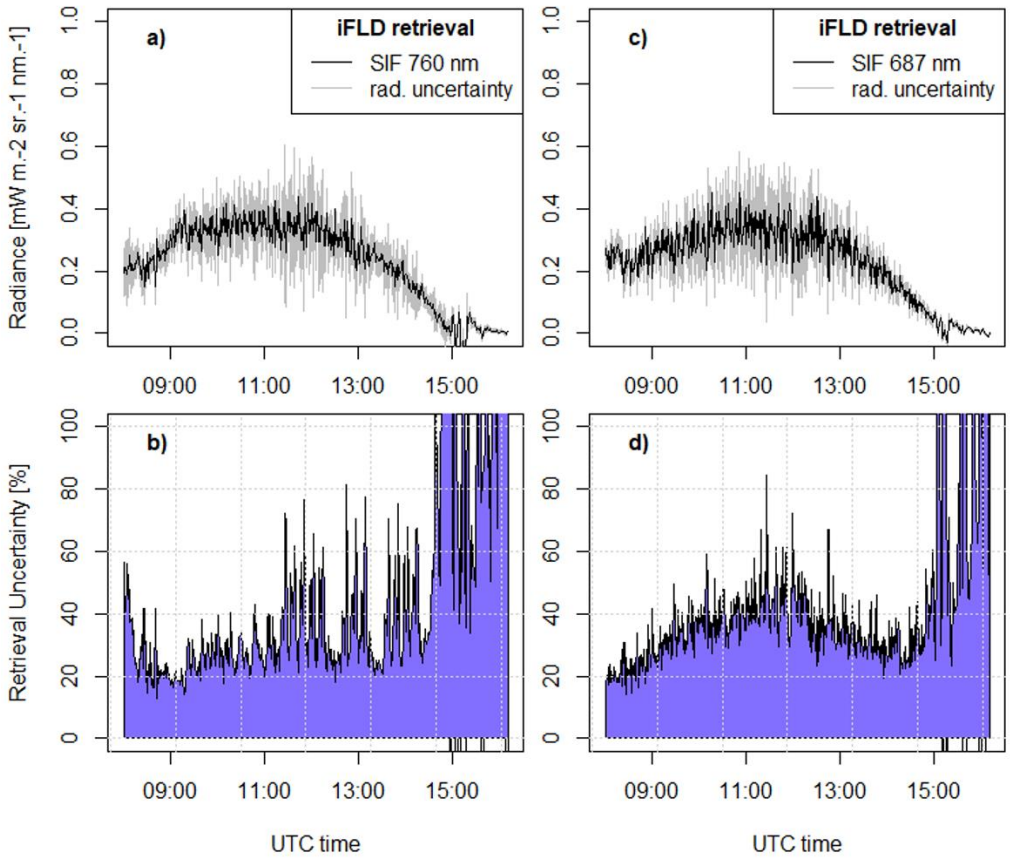

Figure 4: Diurnal far-red SIF around 760 nm a) and red SIF around 687 nm c) retrieved with the iFLD method from FloX measured data in Selhausen, Germany, on November 6, 2020. The mathematically propagated radiometric uncertainty from instantaneous signal noise is shown in grey. The relative uncertainty with respect to signal magnitude is reported for SIF 760 nm b) and SIF around 687 nm d), respectively.

Nevertheless, it is noteworthy that the increasingly complex mathematical propagation of uncertainties for higher products implies increased uncertainties with each processing step. For example, the family of FLD based SIF retrieval methods relies on spectral bands inside and outside of telluric oxygen absorption features (Alonso et al., 2008; Plascyk and Gabriel, 1975). Taking the optimization coefficients as $\alpha_R = 0.9898$ and $\alpha_F = 1.2518$ from (Alonso et al., 2008), the SIF signal from field measurements using the FloX and retrieved with the improved FLF (iFLD) method for far-red SIF around 760 nm results in *0.35 mW m^{-2} sr^{-1} nm^{-1}*, also assuming $L\downarrow_{754} = 119.591$, $L\downarrow_{761} = 46.832, L\uparrow_{754} = 25.367, L\uparrow_{761} = 10.296$, all in *mW m^{-2} sr^{-1} nm^{-1}* (Table 1). Taking the associated radiometric uncertainties from the radiometric noise of field measurements (Figure 3) as $\sigma L\downarrow_{754} = 0.136$, $\sigma L\downarrow_{761} = 0.118, \sigma L\uparrow_{754} = 0.055, \sigma L\uparrow_{761} = 0.052$, all in *mW m^{-2} sr^{-1} nm^{-1}*, yields a radiometric uncertainty of the iFLD far-red SIF around *0.11 mW m^{-2} sr^{-1} nm^{-1}*, which is with 31% relative uncertainty significant (Figure 4). For iFLD red SIF 0.38 *mW m^{-2} sr^{-1} nm^{-1}* with 0.16 *mW m^{-2} sr^{-1} nm^{-1}* uncertainty, 42% were reported in the same fashion. The iFLD method is sensitive to noise (Damm et al., 2011). Therefore, it is observed how the relative uncertainty of the iFLD retrieval is radically increased in the afternoon with decreasing SNR after the automatic signal optimization of the spectrometer was at its limits due to fading daylight (Figure 4). Influences from the automatic optimization in the FloX adjusting the integration time to changing incoming radiation result in noticeable spikes in the relative retrieval uncertainty throughout the diurnal course. Especially the undershooting of the optimal signal levels in the afternoon lowered the raw signal below 80% of the dynamic range due to decreasing light and thus increased the radiometric noise with respect to the integration time not yet adjusted. Furthermore, the iFLD method tends to overestimate especially lower SIF signals and to underestimate higher SIF signals around 687 nm (Cendrero-Mateo et al., 2019), which is also observed in the presented results. Study 1 also presents the results from other SIF retrievals of that day (Figure 10). The poor performance especially in the red SIF suggests the iFLD method not suitable as a mechanistic reference for study 1, which employs the SFM retrieval instead. Note that different retrieval methods have specific uncertainty functions and will propagate uncertainties differently (Chang et al., 2020a). Also, this example is based on a simplification in relation to determining the optimization coefficients base on the reflectance shape. The above presented calculation accounts only for the radiometric noise of the measurements with the dark current removed. In addition, dark-current, non-linearity, temperature, integration time and cosine receptor response need to be considered in a more complete model of the sensor (Pacheco-Labrador and Martin, 2014; Pacheco-Labrador and Martín, 2015). Furthermore, instrument setup and optical alignment (Aasen et al., 2019), target structure and geometry, BRDF, SZA and viewing angel, sensor field of view, surface heterogeneity, temporal misalignments and the atmosphere affect measured radiance data and also propagate as uncertainties into the final product (Chang et al., 2021).

Finally, uncertainties of representativeness, which are associated to the spatial extend of the field spectrometer footprint in comparison to other optical sensors or physical probing strategies require consideration in the final uncertainty budget (Buman et al., 2022). This aspect is particularly relevant in field measurements when cross-comparing data products of multiple optical sensors and outweigh effects of SNR, above all when averaging sufficient repetitions of individual ground measurements minimizes random uncertainties (Hueni et al., 2017; Pacheco-Labrador et al., 2019a). Measurement system analysis describes the complete interactions of the observed object, the instrument, the operator, the measurement method and the outer environment contributing to the overall uncertainty budget of the data product (JCGM, 2020). The complete uncertainty budget includes the full propagation of all random and systematic uncertainties. Conversely, this implies that random uncertainties are addressed by a sufficient number of repetitions and systematic uncertainties by validation and calibration against a trustworthy reference or by using suitable correction models in the reflectance products (Naethe et al., 2023). Further considerations are required when addressing systematic influences of atmospheric distortion in the retrieval of the SIF signal (Naethe et al., 2022). At last, the complete propagation of relevant uncertainties into the data products must be considered for allowing a meaningful interpretation and traceability.

2.3 Validation and calibration of optical data across different sensors

The hyperspectral resolution of automated field spectrometer systems allows cross-comparing of a single instrument with many different multispectral or hyperspectral, imaging or point sensors recording an overlapping spectral range. A common scenario of application is the cross-validation of airborne or satellite instruments using the ground measurements of hyperspectral reflectance as a reference (Barnes et al., 2000; Biggar et al., 2003; Bouvet et al., 2019; Green et al., 1998; Hueni et al., 2017; Peddle et al., 2001; Pompilio et al., 2018; Schaepman-Strub et al., 2008). However, current protocols of reflectance calibration for airborne or satellite sensors oftentimes refer to a single reference only and lack a continuous tracing of changing, down-welling radiance (Ariza et al., 2018; Hakala et al., 2018; Olsson et al., 2021). Continuous changes of illumination over time determine a substantial systematic drift of the calibrated reflectance and require a correction. Furthermore, changing illumination angel and changing viewing angle cause significant alterations of the surface reflectance signature and lead to a distinctive Bi-directional Reflectance Distribution Function (BRDF), which is uniquely dependent on surface roughness, structure, geometry and the materials' optical properties (Aasen and Bolten, 2018; Burkart et al., 2015a; Liu and Liu, 2018; Rautiainen et al., 2018; Vargas et al., 2020). The Hemispherical Directional Reflectance Function (HDRF) considers in addition the scattering of light inside the atmosphere and is therefore also referred to as blue-sky reflectance (Milton et al., 2009; Painter and Dozier, 2004; Schaepman-Strub et al., 2008). Mechanistic correction

methods require sufficient knowledge of those parameters (Richter and Schläpfer, 2002; Schläpfer and Richter, 2002) and are not always feasible. An empirical correction using proximity sensing in the field is therefore oftentimes the best choice (Karpouzli and Malthus, 2003; Peng et al., 2022; Pompilio et al., 2018; Wang and Myint, 2015). However, this proposes the challenge of limiting the transfer of biases from the proximity sensing further into the validation and calibration of airborne or satellite sensors (Liu and Liu, 2018). The automated field spectrometers are very dependable references as they are designed to minimize instrumental uncertainties, allow many rapidly recorded repetitions and support the assessments of systematic offsets at the same time. One possible way to address biased reflectance is the acquisition of ground-based, airborne and satellite measurements at exactly the same time with a nadir viewing angle and ensuring an identical sun angle (Buman et al., 2022). Furthermore, artificial reference targets with known BRDF and reflectance characteristics, which are visible both from ground-based and airborne sensors support cross-validation and calibration (Hakala et al., 2018, 2013; Honkavaara and Khoramshahi, 2018). Spatial representativeness is also an issue especially for the comparison of differently sized pixels and spectrometers footprints on natural surfaces, but is negligible for homogenous, artificial targets (Biggar et al., 2003; Buman et al., 2022; Graf et al., 2023). Furthermore, automated field spectrometer systems are very suitable for the application as ground reference, as they record continuously and unattended down-welling and up-welling radiance of a known point on the ground, while the size of this point is adjusted with the distance between sensor and target. Set up some time before and left for some time after the airborne acquisition, the automated field spectrometer can remain in the field and requires no further human interaction. Eventually, applications such as airborne mapping, land surface classification or change detection greatly benefit from inter-calibrated data (Green et al., 1998; Rahman et al., 2001; Roberts et al., 2002; Ustin et al., 2004). Satellite data, for example ESA's Sentinel-2, are vigorously standardized, validated and repeatedly calibrated to provide a credible and traceable reference for surface reflectance (D'Odorico et al., 2013; Drusch et al., 2012; Origo et al., 2020). Unfortunately, multispectral resolution and acquisition time of this satellite data do not always match with the airborne sensors. Addressing this issue, a suitable transfer instrument is required, which covers the spectral and temporal mismatch. The automated field spectrometer can serve as such a transfer instrument, whether purposefully integrated into the airborne mission planning or already available from long-term monitoring at the investigated sites, as examined in Study 3 and 4 in this thesis (Naethe et al., 2024, 2023). The following essential assumptions must be satisfied by the automated field spectrometer for the consideration of a solid ground reference: (I) The spectrometer ground-sampling points should be homogenous and the surrounding area should be representative in vegetation cover and size with respect to the pixel projection of the satellite and airborne sensors. (II) The hyperspectral

range of the field spectrometer should overlap with the multispectral airborne and satellite sensors. (III) The time of airborne and satellite data acquisition overlap each with the ground measurements.

2.4 Knowledge gain and scientific contribution

This thesis is based on the legacy of field spectroscopy for proximity sensing of the past decades (Milton, 1987; Milton et al., 2009). With the arrival of fully automated field spectrometer systems unprecedented use cases were enabled, e.g. in the retrieval of SIF and continuous vegetation monitoring (Cogliati et al., 2015a; Gamon, 2015; Julitta et al., 2016; Pacheco-Labrador and Martín, 2015). Modern automated field spectrometers enable the retrieval of SIF from long time series, but the small contribution of the signal poses challenges towards the technical requirements especially under lowered light and lowered SIF emission (Mohammed et al., 2019). Under laboratory conditions SNR around 1000 in combination with a spectral resolution FWHM < 0.5 nm was identified suitable for reliable SIF retrievals exploiting absorption feature of telluric oxygen (Julitta et al., 2016). However, telluric oxygen also reabsorbs SIF and causes a distortion of the measured signal even at the level of proximity sensing (Aasen et al., 2019; Sabater et al., 2018). Instead, exploiting SFL is in principle unaffected by atmospheric reabsorption, but technically even more demanding due to the very small absorption features and results in a very noisy signal retrieval (Guanter et al., 2013). Furthermore, propagating the random uncertainties around field-measured radiance is important to enable quality control for SIF retrievals and annotate quantitative uncertainties to the final product (Chang et al., 2020a). We developed a novel SIF retrieval based on the PLS algorithm to exploit SFL unaffected by atmospheric reabsorption and low retrieval noise, using the quantitative radiometric uncertainties to inform realistic modelling of synthetic radiance data for the purpose of training and validating the ML-based model on large spectral windows (Naethe et al., 2022). This study enabled for the first time the application of the PLS regression for SIF retrieval in measured field data, which is distinctively more challenging compared to pure modelling exercises (Rivera-Caicedo et al., 2014; van der Tol et al., 2016; Verrelst et al., 2016a). In addition, the high computation speed of the ML algorithm outperformed other, mechanistic retrievals. Furthermore, purely measured hyperspectral down-welling radiance from the automated field spectrometer RoX and NOx concentration from an urban measuring station were analyzed using ML in our second field study (Naethe et al., 2020). The study investigated the results of fundamentally different ML approaches, suggesting that a qualitative distinction (low uncertainty) and even a quantitative distinction (higher uncertainty) was possible. As major contribution, the potential of exploiting atmospheric properties from the continuous down-welling radiance measurements of automated field spectrometers using ML was demonstrated, further useful for applications in pollution monitoring or investigating natural atmospheric changes (Ehn et al., 2014; Kanniah et al., 2012; Sirignano et al., 2010). At last, ground-based measurement networks of optical

atmospheric properties are relevant for the calibration of satellites, atmospheric correction of top-of-atmosphere reflectance and cloud screening (Bouvet et al., 2019; Giles et al., 2019; Zhang et al., 2021).

The introduction of commercially available, automated spectrometer systems made them accessible to a wider range of users at a large scale, but requires consistent and standardized, radiometric measurements to derived data products including uncertainty support (Buman et al., 2022; Hueni et al., 2023). Due to full instrument characterization, propagation of all uncertainties and full traceability back to the international standard being not always possible nor economically feasible for an ever increasing number of optical instruments in service, an alternative consistency assessment of data products from the automated spectrometer systems FloX/RoX was required. Using Sentinel-2 as a globally stable reference (Graf et al., 2023; Origo et al., 2020), we enabled for the first time the investigation of consistency of automated field spectrometer measurements and harmonized their products from proximity sensing across 10 field sides around the world (Naethe et al., 2024). Furthermore, pixel-based temporal-spatial clustering using continuous time-series of high temporal resolution was used for finding areas considered as sufficiently homogenous for the cross-validation of field spectrometer and satellite. A standardized network of automated field spectrometers contributes to improve integration of data and enhance comparability of products with other systems to ensure long-term usability (Hueni et al., 2009). Field spectrometers are widely used for cross-calibrating proximity sensing and remote sensing products from the ground to the aircraft (Biggar et al., 2003; Hueni et al., 2017; Origo et al., 2020; Peddle et al., 2001). However, the lack of continuously tracing the diurnal fluctuation of incoming light on the ground poses a severe limitation for reflectance calibration, but possible to overcome using automated field spectrometers. The new concept of using trustworthy satellite reflectance for validating proximity sensing was further investigated and brought forth by using automated field spectrometers as a transfer instrument to inter-calibrate other airborne sensors with respect to the satellite in our fourth case study (Naethe et al., 2023). Furthermore, continuous measurements of down-welling radiance were investigated to support the correction of airborne reflectance during the day and inform the detection of clouds from the ground. This case study contributed a detailed, best-practice example using FloX/RoX devices for airborne sensor inter-calibration. Eventually, the presented approach could be easily adapted to other sensors on aircraft for future campaigns.

3 Study 1 - A precise method unaffected by atmospheric reabsorption for ground-based retrieval of red and far-red sun-induced chlorophyll fluorescence

Published in: Naethe, P., Julitta, T., Chang, C.Y.Y., Burkart, A., Migliavacca, M., Guanter, L., Rascher, U., 2022. A precise method unaffected by atmospheric reabsorption for ground-based retrieval of red and far-red sun-induced chlorophyll fluorescence. Agric. For. Meteorol. 325. https://doi.org/10.1016/j.agrformet.2022.109152.

Original manuscript integrated, format, layouts and numberings of elements adjusted, all references included into the bibliography in Chapter 9 of this dissertation.

CRediT Author Statement: **Paul Naethe:** Conceptualization, Methodology, Data curation, Software, Validation, Investigation, Formal analysis, Writing - Original draft, Writing – Review & Editing, Visualization. **Tommaso Julitta:** Validation, Funding acquisition, Supervision. **Christine Yao-Yun Chang:** Resources, Writing – Review & Editing. **Andreas Burkart**: Resources, Funding acquisition. **Mirco Migliavacca**: Conceptualization, Resources, Writing – Review & Editing. **Luis Guanter:** Conceptualization, Resources, Writing – Review & Editing. **Uwe Rascher:** Conceptualization, Supervision, Resources, Writing – Review & Editing.

Keywords: Solar Induced Chlorophyll Fluorescence, Field Spectroscopy, Remote Sensing, SIF Retrieval, Ground Measurements, FloX

3.1 Abstract

Remote sensing employs solar-induced chlorophyll fluorescence (SIF) as a proxy for photosynthesis from field to airborne and satellite sensors. The investigation of SIF offers a unique way of studying vegetation functioning from the local to the global scale. However, the passive, optical retrieval of the SIF signal is still challenging. Common retrieval approaches extract the SIF infilling directly from atmospheric oxygen bands in down-welling and up-welling radiance. They often involve a complex signal correction to compensate for atmospheric reabsorption and require long computing time. In contrast, the exploitation of solar Fraunhofer lines is devoid of atmospheric disturbances. We propose a new retrieval method for red and far-red SIF directly from up-welling radiance spectra in the spectral range between 650 nm and 810 nm by applying Partial Least Squares (PLS) regression machine learning. Solar Fraunhofer lines are exploited for SIF retrieval with the PLS approach by excluding telluric absorption features. The PLS models are trained and tested on synthetic reflectance and SIF data modeled with SCOPE. We identified a logarithmic relationship of the retrieval error with respect

to signal-to-noise ratio of the instrument. The approach has been tested with real-world data measured by the Fluorescence Box (FloX), and evaluated against two well-established retrieval methods: the spectral fitting method (SFM) and the singular value decomposition (SVD). PLS models exploiting solar Fraunhofer lines retrieved meaningful SIF values with high precision and demonstrated robustness against atmospheric reabsorption, including from a 100m tall tower. In addition, PLS retrieval requires no complex correction for atmospheric reabsorption and computes 37 times faster than SFM. Hence, PLS retrieval allows fast and robust exploitation of SIF from solar Fraunhofer lines with high precision under conditions in which other retrieval approaches require complex atmospheric correction.

3.2 Introduction

Remote sensing of solar-induced chlorophyll fluorescence (SIF) has been studied in the past decades as a non-invasive method to track photosynthesis from leaf to global scales (Mohammed et al., 2019). The signal is emitted as light in the red and near-infrared (NIR) wavelengths (Porcar-Castell et al., 2014). It is comprised of contributions from both photosystems II and I (Agati et al., 1995; Magney et al., 2019b). Thus, simultaneous monitoring of red and far-red fluorescence allows for obtaining direct insight into the light reactions and light-use efficiency of photosynthesis (Wieneke et al., 2018). At the leaf level, SIF changes as plants adjust photosynthesis and non-photochemical quenching in response to environmental conditions such as temperature, light, available water, and nutrients (Alonso et al., 2017; Camino et al., 2018; Campbell et al., 2019; Cendrero-Mateo et al., 2016; Martini et al., 2022, 2019; Sun et al., 2017; Zarco-Tejada et al., 2016). Additionally, canopy structure affects light absorption, scattering, and fluorescence emission, thereby also influencing the SIF signal (Dechant et al., 2020; Migliavacca et al., 2017; Van Wittenberghe et al., 2015). The true SIF signal is unknown and difficult to retrieve under natural conditions for its complex nature. The Soil Canopy Observation, Photochemistry and Energy fluxes (SCOPE) model fully integrates leaf-level radiative transfer and heat fluxes in the canopy and produces realistic fluorescence spectra for the validation of canopy SIF retrieval (van der Tol et al., 2009; Verhoef et al., 2018; Verrelst et al., 2016b; Yang et al., 2021). On the other hand, inversion of the SCOPE model allows the inference of parameters related to photosynthesis and energy balance from measured canopy hyperspectral reflectance (Guanter et al., 2012; Pacheco-Labrador et al., 2019b; van der Tol et al., 2016; Verrelst et al., 2015). Evaluation of SIF retrieval methods for the optical exploitation of the signal are performed with SCOPE simulated datasets, including known reflectance and SIF spectra (Cogliati et al., 2015b).

The passive optical exploitation of SIF using hyperspectral sensors at the top-of-canopy (TOC) has great potential to enhance global monitoring of primary production across both natural ecosystems and agricultural landscapes (Damm et al., 2010a; Dechant et al., 2022; Goulas et al., 2017; Guanter et al.,

2014; Magney et al., 2019a; Martini et al., 2019; Migliavacca et al., 2017; Nichol et al., 2019; Sun et al., 2018; Tagliabue et al., 2019; Wohlfahrt et al., 2018). Towards this goal, automated SIF monitoring field spectrometer systems have been developed for deployment on stationary towers (Burkart et al., 2015b; Cogliati et al., 2015a; Daumard et al., 2010; Drolet et al., 2014; Meroni et al., 2011; Rascher et al., 2009; Rossini et al., 2010), UAVs (Bendig et al., 2019; Chang et al., 2020b; Mac Arthur et al., 2014; Wang et al., 2021).Imaging sensors retrieve SIF on aircraft (Frankenberg et al., 2018; Wieneke et al., 2016). Current systems include, for example, TriFLEX (Daumard et al., 2010), Piccolo Doppio (Mac Arthur et al., 2014), PhotoSpec (Grossmann et al., 2018), FAME (Gu et al., 2019), FluoSpec2 (X. Yang et al., 2018), and Fluorescence Box (FloX) (Julitta et al., 2017). These field spectroscopy systems have been invaluable for calibration and validation of airborne and satellite missions (Porcar-Castell et al., 2015; Rossini et al., 2015) as well as investigating temporal, structural, and physiological dynamics of the monitored target (Fournier et al., 2012; Perez-Priego et al., 2015; Rossini et al., 2010). The potential of spectrometers was also further investigated in their own realm on the ground (Magney et al., 2017; X. Yang et al., 2018). Together, these ground-based measurements support the development of upcoming satellites such as the ESA Earth Explorer 8 candidate FLEX (Drusch et al., 2017; Middleton et al., 2017; Mohammed et al., 2019; Rascher et al., 2015), and enable calibration and validation of satellite SIF retrieval methods and data products (Hueni et al., 2017).

Different retrieval methods have been proposed to retrieve the SIF signal from continuous measurements of down-welling and up-welling radiance recorded by systems with different instrument configurations, as comprehensively reviewed by Meroni et al. (2009) and Cendrero-Mateo et al. (2019). The Fraunhofer Line Discrimination (FLD) method (Plascyk and Gabriel, 1975) is the basis for further, more advanced FLD retrieval algorithms, e.g. iFLD (Alonso et al., 2008). FLD estimates the emission of SIF through relative infilling of the telluric absorption bands, located around 687 nm (the Oxygen-B band, from which SIF-B is retrieved) and around 760 nm (the Oxygen-A band, from which SIF-A is retrieved). The Spectral Fitting Method (SFM) models the spectral shape of fluorescence and reflectance as mathematical functions to retrieve and correct signal intensities (Cogliati et al., 2015b; Meroni et al., 2010). SFM is a mechanistic approach based on physical principles and describes the spectral shape of the actual fluorescence signal but suffers from costly computation. Because of its reliability, we used it as the reference for field measurements in this study. The SFM is applied as the standard processing method for fluorescence retrieval with the FloX monitoring field spectrometer, optimizing first guessed SIF values from the iFLD. Both FLD and SFM approaches require high-resolution hyperspectral data around the telluric absorption features to exploit their infilling (Cendrero-Mateo et al., 2019; Cogliati et al., 2019; Julitta et al., 2016). Recently an improvement of the SFM method has been developed: The SpecFit method that allows for the retrieval of the full spectral SIF signal in ground-based field spectrometer measurements (Cogliati et al., 2019). Retrieval algorithms do not

allow the exploitation of the spectral region of telluric water vapor (H_2O) between 715nm and 735nm. Although it overlaps well with the SIF emission spectrum, rapid fluctuations impair signal retrieval (Köhler et al., 2015).

However, current research highlights the necessity for correction of atmospheric influences due to varying air-column in the oxygen bands when retrieving SIF. In particular, reabsorption affects the accurate retrieval of SIF severely in the Oxygen-A absorption band around 760 nm and to a lesser extent in the Oxygen-B band around 687 nm (Sabater et al., 2018). Atmospheric reabsorption remains an issue with the computationally costly SFM and other retrieval approaches based on telluric absorption features. If the instrument is positioned in the midst of the atmospheric column more than a few meters above canopy, this effect is increasingly significant. (Aasen et al., 2019). An empirical correction approach partially addresses the issue but could not successfully demonstrate the retrieval of positive SIF-A values (Liu et al., 2019b). An alternative is the use of solar Fraunhofer lines, which are in principle unaffected by changes in relative aerosol thickness of the atmospheric column and cloud cover. For example, the data driven Singular Vector Decomposition (SVD) method can be configured to either exploit telluric oxygen absorption features or the solar Fraunhofer lines (Chang et al., 2020a; Guanter et al., 2013). SVD is capable of retrieving far-red SIF from satellite or ground-based field spectrometers with spectral resolution around 0.13 nm FWHM (Guanter et al., 2013, 2012; K. Yang et al., 2018). The SVD is limited to the accurate, SIF-free forward modeling of up-welling radiance and computes SIF as an inverse problem from the residuals. Furthermore, studies have shown reliable SIF retrieval solely by exploiting SIF infilling in solar Fraunhofer absorption lines between 757 nm and 771 nm from satellite data (Frankenberg and Berry, 2018; Sun et al., 2018).

Here, we propose a novel retrieval of red SIF-B and far-red SIF-A based on the supervised machine learning algorithm Partial Least Squares (PLS) multivariate regression. The method developed aims at overcoming the shortcomings of the SVD and the SFM in terms of computing time, robustness, precisions, evading forward model inversion and without needing to compensate atmospheric reabsorption. PLS combines dimensionality reduction and statistical multivariate regression. The algorithm origins from quantitative analysis in chemo-metrics and was also applied to other fields of research (Biagioni et al., 2011; Biancolillo and Marini, 2018; Dayal and Macgregor, 1997; Wagner et al., 2018). PLS is widely used for the retrieval of signals in mixture from a large number of variables (Jin and Wang, 2019; Schmidtlein et al., 2007; Wiklund, 2007). Further applications of the PLS algorithm include the analysis of vegetation with regards to leaf mass, canopy foliar chemicals, morphological and functional traits as well as the remote assessment of biodiversity with hyperspectral reflectance data (Cavender-Bares et al., 2016; Ma et al., 2019; Serbin et al., 2019; Serbin and Townsend, 2020; Singh et al., 2015). PLS regression decomposes the predictor data space into components (latent variables). As opposed to the SVD, latent variables are obtained with PLS in an iterative process, which

optimizes the components to explain the most covariance between predictor and response in the transferred orthogonal space of the singular vectors (Dayal and Macgregor, 1997). Component loading and score matrices are computed accordingly. Regression coefficients directly explain the variation in the response variable by using the transferred scores. In contrast to SVD-based SIF retrievals PLS does not compute the measured up-welling signal and residuals in a forward model. Instead, PLS is a supervised machine learning approach which predicts the response variable using a trained model to exploit the covariance structures between predicted variable (SIF) and predictor (preprocessed, up-welling radiance) in the transformed predictor space.

In this study, we developed a new PLS retrieval method for the retrieval of SIF from up-welling radiance and evaluated its performance on a synthetic test dataset and on field measurements collected with the FloX instruments deployed over three field sites with differing vegetation targets. For this purpose, a dataset of synthetic up-welling radiance including SCOPE-modelled SIF was created. Two configurations of the PLS model were evaluated, the first covering the entire spectrum of the FloX sensor between 650 nm and 810 nm and the second excluding the telluric oxygen and water absorption bands. We further modelled a synthetic sensor with an adjustable Signal to Noise Ratio (SNR) to test the robustness of the approach across changing SNR with changing signal intensity. Finally, we compared the performance of PLS exploiting solar Fraunhofer lines against the two state-of-the-art retrieval methods (SFM and SVD) on both synthetic and measured data. The evaluation was focused on different aspects of the method: the performance, the speed, and the robustness against conditions where the SFM and SVD methods are not applicable.

3.3 Materials and methods

First, PLS models were tested for the prediction of red SIF-B around 687 nm and far-red SIF-A around 760 nm in different configurations using synthetic up-welling radiance data in which we could precisely control the spectral SIF contribution. Furthermore, the retrieval error of PLS was assessed against SCOPE simulated SIF in a synthetic test dataset in comparison to SFM and SVD. Secondly, we applied the optimized PLS models to retrieve SIF-B and SIF-A from up-welling radiance, measured at three different sites. The workflow of composing training data, tuning and evaluating the PLS models is described below.

3.3.1 Modelling synthetic data

We created a dataset of synthetic up-welling radiance spectra, which contained modelled fluorescence ranging between 0 and 5 mW m^{-2} sr^{-1} nm^{-1}. To do so, we randomly selected 30 measurements of down-welling radiance from a clear day recorded by each of the three instruments. We used SCOPE to model 265 different SIF and reflectance spectra. The SCOPE dataset has been obtained through inversion

against TOC reflectance collected over grassland (Pacheco-Labrador et al., 2019b). The down-welling radiance spectra were then combined with each of the SIF and reflectance spectra using a strong permutation, which randomly shuffled and 3-fold oversampled each SIF and reflectance spectra. Thus, a total synthetic dataset of 23,850 up-welling radiance spectra (L) at TOC was obtained according to Equation 6. Here $\widehat{\mathrm{T}}$ is the total atmospheric transmittance (including both direct and diffuse radiation) of the entire path-length to the target and back to the sensor, R is the reflectance, E is the down-welling irradiance, F the fluorescence signal and $\check{T}$ considers the reabsorption of fluorescence for the transmittance of the single path-length between target and sensor, specified for wavelength λ and view field direction Ω.

$$\mathbf{L}_{\boldsymbol{\lambda},\,\boldsymbol{\Omega}} = \widehat{\mathbf{T}}_{\boldsymbol{\lambda},\boldsymbol{\Omega}} \times \mathbf{R}_{\boldsymbol{\lambda},\,\boldsymbol{\Omega}} \times \mathbf{E}_{\boldsymbol{\lambda},\,\boldsymbol{\Omega}} + \mathbf{F}_{\boldsymbol{\lambda},\,\boldsymbol{\Omega}} \times \check{\boldsymbol{T}}_{\boldsymbol{\lambda},\boldsymbol{\Omega}} \tag{6}$$

The relative fractional depth of solar Fraunhofer lines remains unaffected by atmospheric attenuation in spectral regions devoid of telluric absorption features (Frankenberg and Berry, 2018; Guanter et al., 2012). Thus, atmospheric modelling is greatly simplified if no telluric absorption bands are present. The influence of total atmospheric transmittance as well as reabsorption can be neglected if retrieving SIF from the fractional infilling of solar Fraunhofer lines in spectral regions with flat telluric absorption. In this study we retrieved SIF from both telluric oxygen absorption features (O_2-A and O_2-B) considering atmospheric attenuation and reabsorption, as well as the solar Fraunhofer lines devoid of telluric absorption features. We resampled the SCOPE-simulated SIF and reflectance spectra, which were initially generated at a resolution of 1 nm. Because they are relatively smooth, linear interpolation was used with respect to the FloX Instrument Spectral Response Function of the down-welling radiance measurements.

SIF-B and SIF-A values were extracted from the SCOPE modelled SIF spectra at 687nm and 760nm, respectively, and used as response variables for the model training, testing and retrieval benchmark. The measured down-welling radiance data already contains atmospheric absorption at sensor height together with characteristic spectral response and noise from the respective instrument. This measured noise was statistically decreased as the same down-welling radiance measurements were repeatedly used to model multiple synthetic up-welling radiances in different combinations with SCOPE-modelled SIF and true reflectance. Thus, the following noise assumptions were added to account for the actual noise levels found in real-world measurements. First, Noise equivalent delta Radiance (NedL) was characterized according to Schaepman and Dangel (2000), using the FloX spectrometer configured for 0.3 nm FWHM spectral resolution and 0.1 nm spectral sampling rate around 820 SNR. As shown in Equation 7, NedL is computed with respect to wavelength for each pixel with the radiometric calibration gain *g*. The detector was characterized with 110 measurements of a stable light source and dark current in digital numbers for an integration time (IT) optimized at 80% of

the detector's dynamic range, with $\sigma^2(N)$ and $\sigma^2(N_{DC})$ being the standard deviation of the lamp and the dark-current, respectively.

$$\boldsymbol{NedL(\lambda) = \frac{\sqrt{\sigma^2(N_\lambda) + \sigma^2(N_{DC,\lambda})}}{IT} \cdot g(\lambda)} \tag{7}$$

In our case, the noise was considered consistent due to an automatic optimization of the integration time (IT) in the FloX, resulting in a steady signal-level around 80% of the detector's dynamic range. Note that this assumption does not hold for devices without automatic optimization of the signal level, as the noise scales with changing signal level at the detector.

To simulate random noise as described in Equation 8, we then applied Monte Carlo simulation using a normal distribution N centered at mean zero and standard deviation equal to NedL to propagate instrument-characteristic uncertainty for ca. 80% optimized signal exposure at detector level to the synthetic dataset.

$$\boldsymbol{Noise_{\lambda,\Omega} = \mathbf{N}(0, c \cdot NedL_\lambda)_\Omega} \tag{8}$$

The artificial noise level was controlled with scaling factor c to replicate the actual SNR in real measured data. Thus, simulated noise was computed individually and added to each instance in the synthetic dataset. Signal to noise ratio (SNR) was calculated as denoted in Equation 9:

$$\boldsymbol{SNR = \frac{\mu L_{\lambda,\Omega}}{\sigma Noise_{\lambda,\Omega}}} \tag{9}$$

with μL being the mean signal intensity with respect to wavelength and $\sigma Noise$ being the standard deviation of the simulated, random noise with respect to wavelength for this detector. Note that zero noise was not simulated as the SNR is not defined or infinite in this case.

Following the approach of Caporaso et al. (2018), we computed the first spectral derivative with respect to wavelength as a final pre-treatment. The first spectral derivative expresses the change in spectral shape rather than the actual intensities in the spectral continuum. Training the PLS on the first spectral derivative ensured that the algorithm exploits relative changes in the up-welling radiance instead of absolute intensities. Thus, offsets from absolute intensities were eliminated. We then split the synthetic dataset into 60% training and 40% testing datasets by randomized selection. The PLS was trained to exploit the covariance in the first spectral derivatives with respect to SIF-B values or SIF-A values given from the SCOPE simulation, decomposing the spectral-temporal domain into orthogonal scores and loadings. This testing dataset was further used for evaluation of the retrieval error against the known SCOPE SIF, where we compared the methods of PLS, SFM and SVD, as described below. We additionally compared the performance of PLS and five other machine learning algorithms against the

baseline of a linear regression model and found that PLS was the most promising with respect to retrieval error and computing time over 30 repetitions (Section 2.3.2).

3.3.2 Evaluation of PLS retrieval performance

Two configurations of the synthetic data simulating the physical instrument were investigated in the spectral range of the detector between 650nm and 810nm for model training, cross-validation and testing of PLS:

(1) Including the full, usable spectral range of the FloX between 650nm and 810nm (hereafter referred to as PLS_{full}),

(2) Excluding the spectral region of telluric absorption bands for O_2-B between 684nm and 700nm, for H_2O between 715nm and 735nm and for O_2-A between 759nm and 770nm (hereafter referred to as PLS).

Each of the two response variables, SIF-B and SIF-A, were extracted from the SCOPE-simulated full SIF spectrum at 687 nm and 760 nm, respectively, and used in separate regression models. The models were trained using the "*pls"* package (Mevik and Wehrens, 2007) in R (R Core Team, 2017) facilitating the orthogonal scores algorithm. Hereafter we refer to these as the SIF-B model and SIF-A model. The SIF-B model can predict only red-SIF values (SIF at 687nm) and the SIF-A model can only predict far-red SIF values (SIF at 760nm) from the first spectral derivative of the up-welling radiance spectrum.

Random k-fold stratified cross-validation with four segments was applied during the training process for 360 latent vectors ranked according to the explained signal covariance. In a second cross-validation step, the models were evaluated in their ability to predict the response variable of the unknown synthetic testing dataset. The Root Mean Squared Error of Prediction (RMSEP) was calculated with respect to the actual known SCOPE-modelled value according to Equation 10:

$$\boldsymbol{RMSEP} = \sqrt{\frac{\sum_{i=1}^{n}(\hat{\boldsymbol{x}}_i - \boldsymbol{x}_i)^2}{\boldsymbol{n}}} \tag{10}$$

where $\hat{x}$ is the actual known fluorescence value and x is the predicted value from the PLS regression model for n instances in the testing dataset. The process was repeated 100 times each for different configurations of the testing and training data to determine mean and standard deviation goodness-of-fit metrics. The average RMSEP and standard deviation were then calculated with respect to the number of components of prediction in the testing data.

To investigate the algorithm's limitations on scaling noise, we assumed an ideal, synthetic detector with controllable noise. Using a single down-welling measurement, a training and testing dataset was modelled which was practically free of random noise but still included the specific response

characteristics of the sensor. Increasing amounts of Monte-Carlo simulated noise were added by changing the scaling factor c in Equation 10 stepwise in 100 iterations to simulate detector SNR between 10000 and 10 to account for scaling noise with changing signal intensity (see Equation 9). RMSEP was reported with respect to simulated SNR.

The covariance scale was calculated for both of the abovementioned spectral configurations for the standardized covariance of the SIF signal with the first spectral derivative of synthetic up-welling radiance continuum, i.e., $cov\left(F_{\lambda,\Omega}, L_{\lambda,\Omega}\frac{dL}{d\lambda}\right)$. Each covariance value was scaled by the standard deviation of the total covariance in the respective waveband to normalize the covariance in the spectral continuum. Inversely, the covariance scale multiplied with the standardized latent variables results in the regular, temporal covariance of the computed components (scores) in the deflated spectral continuum.

3.3.3 Instruments for field measurements

The FloX monitoring field spectrometer(JB-Hyperspectral Devices, Düsseldorf, Germany) is a fully autonomous dual field of view system, which records long term time-series of down-welling and up-welling radiance computed towards hyperspectral reflectance and SIF (Acebron et al., 2021; Burkart et al., 2015b; Dechant et al., 2022; Julitta et al., 2016; Krämer et al., 2021).

We measured hyperspectral reflectance using three different FloX systems installed in France, Germany and Italy (Table 2). The instruments at both the Italian and German sites were installed at close distance to canopy. In contrast, the instrument in France was mounted at a 100 m distance from the canopy, to evaluate atmospheric reabsorption of the SIF signal with increasing air-column between sensor and canopy.

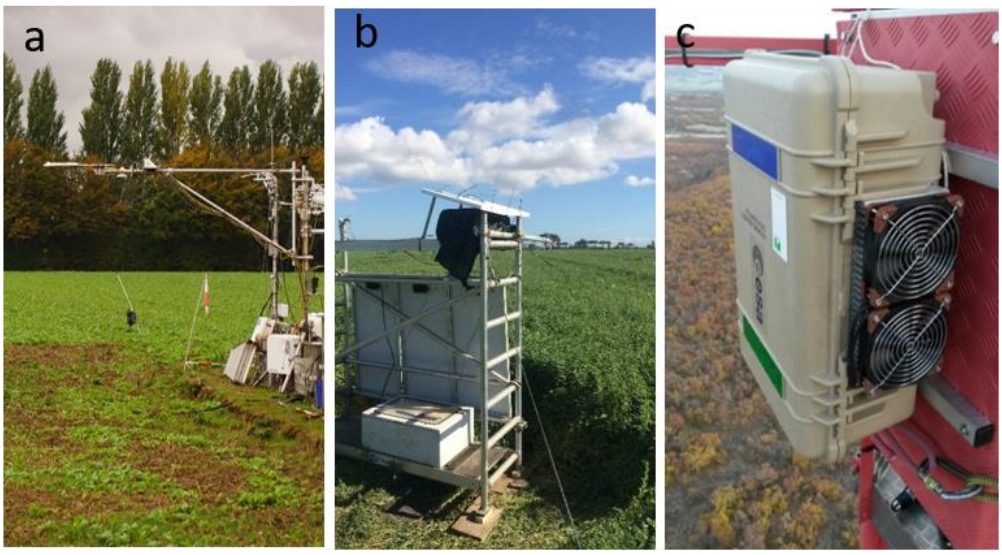

Figure 5: From left to right, setup of the FloX systems a) at TOC over Rumex in Germany, b) at TOC over Alfalfa in Italy and c) at 100m distance to canopy over oak forest in France.

Figure 5 shows the setup conditions of the instruments in the field. Data processing and further use of the data is described in the next sections.

Table 2: Description of field sites where FloX measurements were obtained for SIF retrieval testing

Place	**GPS Coordinates: Lat / Lon**	**Target**	**Distance to canopy**	**Dates of clear sky days**	**SNR: red / NIR shoulder**
Research Center Jülich, Selhausen, Germany	50.87/6.44	Cover crop (mainly Rumex sp., *Poa sp.)*	3 m	Nov. 5th – 7th, 11th, 18th, 24th 2020	396 / 815
Grossetto, Italy	43.93/5.71	Alfalfa (*Medicago sativa)*	1.5 m	April 7th, 16th, 20th – 22nd, 25th 2018	383 / 796
		Forage (*Lolium sp.)*		May 25th, June 10th 2018	
Observatoire de Haute-Provence (OHP), France	42.83/11.08	Oak forest (*Quercus robur)*.	100 m	April 1st, 5th-6th, 18th – 22nd, 24th – 26th, May 25th 2018	382 / 794

3.3.4 Evaluation of retrieval methods using simulated and field measurements

Finally, the SFM and SVD retrievals were compared with PLS retrieval of SIF-B and SIF-A in synthetic testing data against known SCOPE modelled SIF values.

*Table 3: Fitting windows and spectral points acquired by the FloX field spectrometer used for the retrieval of SIF-B and SIF-A with SFM, PLS, SVD-O2 and SVD-FL. * the full spectral configuration of PLS was tested in synthetic to estimate the loss of information when excluding the telluric absorption features under ideal conditions.*

Retrieval method	**SIF-B**		**SIF-A**	
	Fitting window	Spectral points	Fitting window	Spectral points
SFM	684-700 nm	96 pixels	750-780 nm	196 pixels
PLS	651-684 nm, 700-715 nm, 736-759 nm, 770-810 nm	718 pixels	651-684 nm, 700-715 nm, 736-759 nm, 770-810 nm	718 pixels
PLS_{full}*	651-810 nm	1010 pixels	651-810 nm	1010 pixels
SVD-O_2	684-700 nm	96 pixels	750-780 nm	196 pixels
SVD-FL	651-686 nm	202 pixels	745-759 nm	90 pixels

Fitting windows used for each retrieval method are shown in Table 3. We used the SFM algorithm implemented in the R packages FieldSpectroscopyCC [1] and FieldSpectroscopyDP [2] as part of the standardized open source FloX processing. Here, SFM was applied as the standard processing method for fluorescence retrieval in the FloX monitoring field spectrometer, after optimizing first guessed SIF values based on iFLD retrieval. The SVD was implemented as reported in Guanter et al. (2013) and Chang et al. (2020a) to exploit the telluric oxygen absorption bands (SVD-O_2) and solar Fraunhofer lines (SVD-FL). We calculated RMSEP with respect to the known SCOPE SIF values in each instance. The error was investigated with respect to changes in the SCOPE-modelled SIF, respectively. Following the approach of Cogliati et al. (2015b), SCOPE simulated SIF and reflectance spectra (Appendix A2) were used to assess the retrieval performance of the SFM, SVD-FL and SVD-O_2 retrievals with a known "true SIF". We then used the three field datasets (Table 2) to retrieve SIF-B and SIF-A with SFM, SVD-FL and SVD-O_2, respectively. Given that the true SIF signals in the measured data is unknown, the SFM retrieval was used as reference for later comparison.

We trained individual PLS models specifically for each instrument and response variable to retrieve red SIF-B at 687nm and far-red SIF-A at 760nm. The optimal number of components for prediction was selected with respect to the first minimum in average RMSEP with synthetic testing data simulating each instrument. The number of components for SIF-B and SIF-A retrieval were thus individually identified for the PLS models. SIF was then retrieved with PLS models trained with noise contribution according to in-field conditions, excluding major telluric absorption features, or with SFM, SVD-O_2 or SVD-FL models, as described in Table 3. To compare the performance of PLS, SVD-O_2, SVD-FL retrievals from measured observations, we calculated RMSEP as well as the coefficient of determination (R^2), incident and slope from linear regression with respect to the SFM-retrieved SIF values.

3.4 Results

The results of the model training, testing and retrieval validation against SCOPE SIF with synthetic data are described in the following section, followed by the retrieval results from field measurements of up-welling radiance.

3.4.1 Model training and testing

The covariance of the PLS model across the spectrum describes the influence of spectral regions in the predictor space which covary with the response variable of the model. In this section we investigate the covariance of the two PLS Models for SIF-B and SIF-A response, respectively, and the impact of the

[1] Julitta, T. "FieldSpectroscopyCC". Github, Inc. Accessed April 5, 2024. https://github.com/tommasojulitta/FieldSpectroscopyCC.
[2] Julitta, T. "FieldSpectroscopyDP". Github, Inc. Accessed April 5, 2024. https://github.com/tommasojulitta/FieldSpectroscopyDP.

exclusion of the telluric absorption features in the fitting window. When trained for the data configuration including telluric absorption features, the PLS model found high covariance predominantly at the O_2-A band at 760 nm, with increased covariance also observed in the water vapor absorption band between 715 nm and 735 nm and in the O_2-B band at 687 nm (Figure 6b). In the model configuration excluding atmospheric absorption features, the covariance was predominantly observed around 660 nm and a large number of smaller yet pronounced peaks across the remaining spectrum (Figure 6c). The fitting window excluding atmospheric absorption bands between 650 nm and 810 nm is an almost perfect overlay of the top of atmosphere solar irradiance spectrum (Figure 6a) based on satellite data (Brault and Neckel, 1999; Thuillier et al., 2004). As a result, the latter model configuration is trained to exploit solar Fraunhofer lines as relevant spectral features for the fluorescence retrieval.

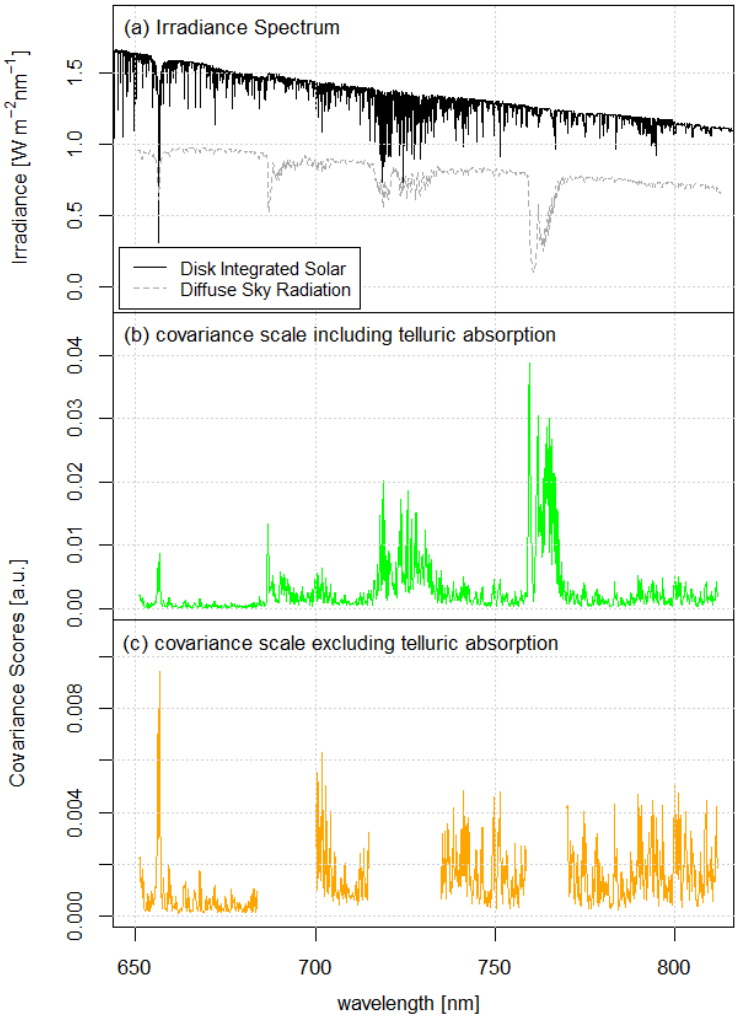

Figure 6: Disk Integrated Solar Irradiance spectrum with Fraunhofer lines at 0.05 nm resolution after Thuillier et al. (2004) (black solid line) and measured Diffuse Sky Radiation Irradiance spectrum with telluric absorption features at 0.3 nm resolution (grey dashed line) (a). Covariance between SIF and the first spectral derivative of up-welling radiance across the spectrum exploited by the PLS algorithm including telluric absorption features (b) and excluding telluric absorption features (c).

We simulated a synthetic FloX sensor with adjustable SNR between 10000 and 10 to investigate the PLS algorithm limitations with respect to scalable noise. Both SIF-B and SIF-A PLS regression models

are very sensitive to noise across all components (Figure 7). The propagation of uncertainties increases RMSEP directly in proportion to the amount of SNR on a logarithmic scale and becomes increasingly unstable below 150 SNR (dotted line). The SIF-A model is slightly more susceptible to very low SNR at the NIR shoulder in comparison with the SIF-B model. Furthermore, the worst error is exceeding 0.5 mW m^{-2} sr^{-1} nm^{-1} in both models and varying largely due to the random noise contribution for very low SNR below 150. Thus, retrieval errors beyond SNR 150 cannot be reliably predetermined and is not suitable for the fluorescence retrieval. With the SNR of FloX instruments ranging around 390 in the red and 800 in the NIR shoulder wavelengths in operational scenarios due to automatic optimization of the signal level, we predicted a retrieval error of below 0.1 mW m^{-2} sr^{-1} nm^{-1} in both SIF-B and in SIF-A, using synthetic training and testing data.

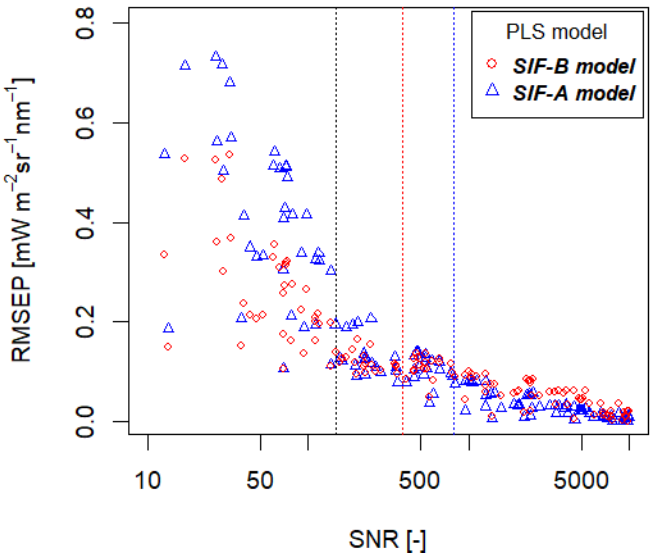

Figure 7: Root Mean Square Error of Prediction (RMSEP) from testing data of PLS models with response variable SIF-B (red) and SIF-A (blue) for simulated spectrometer SNR on logarithmic scale in 100 simulations with scaled Signal to Noise Ratio (SNR). SNR 150 is indicated by black dotted line. Operational SNR around 390 in the red and around 800 in the NIR shoulder wavelengths are marked with a red dotted line blue dotted line, respectively.

When including telluric absorption and noise simulated according to field conditions, RMSEP significantly varied by model complexity over 100 randomized training and test datasets (Figure 8a). Testing error significantly increased when model complexity deviated from the optimal number of components. We found an optimum of lowest RMSEP at 134 components for prediction of SIF-A with RMSEP around 0.07 mW m^{-2} sr^{-1} nm^{-1} and 245 components of SIF-B and RMSEP around 0.09 mW m^{-2} sr^{-1} nm^{-1}. The standard deviation of the error also increased below and above the optimal number of components for prediction. When a low number of components was used, the error of the SIF-B model tended to be slightly lower than the error of the SIF-A model. This tendency was inverted as the number of components increased and resulted in an overall lower error of the PLS model for SIF-A prediction compared with SIF-B prediction.

In contrast, when excluding telluric absorption and using noise simulated according to field conditions, very little increase in RMSEP was observed with respect to PLS_{full} (Figure 8b). The error of SIF prediction was similar excluding telluric absorption features compared to the previous case which included those spectral regions (Figure 8a). The mean RMSEP is minimal with 0.09 mW m^{-2} sr^{-1} nm^{-1} around 136 components for SIF-A model and 0.11 mW m^{-2} sr^{-1} nm^{-1} for the SIF-B model with 169 components, respectively. Furthermore, less complex PLS models performed with less error for SIF-B retrievals than for SIF-A retrievals. At higher complexity, the performance of the SIF-A models was again superior compared to the SIF-B model. The standard deviation increased slightly more compared to the former configuration with increasing number of components for prediction. While the PLS models for SIF retrieval showed a slightly enhanced performance when including telluric absorption features (i.e., RMSEP with respect to model complexity and standard deviation with respect to randomly permuting training and testing), the difference was not significant.

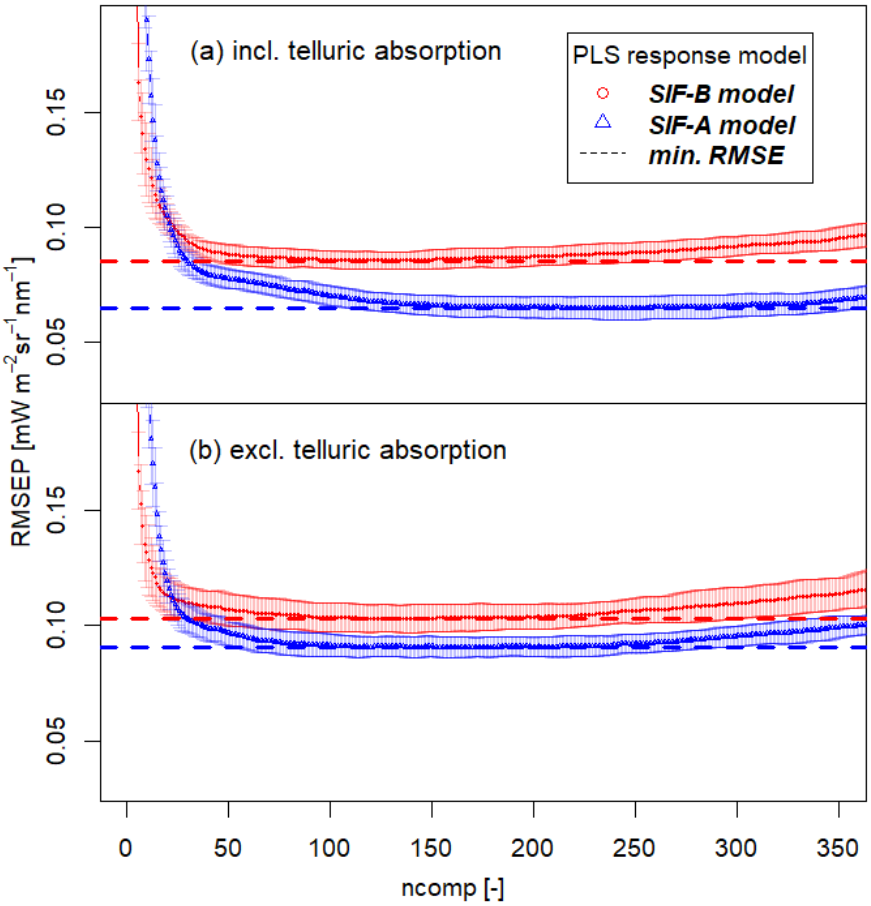

Figure 8: Root Mean Square Error of Prediction (RMSEP) and its standard deviation across 100 PLS model training and validation cycles is shown for each of the separate PLS models in predicting the response variable SIF-B (red dots) and SIF-A (blue triangles), respectively, with increasing number of components (ncomp). Telluric absorption features are included in (a) and excluded in (b).The optimal number of components and associated lowest RMSEP is indicated with dashed lines for the SIF-B and the SIF-A model, respectively in red and blue.

The retrieval performance of PLS, SFM, SVD-O_2 and SVD-O_2 was assessed with respect to known SCOPE-modelled SIF, extracted at 687 nm and 760 nm (Figure 9). SVD-FL exhibited a strong dependence on the actual signal intensity, scaling the median RMSE almost proportional to the SCOPE-modelled SIF signal intensity. This behavior was not observed with the other retrieval algorithms, which exhibited a steady error across the investigated SCOPE SIF value range. In SIF-B exhibited PLS median RMSE very close or slightly below median RMSE of SFM (Figure 9a). The median RMSE of SFM was lowest in SIF-A, while RMSE of SFM and SVD-O_2 were very similar (Figure 9b). PLS exhibited a slightly larger error with respect to SFM, even if the median value did not exceed 0.1 mW m^{-2} sr^{-1} nm^{-1}.

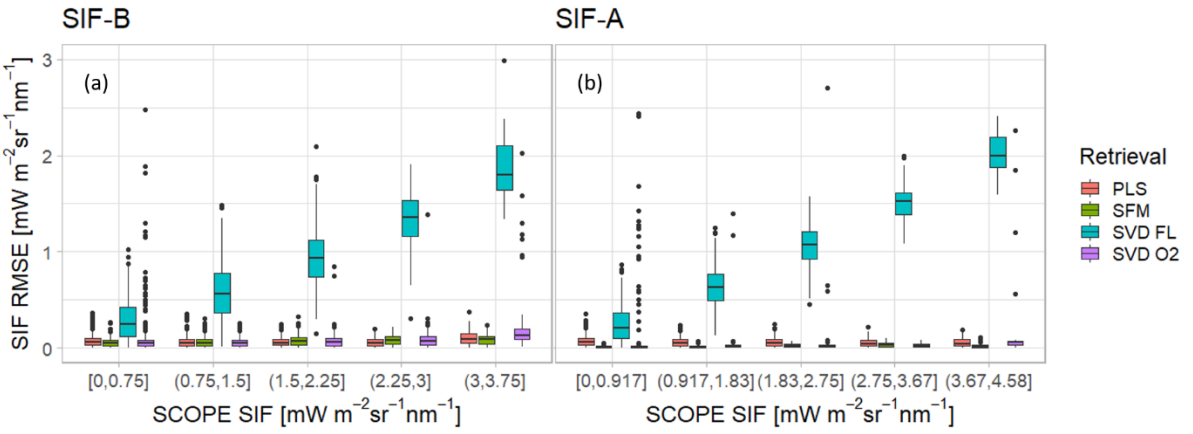

Figure 9: RMSE of the PLS (red), SFM (green), SVD-FL (turquois) and SVD-O2 (purple) with respect to SCOPE simulated SIF for SIF-B extracted at 687nm (a) and SIF-A extracted at 760nm (b), with respect to changing SIF intensities in five equally large intervals given with [including boundary and (excluding boundary marks. Interquartile range is indicated by the expand of the boxes in y-direction, the median RMSE by a solid line. Whiskers expand to the last member inside 1.5 x interquartile range and outliers are marked with dots.

3.4.2 Retrieving sun-induced fluorescence from field data

The previously tested PLS models excluding telluric absorption features were transferred to measured data. Typical diurnal cycles out of the entire measured data set are presented in detail for each instrument (Figure 10). Retrieval results for the entire set are presented in Figure 11. Finally, PLS, SVD-O_2 and SVD-FL were compared with respect to SFM retrieved SIF across the entire dataset for each instrument and results are reported in Figure 12. The differences of the PLS, SVD-O_2 and SVD-FL retrieval with respect to the SFM were tested and are reported in Table 4.

3.4.2.1 Diurnal cycles and time series

Measured up-welling radiance data from three different instruments were processed with SFM, SVD-O_2, SVD-FL and PLS. A representative diurnal cycle was selected for each site to illustrate a typical clear-sky day for a canopy in different stages of development under non-stressed conditions, and aggregated to half-hour intervals for presentation clarity. At the German site, the diurnal pattern of SIF exhibited an inverted smile shape for PLS, SVD-O_2, SVD-FL and SFM (Figure 10 a,b). This pattern is typical for non-stressed vegetation. The magnitude of the SIF-B and SIF-A signals were low (< 1 mW m^{-2} sr^{-1} nm^{-1})

across all retrieval methods, possibly because measurements were collected towards the end of the growing season. SVD-FL overestimated SIF-B with respect to all other methods and underestimated SIF-A with respect to all other methods. The standard deviation for SVD-FL across the diurnal course was also noticeably higher, compared to all other presented retrieval methods. For SFM and SVD-O_2, half-hourly means and standard deviations of retrieved SIF-B and SIF-A values were almost indistinguishable. SIF values retrieved with PLS also agreed well with both SFM and SVD-O_2 in SIF-B and SIF-A. At the Italian site, very high values were retrieved for SIF-B and SIF-A during the peak of the growing season (Cogliati et al., 2019). Again, the SVD-FL retrieval of SIF-B exhibited significantly higher values compared to all other methods (Figure 10 c,d). Standard deviation, and therefore the uncertainties around the diurnal trend, were very high for SIF-B and SIF-A retrieved using the SVD-FL. SIF-B values retrieved using PLS were slightly above those from SVD-O_2 and SFM retrieval. Differences between the SFM, the SVD-O_2 and PLS were almost indistinguishable in SIF-A, except for a slight overestimation of the PLS round midday after 10am UTC until 12am UTC with respect to the other methods.

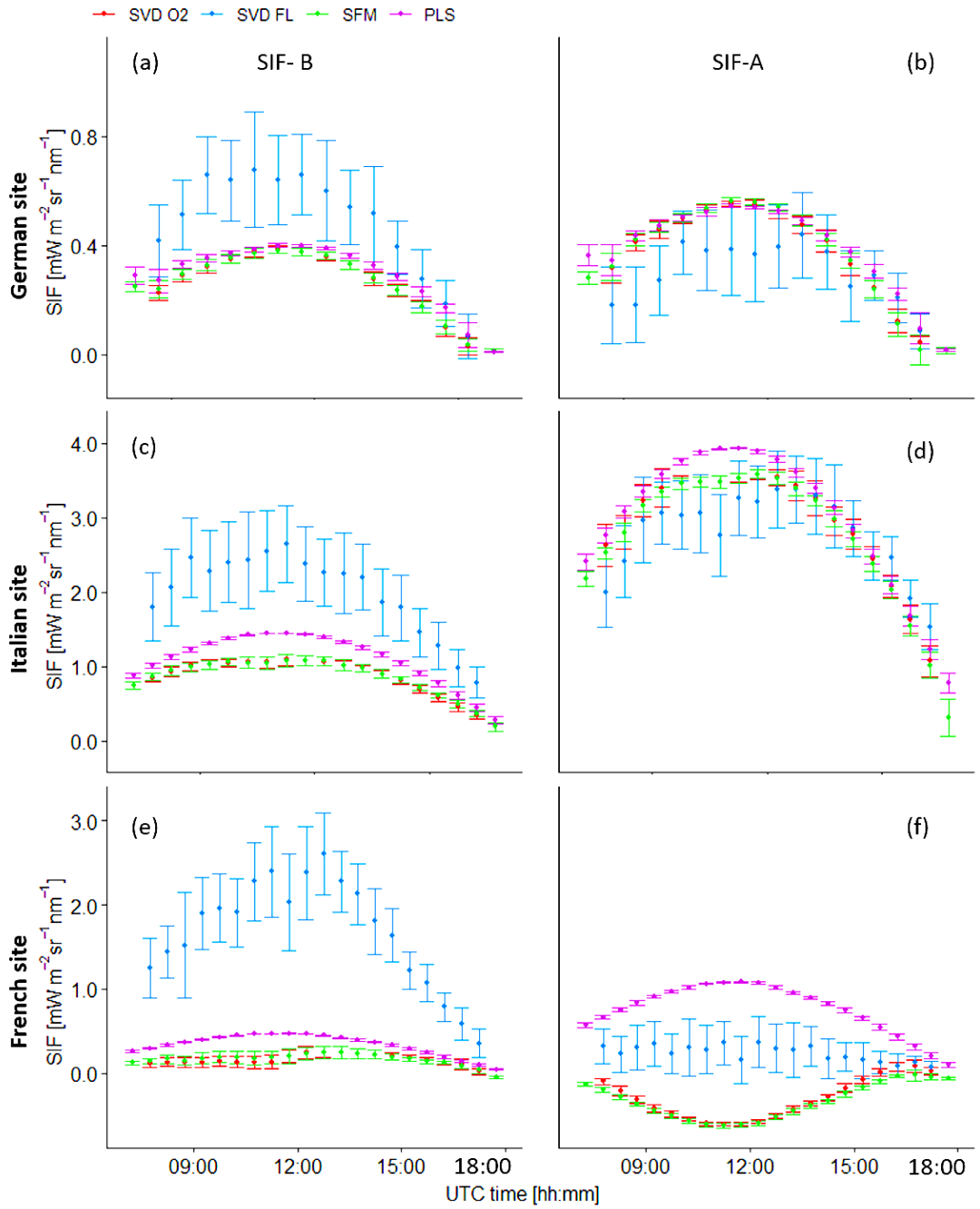

Figure 10: Diurnal cycles of red SIF-B, resp. at 687nm (left panel) and far-red SIF-A, resp. at 760nm (right panel) retrieved with SVD-O2 (red), SVD-FL (blue), SFM (green) and PLS (purple). PLS models for retrieval have been trained on synthetic up-welling radiances data considering noise according to in-field conditions, excluding telluric absorption features. Data was measured at TOC in Germany over Rumex on November 6th 2020 (a, b), at TOC over Alfalfa in Italy on April 21st 2018 (c, d) and 100m above oak forest canopy in France on April 25th 2018 (e, f). Measurements of one day were aggregated to half-hourly intervals; points indicate mean and error bars show standard deviation.

Lastly, the French site exhibited very low to negative SIF from SFM and SVD-O_2 retrievals, with the diurnal pattern inverted in SIF-A, compared to SVD-FL and PLS (Figure 10 e,f). At this site, data collected by the FloX mounted at 100 meters above the canopy were used without any atmospheric compensation for retrieving SIF-B and SIF-A with the SFM, SVD-O_2, SVD-FL and PLS. This setup is known to cause errors in the SIF retrievals based on telluric absorption bands. In contrast, PLS and SVD-FL

both exhibited positive, inverted smile patterns, typical for this kind of vegetation. Still, a difference between SVD-FL and PLS was noticeable in both SIF-B and SIF-A. SVD-FL predicted SIF-A values were lower and partially negative with a larger standard deviation around the half-hourly mean. Consequently, we retrieved only positive SIF-B and SIF-A values with lower noise using PLS. Differences between SVD-O_2 and SFM were barely noticeable.

Across the entire time series, very similar values were retrieved using the three retrieval methods SVD-O_2, SFM and PLS at the German site (Figure 11 a,b). Especially SFM and SVD-O_2 were always consistent. SVD-FL values for both SIF-A and SIF-B were noisier than telluric band retrievals or the PLS retrieval. Again, SVD-FL retrieval had a tendency to overestimate SIF-B. Towards the end of the growing season, magnitude of SIF was quite low, with midday peaks around 0.5 mw m^{-2} sr^{-2} nm^{-1} in SIF-A.

At the Italian site, very high values were retrieved in SIF-B and SIF-A across the entire time series over both maturing alfalfa and forage canopies (Figure 11 c,d). The error around the diurnal trend was slightly higher for SFM and SVD-O_2 retrieval compared to PLS, while retrieved values were very similar in SIF-A. PLS SIF-B values were slightly above the values of SFM and SVD-O_2 but remained well below the SVD-FL values. A difference in diurnal shape as well as in magnitude of SIF-A values was observed between the forage and alfalfa canopies before and after May 8th (Figure 11 c,d). In SIF-B, the difference between the canopies was less pronounced.

At the French site, both, SIF-B and SIF-A showed mostly negative values across the entire time series when retrieved with SFM and SVD-O_2 due to atmospheric distortion (Figure 11 e,f). Notably, although PLS did not correct for atmospheric impacts, retrieval results were always positive. SVD-FL retrieved partially negative values with the seasonal pattern exhibiting a random jump in the second half of April. Furthermore, SVD-FL values in SIF-B were significantly higher in comparison with all other retrieval methods. The PLS results showed a gradual increase of SIF-B and SIF-A between April 18th and April 26th, which is in temporal agreement with the greening-up and increase of photosynthetic activity in the target canopy. This gradual increase was also present in the SVD-FL SIF-A values, while the diurnal pattern was barely distinguishable due to the high noise in the signal. Using the PLS retrieval, diurnal pattern in both SIF-B and SIF-A were exhibited with high precision.

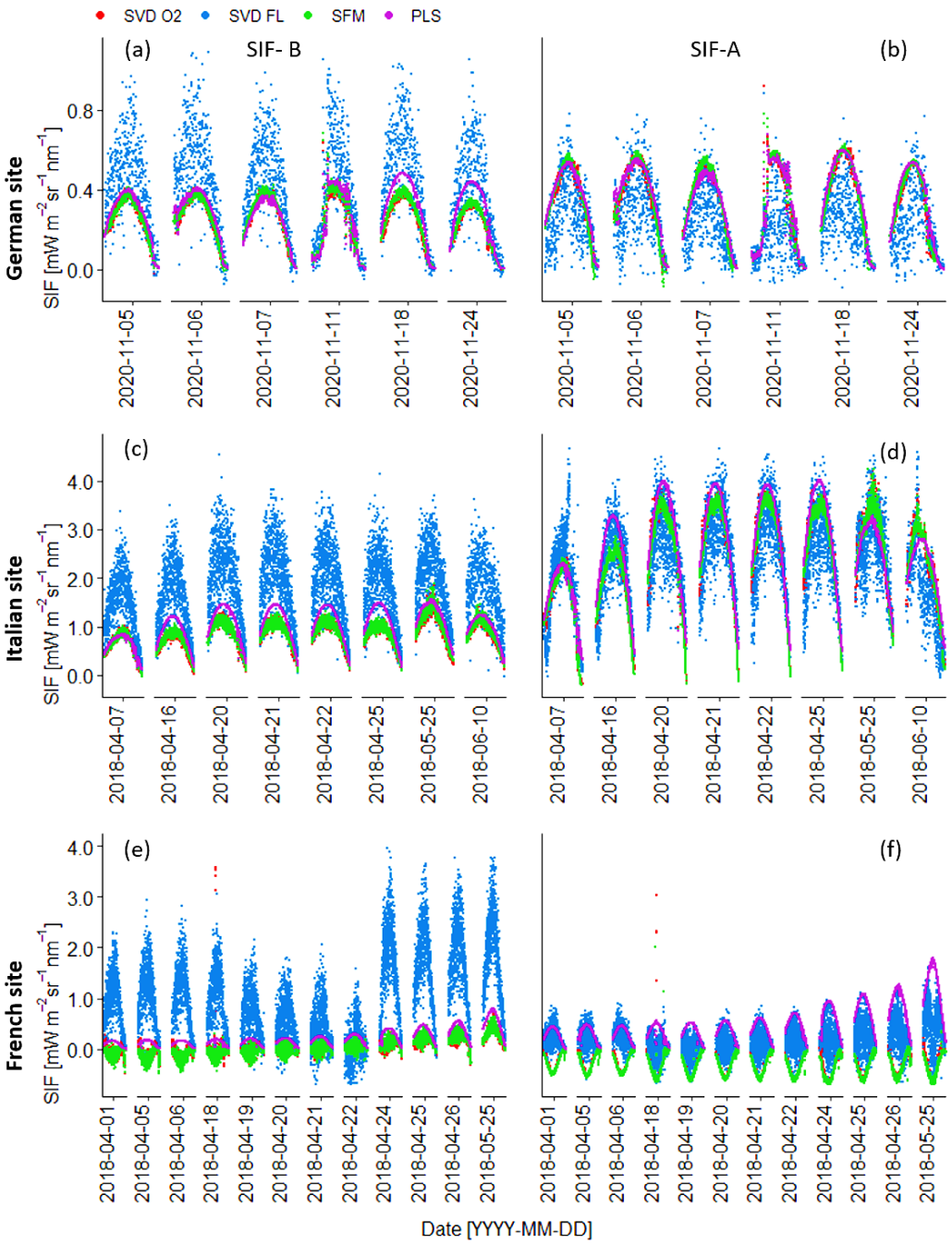

Figure 11: Clear sky days selected for the retrieval of red SIF-B at 687nm (left panel) and far-red SIF-A at 760nm (right panel) with SVD-O2 (red), SVD-FL (blue), SFM (green) and PLS (purple). PLS models for retrieval have been trained on synthetic up-welling radiances data considering noise according to in-field conditions, excluding telluric absorption features to exploit solar Fraunhofer lines. Measurements were obtained at TOC over Rumex in Germany (a, b), at TOC over Alfalfa and Forage in Italy (c, d) and 100m above an oak forest canopy in France (e, f).

3.4.2.2 Comparison of the result from the different retrieval methods

The performance of the PLS and SVD-FL for SIF retrieval based on solar Fraunhofer lines, and SVD-O_2 based on telluric oxygen absorption bands, were evaluated against SFM retrieved SIF over 26 clear-sky days for three different instruments.

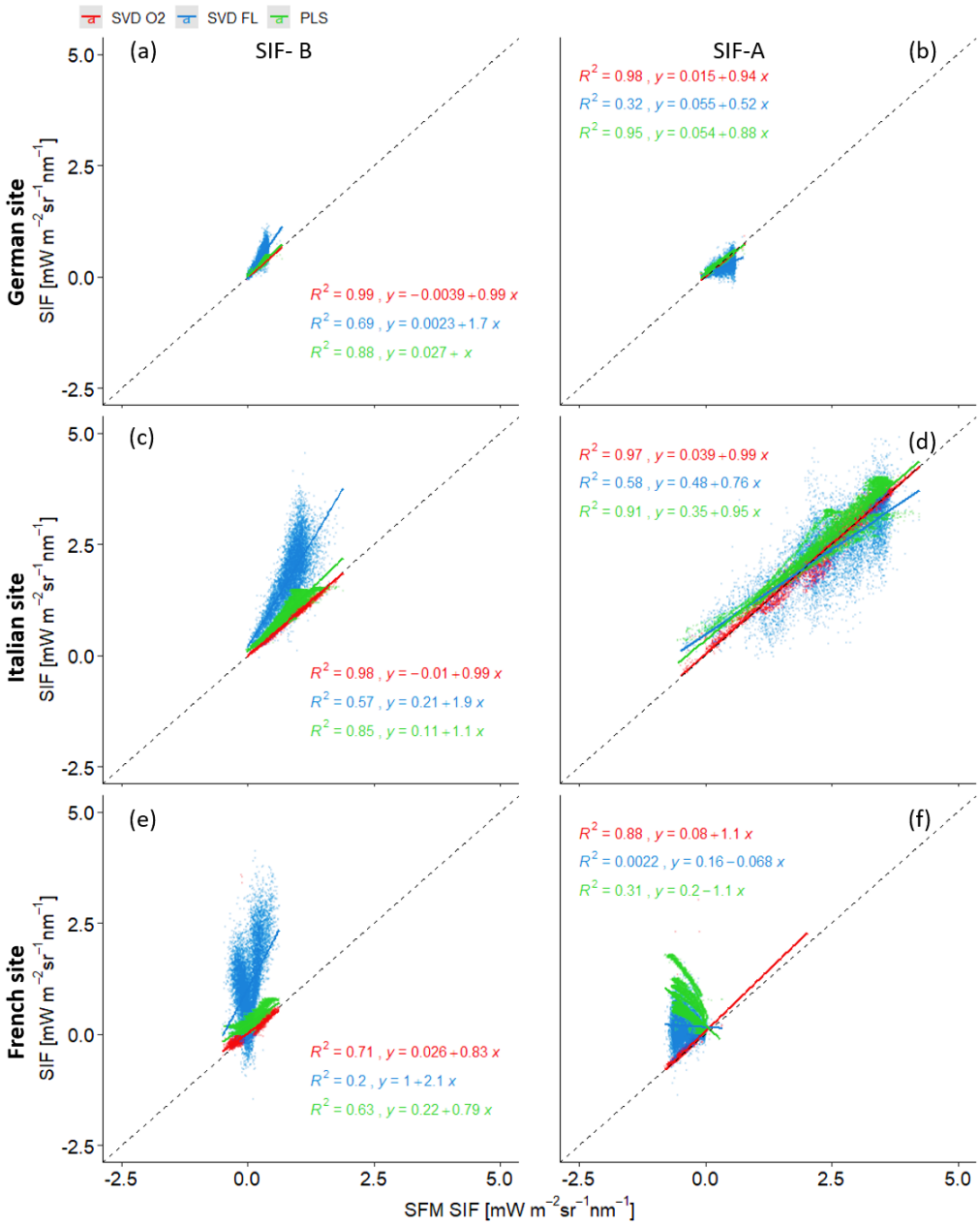

Figure 12: Correlation of red SIF-B at 687nm (left panel) and far-red SIF-A at 760nm (right panel) with SVD-O2 (red), SVD-FL (blue) and PLS (green) with respect to SFM SIF from field measurements. PLS models were trained on synthetic up-welling radiances data considering noise according to in-field conditions, excluding telluric absorption features. Measurements were obtained from field sites located at TOC in Germany (a, b), at TOC Italy (c, d) and 100m above canopy France (e, f).

Similar RMSE values and, thus, difference with respect to SFM was found for PLS for the two instruments in Germany and Italy, which were both positioned relatively close to the canopy (Table 4). At the same time, SVD-O_2 performed with very similar results to SFM in the two sites. This behavior was also reflected in the correlation of the SVD-O_2 and PLS retrievals with respect to SFM, with very high R^2 values (Figure 12 a, b). The strongest correlation was observed between the telluric oxygen-line-based SVD-O_2 and SFM with R^2 0.99 and 0.98 in SIF-B and SIF-A, respectively. The slope and intercept described almost a one-to-one conversion from SFM to PLS with very low offset in SIF-B and a small multiplicative underestimation in SIF-A. The SVD-FL retrieval exhibited the highest

disagreement with SFM (Table 4), poorest correlation and lowest R^2 with SFM in the German site (Figure 12 a, b). A multiplicative overestimation was recognized in SIF-B using SVD-FL retrieval with respect to SFM, with slope 1.7 and offset close to zero. On the contrary, a multiplicative underestimation with slope around 0.5 and very low offset was exhibited for SVD-FL with respect to SFM in SIF-A.

At the Italian site, PLS exhibited similar absolute but lower relative RMSE in SIF-A with respect to SFM, due to the higher absolute signal intensity compared to the German site (Table 4). The correlation with the SFM is high in SIF-B and SIF-A, with a small additive offset (Figure 12 c, d). The multiplicative offset ranges around one. As with the German site, SVD-O_2 exhibited strong agreement with SFM. SVD-O_2 retrievals were highly correlated with SFM, with R^2 around 0.98 in SIF-B and 0.97 in SIF-A, with slopes of 0.99 and offsets below 0.04. In contrast, SVD-FL retrieval in SIF-B and SIF-A exhibited the poorest correlation with SFM. The absolute and relative discrepancies were larger in SIF-B and SIF-A with SVD-FL in comparison to the other methods (Table 4), with intercept and slope deviating strongly from the one-to-one conversion (Figure 12 c, d).

The instrument in France was positioned at 100 m distance to canopy without atmospheric correction applied to any of the SIF retrievals. High disagreement of PLS with respect to SFM and SVD-O_2 were observed in both SIF-B and SIF-A (Table 4). Very high absolute and percentage RMSE was also found for SIF values retrieved using SVD-FL with respect to SFM. The performance of PLS and SVD-FL, which both exploited solar Fraunhofer lines and remained in principle unaffected by atmospheric distortion, differed from the telluric oxygen band based SFM and SVD-O_2 in this site. SVD-O_2 was again highly consistent with SFM with high R^2 values in SIF-B and SIF-A (Figure 12 d, e). In SIF-B, all retrieval methods exhibited regression lines with positive slope, with SVD-O_2 and PLS below one and SVD-FL even above two. While the offset for SVD-O_2 was negligible, SVD-FL exhibited a high offset in SIF-B. A smaller offset was recognized in SIF-B using PLS retrieval. Notably, PLS retrieved SIF-A was negatively correlated with SFM as a result of the atmospheric influence on the signal for this site. The SVD-FL retrieval exhibited a flat, negative slope around -0.07. The offsets in SIF-A for the two methods PLS and SVD-FL were both positive and similar (0.16 and 0.2, respectively).

Table 4: Root Mean Square Error (RMSE) of PLS retrieval excluding telluric absorption features, SVD O2 in the related atmospheric absorption bands and SVD FL in the solar Fraunhofer lines for SIF-B and SIF-A with respect to the SFM retrieved SIF, calculated in absolute values and percentage of the signal for the entire time-series.

Dataset	RMSE PLS SIF-B	RMSE PLS SIF-A	RMSE SVD FL SIF-B	RMSE SVD FL SIF-A	RMSE SVD O2 SIF-B	RMSE SVD O2 SIF-A	Unit
German site (TOC)	0.054	0.043	0.227	0.297	0.014	0.024	mW m^{-2} sr^{-1} nm^{-1}
	27.5	17.7	79.8	30.2	4.5	2.2	%
Italian site (TOC)	0.15	0.044	1.166	0.639	0.041	0.16	mW m^{-2} sr^{-1} nm^{-1}
	26.9	5.0	117.9	19.9	4.6	1.6	%
French site (100m above canopy)	0.724	1.572	1.443	0.718	0.067	0.050	mW m^{-2} sr^{-1} nm^{-1}
	55.3	366.1	187.7	178.1	4.3	3.4	%

3.5 Discussion

In the following two sections, we first discuss the results from modelling and testing with synthetic up-welling radiance data. We then discuss real world retrieval (i.e., observational data) results from up-welling radiance measured using FloX monitoring field spectrometers at three field sites.

3.5.1 Testing against modelled data

SIF was retrieved using a multivariate PLS model. We showed that the algorithm finds and exploits the covariance between SIF and specific spectral features in the first spectral derivative of up-welling radiance in the fitting window between 650nm and 810nm. For the spectral configuration including telluric absorption, covariance is predominantly observed around the O_2-B band, centered around 687nm, the water absorption feature between 715nm and 735nm, and the O_2-A absorption feature around 760nm. Solar Fraunhofer lines are of minor contribution across the spectral range in this configuration, for they are very narrow. However, for training and testing data excluding telluric absorption features we identified significant covariance in the solar Fraunhofer lines across the spectral range of the detector. This means that the first derivative of up-welling radiance varies within the Fraunhofer lines due to the infilling of the varying SIF contribution.

Noise in the synthetic training and testing data significantly influenced the retrieval RMSEP in synthetic testing data. The retrieval error increased on a logarithmic scale by more than an order of magnitude when scaling noise was added to the ideal, noise-free, synthetic detector. In order to represent the expected characteristics of the FloX instruments in the field, noise must be included in the training data with respect to the automatic optimization at 80% signal of the total dynamic range of the detector. In operational scenarios were SNRs around 390 in the red and around 800 in the NIR shoulder region reported. SNR depends on the signal level at the detector and therefore changes with respect

to wavelength depending on the spectral shape of the target. In effect, high noise and spectral drift affect the depicted shape and, thus, the accurate approximation of the infilling in the small solar Fraunhofer lines. Thus, instrumental noise is considered as an important limiting factor to the performance of the approach. This will be especially relevant when using the retrieval with different ground-based and airborne SIF systems with varying SNR because of their various optical configurations. Therefore, we recommend a minimum operational SNR of around 150 in the NIR shoulder spectral region for the application of PLS retrieval based on the presented results.

In addition to the SNR, the spectral resolution (FWHM) of the spectrometer limits the maximum depth of the absorption bands which can be effectively exploited for SIF retrieval (Julitta et al., 2016; Pacheco-Labrador et al., 2019a). The investigated FloX sensors featured a spectral resolution around 0.3nm FWHM. Further research should investigate the PLS retrieval with other optical configurations, especially with different FWHM and SNR, to reproduce other instruments currently used in the community. The challenge of the PLS approach resides in the composition of the synthetic training and testing dataset with respect to the optimal level of added noise to model real conditions as closely as possible. Many other factors superimpose the fluorescence signal in remote measurements and require consideration to provide comparable readings (Damm et al., 2010b). One has to cover enough variance of these superimposed factors and instrumental noise for to identify these as components that are not correlated with the signal. At the same time, the synthetic data has to cover enough variance of fluorescence in the continuum so that the algorithm can correlate the components related to the actual signal. However, if the modelled data is very noisy, instances can potentially fall on multiple components at the same time and, thus introduce artifacts into the retrieved values. These artifacts are rather tricky to identify with common statistical error measures, as they often still represent the solution of best fit. In the retrieval of real measured SIF appear artifacts often as singular outliers, sudden jumps or shape inversions. However, since we cannot assume continuous trends in unknown data, contingency in real measurements must be respected. Thus, we strongly recommend to strive for an instrumental solution with optical specifications, accordingly. The performance of the algorithm is severely limited by the detector's capability to accurately measure the depth and infilling in relatively small spectral features. This was especially obvious when using the SVD-FL retrieval for SIF-B in this study. Other sensors, such as FLORIS and HyPlant, designed for SIF retrieval, exceed FloX-similar optical requirements (Drusch et al., 2017; Siegmann et al., 2019).

We investigated the model training and testing performance for two different configurations of the synthetic up-welling radiance data with noise to resemble in-field measurements: (1) including the full spectrum between 650nm and 810nm, (2) excluding spectral regions of major telluric absorption features. In all configurations, we observe for each model an increasing uncertainty of prediction with increasing number of components. This is known as overfitting, where the model increasingly tracks

noise instead of the real signal. Conversely, the uncertainty of prediction also increases for a very low number of components. This is due to the model not tracking enough of the signal at low complexity (under-fitting). We identified the optimum where the mean error is lowest and the variation in the error is small. As demonstrated in Wagner et al. (2018), the first minimum of absolute RMSEP and smallest standard deviation indicate the optimal number of components for prediction for each model. No significant difference in mean RMSEP of the two configurations, i.e. either including or excluding the spectral regions of major telluric absorption features, was found in the PLS model testing with synthetic data. In particular, the variability attributed to changing detector noise or model complexity was significantly larger than the variability attributed to spectral configurations. The full spectral configuration performed slightly less retrieval error than the configuration excluding telluric absorption. Due to the higher complexity of spectral information available from the full spectrum, this difference in performance was anticipated. However, an RMSE around 0.1 mW m^{-2} sr^{-1} nm^{-1} for the PLS configuration excluding telluric absorption is still very similar to the SFM (Cogliati et al., 2015b). Atmospheric absorption is known to distort telluric retrievals of the SIF signal with increasing distance over the canopy, which requires correction using complex atmospheric compensation (Aasen et al., 2019). Therefore, we further investigated the PLS model configuration, which excludes the telluric absorption features and only exploits the solar Fraunhofer lines, thereby circumventing atmospheric reabsorption (Guanter et al., 2013).

We emphasize that the PLS regression model is a data driven approach similar in some aspects to SVD, nevertheless with some important differences. Both SVD and PLS employ dimensionality reduction. SVD uses a forward model and residuals to estimate the SIF signal, whereas PLS utilizes a direct regression between SIF and the deflated first spectral derivative of up-welling radiance spectra. SVD decomposes the variable space into principal components which are identified and ordered according to the amount of variance covered (Mardia et al., 1979). In contrast, PLS determines the response variable SIF through the projection of latent variables in such a way that scores and loadings explain as much covariance between predictor and response variable as possible (Mevik and Wehrens, 2007). Typically, the first latent variables represent highly correlated components of the predictor data space with respect to the response variable. However, it is possible that latent variables are equally weighted with respect to explained covariance between predictor and response variable (De Jong, 1993). Note that neither SVD nor PLS can model variations in the measurements which they were not trained for. The PLS algorithm has been specifically optimized for detection of signals in mixture in general and relies on a considerate construction of synthetic training and testing data to accurately resemble real measurements with modelled SIF contribution in this study.

We assumed that the modelled synthetic up-welling radiance data can resemble in-field conditions and, thus, can be transferred to a SIF retrievals applied to the real measurements (Pacheco-Labrador

et al., 2019b). This assumption was further investigated with a comparison of the SFM, SVD-O_2, SVD-FL and PLS retrieval against SCOPE simulated SIF as a reference. The results suggest a strong dependency of the SVD-FL retrieval error on the signal levels in both SIF-B and SIF-A. Thus, the spectral shape of the SIF signal is affecting this retrieval significantly. The spectral resolution of 0.3nm FWHM of the FloX, compared with 0.13nm in the literature is another limiting factor for the SVD-FL retrieval (Guanter et al., 2013). SFM was the most stable retrieval in this regard and therefore SFM was considered the reference to evaluate the other retrieval methods with field measurements. SVD-O_2 and PLS showed similar errors compared with the SFM. Only very low SIF values were retrieved with an increased number of outliers. Note that SVD requires information about the fluorescence shape for precise retrieval, which can introduce error if the assumed fluorescence shape is incorrect (Chang et al., 2020a). PLS avoids this issue as no forward model is fitted to the up-welling radiance spectrum. Instead, the algorithm computes regression coefficients in each waveband across the fitting window by rotating the input matrix of spectral derivatives in such a way that covariance with the SIF variable is maximized.

3.5.2 Real world retrieval

SIF-B and SIF-A were retrieved with a PLS regression model approach configured to exploit solar Fraunhofer lines, considering instrumental noise according to in-field conditions from measured data from three different sites. Speeding up the measurement can be beneficial, especially for experiments aimed at investigating fast dynamics in fluorescence. However, simultaneous (or near-simultaneous) down-welling measurements are of great benefit for computing fluorescence yield and light use efficiency, even if more time consuming (Damm et al., 2010a; Rascher et al., 2010). The retrieval with SFM also required continuous down-welling light measurements, which are included together with automatic signal level optimization in each FloX measurement cycle.

We were able to retrieve positive and meaningful values both in SIF-B and SIF-A from FloX measurements with the PLS configuration in all sites. In close distance to canopy, PLS results agreed well with the oxygen-band-based retrieval methods SFM and SVD-O_2. The most striking differences were found between retrievals based on telluric oxygen absorption lines and PLS retrieval at the 100 m tall tower in France. Complex atmospheric correction methods are required for SFM and SVD-O_2 retrievals to achieve meaningful results with increasing distance to canopy (Sabater et al., 2018). With no atmospheric correction in place, SFM and SVD-O_2, both based on telluric oxygen absorption, retrieved negative SIF from the French site and were therefore unusable for further analysis. The German and Italian setups were both in relatively close proximity to their target canopies, and both sites exhibited similar agreement across PLS, SVD-O_2 and SFM. In particular, SVD-O_2 and SFM based on telluric absorption performed equally well with almost identical results. PLS slightly overestimated SIF

with respect to SVD-O_2 and SFM in the Italian site but exhibited very good agreement in the German site. Similar tendencies were observed comparing the retrieval methods against SCOPE simulated SIF in synthetic data. By exclusively exploiting solar Fraunhofer lines, the PLS retrieval is in principle unaffected by atmospheric distortion and clouds (Sun et al., 2018). Furthermore, by using large fitting windows and exploiting multiple solar Fraunhofer lines between 650nm and 810nm, retrieval noise is kept very low and good robustness against atmospheric reabsorption is achieved with PLS. At the French site PLS also captured a gradual increase in SIF-B and SIF-A over time, which was related to the onset of photosynthesis during the greening-up of the forest canopy. This increase in fluorescence was also observed through SVD-FL but was not sufficiently resolved on a diurnal scale due to the high retrieval noise.

Overall, SVD-FL results were much noisier than PLS, SFM or SVD-O_2. This could be due to instrumental limitations, mainly FWHM, and the small fitting window of the algorithm. The performance of the SVD algorithm also relies on accurate fits of a SIF-free model with measured up-welling radiance data (Du et al., 2018). Previous studies indicate that the exploitation of solar Fraunhofer lines using SVD was superior with a spectral resolution around 0.13nm FWHM (Chang et al., 2020a; Guanter et al., 2013). FWHM and SNR affect the accurate exploitation of the SIF infilling and thus limiting retrieval accuracy further (Frankenberg and Berry, 2018; L. Liu et al., 2015). The FloX is commonly configured with 0.3 FWHM. Evidently, Frankenberg and Berry (2018) show the influence of spectral resolution affecting the apparent depth of the measured solar Fraunhofer lines in the same spectral window, which is also used for the SVD-FL retrieval in this work. As FWHM increases, the difficulty of accurately measuring the line depth increases, and the effect of atmospheric scattering on the infilling becomes more noticeable. When applied to the telluric oxygen absorption features, SVD exhibits similar retrieval noise as SFM, but loses the benefit of independence from atmospheric conditions. When exploiting narrow solar Fraunhofer lines, the SVD-FL is considered more sensitive to instrument noise, spectral resolution or drift due to the low SIF signal and narrow spectral features from field measurements (Chang et al., 2020a). Scattering and hotspot effects related to canopy structure and BRDF depending on the angle of incident light can substantially influence up-welling radiance and retrieved SIF (Pacheco-Labrador et al., 2016). Furthermore, SIF signals are known to be angle-dependent and directed in complex canopies (Rautiainen et al., 2018; Van Wittenberghe et al., 2015). Thus it is necessary to clarify that only at-sensor fluorescence can be directly measured without any inference of target canopy structure or scattering in the atmospheric path (Damm et al., 2014). Bearing this consideration in mind, a slight disagreement in absolute values between the different retrieval methods is expected due to the different physical principles on which they are based. Still, the diurnal shape of all retrievals should still produce similar patterns, unless the physical principle is obstructed by independent factors, e.g., atmospheric distortion. PLS outperformed SVD-FL in terms of retrieval

noise and precision based on the presented results. Hence, the PLS algorithm appears more robust and suitable for SIF-retrieval based on solar Fraunhofer lines with a spectrometer of lower resolution (around 0.3nm FWHM), as it exploits many more solar Fraunhofer lines in a wider fitting window.

Since PLS is a data driven approach, it requires training. A limiting factor to the retrieval of real-world data is the composition of the synthetic data for the PLS model training process. The employed SCOPE modelled vegetation data is based on actual in-field measurements over a grassland to allow for realistic variances of the signal covered in the synthetic dataset. We are aware that the vegetation spectra modelled with SCOPE do not represent all possible variations in canopy characteristics. Therefore, uncertainties in SIF retrieval can vary with other canopy characteristics, especially for complex structures. We assumed in this work that the modelled spectral fluorescence based on grassland can be extrapolated and transferred to other canopies. This assumption is based on the findings that the presented PLS algorithm exploits covariance between the pure SIF signal and first spectral derivative of up-welling radiance in the solar Fraunhofer lines. Furthermore, the assumption is supported by the results from comparing SFM, SVD-O_2, SVD-FL and PLS against SCOPE simulated SIF, following the approach of Cogliati et al. (2015b) and achieving comparable retrieval errors. Finally, our retrieval results of PLS were similar to SVD-O_2 and SFM in TOC settings. However, we anticipate increased uncertainty of prediction in structurally complex canopies. To address this limitation and account for structurally more complex canopies, a strong permutation of SCOPE modelled SIF and reflectance spectra is used in the training of the PLS models. Thus, each simulated SIF spectrum was combined with each simulated reflectance spectrum. This strong permutation by oversampling increases the distinct instances in the training data and provided larger variation of canopy characteristics. Thus, the PLS model becomes more capable of disentangling SIF from more diverse measured data, and improves the transferability of the PLS retrieval. At the same time, ambivalence and retrieval noise is reduced. However, this trick does not account for all variability in the spectral continuum of SIF and reflectance which can be affected by multiple factors in natural canopies in the field (Verrelst et al., 2016a, 2015). A thorough investigation optimizing a SCOPE dataset, specifically modelled for the training of statistical retrievals, could improve the robustness and transferability of machine-learning-algorithm-based retrieval approaches into specific canopy characteristics. However, this was beyond the scope of this study.

3.6 Conclusion

PLS models trained with SCOPE modelled SIF and reflectance transfer well to real measurements and retrieve values in agreement with other mechanistic (SFM) and statistical (SVD) telluric retrieval methods in TOC settings. As PLS is a supervised approach, its main limitations are identified in the model training and testing with SCOPE modelled up-welling radiance data of known SIF contribution.

Further research is recommended to improve the performance of the PLS model in various and more complex canopies. We partially addressed this issue with a robust permutation approach, which oversamples the SCOPE modelled data to increase the number of possible SIF and canopy reflectance combinations. In addition, PLS models are sensitive to instrumental noise. The retrieval error increases with poorer SNR in a logarithmic relationship. For the retrieval of SIF in very noisy data, for example due to low-light conditions in which automatic signal optimization of the FloX is not possible, the PLS method is not very well suited. Furthermore, PLS and SVD retrieval methods require measurements of down-welling light for the model training process. Thus, it is recommended to acquire the measurements of down-welling light preferably with a white panel through the up-welling channel to accurately include the instrument's optical response. The instrumental configuration with a spectral resolution of 0.3nm FWHM provides a further limitation to the exploitation of the solar Fraunhofer lines with the FloX, especially recognized in the SVD-FL retrieval in combination with narrow fitting windows. In this context, the PLS approach was found more robust. For the first time, we have been able to retrieve positive and meaningful SIF-B and SIF-A values without any atmospheric correction from measured up-welling radiances on a 100m tower above ground, regardless of the reabsorption of signal in the atmospheric column, using PLS. The exploitation of solar Fraunhofer lines for SIF retrieval is very promising for being in principle independent of changing atmospheric disturbances. Since the solar Fraunhofer lines are distributed across the entire spectrum of SIF, more spectral information is available for the detection of SIF using the PLS regression. This additional spectral information reduces retrieval noise and could open a way to unveil the full spectral shape of fluorescence using PLS in the future. We consider the PLS regression model for SIF retrieval from solar Fraunhofer lines particularly promising under conditions for which retrieval methods based on telluric oxygen absorption require complex and computationally costly data correction. In consequence, PLS does not account for atmospheric correction but simply bypasses atmospheric reabsorption. Future research is encouraged to investigate also the performance of SIF retrievals under diffuse light conditions. On an ordinary consumer-grade laptop, PLS models were computed for an entire diurnal dataset within 6.62 seconds. Compared to the SFM method, this is 37.25 times faster. This is also superior to five other machine learning algorithms tested with and without dimensionality reduction in advance of this study.

In summary, we investigated the potential of PLS as an approach for SIF retrieval in modelled data and real measurements from autonomous field spectrometers with promising results. Our results suggest that PLS is superior, compared with other machine learning algorithms, in retrieving SIF signals in the mixture of hyperspectral, up-welling radiance. The fast computation time makes the approach especially appealing for fast processing to overview large datasets for which complex atmospheric correction was required otherwise and for future application of PLS with imaging high-resolution

hyperspectral data. Furthermore, PLS exhibits very high precision compared with solar Fraunhofer line-based SVD. At the same time, PLS based on exploiting the infilling of solar Fraunhofer lines is highly robust against atmospheric reabsorption, compared with telluric oxygen-based methods.

3.7 Acknowledgement

Field measurements were carried out under lead management and funding of European Space Agency in the frame of AtmoFLEX (4000122454/17/NL/FF/mg). This research was supported by the Action CA17134 SENSECO (Optical synergies for spatiotemporal sensing of scalable ecophysiological traits) funded by COST (European Cooperation in Science and Technology, www.cost.eu). The SCOPE modelled dataset and field-measured dataset from the instruments used in this study are available at DOI https://doi.org/10.5281/zenodo.7040578.

3.8 Appendix 1 - Assessment of machine learning for hyperspectral SIF retrieval

Machine learning algorithms (MLA) are tools from data science, which provide methods to extract useful information from a large number of input variables. Emulators and toolboxes have been developed to aid model inversion and retrieval of biophysical parameters from RTM using a variety of MLA (Berger et al., 2020; Rivera-Caicedo et al., 2014; Rivera et al., 2015; Verrelst et al., 2012). Typically, supervised MLA models are trained to predict the variable Y in the predictor space of X. Redundant information in a high-dimensional, hyperspectral predictor spaces are identified and eliminated using dimensionality reduction in a pre-processing step (Verrelst et al., 2017). Principal component analysis (PCA) decomposes the hyperspectral predictor space into components in such a way, that most of the variance in the data is explained by the first few components.

Six MLA and a linear regression model with and without applying PCA during the preprocessing were tested. Neural Network (NN), Partial Least Squares regression (PLS), Gaussian Process Regression (GPR), Elastic Net regression (ENet), Conditional Inference Random forest (CForest), Support Vector Machine (SVM) and a Linear Model (LM) were examined. Training and testing data were composed in the same fashion as presented in Study 2 computing the first spectral derivative as preprocessing. Likewise, 60% training data and 40% testing data were split with a total number of 718 variables in the predictor space. PCA was performed in the preprocessing and the principal components were tested for significance with the randomization procedure (Dray, 2008). For that purpose, axis in the training data were randomized in 900 repetitions. According to Equation 11 the cumulative proportion of variance explained $\sigma^2_{\mathrm{cum}[\%]}$ for n components was computed from the standard deviation σ^2 of each component i, with respect to the total variance of all m=718 components, expressed by the Eigenvalues of the rotated matrix using PCA:

$$\sigma^2_{\mathrm{cum}[\%],\mathrm{n}} = 100 \cdot \sum_{i=1}^{n} \sigma_i^2 \,/\, \sum_{i=1}^{m} \sigma_i^2 \tag{11}.$$

We identified no components, which were significant on a 95% confidence interval. Thus, 95% explained variance was statistically not missing any important information from the original dataset. In consequence, the number of reduced dimensions from the PCA was selected to explain 95% of the variance in the total predictor space, which resulted in using the first five components (see Figure 13).

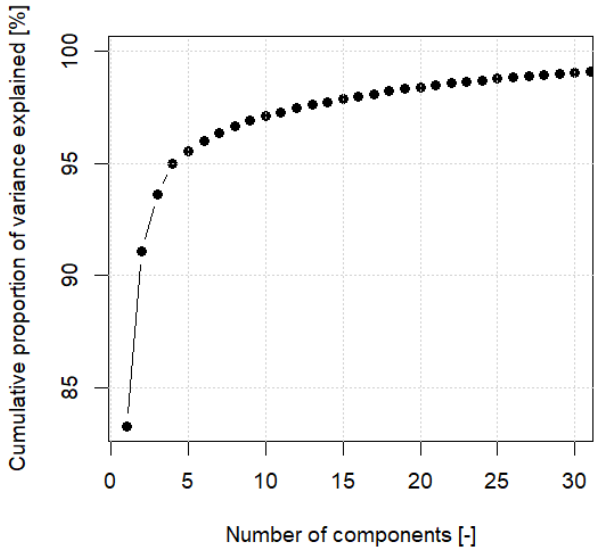

Figure 13: Cumulative proportion of variance of the total predictor space explained in the training data by the first 30 principal components, computed by PCA in the preprocessing of training the different MLAs.

A k-fold, random, segmented (k=4) cross-validation approach with four repeats was used during the training. Training and testing procedures were repeated 30 times for each algorithm in SIF-A and SIF-B, respectively. The RMSE was computed in each run using k-fold cross-validation for the training fraction of the dataset during the training and for the predicted SIF values using the testing fraction of the dataset during the testing with respect the actual SCOPE SIF.

The mean errors and standard deviation are reported for each MLA with and without dimensionality reduction in Figure 14. The associated mean computing time and standard deviation for one training are reported in Figure 15. Our results suggest that PLS exhibited similar prediction errors to GPR, ENet or SVM without applying PCA during the preprocessing. The MLAs exhibited a significantly increased training and testing error in SIF retrieval when combined with PCA. Only in terms of computing time benefit CForest, Enet and SVM from dimensionality reduction slightly. On the contrary, GPR, NN and LM need even more time to converge. PLS outperformed all other MLA significantly in terms of computing time.

Figure 14: Error of SIF prediction from six different MLA and linear regression with and without using PCA in the preprocessing with respect to SCOPE simulated SIF. RMSE was calculated separately for training and testing in 30 repetitions, with SIF-A or SIF-B as response variable, respectively. Whiskers show standard deviation.

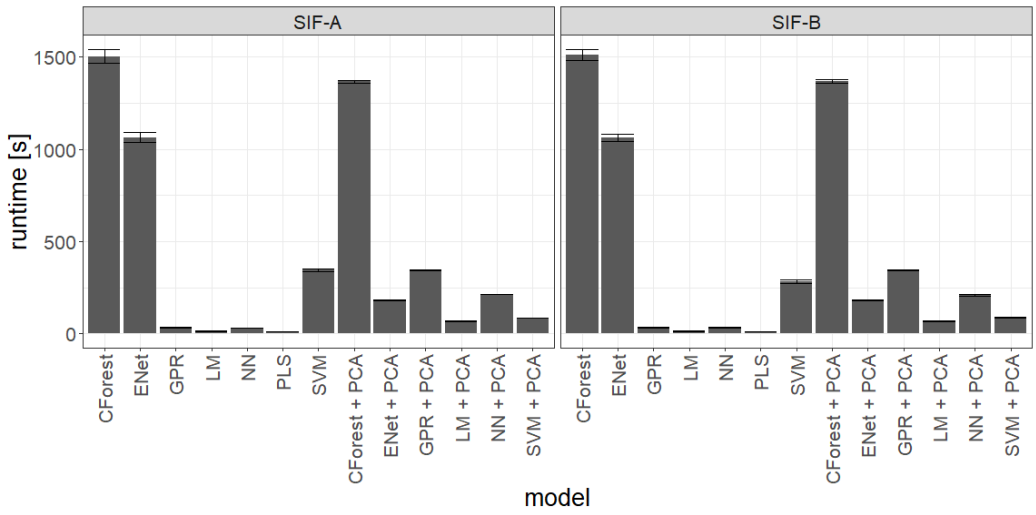

Figure 15: Computing time in seconds from six different MLA and linear regression with and without using PCA in the preprocessing. Mean runtime was calculated separately for training with SIF-A or SIF-B as response variable, respectively. Whiskers show standard deviation.

The SIF signal contributes only about 2% to the variance of the total spectral continuum of up-welling light. However, PCA compresses the components in such a way, to maximize the total variance of the predictor space within the first components. However, due to this compression information is lost, which has only a small contribution to the continuum. However, the exact information loss is unpredictable. Thus, PCA limits the MLAs to find and exploit the fluorescence contribution, which is very small and likely to be lost due to the compression. Note that differences in implementation of the MLAs between different environments (e.g. MATLAB, R, Python.) should also be considered when comparing the results with different studies. Given the high dimensionality of the hyperspectral data

with 718 bands and the computed PCA explaining 95% of its variance within the first five components, we consider the results meaningful. In contrast, PLS exploits covariance between the predicted parameter (SIF in this case) and the predictor space (entity of first spectral derivatives of up-welling radiance in this case) by reducing the number of variables into correlated orthogonal scores. The PLS algorithm has been optimized to find and to obtain quantitative information, which contribute only as small covariance in hyperspectral VIS/NIR spectroscopy (Biancolillo and Marini, 2018; Jiang et al., 2020; Jin and Wang, 2019). PLS outperformed all other tested MLAs with and without PCA preprocessing in this investigation. The most critical drawback of PCA was losing information of small covariance unpredictably when compressing the data into principal components and renders PCA unsuitable for SIF retrieval approaches. In contrast, PLS is by design adequate for finding and exploiting small signals in mixture and therefor considered suitable for the hyperspectral retrieval of SIF.

3.9 Appendix 2 – SCOPE simulated data

Following the approach of Cogliati et al. (2015b), SCOPE simulated SIF and reflectance spectra were used to assess the retrieval performance of the SFM, SVD-FL and SVD-O2 retrievals. The simulated spectra were used to compute up-welling radiance which resembles the optical configuration of the FloX. The range of SIF and reflectance is given for 212 different instances (Figure 16).

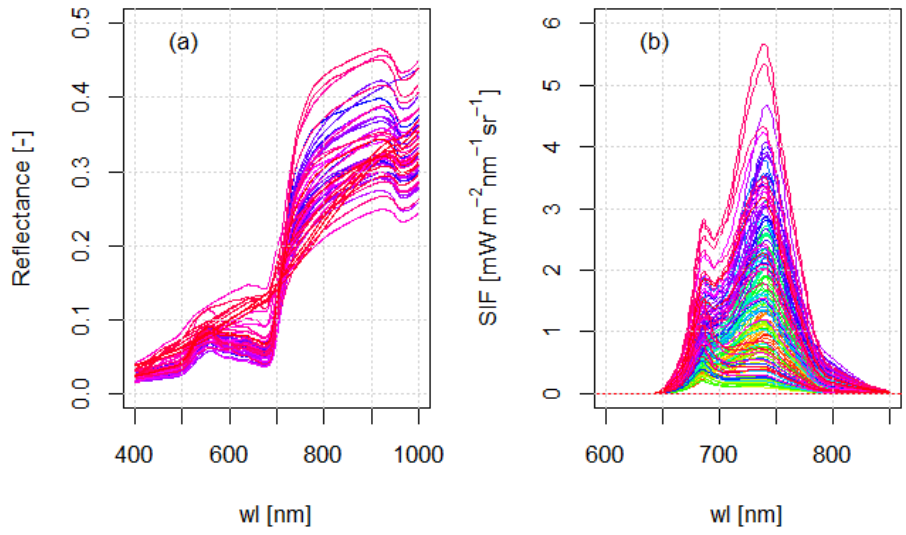

Figure 16: Range of SCOPE simulated reflectance (a) and SIF (b) of the 212 different cases used for the composition of the combined training and testing datasets.

4 Study 2 - Changes of NOx in urban air detected with monitoring VIS-NIR field spectrometer during the coronavirus pandemic: A case study in Germany

Published in: Naethe, P., Delaney, M., Julitta, T., 2020. Changes of NOx in urban air detected with monitoring VIS-NIR field spectrometer during the coronavirus pandemic: A case study in Germany. Sci. Total Environ. 748, 141286. https://doi.org/10.1016/j.scitotenv.2020.141286.

Original manuscript integrated, format, layouts and numberings of elements adjusted, all references included into the bibliography in Chapter 9 of this dissertation.

CRediT Author Statement: **Paul Naethe:** Conceptualization, Methodology, Resources, Data curation, Software, Validation, Investigation, Formal analysis, Writing - Original draft, Writing - Reviewing & Editing, Visualization. **Michael Delaney**: Software, Writing - Reviewing and Editing. **Tommaso Julitta**: Validation, Funding acquisition, Supervision

Key Words: air pollution, field-spectrometer, hyperspectral remote-sensing, coronavirus

4.1 Abstract

The global outbreak of the Corona pandemic has led to a significant reduction of traffic and traffic-related urban air pollution. One important pollutant in this context is NO2. Sudden change in NO2 emissions related to reduction of urban traffic due to infection protection measures can be detected in Düsseldorf, Germany with continuous measurements of down-welling light with a RoX automated field-spectrometer. In comparison to a nearby reference instrument, a waveband around 590 nm was identified as significant for the retrieval in the VIS-NIR spectral range. A decision tree based on principal components which were decomposed from down-welling radiance spectra has been the most robust approach to retrieved NO2 values. Better differentiation of the NO2 value-range is achieved with a partial least square regression model. The results suggest that traffic-related changes of NOx pollution in urban air can be detected through continuous down-welling radiance measurements with inexpensive automated field-spectrometer systems.

4.2 Introduction

Air quality is critical for the well-being and health of humans living in urban areas. Nitrous oxides (NOx) are produced as anthropogenic pollutant and are found in elevated concentrations in densely populated, urban areas. Recent studies suggest that long-term exposure to elevated NO2 has an

impact on fatalities due to the coronavirus, especially in areas with low wind speed and low airmass exchange (Coccia, 2020a; Frontera et al., 2020; Ogen, 2020). In particular, stagnation of air pollutants due to the typical climatology of urban areas in the backcountry supports the spread of viral infective agents (Coccia, 2020b). In recent years, efforts have been made to reduce NOx emission of combustion engines as a consequence of the legal obligations and stricter regulations from governments in response to the Volkswagen emission scandal in 2015. A network of permanent monitoring stations has been established in Germany under state-authority to monitor complete levels of typical air pollutants in urban hotspots. These monitoring efforts provide comprehensive data of NO, NO2 and other typical pollutants at various locations.

As a result of the COVID-19 outbreak in Wuhan, China, and the subsequent global pandemic, most affected countries have responded with varying shut-down measures. In effect have been social interactions reduced, economic activities largely halted and personal mobility discouraged. The resulting reduction of anthropogenic activities has also affected the emission of urban air pollutants noticeably (Muhammad et al., 2020; Wang et al., 2020). A better approach to monitoring and regulating urban air pollutants may very well be part of an integral strategy to address the current coronavirus pandemic and reduce environmental risk factors also for future diseases similar to the COVID-19 infection (Coccia, 2020b).

Geostatistical data fusion approaches are promising in combining real-time data from high-density low-cost sensor-networks with high-grade stationary instruments for improved observation of urban air quality (Schneider et al., 2017). Portable quantum cascade laser spectrometers have been shown to accurately record NO2 in ambient air (Hundt et al., 2018). A waveband in the infrared is shown optimal for NO2 retrieval (X. He et al., 2019). However, previous studies indicate typical absorption cross-sections for opto-electronic detection of the urban air pollutant also in the VIS-NIR range (Zheng et al., 2018). Furthermore, high-grade imaging UV-VIS sensors and UV-VIS point-spectrometers have measured columnar amounts of NO2 in the atmosphere (Park et al., 2019). Thus, it may be possible to consider also inexpensive VIS-NIR spectrometer systems as suitable devices for detecting NO2 pollution in urban air through the continuous monitoring of downwelling light passing through the earth's atmosphere. Hence, inexpensive VIS-NIR field-spectrometers could support the deployment of widespread monitoring networks of urban air pollution. We observe significant changes in NO2 concentration following the reduction of traffic as an immediate effect of the coronavirus pandemic. This case study explains how continuous measurements of down-welling light with inexpensive field-spectrometers can be exploited to retrieve concentration of urban NOx pollution for the purpose of calibration and validation. The presented analysis showed promising results in that sense with significant correlation and an accuracy of up to 87.3% between retrieved and measured NO2 concentration across three different retrieval models.

4.3 Data and Methods

In the following details are provided on the study area, ancillary data, measures of this study, data analyses and procedures.

4.3.1 Study area, data and sources

This study was conducted in close proximity to Südring, a 6-lane street in the south of central Düsseldorf (N51.201745, E6.761245).

Continuous long-term measurements of urban air quality are available as open data from the State Department for Nature, Environment and Consumer Protection North-Rhine Westphalia (LANUV NRW[3]). NO2 levels were extracted from the nearest automated measuring station. Data from the station DDCS, Düsseldorf, Corneliusstraße is available for the time period of interest (Figure 17).

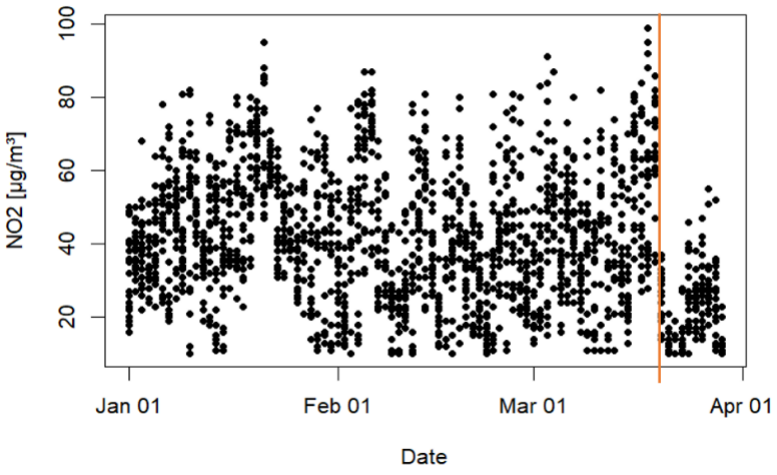

Figure 17: Time-series of continuous NO2 measurements under the authority of LANUV NRW at Düsseldorf Corneliusstr. (DDCS). The vertical line highlights a significant drop in values after March 19th 2020.

4.3.2 Measurements of the study

Automated long-term measurements of down-welling light were performed with a RoX monitoring field spectrometer system by JB-Hyperspectral Devices, Düsseldorf, Germany (Figure 18). The solar-powered instrument was installed for that purpose on a rooftop at the study site.

[3] "Einzelwerte kontinuierlicher Messungen ". LANUV NRW. Accessed April 5, 2024. https://www.lanuv.nrw.de/umwelt/luft/immissionen/berichte-und-trends/einzelwerte-kontinuierlicher-messungen.

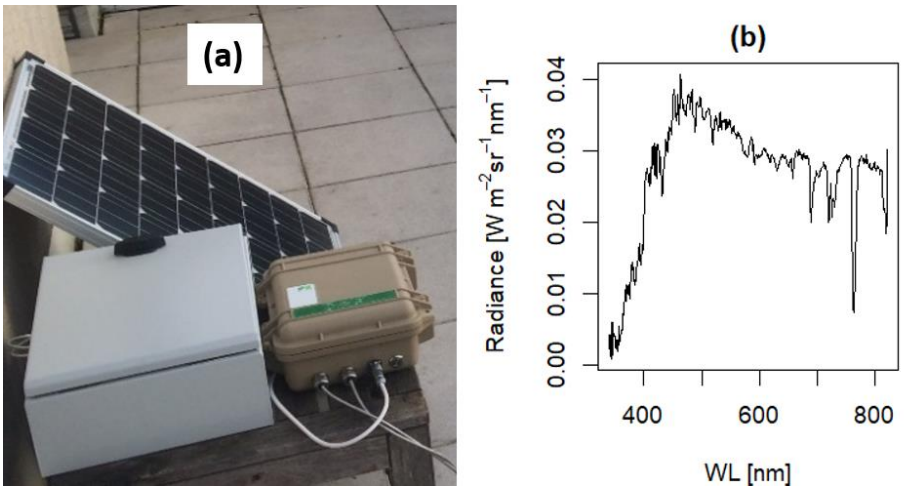

Figure 18: Instrumental Setup. Solar powered, urban installation of autonomous, monitoring field spectrometer RoX – (a). Example spectra of calibrated down-welling radiance spectrum measured with this device – (b).

The data recorded covers the period between December 1st, 2019 and March 29th, 2020. The hyperspectral data was processed from raw digital numbers to calibrated radiances using the FieldSpectroscopyDP[4] and FieldSpectroscopyCC[5] packages in R (R Core Team, 2017).

4.3.3 Data analyses and procedure

Overall, three statistical models were selected for the retrieval of NO2 concentration levels from hyperspectral radiance data: an unsupervised classification model, a decision tree model and partial least squares regression model. These methodologies are in the named order increasing in complexity and are capable of retrieving better NO2 differentiation from the optical measurements. However, with increasing complexity require those methods more information from the underlying data and thus are more sensitive to propagation of uncertainty from the hyperspectral measurements. The analyses of the hyperspectral data were performed in R (R Core Team, 2017). In particular the packages tidyverse (Wickham et al., 2019), mdatools (Kucheryavskiy, 2020), rpart (Therneau and Atkinson, 2019) and partykit (Hothorn et al., 2006) were used. Initially, the hyperspectral data was aggregated by a one-hour interval and the mean of each waveband calculated for each interval step to match the hourly NO2 measurements.

A binary class was introduced, labeled before Corona (bC) and after Corona (aC). A noticeable drop in the NO2 time-series was identified as breakpoint for the separation of this binary class (Figure 1). This breakpoint has been validated as one day after the TV-oration of German Chancellor Angela Merkel on the evening of March 18th, 2020, in which she announced contact prohibition and advanced protective measures in response to the coronavirus pandemic. Both, the hyperspectral radiance time

[4] Julitta, T. "FieldSpectroscopyDP". Github, Inc. Accessed April 5, 2024. https://github.com/tommasojulitta/FieldSpectroscopyDP.
[5] Julitta, T. "FieldSpectroscopyCC". Github, Inc. Accessed April 5, 2024. https://github.com/tommasojulitta/FieldSpectroscopyCC.

series and NO2 time-series were combined in a large dataset. As suggested in Grolemund and Wickham(2016), the data was transformed in an effort to improve accessibility. A spectral window between 550nm and 680nm (Figure 18) was selected for further analysis in agreement with the spectral range of the known NOx absorption cross-section (Zheng et al., 2018) and to excluded unrelated spectral regions as potential source of error. A supervised classification model was built with a conditional inference tree, using the hyperspectral radiance data to predict the binary class response. The model performance was recorded and a confusion matrix created. The positive predictive values of the model were reported separately for each group and the entire set.

Furthermore, the down-welling radiance data was decomposed into principal components (PCs). These principal components served as the predicting variables for an unsupervised decision tree model for the regression with the measured NO2 values. A penalty was introduced to limit tree complexity and avoid over-fitting. With R^2 increasing by at least 0.01 per additional level can the model discriminated 10 discrete NO2 levels. Tree structure and most significant variable are reported in Figure 19. The model was built of nine PCs at nine nodes, with PC2 as most significant for the differentiation of NO2, which is reflected by its position at the top of the decision tree.

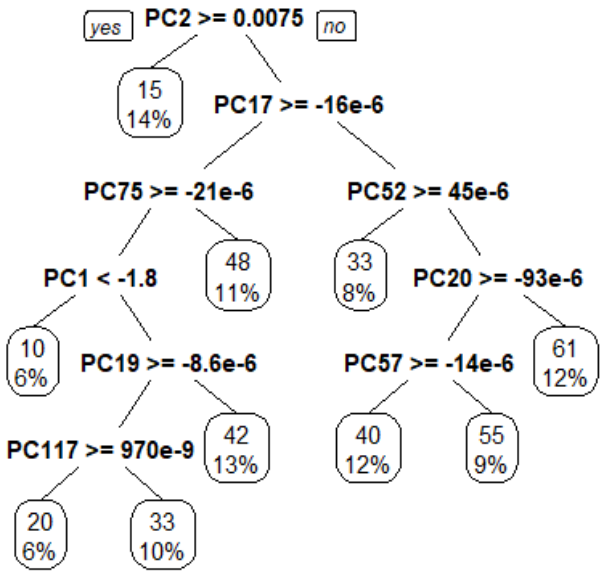

Figure 19: Tree structure of the decision tree model for the prediction of NO2 built from principal components computed from hyperspectral down-welling radiance measurements. Nodes show principal components and their threshold value for the model. The leaves show the distinguishable NO2 values and their proportional percentage of occurrence, which can be still differentiated on the assumption that R^2 increases by at least 0.01 with each step of increasing tree-complexity.

The decision tree model has been used to predict NO2 levels from the actual measurements.

The predicted NO2 values were compared with the true measured values and confidence of determination (R^2) was calculated for a linear regression. In addition, intercept and slope for the linear

fit and the p-value for significance of correlation are reported. Furthermore, the F-test for ratio of variance and its p-value for significance are reported.

Moreover, partial least square regression was employed with the down-welling radiance data to predict actual NO2 values with a supervised model. This model is built on the assumption of a linear regression between NO2 concentration and a covariance in the mixture of signals in the down-welling light measurements. Based on this correlation between NO2 levels and down-welling light measurements was the variable space of the calibration matrix decomposed into optimized latent variables (components) in an iterative process. The resulting components of the spectral radiance data were then utilized in a model to predict the actual NO2 levels from the down-welling light measurements with the instruments. The full dataset was split even into training and testing data for model training and cross-validation. The Root Means Square Error (RMSE) was calculated as following:

$$RMSE = \sqrt{\frac{1}{n}\sum_{i=1}^{n}(\hat{x_i} - x_i)^2} \tag{12}$$

with $\hat{x}$ being the actual measured NO2 value and x being the predicted NO2 value was reported as in Equation 12 for increasing number of components, and thereby an increasing model complexity. For prediction, the number of components with lowest RMSE in the cross-validation was selected. The absolute regression coefficients were reported for this model complexity with respect to wavelength. Finally, the predicted NO2 values were compared with the actual measurements across the entire dataset through linear regression, reporting R^2 and RMSE of prediction.

4.4 Results and Discussion

Hyperspectral down-welling radiance time-series were exploited to retrieve NO2 from urban sources. The results from three different retrieval approaches were compared to actual measurements of the urban monitoring. Results are presented according to the previously described methodology.

The inter-quartile ranges (IQR) of NO2 values of the group before the Corona (bC) is above the one of group after the Coronavirus (aC), both IQR do not overlap. Both groups, bC and aC are therefore significantly different (Figure 20). On the weekend after the announcement of German Chancellor Merkel, on March 21st and 22nd, were the lowest daily maximum values recognized in the entire NO2 series (Figure 17). These findings suggest reduced NO2 emissions in response to the official recommendation for people to stay home.

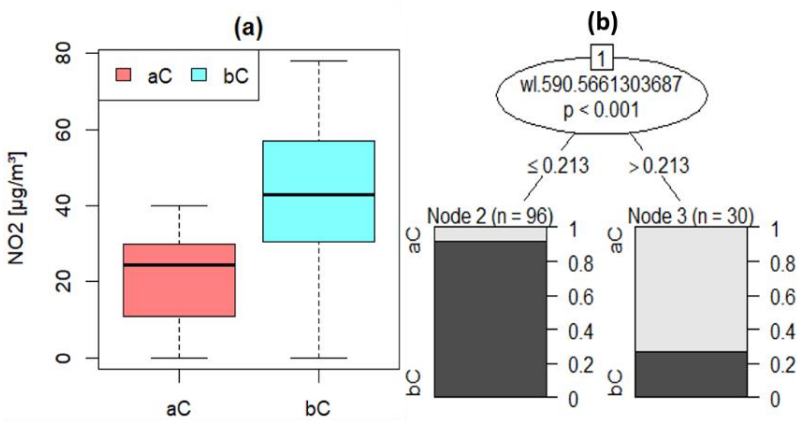

Figure 20: Panel (a) shows boxplot with two groups of NO2 values, before Corona (bC) in green and after Corona (aC) in red. Panel (b) shows the conditional inference tree for the classification of nominal NO2 levels from hyperspectral down-welling measurements.

Further, a conditional inference tree based on hyperspectral down-welling radiances suggested a waveband around 590.56nm as most significant for the classification of bC and aC within a 99.9% confidence interval. The absorption cross-section of both NO2 and NO3 presented in Zheng et al. (2018) overlap with this waveband around 590nm. Hence, co-occurrence of NO2 and NO3 is assumed on the basis of traffic-related emission sources. The model classified the NO2 correctly from down-welling light in 91.9% of the bC cases and in 73.3% of the aC cases. Overall, 87.3% of the cases are distinguished correctly, based on hyperspectral down-welling radiance data (Table 5).

Table 5: Confusion matrix for prediction of nominal NO2 levels after Coronavirus (aC) and before Coronavirus (bC) with the conditional inference tree. The percentage of true positive classification is given per class and per total.

	aC	bC	positive predictive value
aC	22	8	73.3 %
bC	8	88	91.6 %
total	30	96	87.3 %

The decision tree model has been employed to correlate NO2 values with combinations of PCs, derived from continuous downwelling light measurements. Figure 21 illustrates the regression between predicted and actual measured NO2 values. The F-test indicates a significant difference within a 99.9% confidence interval between the decision tree model and an intercept-only model for the prediction of NO2 (Table 6). Therefore, it can be concluded that the specified decision tree model describes the measured data better than a linear model with no predictors.

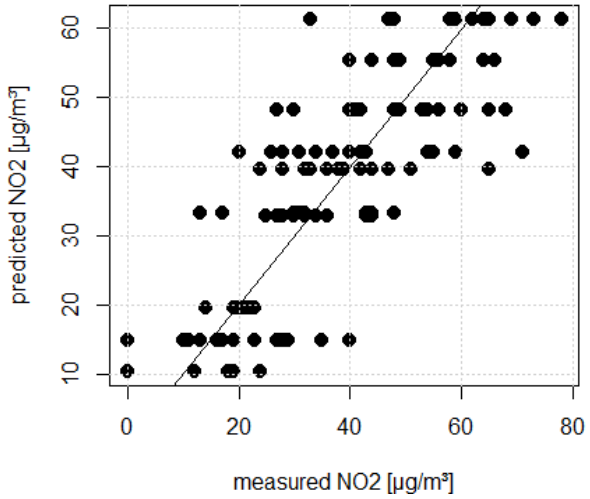

Figure 21: Measure and predicted NO2 values from the decision tree model. The line represents the function of the linear regression between measured and predicted values.

Hence, the decision tree model can reconstruct absolute NO2 values with $R^2 = 0.67$ from hyperspectral data, showing a significant linear correlation within a 99.9% confidence interval (Table 6). Slope and intercept indicate furthermore a one-to-one relationship between measured and predicted NO2.

Table 6: Test statistics of the regression and F-test performed on measured and predicted NO2 data with the decision tree model based on principal components of hyperspectral down-welling radiance data.

Statistic	Test value
F-test	253.3
F-test p-value	$<2x10^{-16}$
Intercept of linear regression	0
Slope of linear regression	1
R^2	0.67
Correlation p-value	$<2.2x10^{-16}$

Partial least squares regression was applied, relating NO2 to downwelling radiance measurements, and the performance reported in Figure 22. During the model calibration decreases the error of prediction with increasing model complexity, reaching an almost perfect fit of the training data. However, this is a typical case of overfitting as the error of prediction increases rapidly with increasing model complexity during the cross-validation. The optimal number of components for prediction with minimal error in the cross-validation process is at 10 components. The regression coefficients are plotted in absolute values to improve readability. These coefficients can also be negative as their sign arbitrarily depends on the orthogonal loadings. The highest regression coefficient is computed for a waveband around 590nm and deemed the most influential for the prediction of NO2. The 10 components model predicts measured NO2 with $R^2 = 0.45$ and RMSE = 14.22 µg/m³ with respect to the actual measured values.

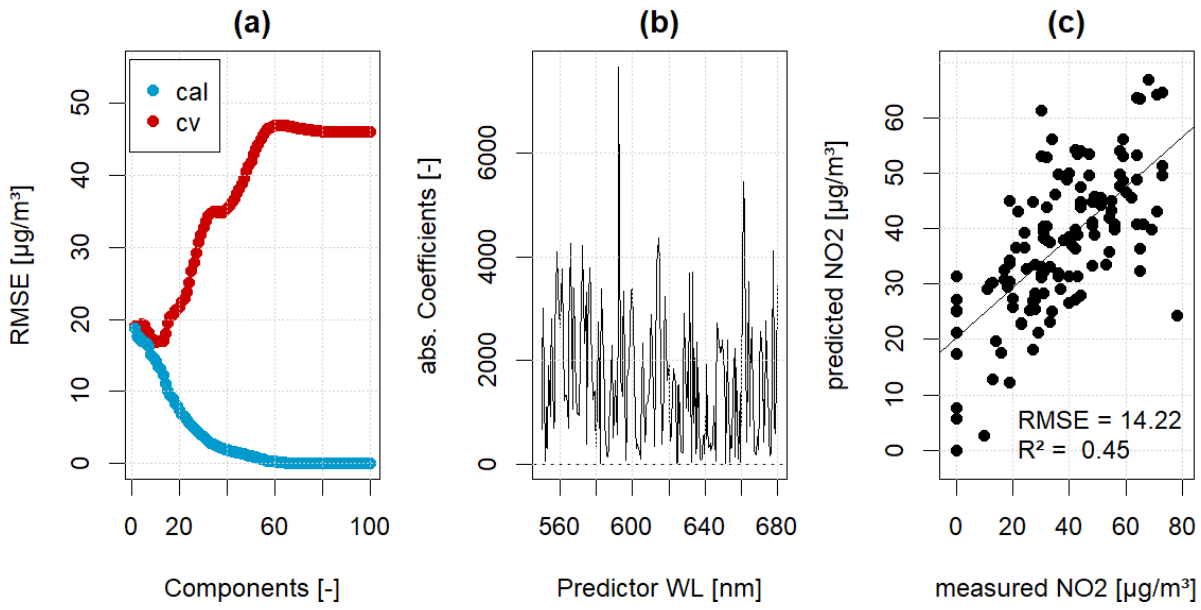

Figure 22: Root Mean Square Error (RMSE) of calibration (blue) and cross-validation (red) with respect to number of components used – (a). Absolute regression coefficients of the 10 components model with respect to wavelength – (b). Benchmarking prediction of NO2 values with the 10-components model – (c).

Best accuracy of the three statistical models tested for the retrieval of NO2 was achieved with the classification through a conditional inference tree. The presented classification approach, on the other hand, is limited due to the repeated temporal occurrence of similar values within the outliers in each group. This overlap is especially noticeable for the group aC, while the group bC can be distinguished through a unique value-range. Therefore, misclassification of spectra that would actually fall into aC is more likely. This, in turn, is directly reflected in the ambiguity of the conditional classification. The positive predictive value for bC is significantly higher in comparison to aC. To reduce classification bias by cooccurrence with other trends in the hyperspectral data the classification should be carried out with an extended time-series, comparing similar episodes in subsequent years. Unfortunately, due to the limited timeframe of field spectrometer data available in this instance, this has not been possible. For the complexity of changes in the atmospheric transfer across the entire spectral range statistical de-trending methods were considered unsuitable. The unsupervised regression model presented remains unaffected by those limitation. In contrast to comparing classes split at a specific point in time, the unsupervised model aims to directly differentiate levels in the NO2 value-range. Thus, robustness of the model benefits from multiple temporal occurrences of the same or similar NO2 values. The presented unsupervised regression model shows the highest R^2 of all three investigated approaches but remains rather crude in value-resolution as only 10 levels of NO2 values can be effectively differentiated from hyperspectral PCs.

In comparison, the presented supervised regression is more capable of reproducing the actual value-range in NO2 but shows a lower R^2 value. A cross validation process in the supervised approach is testing the model's robustness with previously unknown data from repeated random segments and

minimizes over-fitting. However, the algorithm is highly sensitive to noise in the hyperspectral radiance data which is also reflected in the model's spectral regression coefficients. Moreover, a waveband around 590nm was recognized as the most influential in the supervised model. This outcome aligns with the previous findings in the unsupervised classification and is in accordance with the absorption cross-section for NOx in the VIS-NIR spectral range. In Figure 18 a small absorption feature is noticed around 590nm in the down-welling light spectrum. However, the immediate exploitation remains challenging, as there are multiple atmospheric influences in this spectral region.

Nevertheless, the observed significant drop in urban air pollution with NOx in this case study can be considered a beneficial byproduct of the lockdown and reduces environmental risk factors for COVID-19 and similar diseases, threatening to human health (Fattorini and Regoli, 2020). Our results encourage further investigation of field-spectrometers as inexpensive instruments towards a wide-spread monitoring network of anthropogenic air pollution as a part of an integrated strategy to reduce further environmental risk factors for the coronavirus and similar pandemics in the future.

4.5 Conclusion

Three different classification and regression approaches were tested in this case study to retrieve information on urban air pollutants from continuous down-welling radiance measurements with an automated monitoring field-spectrometer system during the coronavirus pandemic. Significant differences in urban NO2 emissions were reported before and after severe reduction of urban traffic due to measures in response to the coronavirus pandemic which were enacted by governmental authorities in Germany. The investigated methods reproduce these differences in measured NO2 successfully with relatively inexpensive equipment. As an alternative, physical modelling based on mechanistic radiative transfer models can be considered for the retrieval of urban air pollutants from down-welling hyperspectral measurements. However, further direct exploitation of absorption features of NO2 is considered very tricky, as they are typically overlaid with other absorption features of atmospheric trace gases and aerosols. In addition, geographical position is known to influence the stagnation of air pollutants under certain conditions which has to be considered as a limitation to this investigation. It has to be further noted that the location of measurements for NO2 and down-welling light were not identical due to the availability of data. Therefore, uncertainties with respect to the spatial distribution have to be considered. Further limitation from windspeed as a variable for airmass exchange and the distribution of NO2 in different air layers need to be considered. Additional experiments for calibration and validation over an extended period of time with a dedicated instrumental setup of a monitoring field spectrometer systems in close proximity to conventional measurements of urban air pollutants are encouraged. Future efforts should also consider the windspeed, wind direction and the resulting dispersion of NO2 in the air as influencing variables.

Nevertheless, in this context we consider the potential of inexpensive, automated field-spectrometers a valuable contribution towards wide-spread monitoring of urban air pollutants, especially since these systems are easy to handle, cheap to maintain and observe a large spectral range containing various other information.

4.6 Acknowledgement

This work was supported in part through the joint research project "mDRONES4rivers" by the Federal Ministry of Transport and Digital Infrastructure – BMVI (19F2054A-D). Special thanks to Andreas Burkart for inspirational discussions and contributing excellently designed monitoring field-spectrometer systems.

5 Study 3 - Towards a standardized, ground-based network of hyperspectral measurements: combining time series from autonomous field spectrometers with Sentinel-2

Published in: Naethe, P., De Sanctis, A., Burkart, A., Campbell, P.K.E., Colombo, R., Di Mauro, B., Damm, A., El-Madany, T., Fava, F., Gamon, J.A., Huemmrich, K.F., Migliavacca, M., Paul-Limoges, E., Rascher, U., Rossini, M., Schüttemeyer, D., Tagliabue, G., Zhang, Y., Julitta, T., 2024. Towards a standardized, ground-based network of hyperspectral measurements: Combining time series from autonomous field spectrometers with Sentinel-2. Remote Sens. Environ. 303, 114013. https://doi.org/10.1016/j.rse.2024.114013.

Original manuscript integrated, format, layouts and numberings of elements adjusted, all references included into the bibliography in Chapter 9 of this dissertation.

CRediT Author Statement: **Paul Naethe:** Conceptualization, Methodology, Software, Validation, Resources, Writing – Original Draft, Writing – Review & Editing, Visualization. **Andrea De Sanctis:** Methodology, Software, Formal analysis, Investigation, Data Curation, Visualization. **Andreas Burkart:** Data Curation, Writing – Review & Editing, Funding acquisition. **Petya K. E. Campbell:** Resources, Data Curation, Writing – Review & Editing. **Roberto Colombo:** Resources, Data Curation, Writing – Review & Editing. **Biagio Di Mauro:** Resources, Data Curation, Writing – Review & Editing. **Alexander Damm:** Resources, Data Curation, Writing – Review & Editing. **Tarek El-Madany:** Resources, Data Curation. **Francesco Fava:** Data Curation. **John A. Gamon:** Resources, Data Curation, Writing – Review & Editing. **Karl F. Huemmrich:** Resources, Data Curation, Writing – Review & Editing. **Mirco Migliavacca:**

Resources, Data Curation. **Eugenie Paul-Limoges:** Resources, Data Curation, Writing – Review & Editing. **Uwe Rascher:** Conceptualization, Resources, Data Curation, Writing – Review & Editing. **Micol Rossini:** Resources, Data Curation, Writing – Review & Editing. **Dirk Schüttemeyer:** Resources, Data Curation, Funding acquisition. **Giulia Tagliabue:** Resources, Data Curation. **Yongguang Zhang:** Resources, Data Curation, Writing – Review & Editing. **Tommaso Julitta:** Conceptualization, Software, Writing – Review & Editing, Visualization, Supervision, Funding acquisition, Project administration.

Keywords: Field Spectrometer; Sentinel-2; Time Series; Cloud Filtering; Data Fusion, FloX, RoX

5.1 Abstract

Sentinel-2 satellite data enables multispectral monitoring of the earth at a high temporal revisit rate. Combining this information with a network of optical ground measurements enables a more detailed and a more complete understanding of terrestrial ecosystems. However, independent optical ground measurements often lack consistency, especially when comparing different sites in geographically remote locations. Using the very high temporal and spectral resolution offered by the automated field spectrometer systems FloX and RoX (Fluorescence Box and Reflectance Box, respectively, JB-Hyperspectral Devices GmbH, Duesseldorf, Germany), we investigated continuous time series ranging over three years and in ten different locations across Europe, Africa, America and Asia. The continuous records of ground-measured reflectance were first validated against Sentinel-2 top of canopy (TOC) reflectance to evaluate the consistency of the in-situ network. Our results suggest a good agreement of ground-measured reflectance with Sentinel-2 TOC reflectance in vegetation and snow with R^2 around 0.79 in the 833 nm band and R^2 up to 0.94 in the bands around 559 nm and 492 nm, demonstrating good consistency across the network. Spatial misalignment of Sentinel-2 pixel-sizes with respect to the different footprint sizes of the ten automated spectrometers on the ground, atmospheric uncertainties, sub-optimal instrument setup and spatial-temporal variable landscape heterogeneity were identified as the most relevant sources of uncertainties in the network. Comparing the Normalized Difference Vegetation Index (NDVI), Transformed Chlorophyll Absorption in Reflectance Index (TCARI) and Enhanced Vegetation Index (EVI) between ground and satellite revealed a decreasing agreement with increasing complexity of index formulation. The best agreement between satellite and ground was exhibited by NDVI with R^2 around 0.96 and relative error of 4.3% investigating vegetation and snow across all ten sites. Furthermore, we identified a seasonal pattern in residuals of NDVI between ground and satellite in an alpine ecosystem in northern Italy, which was associated with increased spatial heterogeneity due to the effects of diverse vegetation phenology and snowfall. In contrast, a random distribution of residuals was recognized in a rather uniform oak forest canopy in southern France. Clustering Sentinel-2 pixels with respect to their temporal patterns in NDVI identified similar areas seen as homogenous in the canopy of Torgnon, Italy, and Observatoire de Haute-

Provence (OHP), France, each. The very high temporal resolution of NDVI measured on the ground confirmed overlap with matched homogenous areas, but must consider seasonal landscape heterogeneity. Using well-standardized and globally homogenous Sentinel-2 TOC reflectance enabled the assessment of uncertainties in ten field spectrometer sites around the world. The standardization of the automated field spectrometers, their data products and data annotation were essential prerequisites that enabled joint validation against Sentinel-2. Harmonizing optical ground measurements with respect to a satellite is promising for future research to ensure the valid intercomparison and transfer of data products across different sites in a network worldwide.

5.2 Introduction

Remote sensing of the earth's terrestrial surface from satellites provides a valuable source of information, often combined with insight from ground-based sensors across scales and domains (Bioucas-Dias et al., 2013). With the Copernicus program, the European Space Agency (ESA) has launched seven Sentinel satellite missions up to now. ESA's Sentinel-2 (S-2) program has two satellites in operation with the primary objective to retrieve high-resolution, multispectral images with a high temporal revisit rate (Drusch et al., 2012). The multispectral configuration is suitable to examine land surface properties, especially for the investigation of coastal waters, land-cover and vegetation (Ariza et al., 2018; Caballero et al., 2020; Hank et al., 2019; Ma et al., 2019; Oxoli et al., 2020; Vincini et al., 2016). Surface reflectance is provided at the bottom of the atmosphere using an atmospheric correction and automated data processing, which is further supported through cloud masks and cloud shadow masks (Baetens et al., 2019). Due to the high temporal resolution and good spectral coverage of the S-2 visible to near- infrared (VIS-NIR) spectral range, this satellite mission is especially suitable to compare with a network of identically specified, automated spectrometer systems, installed in various locations for long periods of time (Wang et al., 2018). Extended time series not only reveal specific spectral signals from different types of land cover, but also provide unique temporal signatures, suitable for change detection of land use classes and inferring plant functional traits (Debella-Gilo and Gjertsen, 2021; Ma et al., 2019). Both, advanced experimental and modelling analyses are of high value for predicting environmental phenomena, for example in estimating burned areas or eroded soil (Lense et al., 2023; Mohammad et al., 2023). Extended time series are particularly useful when temporal and spectral signatures are compared between ground and satellite (Nagai et al., 2020; Sefrin et al., 2021). Especially interesting for the purpose of this study is the unprecedented investigation of the highly consolidated S-2 data for validating and harmonizing a worldwide network of standardized, automated field spectrometers.

Autonomous field spectrometer systems have been increasingly used for the continuous long-term monitoring of vegetation, water, atmosphere and snow (Campbell et al., 2019; Cogliati et al., 2015a;

Kokhanovsky et al., 2021; Meroni et al., 2011; Naethe et al., 2020; Wagner et al., 2018). While the field spectrometer system FloX (Fluorescence Box) by JB Hyperspectral Devices, Düsseldorf, Germany, was designed primarily for the retrieval of sun-induced chlorophyll fluorescence, both, FloX and RoX (Reflectance Box) share the identical optical configuration in VIS-NIR and are suitable for the retrieval of hyperspectral reflectance and vegetation indices (VI) (Acebron et al., 2021; Burkart et al., 2015b; Dechant et al., 2022; Julitta et al., 2016; Krämer et al., 2021; Mohammed et al., 2019; Siegmann et al., 2021; Vargas et al., 2020). High temporal resolution in combination with the high hyperspectral resolution enable investigation of detailed temporal patterns, both, in VI and reflectance with regards to a very defined field of view (FOV) in one location (Martini et al., 2022). Standardization of spectral ground measurements using automated point-spectrometers has been a longstanding challenge in the field of remote sensing (Cavender-Bares et al., 2020; Gamon, 2015; Milton et al., 2009). Standardized hardware as well as standardized calibration, data processing, data annotation and traceability including uncertainty budgets are necessary to transfer calibrated data in absolute physical unit across a network of instruments (Buman et al., 2022; Hueni et al., 2017; Porcar-Castell et al., 2015). The automated spectrometers investigated in this study fulfilled those requirements and, therefore, could be considered a network. On the one hand, such a network allows to investigate spatial-temporal dynamics at a larger scale worldwide. However, verification of those ground measurements with respect to a globally aligned reference is indispensable for combining insights of great temporal and spectral details across the network and harmonizing data products on the other hand.

Numerous networks and communities were established in the past with the aim to provide a standardized approach to spectral ground measurements, for the purpose of calibration and validation of satellite data, e.g. Aerosol Robotic Network - AERONET (Li et al., 2018) and Spectral Network - SpecNet (Gamon, 2015; Gamon et al., 2006), and to facilitate these optical measurements in the context of a network of carbon flux sites (FLUXNET)(Gamon et al., 2010) such as the Integrated Carbon Observation System (ICOS) (Etzold et al., 2022; Gielen et al., 2017) and the National Science Foundation's National Ecological Observatory Network (NEON) (Ma et al., 2022; Metzger et al., 2019). Ground measurements of ecosystem parameters are important for the understanding, modelling and forecasting of natural phenomena broadly speaking, which globally interlink vegetation dynamics and primary production with the water cycle, carbon cycle and local micro-meteorology (Lama et al., 2021a, 2021b; Migliavacca et al., 2017; Norton et al., 2019; Pirone et al., 2023; Rossini et al., 2010). In the context of those existing networks are automated, temporally dense, hyperspectral ground measurements of down-welling and up-welling light interesting, because optical in-situ measurements oftentimes serve as proxies for local ecosystem status parameters and enable the fusion of multiple optical sensors across scales (Naethe et al., 2023; Pérez-Harguindeguy et al., 2013).

Due to rapid changes in the atmosphere and low light conditions, ground-based spectroscopy measurements under cloudy conditions are challenging but valuable for enabling specific insights at the same time (Buman et al., 2022; Kanniah et al., 2012; Kaskaoutis et al., 2008). Optical satellite images are adversely affected by clouds so that cloud-covered areas are unusable and typically masked out, making impossible to observe vegetation canopies under cloudy conditions with optical satellites (Baetens et al., 2019; Petitjean and Weber, 2014). Shadows of clouds and large structures are an increasing issue with increasing spatial resolution of remote sensing images (Liu et al., 2017; Shahtahmassebi et al., 2013). While being especially challenging at lower levels, e.g. on drones and on the ground, effective shadow detection methods are essential for robust data filtering, as remote sensing products such as reflectance or VI are substantially biased under shadows (Adler-Golden et al., 2002; Damm et al., 2015; Liu et al., 2017; Wemett et al., 2009). However, often studies investigate a limited area only where local cloud-shadow detection on the ground would be sufficient. However, robust cloud detection and filtering are mandatory prerequisites for validating and harmonizing information of multiple optical sensors across scales and domains.

This study used data from S-2 as a reference for validating a worldwide network of standardized field spectrometers and for harmonizing their data products. For the first time, satellite TOC data was used to validate continuous time series of reflectance measured from automated field spectrometers at very high temporal resolution in 10 different locations around the world. We use the very high temporal resolution of ground-measured down-welling radiance to investigate suitable cloud-shadow detection. Reversing the common practice of cross-validating in-situ point-spectroscopy and airborne imaging spectroscopy, as presented in Hueni et al. (2017), 10 identically equipped field spectrometer sites were harmonized and challenges of temporal variability in spatial heterogeneity were unveiled. Considering that S-2 offers global coverage of highly standardized data products, this satellite data served as a stable reference for the independent validation of each site and investigation of site-specific uncertainties in continuous time series recorded by standardized field spectrometer systems over several years on the ground.

5.3 Materials and Methods

We compared dense, hyperspectral time series recorded with FloX and RoX spectrometers in ten different locations in Africa, America, Asia and Europe with time series extracted from simultaneous S-2 overpasses. Combining ground measured and satellite measured data is challenging due to rapid changes in the atmosphere. Therefore, we applied cloud filtering based on both, S-2 cloud masks and on a novel approach using ground-based measurements of incoming light. Top of Canopy (TOC) Reflectance, Normalized Difference Vegetation Index (NDVI) (Tucker, 1979), Enhanced Vegetation Index (EVI) (Liu and Huete, 1995) and the Transformed Chlorophyll Absorption in Reflectance Index

(TCARI) (Haboudane et al., 2002) were compared under cloud-free conditions. TOC reflectance was used for absolute and quantitative comparison per spectral band, extracted from satellite and convolved from hyperspectral ground measurements. NDVI is very robust against diurnally variable amounts of solar radiation on the ground and is not sensitive for short-term variations in plant's physiological adaptation processes due to its band selection and formulation (Gamon et al., 2015, 1992), and was therefore considered ideal to compare ground and satellite data. EVI is a more complex modification of NDVI that minimizes effects of soil and atmosphere, which is still mostly stable throughout the diurnal cycle and was considered for that reason. TCARI was used as a more modern, very complex soil-adjusted chlorophyll index, which predicts canopy chlorophyll content regardless of the background of changing land cover (Herrmann et al., 2010; Main et al., 2011). NDVI, EVI and TCARI were feasible to compute from the available S-2 bands in this study and were used to examine the effects of increasing complexity of VI affecting the agreement between ground and satellite data. Finally, the robust NDVI was used to investigate further temporal and spatial aspects affecting the direct validation of ground and satellite data.

5.3.1 Instruments and sites

A variety of different agricultural and natural vegetation canopies as well as snow were monitored with FloX and RoX field spectrometers in ten different sites across Europe, America, Asia and Africa (see Figure 23). FloX and RoX share in common identical VIS-NIR spectrometers featuring 450 nm – 900 nm spectral range, 1.5 nm full width at half maximum (FWHM) spectral resolution and a hemi-conical optical configuration with up-welling light recorded through bare fiber optics with 25° opening angle and down-welling light recorded through a cosine diffusor with a theoretical 180° opening angle (Chang et al., 2021). Time series were recorded completely unattended with a very high temporal resolution up to one measurement per minute, depending on light conditions in the field (Cogliati et al., 2015a). Further processing of the data enabled filtering based on standardized, system-internal quality flags and quantitative parameters indicating goodness of each measurement, accounting for saturation, unstable measurements, automatic optimization and low solar angles.

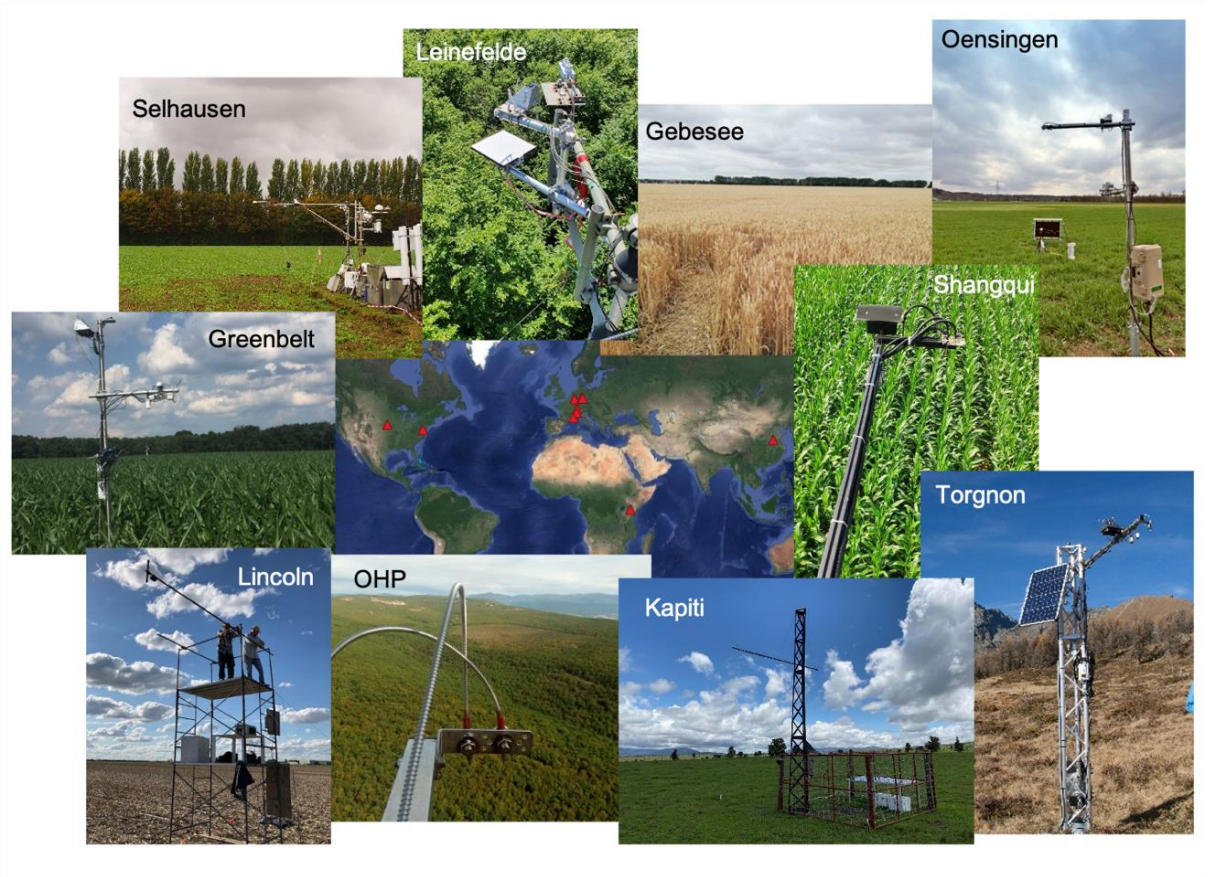

Figure 23: Selected field sites, equipped with FloX or RoX. Spread over Europe, America, Asia and Africa, covering different vegetation and non-vegetation targets. World Imagery (ESRI, 2021).

The ten field sites were set up similarly for the investigation of extended, temporally dense time series of TOC reflectance and VI. For this purpose, all spectrometers were set up on towers in such a way that down-welling light was monitored though the up-facing cosine optics without obstruction from nearby structures. The down-facing bare optics were mounted in a southerly direction (in the southern hemisphere in a northerly direction) on an extended arm to minimize self-shading and ensure unobstructed nadir view onto the desired footprint. Details to the sites, spectrometers and installations are provided in Table 7. The shortest time series covers 6 months and the longest over 3 years of continuous data recording, for which representative parts were selected. An important criterion for the selection of data was the temporal agreement with available S-2 overpasses. Furthermore, ambient light conditions and instrumental quality criteria, as described in the following section were considered for the selection of ground measured data.

Table 7: Experimental setup giving site name, country, coordinates, spectrometer incl. serial number, site and installation description, target, period investigated

Site name	Country	Lat	Lon	Target	Dist. from TOC	Footprint radius	Period investigated
Torgnon	Italy	45.844	7.578	Alpine pasture	2 m	0.4 m	06 Dec 2017 - 05 Mar 2021
OHP	France	43.934	5.711	Oak forest	90 m	20.0 m	06 Dec 2017 - 16 Sep 2020
Leinefelde	Germany	51.327	10.367	Mixed broadleaf forest	8 m	1.8 m	12 May 2019 - 03 Oct 2020
Gebesee	Germany	51.100	10.914	Wheat field	2 m	0.4 m	15 Apr 2019 - 07 Jul 2019
Kapiti	Kenya	-16.144	37.133	Savannah	4.5 m	1.0 m	01 Oct 2019 - 12 Jul 2020
Lincoln	USA	41.179	-96.441	Corn field	2 m	0.4 m	02 Sep 2019 - 17 Oct 2019
Greenbelt	USA	39.029	-76.843	Corn field	2 m	0.4 m	25 Jul 2020 - 24 Aug 2020
Shangqui	China	34.515	115.59	Corn field	4 m	0.9 m	08 Jul 2020 - 16 Nov 2020
Oensingen	Switzerland	47.286	7.733	Corn field	2 m	0.4 m	25 Jul 2020 - 24 Aug 2020
Selhausen	Germany	50.865	6.447	Grassland	2 m	0.4 m	18 Nov 2020 - 27 Apr 2021

5.3.2 Data processing, cloud detection and statistical analyses

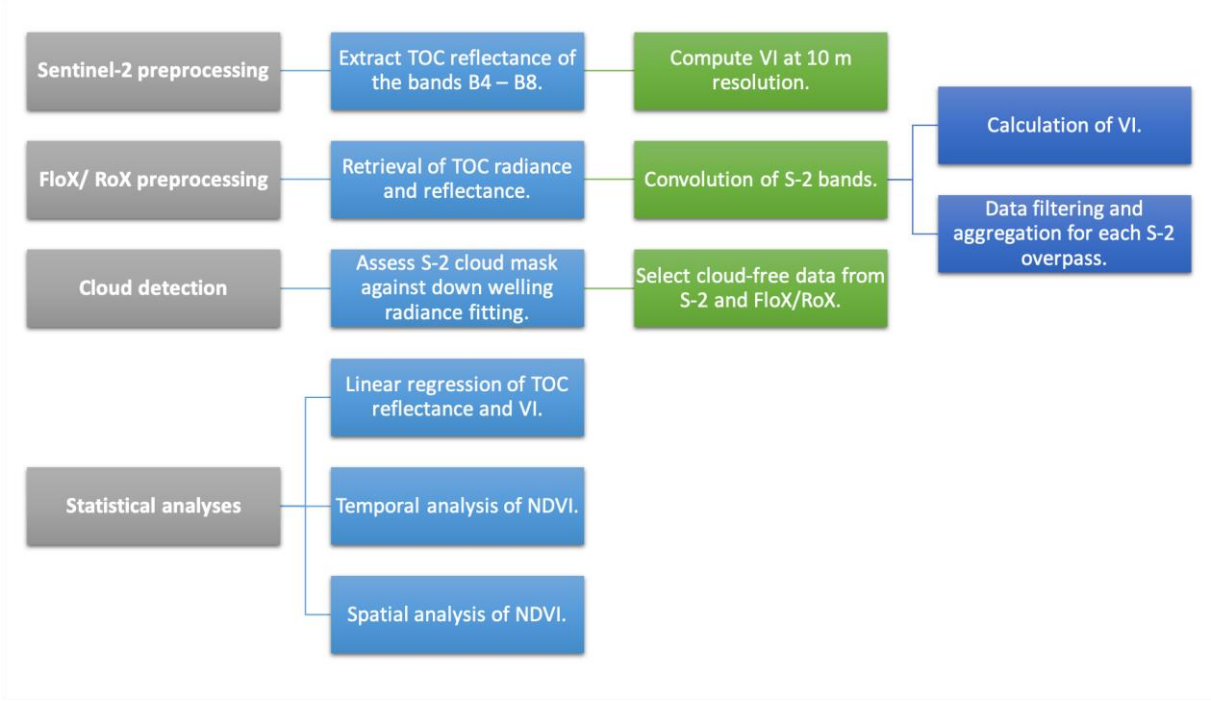

Figure 24: Schematic of data processing and analyses conducted during this study.

The data from S-2 and from the automated spectrometer network were pre-processed to enable their joint use for cloud detection and filtering (Figure 24). Finally, only data pairs from ground and satellite filtered and validated as cloud-free using down-welling radiance fitting from the ground were used for further analyses. Each of the steps are described in detail below.

Sentinel-2 preprocessing

Satellite data were selected to match the exact position of the footprint recorded by the automated spectrometers based on the natively annotated GPS-coordinates. The level 2-A products from the Copernicus hub were downloaded and time series extracted for the single pixel at the positions of the spectrometer footprint, a 3x3 pixel matrix and a subset of ca. 200 pixels for each site around the instrument using Google Earth Engine (Gorelick et al., 2017). Atmospherically corrected TOC reflectance using the Sen2Cor algorithm included cubic spline resampling (Li et al., 2018) was extracted at 10 m spatial resolution for those S-2 bands overlapping with the spectral range of the field spectrometers between 450 nm and 900 nm shown in Table 8. VIs were computed directly from the S-2 reflectance bands at 10 m spatial resolution in the same way as for ground measurements according to Table 9.

Table 8: Sentinel-2 B bands used for TOC reflectance extraction overlapping with the spectral range of the ground instruments

Sentinel-2 band name	**B2**	**B3**	**B4**	**B5**	**B6**	**B7**	**B8**
Central wavelength	492 nm	559 nm	665 nm	704 m	740 nm	780 nm	833 nm
Band width	65 nm	35 nm	31 nm	15 nm	13 nm	19 nm	104 nm
Pixel size on ground	10 m	10 m	10 m	20 m	20 m	20 m	10 m

FloX and RoX preprocessing

Raw data from the field spectrometer systems were processed to retrieve calibrated radiance and surface reflectance using the packages FieldSpectroscopyCC[6] and FieldSpectroscopyDP[7] with the statistical computing software R (R Core Team, 2017). The hyperspectral reflectance was then convolved to match the multispectral characteristics of S-2 (Table 8) within the VIS-NIR spectral range of FloX and RoX, using Gaussian convolution. Only band 2 to band 8 of the total 13 multispectral bands from S-2 were covered in the convolution, considering the central wavelength and full width at half maximum (FWHM) in each band, which were respectively overlapping with the usable spectral range between 450 nm and 900 nm of the automated field spectrometers.

Table 9: Index formulations used for the calculation from Sentinel-2 multispectral bands and convoluted bands from field spectrometers identified by their central wavelength.

Index name	**Formula**	**Index Reference**
NDVI	$\frac{(R_{833} - R_{665})}{(R_{833} + R_{665})}$	(Tucker, 1979)
EVI	$2.5 \times \frac{(R_{833} - R_{670})}{(R_{833} + 6 \times R_{665} - 7.5 \times \mathrm{R}_{492} + 1)}$	(Liu and Huete, 1995)
TCARI	$\frac{3 \times (R_{704} - R_{665}) - 0.2 \times (R_{704} - R_{559}) \times {R_{704}}/{R_{665}}}{1.16 \times {(R_{833} - R_{665})}/{(R_{833} + R_{665} + 0.16)}}$	(Haboudane et al., 2002)

[6] Julitta, T. "FieldSpectroscopyCC". Github, Inc. Accessed April 5, 2024. https://github.com/tommasojulitta/FieldSpectroscopyCC.

[7] Julitta, T. "FieldSpectroscopyDP". Github, Inc. Accessed April 5, 2024. https://github.com/tommasojulitta/FieldSpectroscopyDP.

NDVI, EVI and TCARI were calculated for FloX and RoX from the convoluted spectral bands according to Table 9 in order to properly match with the S-2-based products.

The spectrometer data were filtered according to Cogliati et al. (2015a) to eliminate unstable, saturated spectra and measurements at low solar zenith angles. In addition, outliers of negative NDVI were identified as measurements of snow and verified as such by time and place of recording. Data were extracted from the continuous time series at a temporal resolution per ca. 1 minute using a 20-minute time-window around each Sentinel-2 (S-2) overpass and aggregating by the mean of the reflectance and VI values within each time-window.

Cloud detection

Two independent routines were used for cloud detection eliminating cloud-shaded data. The first filtering routine was based on the S-2-inherent cloud masks (Baetens et al., 2019). Data above 0% cloud coverage were excluded, as fractional cloud cover could not be consistently checked otherwise.

A second filtering routine was applied using dense temporal information of down-welling radiance from ground measurements. The method was based on the assumption that incoming light can be considered stable enough to be expressed by a linear model for a short time period. Thus, a time window of 20 minutes was selected around the time of the S-2 overpass. A linear model was fitted to the down-welling radiance at 750nm within this time window. The down-welling radiance within this time-window varied a lot during cloudy conditions, resulting in a poor fit of the linear model with the down-welling radiance and a low correlation coefficient R^2 (see Figure 25a). Conversely, under clear sky conditions the linear fit resulted in a high correlation with the measured down-welling radiance (see Figure 25b). Applying ground-based cloud detection, we investigated pairs of S-2 and ground data under clear-sky conditions only.

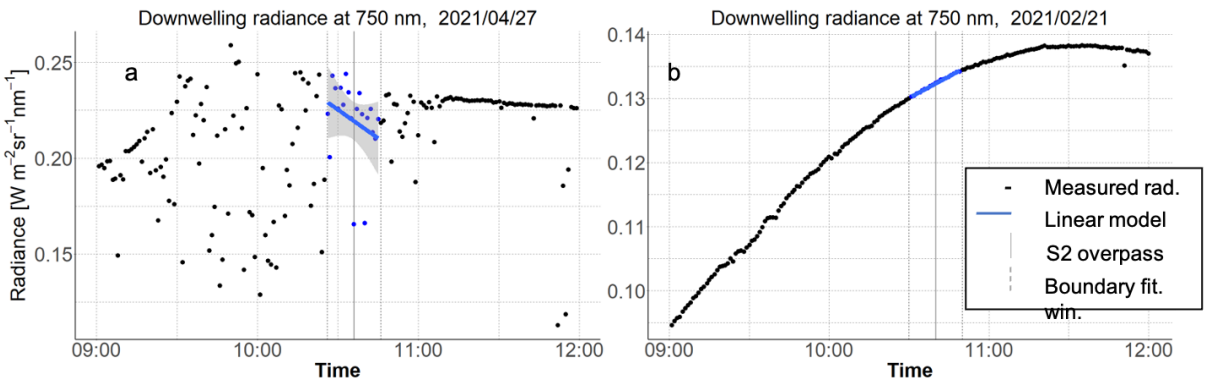

Figure 25: Principle of data filtering approach based on downwelling radiance. Diurnal course of cloudy incident radiance (a) compared to clear incident radiance (b). Measurements are printed in black while the linear fit is printed in blue, dashed grey vertical lines indicate the 20 min. time-window around the S-2 overpass, which is marked by a solid grey line.

Statistical analyses

TOC reflectance and VI from S-2 were compared with ground measurements by using linear regression of a 3x3 pixel matrix around the position of ground measurements to ensure fully covering the spectrometer footprint. The S-2 pixels were summarized by their mean value around the position of the field spectrometer. The coefficient of determination (R^2), the confidence of significance (p-value) and slope were computed for each linear regression of reflectance bands and VI, respectively. In addition, the root mean square error (RMSE, eq. 13) and relative RMSE (RRMSE, eq. 14) in percent were calculated, using $\hat{x}$ as the measured reflectance or VI from S-2 and x as the measured reflectance or VI from FloX/ RoX with respect to the total number of n measurements.

$$RMSE = \sqrt{\frac{\sum_{i=1}^{n}(\hat{x}_i - x_i)^2}{n}} \tag{13}$$

$$RRMSE = \frac{\sqrt{\sum_{i=1}^{n}(\hat{x}_i - x_i)^2}}{\sum_{i=1}^{n}\hat{x}_i} \cdot 100\% \tag{14}$$

Also, the temporal residuals in NDVI were calculated as the difference between satellite and ground measurements for each data pair in the entire time series. A histogram of the residuals was created to investigate their distributions. Furtermore, median and standard deviation (sd) were calculated.

Finally, spatial clustering using the "tsclust" algorithm from the R-package "dtwclust"[8] was conducted on each pixel of the subset (ca. 200 pixels) around the automated field spectrometers. Hierarchical clustering of NDVI time series per pixel was performed in the two three-years-long datasets. The time series of NDVI pixels were grouped into three clusters based on normalized dynamic time warping distances (Aghabozorgi et al., 2015; Wallace and Dale, 2005).

[8] Sarda, A. "dtwclust". Github, Inc. Accessed April 5, 2024. https://github.com/asardaes/dtwclust.

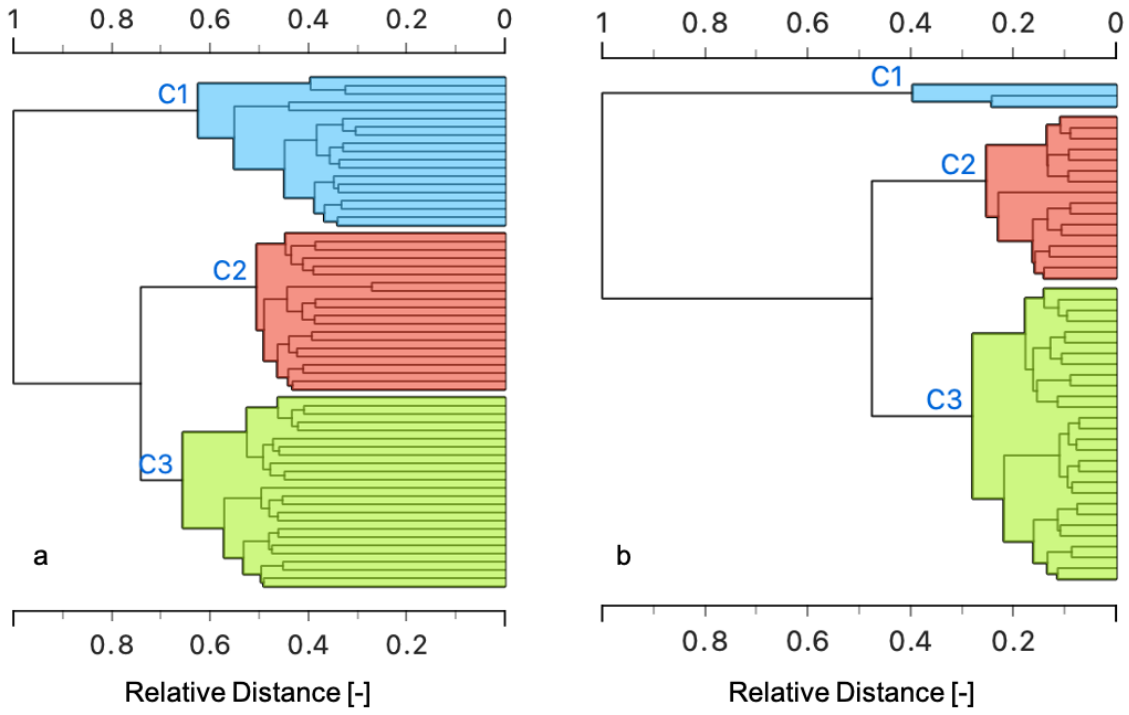

Figure 26: Cluster dendrogram from the hierarchical clustering of NDVI time series associated with a pixel of the subset each in Torgnon (a) and OHP (b). Clusters C1, C2 and C3 are marked each in a different color. The tree depth is given in relative Euclidian distance between 0 and 1. The leaves correspond to pixel IDs in the mosaics. Note that the level of displaying was pruned and not all pixels are listed for improved readability, pruning to a maximum depth of 7.

Pixels of similar temporal patterns in NDVI around the location of ground measurements were identified and allocated in 3 groups by the algorithm (Figure 26). The depth of differentiation of the clusters was indicated by the relative distance of the top node of each cluster. Note that the NDVI pixels from the canopy in Torgnon were identified more diverse than those from OHP, accordingly. Finally, the temporal patterns in each cluster were compared with the ground measured temporal patterns. A visual inspection was conducted comparing the location of pixels associated to each cluster with respect to the location of ground measurements for both sites. Agreement of the clusters of NDVI pixels with respect to the spectrometer footprint verified temporal and spatial representativeness of the ground measurements for the area covered by clustered pixels.

5.4 Results

5.4.1 Cloud filtering

Filtering by ground-measured down-welling radiance fitting was applied to deselect clouded satellite data of overpasses during which the linear fit yielded an R^2 value below 0.7. This resulted in an overall acceptance rate of 49% of the available data pairs from ground and satellite (Figure 27), compared with an average acceptance rate of 86% using conventional cloud masks. A detailed comparison of retained data using filtering by cloud masks and ground-measured down-welling radiance fitting are

provided in Table 10. A significantly larger number of S-2 overpasses was identified cloud-free using cloud masks, but still showed in parts effects of clouds in the ground-measured data within the region of interest (ROI).

Table 10: Number of Sentinel-2 overpasses paired with ground measurements available for each site in total and after the filtering using Sentine-2 cloud mask or ground measured incoming radiance, respectively.

Sites	All Sentinel-2 overpasses paired with ground measurements	Remaining instances filtered by Sentinel-2 cloud mask	Remaining instances filtered by down-welling radiance
Gebese	15	14	7
Kapiti	14	11	3
Leinefelde	44	36	14
Greenbelt	8	8	6
Lincoln	23	22	7
Shangqui	7	7	3
OHP	105	100	67
Selhausen	7	6	3
Oensingen	14	12	5
Torgnon	169	133	94

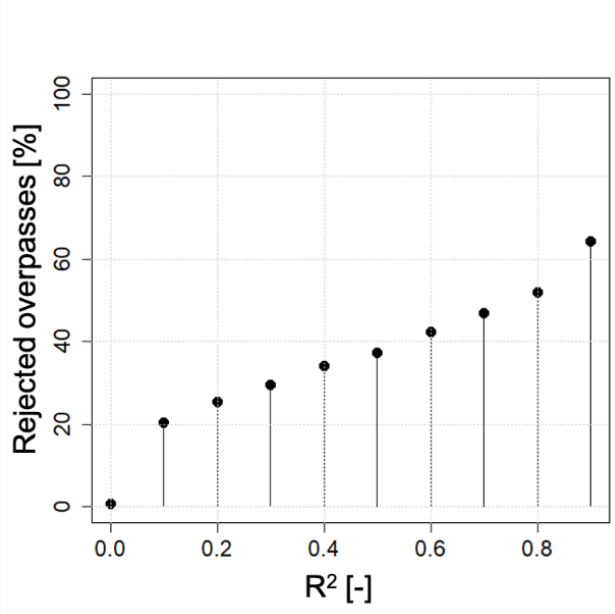

Figure 27: Rejection rate of all data given in % with respect to changing R^2 of the linear fit for ground measurements around the S-2 overpass set as threshold for filtering cloudy conditions

Therefore, cloud filtering based on down-welling radiance measurements was considered more conservative and suitable for the further analyses compared to S-2 cloud masks. Since the S-2 cloud-mask included also data pairs which were evidently affected by clouds, the ground-based filtering was used for all further investigation.

5.4.2 Spectral Reflectance and VI

Ground measured and satellite measured reflectance were compared for all eight multispectral bands, which fell within the spectral range of FloX and RoX. To visually compare measurements across all sites, band 5 around 704 nm, band 6 around 740 nm and band 7 around 780 nm were selected from the central region of the FloX's/RoX's detector (Figure 28).

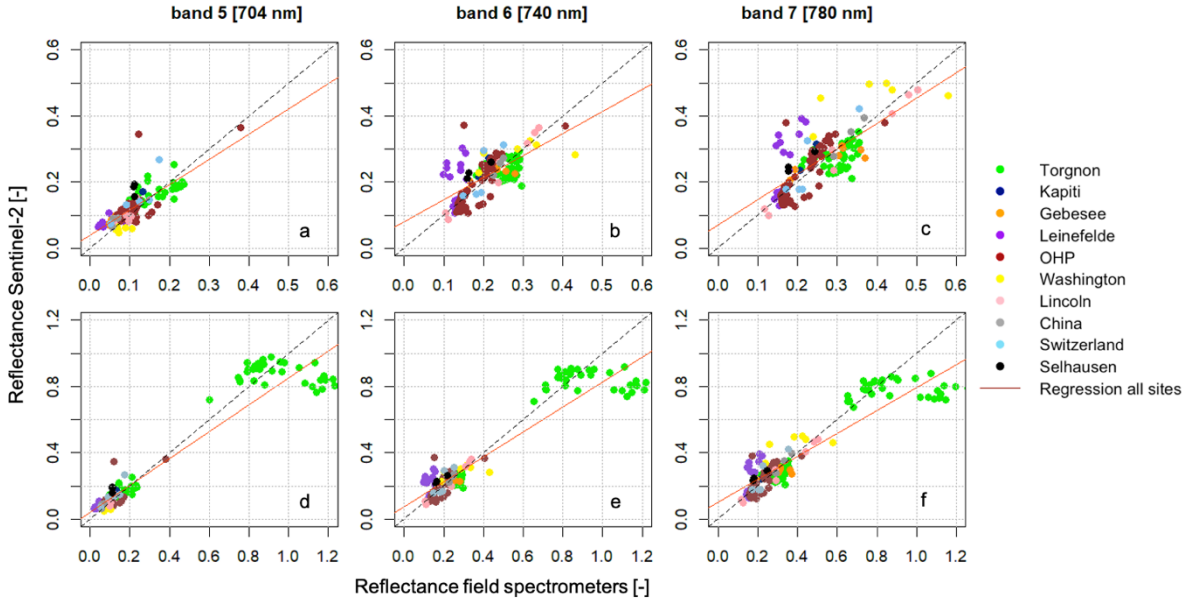

Figure 28: Scatterplots show reflectance at bands around 704nm, 740nm and 780nm from Rox/FloX vs Sentinel-2 measurements, respectively. Data in panels a, b and c excludes measurements of snow, in panels d, e and f are results for all measurements displayed. Regression line in dashed red indicates deviation from line of identity in dashed black.

A noticeable deviation from a slope of one was exhibited in all panels of Figure 28. Overall, lower R^2 and larger deviation from a slope around one was recognized in the reflectance bands when excluding measurements of snow. Likewise, a smaller dynamic range of reflectance was recognized for pure vegetation samples only. Noticeable outliers with respect to the regression's trendline were noticed for the field sites in Linefelde, affected by the off-nadir tilted up-welling optics and for some recordings of snow in Torgnon, both of which were affected by reflection hotspots in the target. Reflection hotspots in the snow caused reflecting direct sunlight, which entered the downwards facing optics of the instrument. This is a known issue of snow, caused by a series of variables related to acquisition, illumination geometry, and surface topography. Taking a purely diffuse reference for the down-welling

light using cosine diffusors in combination with direct sunlight in the up-welling resulted in a calculated reflectance greater 1, which must be understood as an artifact.

Table 11: Correlation between satellite-measured and ground-measured reflectance. Statistics of regression for the different bands (only for rigorous filtering), p-value, RMSE, %-RRMSE, across all sites vegetation only and included snow, respectively.

BAND (nm)	R SQUARED	P VALUE	SLOPE	RMSE	% RRMSE
VEGETATION ONLY					
492	0.59	<0.01	0.91	0.023	11.82
559	0.58	<0.01	0.84	0.025	10.73
665	0.72	<0.01	0.89	0.029	11.56
704	0.59	<0.01	0.76	0.035	11.65
740	0.45	<0.01	0.67	0.051	4.79
780	0.53	<0.01	0.77	0.061	4.10
833	0.45	<0.01	0.71	0.065	5.48
INCLUDING SNOW					
492	0.94	<0.01	0.84	0.104	7.47
559	0.94	<0.01	0.83	0.106	6.81
665	0.93	<0.01	0.83	0.105	5.43
704	0.92	<0.01	0.81	0.109	3.06
740	0.88	<0.01	0.75	0.117	4.31
780	0.83	<0.01	0.69	0.127	4.82
833	0.79	<0.01	0.66	0.138	2.79

A detailed assessment of each band is reported in Table 11. The coefficient of determination between satellite-measured and ground-measured reflectance varied a lot between the different multispectral bands across all sites. The lowest coefficient of determination was recognized in band 6 around 740 nm with R^2 of 0.45, a slope of 0.67 and RRMSE around 4.8%, as well as in band 8 around 833nm with R^2 of 0.45, a slope of 0.71 and relative RMSE around 5.5% in the subset of vegetation only. Taking also reflectance of snow into account, all R^2 values increased significantly. Due to a higher variance and covariance in the data also the absolute and relative error increased (Figure 28). The RMSE increased almost consistently with increasing wavelength of the multispectral bands. The RRMSE was affected by the typical reflectance shape of pure vegetation targets, resulting in higher relative values for visible wavelength at lower intensities and in lower relative error of near-infrared wavelength of higher intensities (compare Figure 29 and Table 11). The RRMSE values were more similar across all spectral bands when including snow, since a larger diversity of non-vegetative spectral reflectance shapes was introduced in addition to a larger variance of reflectance. Lowest coefficient of determination was recognized in band 8 around 833 nm in the dataset including snow with R^2 of 0.79, slope of 0.66 and a

RRMSE of 2.8%. This is half of the RRMSE value compared to data including vegetation only. When including snow, the agreement for the bands up to band 5 were very good with R^2 above 0.9 and RRMSE between 3.1% and 7.5%. All reported results were significant according to a 99.9% confidence interval, applying the p-value test.

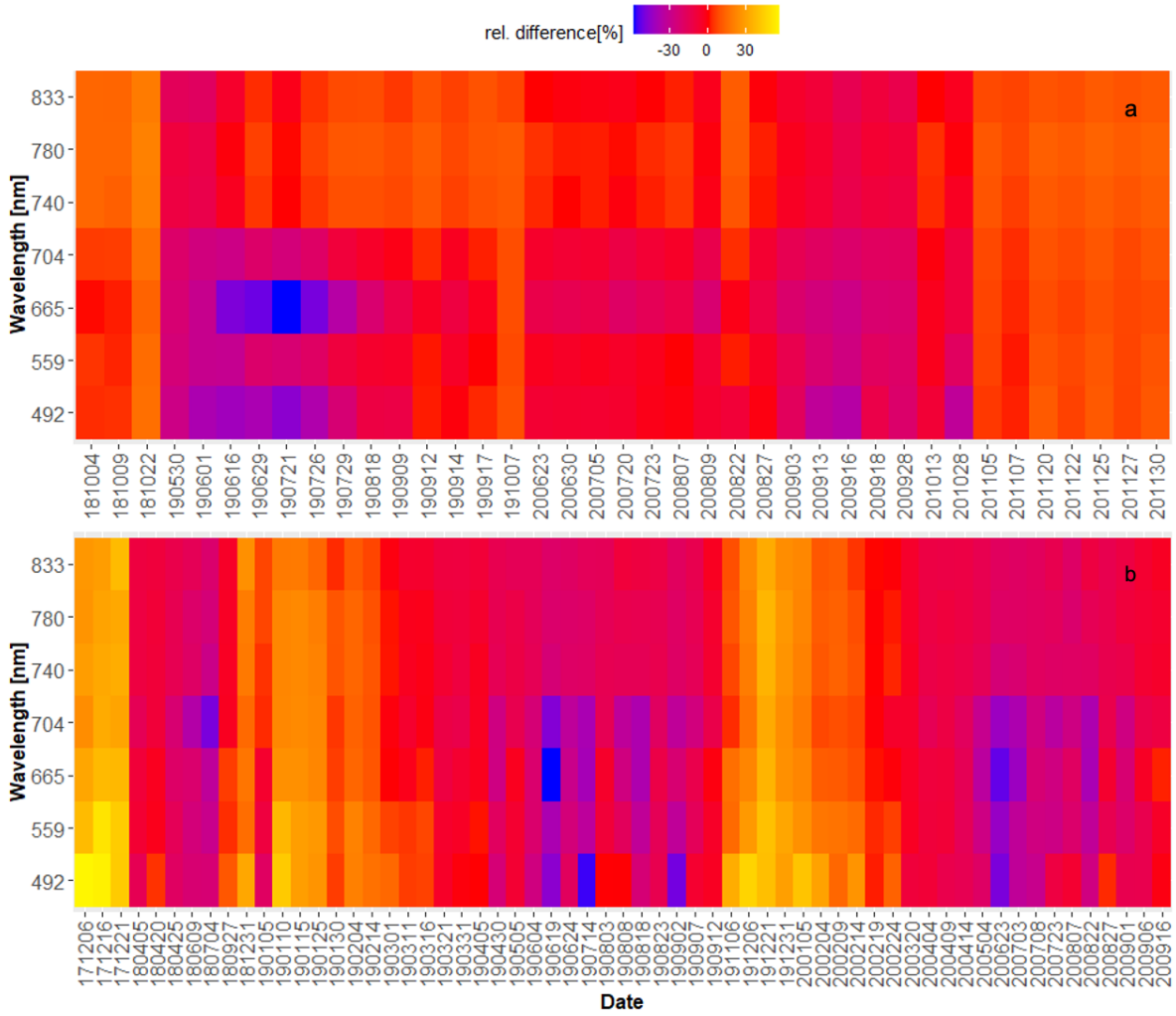

Figure 29: Heatmap indicating the relative difference percentage (%) of convoluted ground-measured reflectance using autonomous field spectrometers with respect to Sentinel-2 TOC reflectance, covering over three years of investigation in Torgnon (a) and in OHP (b).

Good agreement was recognized in the reflectance shape between the two platforms (see Figure 29). Especially the spectral shape typical for vegetation was well retained in the selected cases. A very clear seasonal pattern in the relative differences between satellite-based reflectance and ground-based reflectance was observed in Figure 29 especially at OHP. In contrast, the relative discrepancy was more evenly distributed in Torgnon across the temporal domain and exhibited less seasonality due to a lack of usable data pairs during winter. Most stable across the temporal domain was the band around 780 nm for both Torgnon and OHP, yielding the lowest associated relative RMSE in pure vegetation (compare Figure 29 and Table 11).

Similar to the investigation of absolute reflectance for individual multispectral bands, VIs were examined for their agreement between ground and satellite measurements. For this purpose, NDVI, EVI and TCARI were computed, both from the convoluted bands of the ground measurements and the multispectral bands of S-2 reflectance, including atmospheric correction. A regression analysis was performed, indicating that NDVI, EVI and TCARI agreed well across both platforms, recognizing a noticeable difference in value range between pure vegetation and measurements including snow, especially in NDVI (Figure 30). NDVI exhibited a very good coefficient of determination with R^2 around 0.96 (incl. snow) and 0.90 (vegetation only) and a slope close to one (Table 12). The RRMSE was in both cases very similar around 3.8% and 4.3%. Agreement in TCARI values was overall the strongest affected by the snow and performed very differently with R^2 around 0.75 (incl. snow), while the coefficient of determination in pure vegetation targets was reduced to R^2 around 0.55 due to a larger scattering of values. The RRMSE was almost doubled for those measurements which included vegetation only in TCARI, because a larger variance in the data was introduced due to snow (Figure 30). EVI exhibited a lower coefficient of determination R^2 around 0.88 (incl. snow) between ground and satellite measurements, while the value changed not noticeably to R^2 around 0.86 investigating vegetation targets only. Similar to TCARI, the RRMSE was almost doubled by the exclusion of snow.

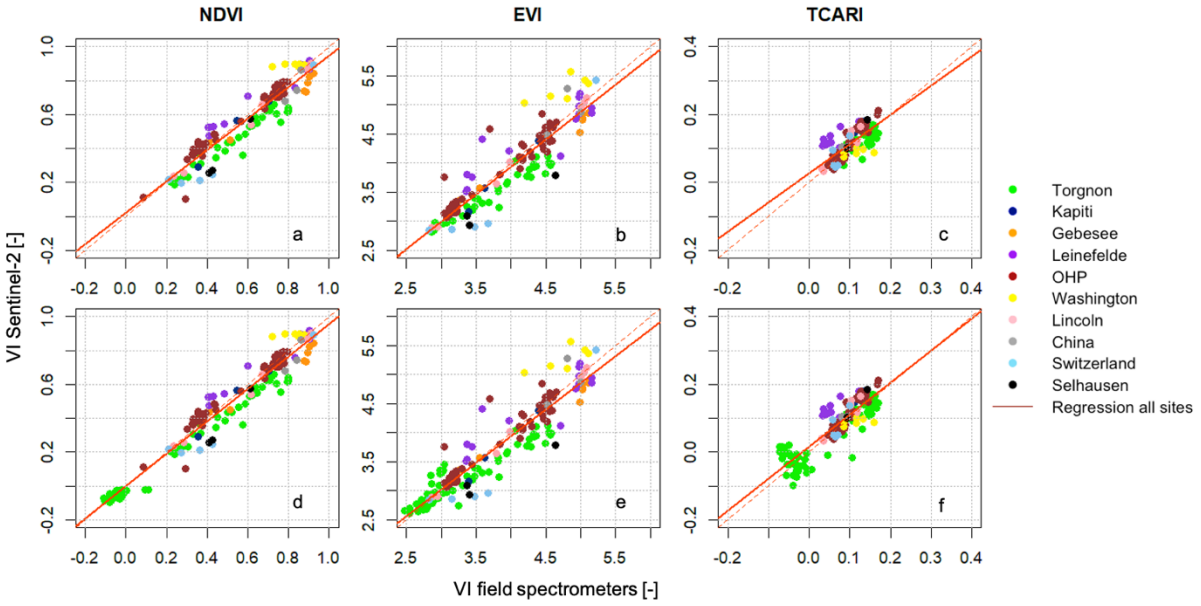

Figure 30: Comparison of field Rox-Flox and S-2 satellite VIs. Scatterplots show NDVI, EVI and TCARI from Rox/FloX vs Sentinel-2 measurements, respectively. Data in panels a, b and c excludes measurements of snow showing vegetation only. In panels d, e and f are results for all measurements displayed. Regression line in solid red indicates deviation from line of identity in dashed red.

Ground measurements and satellite measurements agreed better when examining simple TOC reflectance of the individual bands compared with the more complex EVI and TCARI computed from those bands. The coefficient of determination between ground and satellite measurements decreased

with increasing complexity of the index formulation of NDVI, EVI and TCARI, in that order. EVI was by far the most robust index with respect to influences from snow and exhibited the lowest RRMSE, both in pure vegetation and including snow. Due to the highest variance in values with respect to the spread of datapoints around the regression line in Figure 30, RRMSE of EVI was the lowest. On the contrary, the absolute RMSE was lowest for TCARI in vegetation only and for NDVI including snow.

Table 12: Statistics of regression for the VI (only for radiance-based filtering), p-value, RMSE, %-RRMSE, across all sites vegetation only and included snow, respectively.

INDEX	R SQUARED	P VALUE	SLOPE	RMSE	% RRMSE
VEGETATION ONLY					
TCARI	0.55	<0.01	0.88	0.029	11.25
EVI	0.86	<0.01	0.94	0.291	1.41
NDVI	0.90	<0.01	0.93	0.074	3.80
INCLUDING SNOW					
TCARI	0.75	<0.01	0.83	0.105	5.44
EVI	0.88	<0.01	0.92	0.276	0.76
NDVI	0.96	<0.01	0.96	0.068	4.34

5.4.3 Temporal and Spatial Patterns

When investigating the two longest time series (i.e., the time series from OHP and Torgnon), only a fraction of the ground measurements were usable for further analysis. Only S-2 overpasses under cloud-free conditions were used, previously identified by using the down-welling radiance-based filtering. The resulting gaps with respect to the higher temporal resolution of the continuous monitoring using ground measurements were obvious especially in Torgnon in the Alps (Figure 31). In Torgnon data recorded during winter were filtered out for all three years, due to the exclusion of snow to focus on the analysis of vegetation only. In contrast, a much better coverage of the annual pattern in NDVI was achieved from the ground including all seasons. In OHP in southern France there were a larger number of S-2 overpasses available throughout the investigated years. However, in both cases the high temporal resolution of the ground measurements depicted annual dynamics to a much better degree compared with satellite measurements. This advantage was especially noticeable during seasons of unstable weather conditions. When stable conditions for reliable measurements were difficult to identity using the S-2 cloud-masks, ground measurement still identified locally usable data.

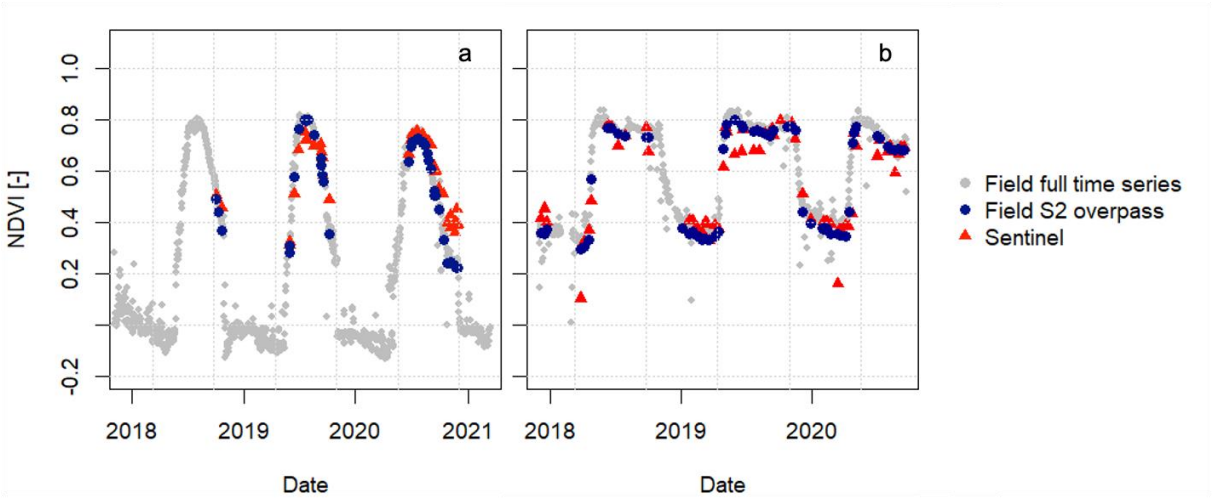

Figure 31: Time series measured from satellite and on the ground in Torgnon (a) and OHP (b), where data over approximately three years were available. The selected data from a usable satellite overpass (red) is compared with the associated ground measurement (blue). Negative NDVI values were caused by snow.

While the temporal evolution of the discrepancy between ground-measured and satellite-measured NDVI followed a right-skewed, normal distribution centered around zero for all data combined, the residuals were not always normally distributed for individual time series, such as Torgnon (Figure 32). A median residual NDVI around -0.02 and a standard deviation of 0.09 was recognized across all sites, indicating very low systematic differences between ground and satellite. In particular, median residual NDVI in Torgnon was around -0.06 with a standard deviation around 0.08. In OHP the median discrepancy was below -0.01 with a standard deviation of 0.07. All these values similarly indicated a negligible systematic tendency of underestimating NDVI on the ground, taking S-2 as reference. However, the random uncertainties significantly exceeded those systematic errors. The highest occurring frequency of residual NDVI in ground measurements with respect to the satellite measurements was found by the mode just below zero in all sites (Figure 32). For the extended two time series the absolute residual NDVI followed the seasonal vegetation cycle in Torgnon, while the residual NDVI in OHP data showed a more random pattern.

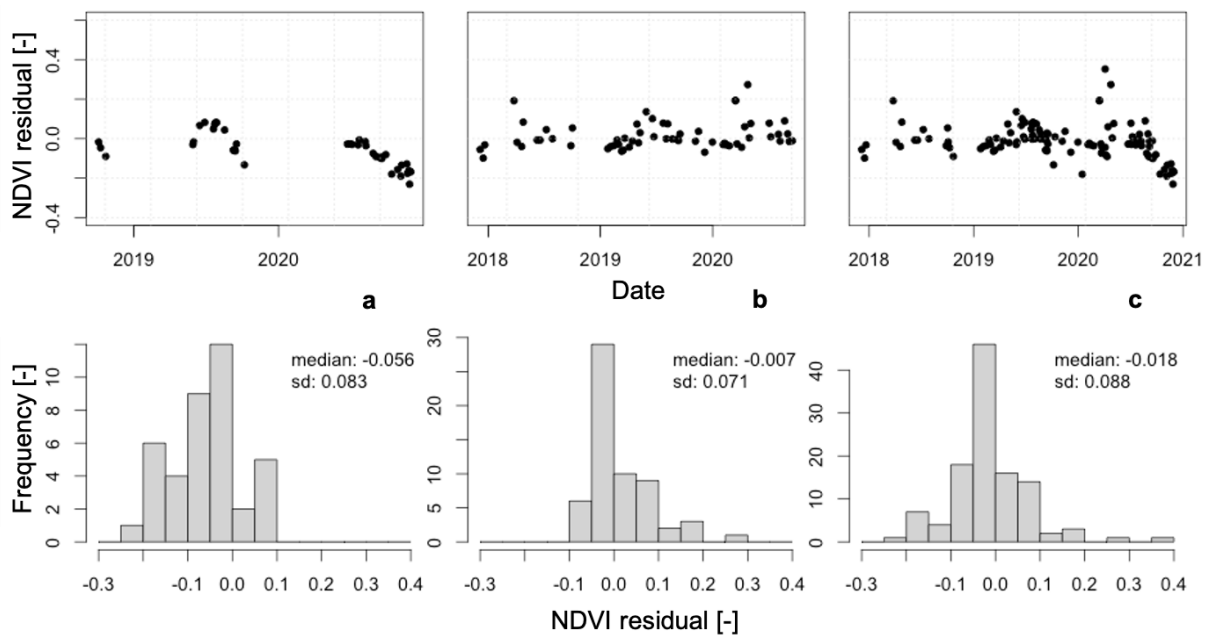

Figure 32: Residual of NDVI over time (top) and distribution of the residual (bottom) for Torgnon (a), OHP (b), and for all available sites (c).

Finally, we investigated the pixels in the sub-section around the location of the RoX in Torgnon and the FloX in OHP with respect to spatial similarity of the NDVI. Each pixel exhibited a specific temporal pattern in NDVI and was compared in with all other subset pixels, so that similar temporal patterns would be summarized into a cluster. In Torgnon the clustering algorithm identified three major clusters in the S-2 pixels and associated specific trends in seasonal pattern accordingly (Figure 33). Those clusters of seasonal patterns were spatially associated with certain spatial features. The seasonal pattern in NDVI recorded by ground measurements in Torgnon was similar to cluster 2 of S-2 based NDVI pixels, at the fringes to cluster 3 during 2018 and 2019 (Figure 33). Likewise, the position of the RoX was located inside pixels, which were spatially associated to cluster 2 at the border to cluster 3. Similarly, in OHP the algorithm identified three clusters, of which cluster one was the major contributor. The spatial location of the ground measurements at the border between the three clusters resembled the temporal pattern of ground measurements falling into cluster 1 mainly during summer and into cluster 3 mainly during winter. Hence, spatial features were successfully associated with the temporal NDVI patterns from both S-2 and ground measurements.

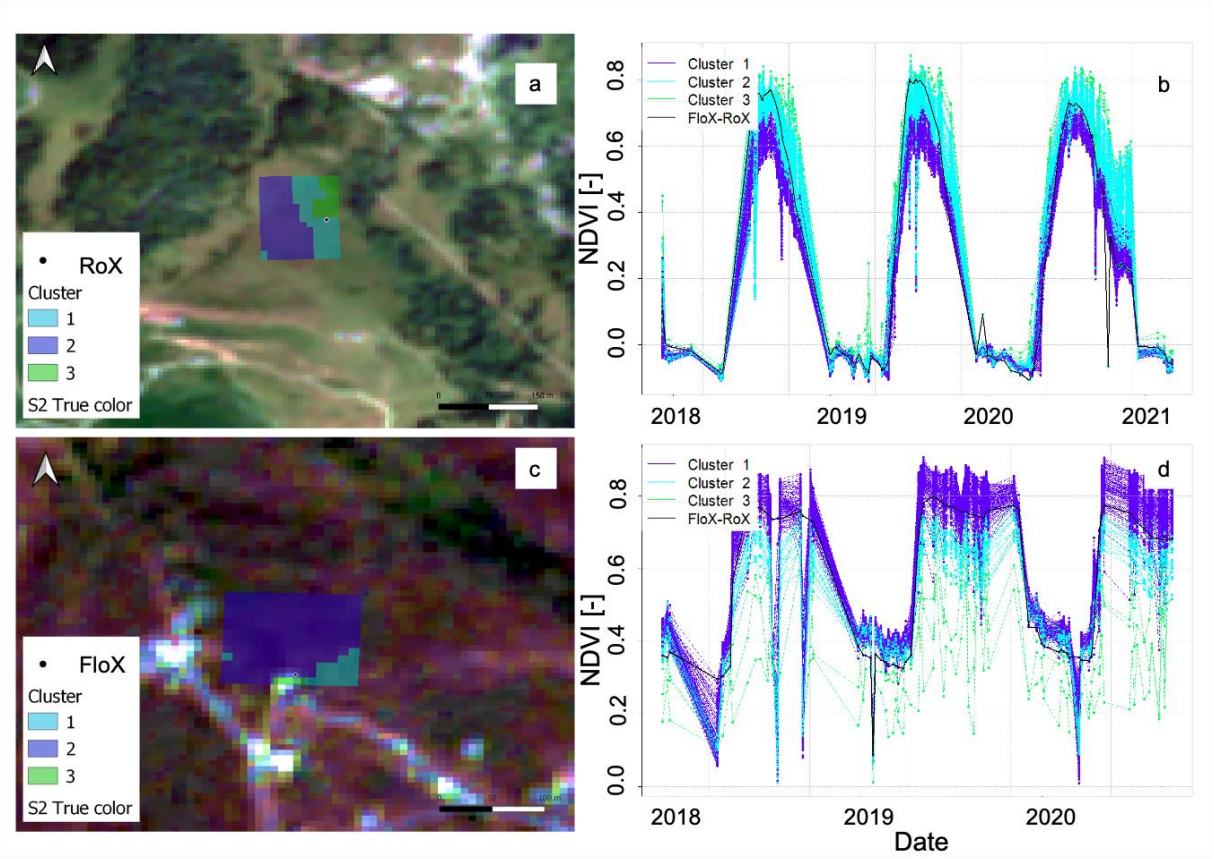

Figure 33: Time series similarity clustering. Rox/FloX was spatially identified in the associated cluster of similar Sentinel-2 pixels with respect to similar temporal patterns in NDVI. Satellite scene of the ROI in Torgnon, Italy (a) and in OHP, France (c). Clustered time series of NDVI with respect to pixels identified as similar using hierarchical clustering in Torgnon (b) and OHP (d).

5.5 Discussion

5.5.1 Spectral Reflectance and VI

Previous studies have compared reflectance measurements using different spectrometer systems on the ground and also investigated differences in VI across ground and satellite (Castro-Esau et al., 2006; Cheng et al., 2006). Our results suggested a better agreement in absolute values compared with these studies, both in reflectance and in VI comparing FloX/RoX measurements with S-2 TOC products. Thus, TOC reflectance and VI data from the network of 10 FloX and RoX sites were considered very coherent with respect to S-2. Similar to (Cheng et al., 2006), a characteristic seasonal pattern was identified in the relative discrepancy of reflectance bands between ground and satellite in the two longest time series in this study. This seasonal pattern suggested temporal-spatial variabilities of uncertainties with respect to the static and continuous ground measurements, which were investigated more closely in this study using the spatial information available from S-2. Best practice in characterization, traceability and standardization will further enable fusing validated ground data to improve the spectral, temporal and spatial details of future studies. Thus, future efforts would benefit from the accreditation of radiometric calibration routines of FloX and RoX and assure traceability with respect to a fiducial

reference (Mihai et al., 2018; Picard et al., 2016; Schaepman and Dangel, 2000). With continuous time series being available from the automated spectrometers, ground-measured data were extracted exactly for the time of the S-2 overpass in order to minimize temporal uncertainties. However, uncertainties around the different spatial resolutions had to be considered, which affected the direct comparison of ground measurements and satellite data (Vogtli et al., 2021; Zagajewski et al., 2017). The varying pixel-sizes of S-2 bands (Drusch et al., 2012) and the varying footprint radius of point spectrometers from 0.5 m to 20 m, depending on the height of installation, limited the best possible agreement between ground and satellite (Milton et al., 2009). In addition, inconsistencies around the setup of the automated field spectrometers yielded another important source for uncertainties. In particular, off-nadir misalignment of the up-welling and down-welling channels of FloX and RoX results in an offset with respect to the satellite TOC reflectance (Drolet et al., 2014; Hueni et al., 2017). Compensation for atmospheric distortion of the light passing from space to the ground is furthermore important for the retrieval of accurate results validated from the satellite (Schläpfer et al., 2020a; Vogtli et al., 2021). While ground measurements by field spectrometers already included the path of light through the atmosphere, S-2 reflectance had to infer these atmospheric influences. We used S-2 TOC reflectance, which was processed using the Sen2Cor algorithm to account for the atmospheric distortion of light (Li et al., 2018). Short-term changes of the atmosphere affect the measurements at the ground level and introduce an additional uncertainty. We tried to address this issue by using a very conservative cloud filtering approach, which aimed to identify those shot-term variations in the atmosphere from the ground. However, some compromises had to be made with respect to retaining a usable amount of data pairs for further analyses. Furthermore, multispectral reflectance was convolved from the hyperspectral ground measurements assuming a Gaussian spectral response of S-2. It has to be noted that this basic assumption is a simplification and the actual spectral response function of S-2 bands is in truth of a more complex shape (Li et al., 2018). Even though the assumption of a Gaussian response did mimic the S-2 multispectral bands closely, it was sufficient for this investigation and introduced only a minor systematic error into the comparison. Combining uncertainties from spatial misalignment, atmospheric correction, radiometric calibration, convolution and setup is essential towards fully characterizing the standardized application of high-resolution hyperspectral ground measurements to be used in fusion with multispectral, imaging satellite sensors (Ariza et al., 2018; Mihai et al., 2018; Schmitt and Zhu, 2016).

The complexity of the VIs affected their behavior in a very distinctive manner in this study. The variance of absolute NDVI values was increased by measurements including snow in contrast to pure vegetation. NDVI is a very widely used VI for the remote sensing of vegetation and is based on the red-edge feature of vegetation (Eitel et al., 2010; Gamon et al., 1995; Yao et al., 2013). Thus, negative NDVI of snow must be considered as an artifact, which affected our presented statistics by increased value

range (Wang et al., 2023a). Those artifacts were caused by the specific bi-directional reflectance distribution function of snow due to a series of variables related to acquisition, illumination geometry or surface topography (Painter and Dozier, 2004; Picard et al., 2020). At the same time, the negative NDVI values exhibited by snow were a criterion for filtering only vegetation measurements (Jiang et al., 2006; Wang et al., 2023b). In comparison to the other more complex VIs, NDVI with R^2 exceeding 0.9 and relative error remaining below 5% between satellite and ground measurements suggested a good inter-site transferability on ground and good transferability between ground and satellite. The increased robustness of EVI against influences from soil and atmosphere resulted in less pronounced outliers produced by snow but differentiated more the vegetation between sites (Liu and Huete, 1995). Thus, the absolute error in EVI was the highest of all the three investigated VIs. Also, the formulation of EVI is more complex than NDVI, resulting in singular uncertainties from the individual multispectral bands propagating more strongly (Stow et al., 2019). Considering our results, an adjustment of EVI values would be recommended to harmonize all sites with respect to S-2. Finally, TCARI exhibited lowest coefficient of determination and highest relative error when comparing ground and satellite. Being the most complex of the three investigated VIs, TCARI was designed for canopy chlorophyll prediction and to be robust against impacts from soil (Malenovský et al., 2006). This resulted in TCARI being affected the most by covariances of uncertainties propagated from the spectral reflectance. Future research should investigate appropriate correction approaches especially for TCARI towards improving transfer of information across platforms (Ariza et al., 2018; Olsson et al., 2021), which was beyond the scope of this study. Thus, NDVI was identified as most suitable to further compare temporal and spatial aspects and reduce effects of spectral uncertainties at the same time.

5.5.2 Temporal and Spatial Analyses

Temporal patterns in NDVI from ground and satellite were compared for the two longest time series recorded in OHP and Torgnon. Both locations provided data recorded over three years. The absolute difference in NDVI between the platforms over time exhibited a seasonal pattern in Torgnon, which had to be compared to a random pattern in OHP. It is followed that the systematic seasonal discrepancy pattern was caused by snowfall and diverse vegetation phenology in the highly dynamic alpine ecosystem (Alberton et al., 2017; Fu et al., 2014; Peano et al., 2021), leading to an increased fractional heterogeneity of the landscape during fall and spring. Heterogeneity of the canopy also increased during certain growth stages and added further spatial uncertainties (Pieruschka et al., 2014). At the same time, larger solar zenith angles during spring and fall can drive bidirectional reflectance artifacts and introduce uncertainties into reflectance of snow measured from ground (Ball et al., 2015). This is especially obvious for those instances of reflectance greater than 1 measured on the ground, caused by reflected direct sunlight in the up-welling with respect to a totally diffuse down-welling reference. We addressed this issue partially by filtering the ground measurements for solar

zenith angle below 75°, but could not rule out bidirectional reflectance artifacts driven by surface anisotropy. Furthermore, additional uncertainties were introduced by the circumstance that satellite measurement varied in viewing angle depending on the position of the ROI in the swath width over both sites, as the bidirectional distribution of reflectance varies significantly in natural canopies (Aasen and Bolten, 2018; Burkart et al., 2015a). This effect is very difficult to assess from the satellite scale and would require a thorough investigation of bidirectional reflectance distribution using goniometers or drones on the ground (Biriukova et al., 2020; Honkavaara and Khoramshahi, 2018; Stow et al., 2019), which was beyond the scope of this study. Investigating spatial uncertainties related to canopy characteristics using spatial clustering is promising (Rejichi and Chaabane, 2015). We investigated spatial homogeneity at satellite level, clustering similar pixels of the subset pixels with respect to their temporal pattern in NDVI. The footprint of the ground measurements in OHP was equal or larger than the S-2 pixel size. This large footprint minimized influences of individual plants and other smaller features. Thus, canopy characteristics were assumed as spatially homogenous for that integrated footprint (Jiang et al., 2006). The same assumption was made for the equally large ground-projection of the S-2-pixel size. In consequence of the rather homogenous canopy in OHP, the algorithm identified the largest number of similar pixels within one cluster but at a shallow depth of differentiation. Thus, it was followed that larger areas could be seen as homogenous and provided little spatial diversity at that scale. This reasoning is supported by the median residual in NDVI between ground and satellite around 0 in OHP. In contrast, the canopy in Torgnon was identified as more diverse, indicated by the 3 larger clusters at greater depth of differentiation. It is noteworthy that the spectrometer footprint on the ground was integrating a smaller area in Torgnon. However, sub-pixel size variations of the canopy remained difficult to track and affected especially the comparison with the smaller footprint of FloX and RoX on the ground. Thus, it is advisable to examine the heterogeneity of the investigated canopy carefully with the best spatial resolution and visually explore the site when installing field spectrometers on the ground. The footprints of the ground measurements were chosen in order to be representative for a larger area with respect to the S-2 pixel-size and to minimize uncertainties related to spatial heterogeneity in this study. In both, OHP and Torgnon was the spatial location of ground measurements correctly recognized within one cluster of similar pixels. The ground measured temporal signatures overlapped with the temporal signatures associated with the corresponding cluster especially well during summer. In consequence, spatial clustering of S-2 pixels with respect to the associated temporal signatures in NDVI is considered a very useful tool to identify similar areas and to extrapolate the high-resolution temporal ground measurements, given that homogeneity of the canopy and representativeness of ground measurements can be assumed (Bador et al., 2015; Duveiller and Cescatti, 2016). However, care must be taken to account for the seasonality of the discrepancy between ground and satellite with respect to the temporal dynamics of the investigated ecosystem.

Hence, extrapolation of information from the field spectrometer readings was not valid for times when the temporal signatures did not overlap well with the associated cluster and absolute temporal residuals were high. Likewise, the variability inside the pixel-associated clusters showed a seasonal pattern and can help to indicate the uncertainties around similar satellite pixels providing abundant ground coverage (Nagai et al., 2020). Uncertainties of field spectrometer readings are affected by morphological diversity of the canopy (Singh et al., 2015) and represent a challenge when generalizing insights into larger areas from the satellite. Thus, valid spatial extrapolation of high-resolution, temporal measurements into a larger area requires the assessment of the spatial uncertainty budget (Wen et al., 2020).

5.5.3 Cloud filtering

The automated field spectrometer systems FloX and RoX are capable of continuously monitoring one ROI at very high temporal and very high spectral resolution (Drolet et al., 2014). In contrast, atmospherically corrected S-2 TOC data depict an entire spatial scene of many pixels at a coarser temporal and coarser multispectral resolution (Linkosalmi et al., 2022). Only the harmonization of cloud-free data from both platforms is possible. Thus, the validation of cloud-free pairs of S-2 overpasses and overlapping measurements on ground was an important pre-requisite for this work. Therefore, an approach for cloud-filtering based on continuous down-welling radiance measured by automated field spectrometers on the ground was employed. The ground-based filtering approach outperformed the S-2 cloud masks and identified also small obstructions from high, thin and small clouds reliably in the limited areas around the spectrometer site. In contrast, using a cloud-mask and setting a threshold of zero for the percentage of cloud-coverage would not suffice to rule out small clouds inside the scene (Baetens et al., 2019). In consequence, total rejection of all data with non-zero cloud-cover was not feasible based on cloud-masks. Consequently, using ground-based down-welling radiance allowed for a much more selective filtering by rejecting data, which was actually affected by clouds at the time of the S-2 overpass at the spectrometer site. Since the hemispherical cosine diffusor of the FloX/RoX monitored rapid changes in irradiance continuously (Burkart et al., 2022), clouds and cloud shadows were identified precisely by measuring the discrepancy from a linear evolution of down-welling radiance for very short time windows, e.g. 20 minutes around the S-2 overpass. Cloud filtering using continuous ground measurements of irradiance is recommended only for experiments of limited spatial expanse around the spectrometer site, not exceeding the direct line of sight of the ground-based optics. The correct identification of clouds in satellite data remains challenging under rapidly changing atmospheric conditions to this day (Linkosalmi et al., 2022; Schläpfer et al., 2020b). Thus, cloud detection should be informed by the use of automated ground measurements when possible.

5.6 Conclusion

A network of standardized, automated field spectrometer systems was validated using Sentinel-2 TOC reflectance as reference in 10 different sites around the globe. Good overall agreement between field spectrometers and Sentinel-2 level 2-A TOC reflectance suggested mostly consistent reflectance data throughout the network. Deviations of individual samples and sites were mainly caused by slight spatial misalignments of Sentinel-2 pixels and the spectrometer footprints, by the instrument setup, atmospheric compensation and variable landscape heterogeneity. Future works should aim at correcting data product deviations from multiple ground sites using Sentinel-2 as a reference and move towards fully harmonized data. We observed a very good agreement between NDVI obtained from the field spectrometers and Sentinel-2, while the propagated errors from individual spectral bands were more noticeable with the more complex TCARI and EVI. The seasonal patterns of NDVI residuals on ground with respect to the satellite demonstrated increased uncertainties from summer to winter for the dynamic, heterogenous alpine ecosystem due to diverse vegetation phenology, snowfall and snowmelt, in contrast to a random distribution of residuals in a snow-free and homogenous oak forest in southern France. Thus, it is recommend to carefully consider the seasonal landscape dynamics when validating continuous ground measurements against satellite data. Furthermore, cloud filtering based on ground-measured irradiance showed a very robust way to eliminate overcast scenes in limited areas and outperformed conventional cloud-mask. We recommend to further exploit the potential for improving cloud-filtering of satellite data based on automated, continuous spectrometer measurements on the ground.

Validating the network of automated field spectrometers around the globe against Sentinel-2 demonstrated the potential of harmonizing standardized, hyperspectral, temporally dense reflectance data with respect to the satellite. The spatial domain of the satellite scale informed the assessment of uncertainties and assumptions of homogenous areas on the ground. Future works combining different optical sensors in various locations will benefit from harmonizing their data against Sentinel-2 as a vigorously standardized refence offering global coverage.

5.7 Acknowledgement

This work was supported in parts through CA17134 SENSECO (Optical synergies for spatiotemporal sensing of scalable ecophysiological traits) funded by COST (European Cooperation in Science and Technology, www.cost.eu).

6 Study 4 - Calibration and Validation from Ground to Airborne and Satellite Level: Joint Application of Time-Synchronous Field Spectroscopy, Drone, Aircraft and Sentinel-2 Imaging

Published in: Naethe, P., Asgari, M., Kneer, C., Knieps, M., Jenal, A., Weber, I., Moelter, T., Dzunic, F., Deffert, P., Rommel, E., Delaney, M., Baschek, B., Rock, G., Bongartz, J., Burkart, A., 2023. Calibration and Validation from Ground to Airborne and Satellite Level: Joint Application of Time-Synchronous Field Spectroscopy, Drone, Aircraft and Sentinel-2 Imaging. PFG – J. Photogramm. Remote Sens. Geoinf. Sci. https://doi.org/10.1007/s41064-022-00231-x.

Original manuscript integrated, format, layouts and numberings of elements adjusted, all references included into the bibliography in Chapter 9 of this dissertation.

CRediT Author Statement: **Paul Naethe**: Conceptualization, Methodology, Software, Validation, Resources, Data curation, Formal analysis, Investigation, Writing – Original Draft, Writing – Review & Editing, Visualization. **Maryam Asgari:** Resources, Data curation, Investigation, Writing – Original Draft, Writing – Review & Editing. **Caspar Kneer:** Resources, Writing – Review & Editing. **Michel Knieps:** Resources. **Alexander Jenal**: Resources. **Immanuel Weber:** Resources. **Tina Moelter:** Resources, Data curation, Investigation. **Filip Dzunic:** Conceptualization, Methodology, Resources, Data curation. **Paul Deffert**: Resources, Investigation. **Edvinas Rommel:** Investigation, Resources, Writing – Review & Editing. **Michael Delaney:** Investigation, **Björn Baschek:** Funding acquisition, Supervision. **Gilles Rock:** Funding acquisition, Supervision. **Jens Bongartz:** Funding acquisition, Supervision. **Andreas Burkart:** Methodology, Funding acquisition, Supervision, Writing – Review & Editing.

Keywords: calibration and validation; field spectrometer; drone; gyrocopter; Sentinel-2

6.1 Abstract

Non-invasive investigation of surfaces from drones and manned aircraft used as camera platforms is a well-established remote sensing practice. However, cross-comparison of multispectral reflectance from different camera systems across different platforms, locations and times can be challenging. We investigate reflectance retrieved from Sentinel-2 and two airborne camera systems with respect to the mobile, radiometrically calibrated, two-channel hemispherical-conical field spectrometer system RoX. This spectrometer system serves in combination with a nine-panel grey scale as ground reference and transfer instrument. In the first step, the ground reference was validated against Sentinel-2 reflectance including atmospheric compensation. Our results suggest significant differences in the uncorrected reflectance from the two airborne sensors with respect to instantaneous calibration across 22 mixed

targets. In the second step, those differences were reduced to a median discrepancy below 10% using the proposed in-field empirical line correction method (ELC). Continuous irradiance correction further improved the agreement across the validation targets and achieved a coherent reflectance dataset from all four different sensor systems, from the satellite level to the ground and airborne level, considering the limitations of instrument and in-field handling. NDVI maps created from drone and manned aircraft achieved an agreement around 89% and 95% compared to the satellite after calibration and correction. We consider in-field calibration with additional, continuous down-welling radiance correction of reflectance promising to support fusion of information across four sensors and platforms. Thus, field spectrometer systems serve as transfer instruments and bridge the gap of information from the satellite down to the ground and airborne scale in future airborne mapping and classification efforts.

6.2 Introduction

Modern remote-sensing systems allow non-invasive, yet detailed insights into various targets from airborne and spaceborne platforms, e.g. for investigation of vegetation and soil (Bioucas-Dias et al., 2013; Hall et al., 2008; Hank et al., 2019; Picard et al., 2016; Schmidtlein et al., 2007; Singh et al., 2015; Vanderbilt et al., 1998). While satellite images provide detailed information in time due to frequent overpasses, satellite images suffer at the same time from poor spatial resolution due to the very large distance between sensor and target (Mulla, 2013). The European Space Agency (ESA) currently operates Sentinel-2 satellites, which provide multispectral maps including 13 spectral bands in the visible and near-infrared, a high revisit rate and robust atmospheric path correction (Ariza et al., 2018; Drusch et al., 2012; Li et al., 2018). In contrast, airborne platforms, e.g. drones or manned aircraft, provide the benefit of high spatial resolution due to lower altitude and airspeed but cannot provide many frequent overpasses (Berni et al., 2009; Siegmann et al., 2019). Multispectral cameras on airborne platforms often lack direct assessment of the atmosphere and incoming light conditions (Mamaghani and Salvaggio, 2019). Thus, calibration of retrieved reflectance values with respect to incoming light is typically achieved in comparison with a well-characterized target, e.g. reference panels or grey-scales, prior to or during the flight (Guo et al., 2019; Von Bueren et al., 2015). While irradiance is considered as rather stable and following a cosine-function on a perfect clear-sky day, changes in the atmosphere can cause a vast deviation from this assumption and result in biased reflectance and indices derived from airborne imagery (Schläpfer et al., 2020a; Stow et al., 2019). In consequence, using a ground reference for the purpose of calibration is essential to allow for a valid comparison between different platforms and imaging sensors (Cogliati et al., 2015a). Radiometric corrections are required to eliminate disturbances related to sensors, atmosphere, clouds and bidirectional reflectance distribution function (BRDF) in airborne and spaceborne imaging data

(Honkavaara et al., 2013; Honkavaara and Khoramshahi, 2018; Schläpfer et al., 2020b). In addition, varying illumination conditions need to be considered and compensated for, while irradiance sensors installed on drone or aircraft are often rendered unusable by flight altitude and movements (Hakala et al., 2013). Thus, changes in the down-welling light can be monitored only by using continuous irradiance measurements on the ground during the flight campaign. At the same time, mobile ground references can validate the multispectral reflectance in aerial images with multiple independent samples in various locations and further inform other aspects of remotely sensed reflectance (Agapiou et al., 2010; Damm et al., 2015; Shi et al., 2020).

Hyperspectral point sampling with field spectrometer systems has been used for decades as ground reference to calibrate and validate airborne sensors (Mihai et al., 2018; Milton et al., 2009; Yao et al., 2013). The emergence of automated, hemispherical-conical spectrometer systems with two inter-calibrated channels allows the assessment of up-welling and down-welling light at the same time and, thus, retrieve calibrated radiance and reflectance in principle even under changing atmospheric conditions (Burkart et al., 2015b; Cogliati et al., 2015a). The RoX field spectrometer system (JB Hyperspectral Devices, Düsseldorf, Germany) is a two-channel system, which includes a high-resolution spectrometer in the visible to near infrared (NIR) spectral range. The device has been used in mobile applications to assess water quality or snow albedo using hyperspectral reflectance characteristics, or in stationary setups to infer air quality through continuous measurements of incoming and reflected light (Kokhanovsky et al., 2021; Maier et al., 2021; Naethe et al., 2020; Wagner et al., 2018). Dual-channel, hemispehrical-conical optical configuration makes the device suitable for reflectance validation without the need for alternating measurements of target and a white reference. Due to the integrated cosine corrector in the down-welling channel and a lightweight gimbal, a white reference in the field is becoming obsolete. This enables mobile ground measurements to be both, more flexible and more mobile.

Grey-scales serve as reference targets for the inter-calibration of reflectance across imaging sensor systems during survey-campaigns with multiple sensor-platforms. (Guo et al., 2019). The defined reflectance of each individual panel differs slightly for this purpose and is typically defined with a reference instrument in the field or in the lab (Klein et al., 2011; Mamaghani and Salvaggio, 2019). An empirical line correction (ELC) uses the reflectance measured with the reference instrument above the grey-scale and relates it by linear regression to the measured reflectance from the airborne camera system (Karpouzli and Malthus, 2003; Pompilio et al., 2018; Wang and Myint, 2015). Regression coefficients are calculated using the linear relationship between reference and airborne reflectance (Wang and Myint, 2015). The derived slope and intercept serve as correction coefficients for the ELC and are applied to rescale the raw reflectance values from the airborne sensor systems. This correction allows the fusion of data from different sensors and their combined use as coherent dataset in further

efforts, e.g. classification and mapping of waters, sediments and vegetation (Bioucas-Dias et al., 2013; Moharana and Dutta, 2014; Pompilio et al., 2014; Smith et al., 2003; Spyrakos et al., 2018; Zhao et al., 2019). In relating all data to a single, radiometrically calibrated reference, a doorway opens up towards analysis of multiple airborne measurements with respect to the temporal domain (Al-Rawabdeh et al., 2017; Guyet and Nicolas, 2016; Oxoli et al., 2020; Petitjean and Weber, 2014; Rejichi and Chaabane, 2015; Shi et al., 2020; Turner et al., 2015).

We present the cross-calibration of two airborne, multispectral camera systems, based on in-situ characterization of a grey-scale using a high-resolution hyperspectral field spectrometer as a radiometrically calibrated reference, which was previously validated against Sentinel-2 BOA reflectance. The correction coefficients are derived from the in-field ELC and are applied to the raw, imaging reflectance data recorded with an unmanned drone and a manned gyrocopter. In addition, we apply a continuous radiance correction to the reflectance retrieved from drone and gyrocopter to account for changes during the flights using continuous measurements of down-welling radiance with the RoX. The corrected, airborne reflectance is compared with the ground reference in 22 validation points, which are spread out across the field site. We investigate the agreement of reflectance from three different sensors and platforms with respect to Sentinel-2 BOA reflectance, aiming for a coherent, joint dataset towards enabling further inter-temporal and inter-spatial analyses.

6.3 Equipment and Methods

The following sections describe site, equipment, data pre-processing, post-correction and validation.

6.3.1 Site

Ground sampling points (GSP) and aerial images were collected on March 30th, 2021 during clear sky conditions in a closed, non-public property in Schmidtheim, Germany, within ca. 6 km distance from the airfield Dahlemer Binz (GPS - WGS84, Lat.: 50.409N, Lon.: 6.590E). The sampling area was located in close proximity to a stone pit, with different areas of bare soil, gravel, low-growing meadow and small, planted trees. Due to the early time in the year, a closed vegetation canopy was not yet developed. Only low grass was growing in the northeastern part of the sampling area. A few, young, evergreen conifers were located in the south of the sampling area. A map of the sampling area is provided in Figure 34. A grey-scale with nine different grey panels was placed in the center of the recorded area on the ground and recorded as GSP 2-10. In addition, 22 GSPs were spread out to cover vegetation and soil targets equally (Figure 34, GSP 11-32).

Figure 34: Orthomosaic recorded with MicaSense RedEdge-M on drone, geo-rectified hyperspectral GSPs of the mobile RoX system were marked with red triangles and labelled in ascending order with respect to the time of recording.

6.3.2 Equipment and data

Field spectrometer

Hyperspectral ground measurements were collected using a customized RoX monitoring field spectrometer with a spectral range of 340 nm – 832 nm across 1024 spectral bands and a spectral resolution of 1.5 nm full-width at half maximum (FWHM). The instrument was equipped with a two-channel optical path that switches continuously between measuring up-welling and down-welling light using optical shutters. The down-welling channel was equipped with a cosine receptor and hemispherical field of view, the up-welling channel with bare fiber optics and a conical field of view of ca. 25° opening angle.

In addition, a full measurement cycle consisted of recordings of the detector's dark-current by closing the shutters for both channels. Automatic optimization of the integration time ensured to cover ca. 80% dynamic range of the detector. Internal quality flags allowed for error tracing and ensured a consistent data quality. Furthermore, the instrument had undergone a thorough laboratory calibration routine, which included radiometric calibration, wavelength calibration and non-linearity characterization. The system was powered by a rechargeable LiPo-battery and mounted on a mobile three-legged tripod.

Figure 35: Mobile setup of JB Hyperspectral RoX monitoring field spectrometer (left) used as ground reference and nine-panel grey scale for in-field calibration and validation of airborne sensor systems (right).

A gimbal-unit installed at the far-end of the boom at a height of 1.5 m above ground automatically maintained the nadir orientation of the optics, and ensured consistent recordings (Figure 35). Ten complete cycles were collected for each GSP, which included the measurement of down-welling light, reflected light, again down-welling light and then dark-current in both channels. In addition, continuous measurements of down-welling light were recorded in-situ during the air time of drone and gyrocopter. For this purpose, a second RoX with identical optical configuration was set up near the airfield in ca. 4800m distance to the sampling site and served as a second reference for down-welling light. The device recorded continuously for 6h incoming radiance to support the correction of changes during the airborne measurements (Figure 36).

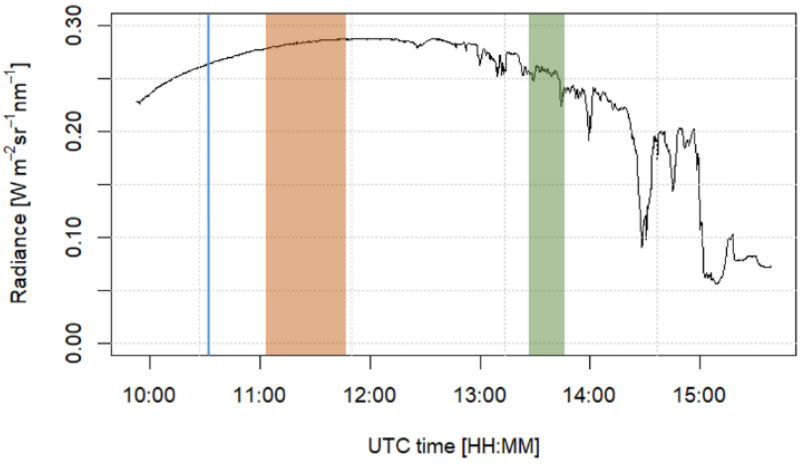

Figure 36: Diurnal course of mean down-welling radiance between 400 nm and 700 nm, continuously measured with the RoX nearby the airfield on March 30th, 2021. Ideal clear-sky conditions exhibited a pattern, which followed a cosine function in the morning. High cirrus clouds affected the later readings and caused shading of the entire area in the afternoon. Time of Sentinel-2 overpass at 10:34 marked in blue, Gyrocopter overpass between 11:08 and 11:46 marked in orange, time of drone overpass between 13:30 and 13:49 marked in green.

Drone and Camera

Multi-spectral image data were collected using the five-band multispectral camera MicaSense RedEdge-M, carried by a DJI Phantom 4 Pro V2.0 UAV with four rotors (Figure 37). The MicaSense RedEdge-M provided information in the five spectral bands blue, green, red, red edge and near infrared (NIR), as specified in Table 13.

Table 13 Optical specification of MicaSense RedEdge-M multispectral camera system as carried with the drone in this study, central wavelength and FWHM are given in nm for each spectral band.

Filter, band	**Blue**	**Green**	**Red**	**Red Edge**	**NIR**
Central wavelength in nm	475	560	668	717	840
FWHM in nm	20	20	10	10	40

A 5-band Down-welling Light Sensor (DLS) was mounted at the top of the drone to correct for changing light conditions during each flight. The measurements of the DLS were stored in the metadata of each image file during the flight. However, the usage of the DLS was recommended for overcast conditions only in the standardized MicaSense processing chain, because the UAV tilted during the flight and the DLS pointed in changing directions with changed orientation of the drone (Mamaghani and Salvaggio, 2019). Thus, the DLS information could not be used for the MicaSense data under clear-sky conditions.

Figure 37: The DJI Phantom 4 Pro V2.0 drone was used to carry a MicaSense RedEdge-M multispectral camera.

A calibrated reflectance panel from MicaSense was captured immediately before the flight in order to transform the Digital Numbers (DN) from the RedEdge-M into raw reflectance values. This raw reflectance was used for the comparison with other sensors and for applying further correction methods.

Images were triggered during flight every two seconds, gain (ISO) and exposure settings were set to automatic. The drone was moving at a speed of about 8 m/s at a flight altitude of 80 m, which resulted in spatial resolution of approximately 6.5 cm/pixel.

Gyrocopter sensor carrier platform

The gyrocopter MTOsport (Figure 38 a) used by Fraunhofer Anwendungszentrum für multimodale und luftgestützte Sensorik (AMLS), Remagen, Germany, provided a comparatively inexpensive and flexible airborne carrier platform, primarily used with custom built spectral camera systems. A customized sensor carrier system “FlugKit” (Kneer et al., 2016) was developed explicitly for the MTOsport and facilitated fast and flexible integration of different imaging sensors. The FlugKit carrier was integrated into the gyrocopter and included an aircraft-independent power supply, the Sensor Management System (SMS), Global Navigation Satellite System (GNSS) receivers, and two external mounts for electromechanically stabilized camera systems. In addition, a Flight Management System (FMS) was temporarily installed on the pilot's instrument panel and connected to the SMS. The FMS handled navigation along a pre-calculated flight path and triggered data acquisition of the camera system through the SMS at specific trigger points. These trigger points were calculated during flight planning according to the selected parameters, e.g., image overlap, flight altitude, or ground sampling distance (GSD). The individual system components have been described in detail in previous publications (Jenal et al., 2015; Weber et al., 2015a). FlugKit has recently been extended with a Real-Time Kinematic (RTK) capable GNSS receiver allowing a Post-Processed Kinematic (PPK) correction as a backup solution.

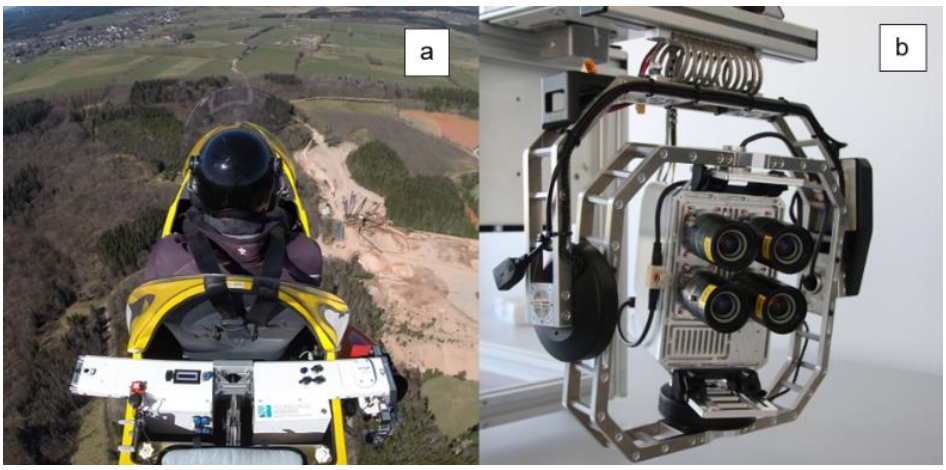

Figure 38: Microlight gyrocopter carrying the base system during the flight on March 30th, 2021 in (a), PanX 3.0 mounted in an electromechanical stabilization platform for laboratory tests in (b).

Gyrocopter Camera Unit

On March 30th, 2021, the FlugKit was operated with the PanX 3.0 camera system as exterior payload. The PanX 3.0 is the latest multispectral camera system developed by AMLS. It is the successor of the PanX camera system (Weber et al., 2015b) and is equipped with four identical industrial board-level cameras (Allied Vision Manta G-1236B).

Table 14 Feature overview of the PanX 3.0 camera system

Parameter	**Specified Value**			
Resolution	4 x 12 Megapixel			
Bit-depth / Dynamic Range	12 bit / 71.8 dB			
Field of View	62.5° (horizontal) / 47.8° (vertical)			
Weight	3.85 kg (including gimbal)			
Filter	**blue**	**green**	**red**	**NIR**
central wavelength	470 nm	532 nm	630 nm	810 nm
bandwidth	50 nm	55 nm	45 nm	50 nm

Every camera was combined with a band-pass filter between 400 and 1000 nm. The filters used on March 30th are specified in Table 14. Those selected band-pass filters were mounted between lens and sensor in the PanX 3.0 system, which also provided a significant advantage over the preceding model. The applied filter wavelengths match typical spectral features of vegetation in the visible (VIS) and near-infrared (NIR) spectrum and allow the calculation of established vegetation indices like NDVI. Each sensor system used in the FlugKit, including the PanX 3.0, was integrated into a custom-made electromechanical gimbal, which ensured a permanent nadir viewing angle during flight (Figure 38). The main features of the PanX 3.0 camera system are summarized in Table 14.

The gyrocopter flew at an altitude of 300 meters above ground level with a speed of ca. 30 m/s. An area of 2.62 km^2 was covered by 300 images per band with a spatial resolution of 9 cm/pixel. A side overlap of 85% and a forward overlap of 62% between the images were guaranteed during the 45-minute-long flight. In order to optimize the dynamic range of each spectral band, the integration time of every camera was individually set by capturing images of a nearly ideal diffuse, Lambertian reference panel before the flight.

Sentinel-2 acquisition

The Copernicus Hub provided by ESA was used to access and download relevant Sentinel-2 data, which were recorded roughly at the same time of field measurements. We used the semi-automatic classification plugin for QGIS to download the multispectral satellite images (Congedo, 2021). An overpass at 10:34 was available in best immediacy with the ground measurements at the field site (see Figure 36). The scene was confirmed to be free from clouds. We downloaded the Level-2A product of flightpath T32ULA including sub-pixel multi-spectral reflectance registration (Ariza et al., 2018). Level-2A reflectance included ESA's SEN2COR atmospheric correction and provides orthorectified, atmospherically corrected BOA reflectance, which was directly used for further analysis with field spectrometer measurements on the ground (Baetens et al., 2019). The multispectral bands 2 to 8 were extracted for further analysis, which overlapped with the usable spectral range of the RoX (see Table 15).

Table 15: Selected Sentinel-2A multispectral bands, which overlapped with the spectral range of the RoX, central wavelength and FWHM are given in nm for each spectral band.

Band	**B2**	**B3**	**B4**	**B5**	**B6**	**B7**	**B8**
Central wavelength in nm	492	560	665	705	740	783	832
FWHM in nm	66	36	31	15	15	20	106

6.3.3 Data pre-processing

Field spectrometer data from the direct output of the instrument in raw digital numbers were processed using R and the packages FieldSpectroscopyCC[9] and FieldSpectroscopyDP[10]. The result of this processing was calibrated upwelling radiance, down-welling radiance and reflectance. These

[9] Julitta, T. "FieldSpectroscopyCC". Github, Inc. Accessed April 5, 2024. https://github.com/tommasojulitta/FieldSpectroscopyCC.

[10] Julitta, T. "FieldSpectroscopyDP". Github, Inc. Accessed April 5, 2024. https://github.com/tommasojulitta/FieldSpectroscopyDP.

calibrated radiance and reflectance data were further processed into a standardized format for the inter-comparison of the different sensors and platforms. In the next step, the spectral characteristic response of Sentinel-2A band 2 - 8, the MicaSense and the PanX3.0 bands were simulated using the calibrated hyperspectral reflectance data from the RoX. Gaussian response functions were assumed for the multispectral bands of the camera systems, following Schaepman and Dangel (2000). Central wavelengths and FWHMs specified in Table 13, Table 14 and Table 15 were used to calculate the multispectral response matching with the actual sensors, respectively. Mean and standard deviation were calculated for each GSP, considering ten individual ground measurements in each point.

Differential GPS with RTK was used for reliable positioning in the field and to locate the GSPs with a precision of 2 cm within the orthorectified geomosaic, following the approach by Schläpfer and Richter (2002). A repeatable sampling of desired Regions of Interest (ROI) was possible only by use of the precise positioning with RTK-GPS, which referenced each ground measurement. GSPs were labeled in ascending order with respect to the time of recording and each assigned with RTK-GPS coordinates. RTK-GPS coordinates were recorded alongside the hyperspectral measurements using a Topcon HiPer V in the field.

Furthermore, the GPS coordinates were used to extract the pixel-based, multispectral information from the Sentinel-2A image. The selected spectral bands had a spatial resolution between 10 m and 20 m per pixel. Using a 20 m x 20 m ROI for extraction around each GSP resulted in 2 x 2 pixels for bands B2, B3, B4, B8, and in 1 x 1 pixel for bands B5, B6, B7, respectively. A recognition of the grey-scale was not possible due to the coarse spatial resolution. Larger, homogenous areas were selected around the site to cross-compare reflectance measured on the ground and satellite-based, BOA reflectance. Thus, only GSP 11 to 32 were used to extract pixel values, mean and standard deviation, as they were recorded over larger features, considered homogenous both, from field spectrometer footprint and from Sentilel-2 pixel projection. The visual inspection of the surfaces on the ground, which were covered by the RoX's field of view and the Sentinel-2 pixels allowed assuming sufficient homogeneity of the examined areas. Linear regression between ground-measured reflectance using the simulated multispectral response and satellite-based BOA reflectance was computed, providing coefficient of determination R^2, slope and intercept. The resulting linear coefficients were applied to adjust the ground measurements using ELC validated with the satellite. Thus, adjusted and validated, hyperspectral reflectance were used as ground reference for later analyses.

The raw MicaSense images containing DNs were converted to radiance and reflectance using the MicaSense calibrated reflectance panel, which was captured prior to the flight. The processing chain

was based on the MicaSense image processing tutorials available for Python 3 on GitHub[11]. The processing included correction for vignette effects, a normalization for automatic exposure and gain settings. DLS sensor values could not be used due to erroneous readings under clear sky conditions. Agisoft Metashape was used for the photogrammetric processing and stitching of a geo-rectified orthomosaic from image data recorded with the MicaSense camera.

Georeferencing of the images recorded with PanX 3.0 was based on post-processing of the GPS positions after the flight (Baeumker et al., 2020), including additional manual referencing using ground control points. The raw pixel values were converted to reflectance based on grey-card readings. The resulting images were processed with the Structure from Motion (sfm) algorithm using the photogrammetric software Metashape from Agisoft (Westoby et al., 2012).

6.3.4 Post correction and cross-validation

A grey scale comprising nine different reflectance intensities was measured simultaneously with the RoX on the ground and from two airborne camera systems on drone and gyrocopter. The grey-scale, as shown in Fig. 2, consists of nine individual 30 cm x 30 cm aluminum panels, fixed in a wooden frame. Each panel has been coated with a different, spectrally linear, matted paint of Lambertian reflectance characteristics. All nine panels exhibited each a defined gradient in reflectance across the investigated spectral range of MicaSense ,PanX 3.0 and RoX (Figure 39). The panels' reflectance was spectrally flat across all multispectral bands and served as a reference for the calibration of MicaSense and PanX 3.0 with respect to the hyperspectral ground measurements.

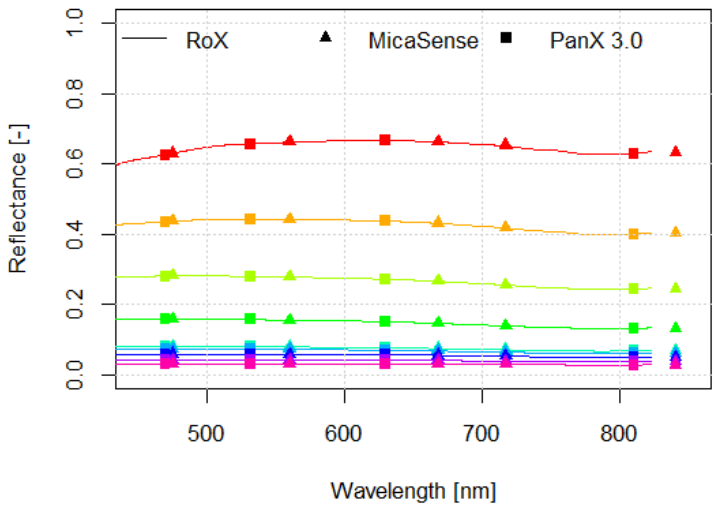

Figure 39: Plot of the nine-panel grey-scale reflectance in different colors for each of the panels, measured by the RoX (line), convolved for MicaSense (triangles) and PanX 3.0 (squares).

[11] MicaSense, Inc. "imageprocessing". Github, Inc. Accessed April 05, 2024. https://github.com/micasense/imageprocessing.

For this purpose, all nine panels were measured in close proximity using the RoX spectrometer. The convolved spectral bands of MicaSense and PanX 3.0 from the hyperspectral ground data (Figure 39) were compared with the actual raw reflectance from pixel values in the aerial images for the entire grey scale. A region of interest with 18cm (4x4 pixels) from the drone and 18 cm (2 x 2 pixels) from the gyrocopter was assumed, centered around the middle of each panel for the extraction of the actual, raw, multispectral reflectance. Mean and standard deviation were extracted for the corresponding pixel values. Assuming a linear regression for each band separately, intercept and slope were computed with respect to the ground reference. Finally, thus computed intercept and slope were applied as correction coefficients for the empirical line correction "ELC field", using each band of the raw MicaSense and PanX 3.0 reflectance data, separately. The corrected results were reported for the validation points, respectively.

Continuous Irradiance Correction (CIC) was performed in addition to the ELC. We applied an approach similar to the irradiance correction with the sunshine sensor in Olsson et al. (2021). Reflectance with respect to the wavelength λ was retrieved by both airborne camera systems, each with respect to a single reflectance calibration of a known reference target prior to the flight, as shown in Equation 15:

$$R_{\lambda,T0} = \frac{L\uparrow_{\lambda,T0}}{L\downarrow_{\lambda,T0}} \tag{15}$$

Measurements of the up-welling radiance $L\uparrow_{T0}$ of each camera system were related to the known reflectance R_{T0} from the reference target with respect to the inherent down-welling radiance $L\downarrow_{T0}$ at the time T0 prior to the flight. Assuming static irradiance for all later times Ti, Equation 16 computes reflectance from the airborne sensors using measured upwelling-radiance during the flight at time Ti with respect to the down-welling radiance $L\downarrow_{T0}$.

$$R_{\lambda,Ti} = \frac{L\uparrow_{\lambda,Ti}}{L\downarrow_{\lambda,T0}} \tag{16}$$

However, the assumption of static down-welling radiance holds true only for very short periods and creates an increasing error in the reflectance retrieval with increasing time Ti due to changes in the down-welling light during the flight. To account for this fact, continuous measurements with the RoX provided a reference for the actual changes of the down-welling light during the entire experiment (Figure 36). Thus, the measured down-welling radiance $L\downarrow_{T0}$ at the time of calibration and the change $\Delta L\downarrow_{Ti}$ in down-welling radiance were used in Equation 17 to correct the retrieved reflectance R_{TCi}.during the flights.

$$R_{\lambda,TCi} = \frac{L\uparrow_{\lambda,Ti}}{L\downarrow_{\lambda,T0}+\Delta L\downarrow_{Ti}} \tag{17}$$

Using the reflectance $R_{\lambda,Ti}$, which was retrieved during the flight from the airborne camera platforms with respect to the fixed down-welling $L\downarrow_{T0}$, we substituted the measured up-welling radiance in Equation 17 with Equation 16 solved for $L\uparrow_{\lambda,Ti}$, calculated the difference in down-welling radiance between $L\downarrow_{T1}$ and $L\downarrow_{T0}$ and further solved to Equation 18:

$$R_{\lambda,TCi} = R_{\lambda,Ti}\frac{L\downarrow_{\lambda,To}}{L\downarrow_{\lambda,Ti}} \tag{18}$$

Validation of the applied ELCs was performed using 22 ground-sampling points, which were measured with the mobile field spectrometer including different vegetation and bare soil targets. Assuming a region of interest of 16 cm radius with respect to the footprint of the ground measurements, mean and standard deviation of raw reflectance as well as the ELC field pixel values were extracted for each point. In addition, CIC using Equation 18 was performed based on ELC field reflectance values to account for changes in irradiance during the flight. Time T0 was assumed at 13:38 for the drone when recording the reference panels and reflectance was corrected for the overpass time Ti of the GSPs between 13:30 and 13:49, accordingly (see Figure 36). For the gyrocopter, we assumed T0 with the reflectance calibration using a grey-card of Lambertian characteristics at the airfield at 11:08 and calculated the corrected reflectance with respect to the actual time of the overpass of the GSPs between 11:27 and 11:46. The extracted and corrected pixel values from the aerial images were compared by means of linear regression with the convolved bands from the ground reference for each camera system individually. Pearson's correlation coefficient R^2, intercept and slope were reported for raw, ELC field and ELC field + CIC reflectance values with respect to the ground reference. The relative percentage difference of raw and corrected pixel values in each spectral band was computed for each GSP with respect to the ground reference.

Finally, corrected orthomosaics from micaSense and PanX 3.0 were resampled to match the 10 m spatial resolution of the Sentinel-2 images. For this purpose, pixels from micaSense and PanX 3.0 were aggregated by calculating the mean for pixels, which fell inside one Sentinel-2 pixel. Sub-pixels on the edge were assorted to the super-pixel with which they shared the largest proportion. Thus, corrected and resampled PanX 3.0 and micaSense maps were created with identical spatial resolution with respect to Sentinel-2. NDVI was calculated for each pixel to better compare the different multispectral bands across the different platforms (Tucker, 1979). The NIR and red band were used for the calculation, both, in resampled micaSense and PanX 3.0 images respectively. NDVI was computed in Sentinel-2 pixels using bands B8 and B4 accordingly. The pixel values were extracted with respect to their position and compared using linear regression. Thus, NDVI pixel values from PanX 3.0 and micaSense were compared with NDVI from Sentinel-2, calculating the coefficient of determination as a result. In consequence, the final validation step was performed against Sentinel-2 NDVI (Figure 40).

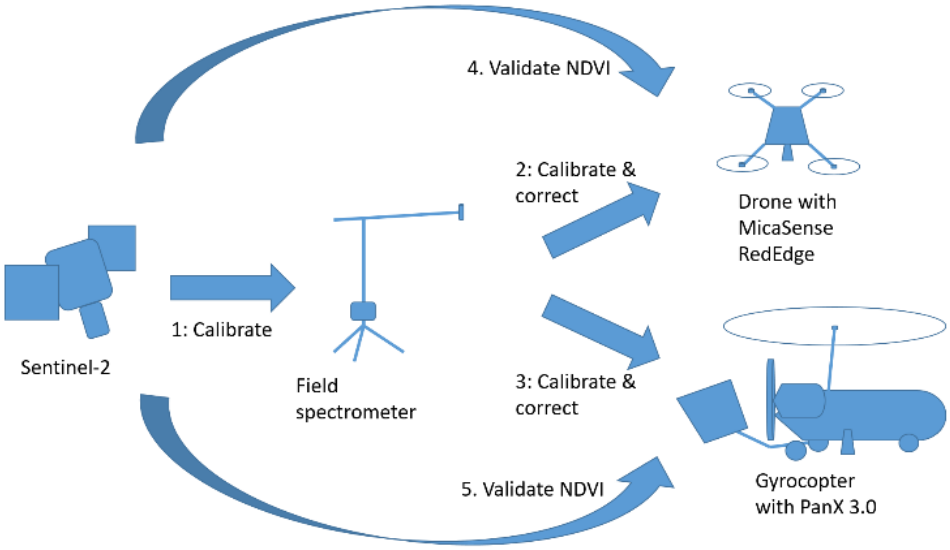

Figure 40: Schematic overview of the performed calibration and validation exercise, including correction for changing irradiance conditions. Hyperspectral field spectrometer measurements were the centerpiece from which all other imaging, multispectral sensors were cross-calibrated and finally validated against Sentinel-2 NDVI.

6.4 Results

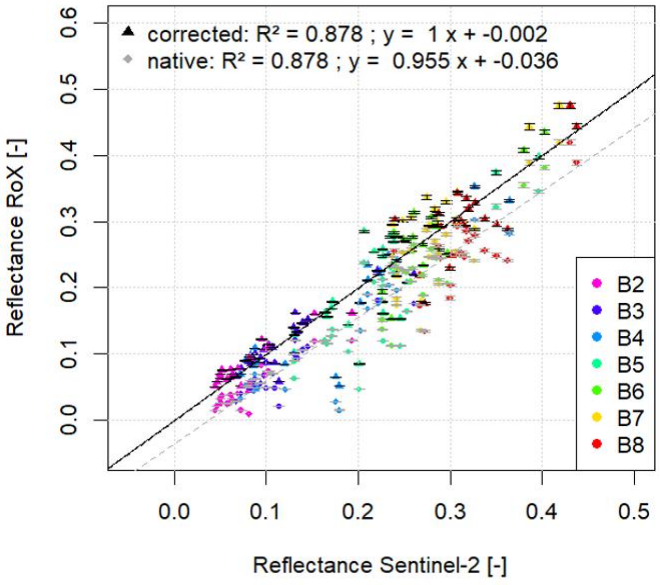

Figure 41: Ground measured reflectance with respect to Sentinel-2 BOA reflectance across 7 bands (B2 – B8), each in a different color, extracted from single pixel for each GSP. The grey dashed regression line and diamond symbols show the native RoX measurements. The black dotted regression line and triangle symbols show the corrected RoX measurements.

Reflectance measured with the RoX was compared with the BOA reflectance including atmospheric correction from the Sentinel-2 overpass. Using the native RoX measurements, a tendency for multiplicative (ca. 0.96) and additive (ca. -0.04) underestimation of the Sentinel-2 reference was observed across all measured GSP (Figure 41). Especially in B4 and B5 a few outliers of strong underestimation were recognized. The rest of the data points were spread without any obvious

patterns with respect to the spectral bands around the regression lines. Assuming that ground measurement were linearly related and proportional to the Sentinel-2 reference, ELC resulted in a regression with R^2 around 0.88, intercept and slope approaching the line of identity after correction. Thus, the accuracy of the ground spectrometer measurements was improved to less than 0.2% additive error, while the precision around 88% would remain the same with respect to Sentinel-2 BOA reflectance.

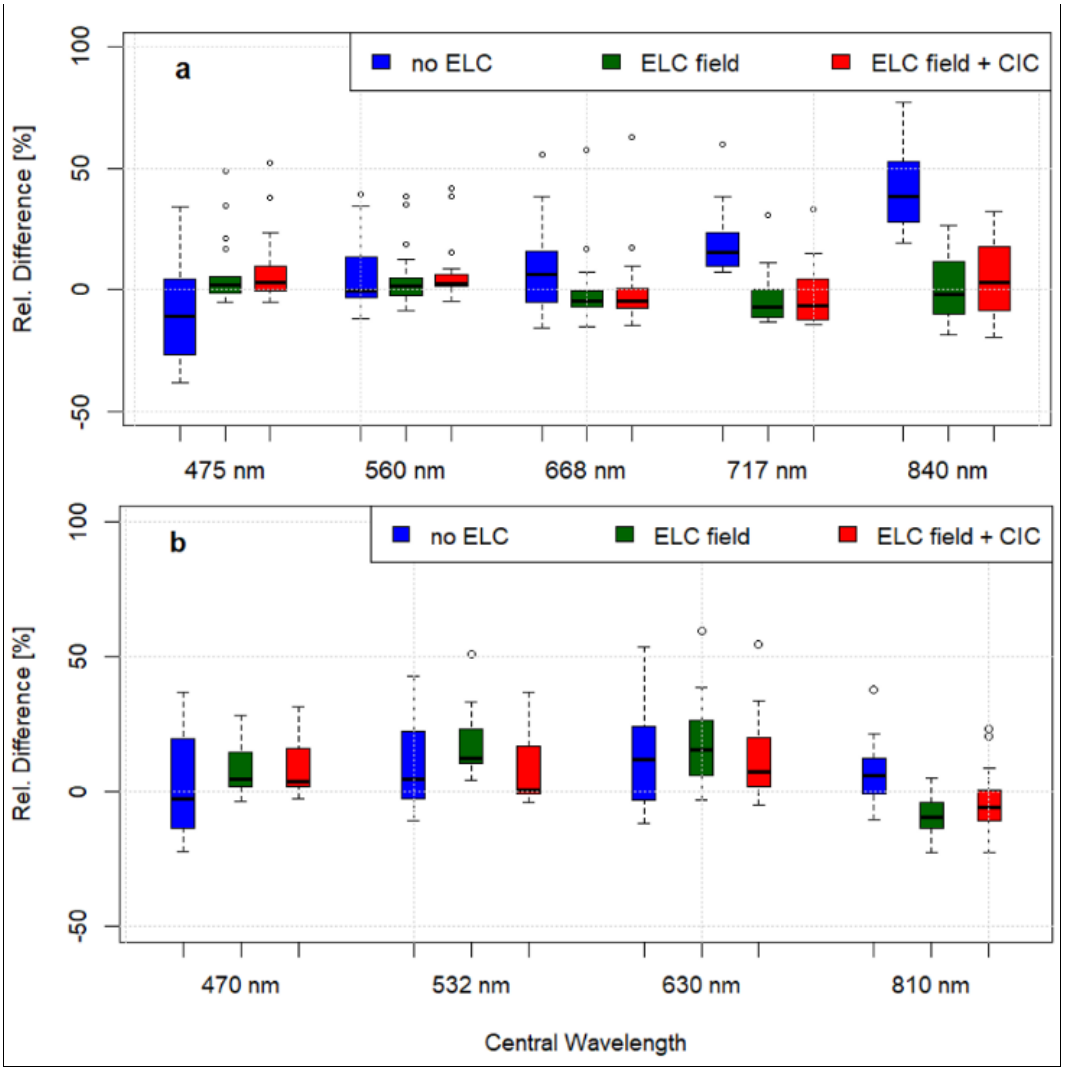

Figure 42: Relative percentage difference for all validation points with respect to the ground reference, calculated in each band for the MicaSense in (a) and for the PanX 3.0 in (b), raw camera reflectance given in blue, ELC field reflectance is given in green and ELC field plus CIC is given in red.

Likewise, raw drone image reflectance and raw gyrocopter image reflectance were corrected using the ELC field and the combination of ELC field and CIC. Relative difference of reflectance values with respect to the ground reference for each band across all validation points were reported in Figure 42a for the drone and in Figure 42b for the gyrocopter, respectively. A relative difference with highest median was reported in the 840 nm band of the MicaSense. Relative differences in other bands were distributed with ascending median across all bands. As a result, relative differences with respect to the reference were significantly reduced using the ELC field. The median relative difference remained

below 10% and suggested a significantly improved agreement between the two systems. Interquartile range decreased also significantly with ELC field in almost all bands, except for the 840 nm and 717 nm bands, which exhibited unchanged interquartile ranges. The relative differences with respect to the ground reference were reduced further using the ELC field + CIC, exhibiting slightly increased spreading and lower median relative difference.

The raw reflectance values extracted for all ground-sampling points from the gyrocopter data exhibited a rather stable relative difference across the four spectral bands of the PanX 3.0 camera system with respect to the ground reference. The lowest median relative difference was below -10% in the 470 nm band, the highest median relative difference was around 20% in the 630 nm band with respect to the ground measurements. Outliers exhibited a similar spreading in the 470 nm, 532 nm and 630 nm band. The smallest range of relative differences was reported in the 810 nm band. Applying the ELC field, corrected reflectance values exhibited even an increased relative difference compared with the raw reflectance with respect to the ground reference. The CIC reduced median relative difference between airborne reflectance and ground reference significantly, resulting in median relative differences below 10% across all spectral bands with the PanX 3.0.

ELC field improved the coherence in retrieved reflectance between all three systems significantly in all recorded wavebands (Figure 43). Taking changing irradiance conditions over time during the flight into account, the CIC improved the agreement between airborne reflectance and ground reference even further. This improved coherence was likewise reflected in the slope and intercept between airborne and ground-based reflectance values for all bands across all validation points extracted from the drone data (Figure 43 a) and from the gyrocopter data (Figure 43 b). Assuming a linear relationship between ground-based and airborne measured reflectance values, a high coefficient of determination with R^2 larger 0.9 was reported for raw and corrected reflectance from PanX 3.0 and micaSense. Slope and intercept of the raw reflectance recorded with the MicaSense camera across all validation points exhibited a noticeable, multiplicative overestimation with respect to RoX reflectance. In consequence, higher reflectance values were systematically more overestimated than lower reflectance values from the raw MicaSense reflectance for the validation points. A significantly improved agreement between drone reflectance and the ground reference was reflected in a slope closer to one and intercept closer to zero for all validation points using ELC field. Thus, reflectance measured from the drone after the correction was more coherent with reflectance measured on the ground. Applying the CIC in addition to the ELC field reduced the intercept by half and improved slope to nearing one. Reflectance measured at the validation points from the gyrocopter also exhibited a strong correlation with the ground measurements, both in the raw and corrected reflectance. Slope higher than one and intercept deviating from zero, respectively, indicated a systematic overestimation of the raw reflectance also by the PanX camera system. This overestimation was eliminated, using the ELC field and resulted in a

slope around 0.9 and intercept closer to zero. Likewise, the agreement between the ground reference and reflectance measured from the gyrocopter were significantly improved applying ELC field and CIC. Airborne reflectance was considered equivalent to the ground reference, with slope nearing one and offset reduced further after full correction. In consequence, reflectance data recorded in the field from all three systems were considered coherent since ELC field + CIC corrected reflectance from micaSense and PanX 3.0 were equivalent with the ground reference.

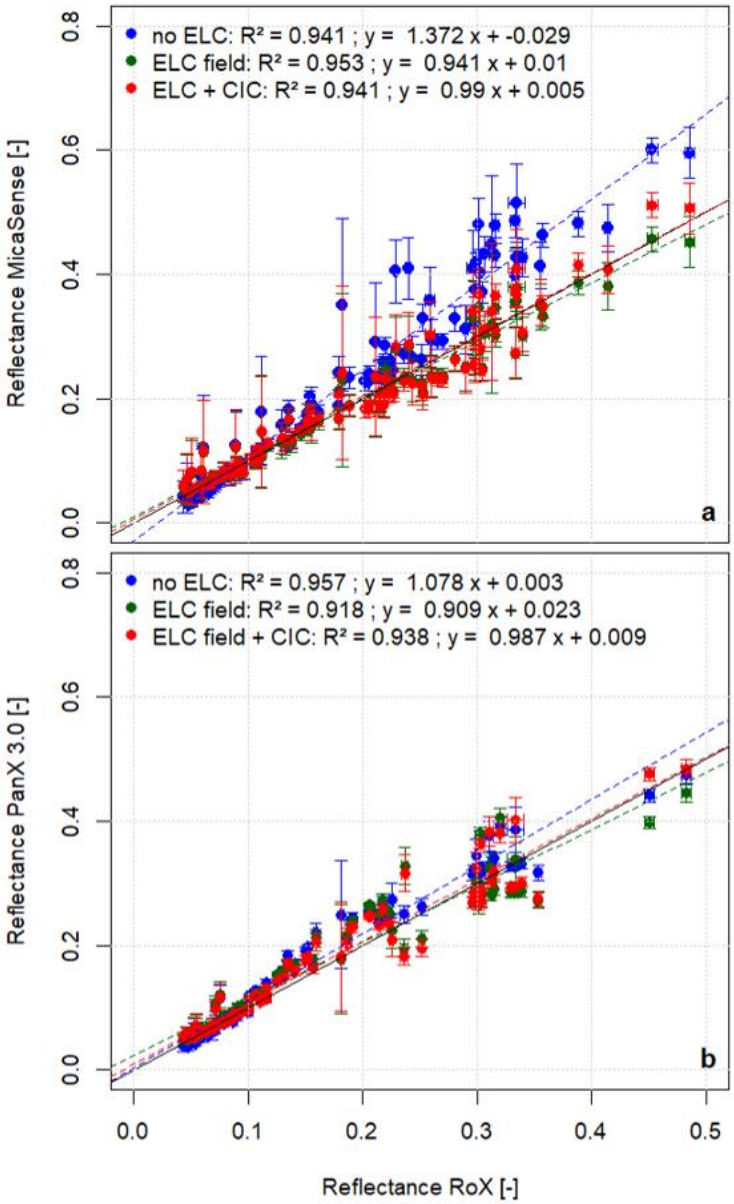

Figure 43: Comparison of raw reflectance extracted from the orthomosaic (blue), ELC field corrected reflectance (green) and ELC field plus CIC corrected reflectance (red), recorded with the MicaSense (a) mounted on the drone and PanX 3.0 (b) mounted on the gyrocopter, with respect to the ground reference. Error-bars indicate the standard deviation and points the mean value in each GSP and for all multispectral bands, respectively.

Finally, we validated the corrected airborne data as NDVI product resampled to Sentinel-2 spatial resolution against the actual satellite product. Visual inspection showed that the Sentinel-2 image provided least spatial details in comparison to higher details in the resampled PanX 3.0 and highest details in resampled micaSense images (Figure 44 a, b and c). Especially the small pond in the right side

of the image was only depicted in the micaSense image with sufficient detail. Likewise, the structures around the bare soil in the bottom of the image were depicted with increasing detail in resampled PanX 3.0 and micaSense, in that order. Vegetation and bare soil could be clearly differentiated by NDVI from all three platforms. NDVI from the micaSense agreed with R^2 around 0.89, NDVI from PanX 3.0 agreed with R^2 around 0.95 with the Sentinel-2-based NDVI (Figure 44 d). MicaSense NDVI exhibited a systematic tendency to underestimate Sentinel-2 NDVI in addition to producing a larger number of random outliers. Pixel based NDVI from PanX 3.0 agrees very well with Sentinel-2 NDVI, showing also a more similar level of spatial detail in the resampled orthomosaic.

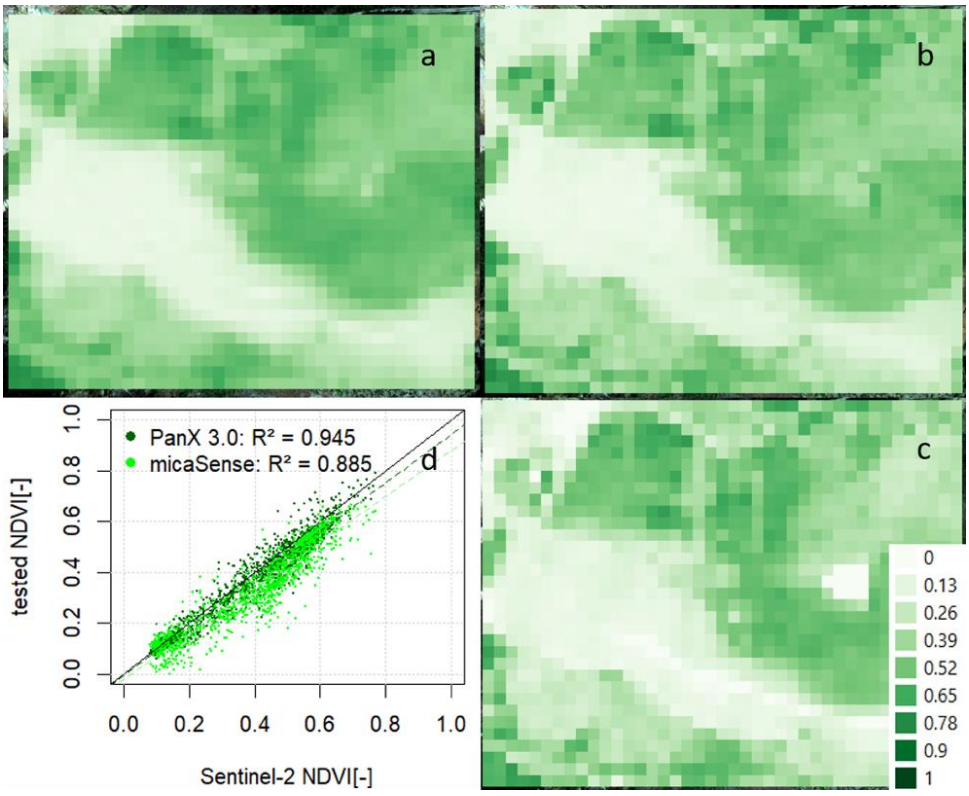

Figure 44: NDVI map of the study site from Sentinel-2 (a), PanX 3.0 (b) and micaSense (c) resampled to Sentinel-2 spatial resolution around 10 m. Pixel values from micaSense and PanX 3.0 are compared with respect to Sentinel-2 NDVI using linear regression (d).

6.5 Discussion

For the fact that the RoX is a radiometrically calibrated instrument, the ground measured reflectance was retrieved with respect to an absolute reference (Slater et al., 1987). When comparing the ground-measured with Sentinel-2 reflectance, we recognized a systematic discrepancy. The ground reference was validated and corrected against Sentinel-2 BOA reflectance to reduce systematic errors from instrument handling, calibration, optical configuration, path geometry, BRDF and the different footprints of the systems, which resulted in an overall agreement around 88% between RoX and

Sentinel-2 BOA reflectance. The line of identity was matched after the correction, indicating comparable dynamics in signal variation across platforms from the satellite to the field spectrometer. We observed only few significant outliers in B4 and B5, which were most likely related to a difference in size of RoX field of view and Sentinel-2 pixel size. The central area of the site provided large surfaces, which were considered as homogenous with respect to the field spectrometer's field of view and the Sentinel-2 pixel projection on the ground. However, small-scale spatial variations are always present in natural surfaces and need to be considered as a source of uncertainty. We minimized this issue by placing the GSPs in locations, which were representative for a larger area after visual inspection on the ground. Significant differences were observed between raw multispectral camera reflectance from, both MicaSense and PanX 3.0, with respect to the ground reference from the hyperspectral field spectrometer. In turn, ELC based on in-situ characterization of a nine-panel grey-scale lead to an improved alignment of the reflectance values measured with drone, gyrocopter and field spectrometer over 22 validation points. This agreement between the three systems was improved further by applying an additional correction to the airborne reflectance, which accounted for the continuous changes in down-welling light during the flight. Since down-welling light conditions could change quickly due to changing atmosphere or solar angle, errors were introduced in the two airborne sensor systems from the assumption of fixed irradiance for the airborne reflectance retrieval (Gilabert and Meliá, 1993). Our continuous measurements of down-welling radiance with the RoX allowed the assessment of the actual irradiance at all times during the flight and served as a reference for correcting reflectance with respect to the changes in irradiance during image acquisition time. However, correction of spatial differences in down-welling light due to low, moving clouds remains difficult, because the reference measurements were taken during the flights in one location only and with some distance to the sampling site. Measuring irradiance ideally at the same time and place would reduce spatial uncertainties of lower clouds and is recommended in the future. In consequence, the presented method for continuous irradiance correction is recommended only for the application in conditions under which the spatial component could be neglected, e.g. for clear sky conditions or high cirrus clouds (Schläpfer et al., 2020b). Fast moving cumulus clouds or low cirrus affect the area with too much spatial heterogeneity and cannot be corrected by the approach (Gao et al., 1993). Since clear sky conditions were reported in the morning and high cirrus clouds affected the entire sampling area uniformly during the afternoon acquisition time, the combined dataset from all three different sensor platforms applying ELC field and CIC was considered coherent (Schmitt and Zhu, 2016). Thus, all three systems were cross-calibrated and temporal biases corrected, which would further allow the valid transfer of information across those systems, e.g. to create a fused data product with spectral information from all airborne sensors to inform classification models and improve their performance by added spectral information (Milton et al., 2009; Schneider et al., 2017; Yao et al., 2013). However,

outliers in the spectral domain exhibited biases in the corrected multispectral reflectance, which could be associated with handling errors, both in the airborne and ground-based sensors, atmospheric distortion, BRDF or erroneous assumption about the optical characteristics of the sensors (Ball et al., 2015; Berni et al., 2009; Liu and Liu, 2018; Mihai et al., 2018; Wen et al., 2020). Especially the lack of an atmospheric correction for the data from drone and manned aircraft represented a significant limitation and introduced another potential source of error. Path length through the column of air between sensor and target is known to cause distortion of the recorded reflected light as a consequence of path radiance, atmospheric transmittance, direct and diffuse solar flux (Richter and Schläpfer, 2002). However, a complete radiative transfer model inversion was beyond the scope of this study because of its complexity (Gómez-Dans et al., 2016). Instead, ELC-based correction methods were previously applied with success to compensate for atmospheric distortion and, therefore, considered to sufficiently address this issue (Ariza et al., 2018; Caballero et al., 2020). Furthermore, multispectral bands of PanX 3.0 and MicaSense were convolved assuming a Gaussian response function, using hyperspectral ground data to compare the actual measured data from each camera system with (Schaepman and Dangel, 2000). A full assessment of the actual spectral and spatial response of the airborne sensors is very complex. The laboratory characterization requires a perfect point source with tunable wavelength at very high resolution, which was not at our disposal. Consequently, a full correction for the actual optical response function was beyond the scope of this study and the simplified assumption of a Gaussian convolution provided a close approximation (Hueni et al., 2017). Consequently, the inherent spectral response function of the RoX and its associated non-linearity, pixel crosstalk, wavelength calibration and radiometric calibration held further sources of uncertainties for the same reason. We reported a median relative difference below 10% between in-field corrected, airborne reflectance and ground-measured reflectance in all multispectral spectral bands of the PanX 3.0 and MicaSense. This quantified error was related to the instrumental handling, nearby objects or the operator affecting the measured reflectance on the ground in addition to uncertainties from atmospheric distortion and simplified assumption about the instruments' optical characteristics discussed above (Kimes et al., 1983). Especially the 840 nm band from the MicaSense fell with its central wavelength outside of the detector range of the RoX. In consequence, spectral information from the edge of the detector were extrapolated to calculate the Gaussian convolution. A linear continuation of the spectral shape was assumed, which would not hold true for the discontinuation of the rising red-edge into the near infrared. The FWHM of the NIR bands in micaSense, PanX3.0 and Sentinel-2 was very wide and, thus, measured data still contributed a large proportion of information and reduced the amount of inference. However, information from the edge of the detector is adversely affected by noise and drifts with temperature (Hueni and Bialek, 2017). Therefore, the comparison with the hyperspectral ground reference for the 840 nm band from the

MicaSense, the 832 nm band from Sentinel-2 and to a certain extent the 810 nm band from the PanX 3.0 included additional uncertainties due to the partially inferred information. Thus, results from those bands must be interpreted carefully and their enhanced uncertainty budget must be noted in addition to above-mentioned errors. Furthermore, angular dependencies diverting from a perfect Lambertian characteristic in the spectral response of reference panels and validation targets have to be considered. Changing sun angle throughout the day caused varying incident light, moving structural shadows and changes in BRDF response due to the different times of recording with each sensor (Rollin et al., 2000). Viewing angles can also differ amongst sensors inside the off-nadir swath width contribution, leading to a changed view onto the same target with different sensors. Thus, structural geometry, terrain topography and surface BRDF need to be considered as an additional uncertainty (Vogtli et al., 2021). In principle, this effect was considered of minor influence and a coherent dataset across all four sensor-platforms using the RoX field spectrometer as transfer instrument would enable a comparison of data recorded at different times and places (Wen et al., 2020). Thus, in-field calibration of airborne multispectral camera systems with respect to an absolute reference opens a doorway towards comparing data recorded at multiple points in time to enable time-series analysis or comparing multiple sites to enable mapping and classification applications (Hueni et al., 2017). The raw MicaSense and PanX 3.0 reflectance lacked those capabilities in consequence of their relative reflectance calibration approach prior to the flight based on a single grey-card reference and inferred irradiance. Furthermore, examining and optimizing exposure settings in MicaSense and PanX 3.0 for future efforts could improve the quality of the data within the dynamic range of the detector while increasing the image acquisition rate due to bypassing time-consuming automatic exposure routines at the same time. Future efforts should investigate the operation of the two airborne sensors with different settings towards minimizing uncertainties introduced from sensor handling. An additional cross-calibration of the two optical channels in the RoX using a white reference in the field is furthermore recommend to track and to correct potential drifts in the radiometric and wavelength calibration when transferring the results from one site or from one time-series to another(Cogliati et al., 2015a). Future effort should thoroughly investigate uncertainties related to the absolute calibration of the ground reference over an extended period of time and across different locations with respect to satellite data. In addition, grey panels were exposed in the fields to dust, which would accumulate on the surface and change their reflectance characteristics during the field campaign. Assessment and correction for the resulting changes of the reflective surface would be complex and were beyond the scope of this study. However, frequent characterization of the panels could track potential degradation and would require ground referencing during each field-campaign to reduce associated uncertainties. Additional care for keeping grey-scales clean should further reduce uncertainties around the reference targets. Adjacency effects of neighboring pixels are a severe source

of error for the extraction of grey-scale reflectance from aerial images (Ariza et al., 2018). An alteration of the reflectance values must be expected due to atmospheric scattering, pixel crosstalk, image definition, focus and geometry of the recorded features. We minimized this error by extracting pixels only around the center of each panel using a ROI, which was significantly smaller than the actual panel size.

Corrected othomosaics from micaSense and PanX 3.0 were resampled to match the spatial resolution of Sentinel-2 around 10 m pixel size. NDVI was calculated from all three platforms and compared accordingly. Increasing degree of spatial detail was observed from Sentinel-2, over PanX 3.0 and to micaSense images, in that order, in despite of the identical pixel size. Different degrees of sub-pixel details contributed to the aggregation due to different spatial resolution and flight altitudes of micaSense and PanX 3.0. Thus, a larger number of micaSense pixels in contrast to a smaller number of PanX 3.0 pixels contributed more spatial information. Differences in spatial details cause varying spectral information in aggregated pixels and need to be considered when investigating NDVI across platforms (Imran et al., 2021). Furthermore, the spatial response function of a Sentinel-2 pixel was assumed flat during sub-pixel aggregation as a simplification. Instead, the true spatial response function is more complex. Changing spatial response function characteristics also affect the comparison of NDVI across different sensors and demonstrate inherent biases due to the spatial response function (Inamdar et al., 2020). A Gaussian spatial response contributes usually blurring effects to the image. A deconvolution of spatial response of the high-resolution sub-pixels followed by a convolution with spatial response of the low-resolution super-pixel would yield the most accurate representation. However, this convolution was not possible since the true spatial response functions were not known. In absence of the actual Sentinel-2 point-spread function, the simplified, box-like behavior was assumed to aggregate the high-resolution data, which must be considered a potential source of error. However, regression results suggested a good agreement of pixel-based NDVI from micaSense and a very good agreement of pixel-based NDVI from PanX 3.0 with Sentinel-2 NDVI. Even though the spectral configuration of the micaSense bands was more similar to the Sentinel-2 bands (D'Odorico et al., 2013), a better agreement in NDVI was observed in PanX 3.0 data. Our findings suggest that similar spatio-geometric characteristics of flight altitude and poorer spatial resolution outweigh spectral-optical similarity of the bands used to compute NDVI in this comparison. Very high spatial resolution of the drone-based NDVI product was not beneficial and introduced random errors when compared with the satellite scale. Considering the lower degree of detail in spatial information from the satellite, a much higher degree of vegetation diversity and soil could be observed from gyrocopter and the drone (Feilhauer et al., 2012; Viscarra Rossel et al., 2016; Zhao et al., 2019). Furthermore, the difference in time between satellite, gyrocopter and drone overpass has to be considered. Similar limitations related to atmospheric distortion, instrument handling, BRDF, structural

geometry, shading and optical assumptions apply as discussed above. In addition, the sensors' point spread functions determine the depiction of objects and influence the results as such (Hueni et al., 2017). Nevertheless, the corrected multispectral images acquired from drone and gyrocopter allow deriving NDVI as a comparable remote sensing product, which was successfully validated against the satellite.

6.6 Conclusion

Consistency of reflectance measurements from two airborne camera systems, field spectrometer and Sentinel-2 BOA reflectance was investigated, using an ELC approach and additional, continuous irradiance correction. A mobile field spectrometer setup was validated against Sentiel-2 in the first place, enabling its use as transfer instrument to combine all four scales with respect to a widely available, reliable and well-defined reference. Applying ELC based on in-field calibration using a nine-panel grey-scale improved reproducibility of the target's spectral shapes and coherency of the reflectance data from the three sensor platforms on the ground, on the drone and on the gyrocopter with respect to the satellite. Additional correction of airborne reflectance using continuous monitoring of down-welling light on the ground further improved the agreement between the three sensor systems. Our results from drone and gyrocopter showed a striking difference between raw reflectance values before and after applying in-field ELC and additional CIC, which were associated mainly with biases from calibrating the mounted cameras using a reference panel prior to the flight. Thus, corrected and resampled NDVI maps from drone and gyrocopter agreed to 89% and 95% with Sentinel-2 NDVI, indicating a successful transfer of information across four remote sensing scales. Uncertainties related to optical characteristics, BRDF, calibration and handling of the instrument contributed to reflectance outliers, resulting in a median discrepancy below 10% between airborne camera reflectance and ground reference. Further investigations of those uncertainties across multiple locations or times is required towards enabling potential correction approaches. As a prerequisite, valid cross-calibration between the up-welling and down-welling channel of the RoX is essential. To ensure a valid and reproducible ground reference, reflectance readings were validated using Sentinel-2 BOA reflectance over homogenous targets and adjusted accordingly. In addition, we recommend the use of a standardized white reference for validation of the ground reference for future efforts. Furthermore, measurement errors from handling of the instruments in rough field conditions affected the results. Inherent systematic and random uncertainties of hyperspectral field spectrometer measurements on the ground as well as of airborne, multispectral images did not allow for a general correction for other missions. In consequence, a solid ground reference is required for each mission to provide an accurate reference. Continuously monitoring the actual field conditions enabled the transfer of multispectral information from satellite to ground and airborne sensors.

Finally, in-situ calibration and continuous irradiance correction of multispectral reflectance from airborne camera systems using grey-scales in combination with ground measurements is highly recommended to substantially increase coherence in the recorded data across different levels. It is advisable to consider the potential of field spectrometers for ground referencing and as transfer instruments when planning future remote sensing missions that involve different sensors, platforms and scales. Creating coherent datasets is at the basis for further attempts towards sensor fusion, temporal and spatial analyses, classification, mapping and change detection across multiple scales from ground to satellite.

6.7 Acknowledgement

We thank Katharina Fricke, Svenja Wick and Laura Giese for supporting the project. This work was supported in part by the Federal Ministry of Transport and Digital Infrastructure through the joint research project “mDRONES4rivers” in mFUND – BMVI (19F2054A-D)

7 Overarching conclusion

This thesis presented four studies, of which each provided a conclusion in their own realm. However, this chapter identifies common aspects of conclusion beyond the individual aspects of each study in the total context of this thesis. Emphasis was placed on (1) the joint application of different optical sensors using different measurement protocols, (2) the standardization of data processing chains including propagation of uncertainties and (3) the reduction of signal biases in the final data product. Point (1) was addressed by applying automated field spectrometers and recognizing their potential as transfer instruments for harmonizing data products across multiple different optical sensors and platforms. Point (2) was addressed by determining the radiometric uncertainties of the measured radiance and considering this in the final product by means of mechanistic propagation rules or included in training data of ML retrieval approaches. However, radiometric uncertainties were also recognized as a very partial aspect of the total uncertainty budget in the data products. Other dependent, systematic and random influences needed further consideration and exceeded effects of radiometric uncertainties by orders of magnitude in reflectance and simple VIs, while the effect of radiometric uncertainty in SIF was significant. Point (3) addressed the systematic influences on the data products, which were quantifiable and corrected either by avoiding distorted retrieval mechanisms or by applying a validation and correction approach with respect to a trusted reference using proximity sensing. Furthermore, independent training and testing data was a central aspect for

cross-validation and post-validation of ML approaches in the presented studies, due to ML algorithm results being profoundly determined by their underlying data.

We developed an ML-based SIF retrieval, which included the radiometric uncertainties of the FloX in operational conditions into a semi-synthetic training data set. Furthermore, this new retrieval method exploited SFL instead of telluric oxygen absorption features to retrieve SIF unaffected by atmospheric reabsorption. Nevertheless, the presented PLS approach was capable of retrieving the SIF signal from SFL within the FLEX mission requirements, yielding radiometric uncertainties around 0.1 mW m^{-2} sr^{-1} nm^{-1} both in the red SIF and in the far-red SIF with operational SNR around 390 and 800, respectively. The PLS uncertainty was determined and compared with other retrieval methods in Study 1, showing a significant increase in precision over the SVD exploiting SFL. For reference, the mathematical propagation of radiometric uncertainties of the iFLD-retrieval exploiting oxygen absorption band was demonstrated using operational SNR, resulting in the red and far-red around 0.13 - 0.16 mW m^{-2} sr^{-1} nm^{-1} uncertainty respectively. In contrast to the negligible effect on VIs or reflectance products, SNR was identified as a significant constraint for SIF retrievals. However, SNR values reflect only the influence of the radiometric noise and cannot account for other sources of uncertainties. The presented retrieval of SIF from SFL was challenged furthermore by the spectral resolution around 0.3 nm FWHM, which was on the edge of accurately determining the depth of the SFL. The employed PLS algorithm addressed the issue using a much larger spectral window compared with previous studies and exploited more, spectral information. Finally, surrogate dependencies required considering a specific design of using training data, cross-validation scheme and independent testing data. A direct validation of SIF was challenging, as the scaling to the canopy would involve very complex considerations about the intra-canopy scattering, reabsorption and anisotropic distribution of the escape probabilities. This allowed only an indirect validation in measured data, e.g. with respect to other mechanistic retrieval methods to identify systematic and dependent uncertainties influencing the results of the ML-based retrieval. Thus, efforts were made towards minimizing the systematic errors by adjusting the dedicated model training procedures and training data, and minimizing the random uncertainties by using sufficient repetitions. Case study 2 demonstrated the application of ML in investigating the retrieval of NOx concentration in the air from continuous time-series of hyperspectral, down-welling radiance. Three different ML algorithms were employed and covariations in dense time-series of down-welling radiance investigated with respect to a significant decrease in NOx concentration reported by an independent NOx sensor station on the ground following the COVID-19 lock-down. While a conditional inference tree classified a binary, nominal differentiation of NOx levels before and after the COVID-19 lock-down successfully, a decision tree using principal components was able to distinguish discrete scale levels of the NOx concentration. Eventually, the PLS regression model allowed the retrieval of NOx values at the most differentiated ratio. While the levels

of differentiability increased with the complexity of the model, also a larger amount of hyperspectral dimensions was required to build the models. Thus, the uncertainty of the final products increased due to including also more un-correlated uncertainties. This trade-off between graduation and confidence presented a typical limitation of the ML algorithms, fundamentally caused by the propagation of uncertainties. In case study 2, this issue was address by monitoring uncertainties using the errors of prediction during the training and independent cross-validation processes of the models with respect to the independent gas measurements.

The propagation of uncertainties needed further consideration also for the in-field validation and calibration of reflectance across multiple remote sensing platforms. Fundamentally, the amount of light received at the sensor together with its sensitivity determined the physical limit of detection for each measurement. Integration time being on the one hand side and spectral-spatial resolution on the other side, a trade-off is required for each sensor to be balanced for its specific application. Stationary, automated field spectrometers are less constrained e.g. to allow longer integration times, which made them suitable for reference measurements to calibrate and validate imaging sensors. However, the growing number of automated field spectrometers and use cases required consistent and harmonized data products, while full traceability back to the international standard was not always feasible to obtain. Assuming Sentinel-2 satellites as well calibrated and stable, long time-series of hyperspectral reflectance recorded by 10 automated field spectrometers around the world were harmonized in the enabling study 3 in this thesis. The presented study investigated temporal and spatial aspects of uncertainties in bottom-of-atmosphere reflectance and recognized seasonal changes in the spatial representativeness of the spectrometer footprint comparing ground and satellite measurements. Therefore, seasonal dynamics in vegetation and landscape heterogeneity as well as short-term events, e.g. cloud formation, were shown to outweigh radiometric uncertainties by orders of magnitude in the uncertainty budget of proximally sensed reflectance. The introduced cloud filtering approach based on continuously ground-measured down-welling radiance detected clouds more effectively and minimized the associated uncertainties of the reflectance products across platforms. Finally, case study 4 revealed temporally mismatching reflectance calibration with respect to a grey-card calibration in the field causing significant errors between the two examined airborne sensors. Continuous down-welling radiance measurements on the ground successfully corrected airborne reflectance considering variations of incoming light. Consecutively, the reflectance readings of the field spectrometer were calibrated over a large, homogenous area against Sentinel-2 bottom of atmosphere reflectance, as previously demonstrated by enabling study 3. Thus, the ground reference enabled the transfer of the reflectance calibration from the satellite to two airborne sensors using a ground-measured reflectance gradient over artificial panels in the field in the second step. The presented two-step approach significantly improved the agreement of the two airborne imaging sensors with each other and with

Sentinel-2, while reducing uncertainties around the spatial representativeness and dependent errors from temporal fluctuation of received radiation at the bottom of the atmosphere. Furthermore, the results implied a fusion of the multispectral data from a radiometric perspective. The approach was limited by propagating the total random uncertainties of the ground-measurements and satellite reflectance into all airborne measurements. This issue was addressed by using many repetitions, validating the ground-measured reflectance against Sentinel-2 across multiple ground sampling points and several repetition in each over a homogenous area. Still, random uncertainties remained around the representativeness of the various pixel sizes and spectrometer footprint, and were quantified for the airborne reflectance data using the relative difference of pixels inside the footprint of each ground sampling point.

Ideally, a consistent tracking of uncertainties in meta-data alongside the retrieval of higher data products enables full traceability with respect to the international standard. However, such traceability was not always possible due to technical or economical aspects. Our results demonstrated that uncertainties of spatial representativeness, atmospheric influences and dependent errors exceed random radiometric uncertainties by orders of magnitudes for reflectance and simple VI products measured with FloX/RoX. However, random radiometric uncertainties were relevant for SIF retrievals and for machine-learning models to exploit effectively proximally sensed hyperspectral data. Those results suggested to include operational, quantitative uncertainties during supervised cross-validation and model testing approaches for obtaining precise results. In the age of big-data, fusion of information across different optical sensor allows an unprecedented combination of information details for the investigation of ecosystems. Future research unifying data from multiple optical sensors and retrieving data products for holistic ecosystem monitoring will benefit from standardized, automated field spectrometer measurements on the ground. Consequently, the results also emphasized a continued need for quantifying, minimizing and tracking random, systematic and dependent uncertainties from the input data, which propagate into the specific uncertainties of the data products.

8 List of peer-reviewed publications

8.1 Integral part of dissertation

Naethe, P., De Sanctis, A., Burkart, A., Campbell, P.K.E., Colombo, R., Di Mauro, B., Damm, A., El-Madany, T., Fava, F., Gamon, J.A., Huemmrich, K.F., Migliavacca, M., Paul-Limoges, E., Rascher, U., Rossini, M., Schüttemeyer, D., Tagliabue, G., Zhang, Y., Julitta, T., 2024. Towards a standardized, ground-based network of hyperspectral measurements: Combining time series from autonomous field spectrometers with Sentinel-2. Remote Sens. Environ. 303, 114013. https://doi.org/10.1016/j.rse.2024.114013

Own contribution: Conceptualization – 50%, Measurements – 10%, Analysis – 20%, Interpretation – 90%, Writing - 90%

Naethe, P., Asgari, M., Kneer, C., Knieps, M., Jenal, A., Weber, I., Moelter, T., Dzunic, F., Deffert, P., Rommel, E., Delaney, M., Baschek, B., Rock, G., Bongartz, J., Burkart, A., 2023. Calibration and Validation from Ground to Airborne and Satellite Level: Joint Application of Time-Synchronous Field Spectroscopy, Drone, Aircraft and Sentinel-2 Imaging. PFG – J. Photogramm. Remote Sens. Geoinf. Sci. https://doi.org/10.1007/s41064-022-00231-x

Own contribution: Conceptualization – 50%, Measurements – 30%, Analysis – 90%, Interpretation – 100%, Writing - 85%

Naethe, P., Julitta, T., Chang, C.Y.Y., Burkart, A., Migliavacca, M., Guanter, L., Rascher, U., 2022. A precise method unaffected by atmospheric reabsorption for ground-based retrieval of red and far-red sun-induced chlorophyll fluorescence. Agric. For. Meteorol. 325. https://doi.org/10.1016/j.agrformet.2022.109152

Own contribution: Conceptualization – 90%, Measurements – 20%, Analysis – 100%, Interpretation – 100%, Writing - 95%

Naethe, P., Delaney, M., Julitta, T., 2020. Changes of NOx in urban air detected with monitoring VIS-NIR field spectrometer during the coronavirus pandemic: A case study in Germany. Sci. Total Environ. 748, 141286. https://doi.org/10.1016/j.scitotenv.2020.141286

Own contribution: Conceptualization – 90%, Measurements – 100%, Analysis – 100%, Interpretation – 90%, Writing - 95%

8.2 Additional, co-authored publications

Rommel, E., Giese, L., Fricke, K., Kathöfer, F., Heuner, M., Mölter, T., Deffert, P., Asgari, M., **Näthe, P.**, Dzunic, F., Rock, G., Bongartz, J., Burkart, A., Quick, I., Schröder, U., Baschek, B., 2022. Very High-Resolution Imagery and Machine Learning for Detailed Mapping of Riparian Vegetation and Substrate Types. Remote Sens. 14, 954. https://doi.org/10.3390/rs14040954

Burkart, A., Kennedy, M., **Näthe, P.**, Julitta, T., 2022. Iterative design of a high light throughput cosine receptor fore optic for unattended proximal remote sensing. SPIE J. Appl. Remote Sens. 16, 1–9. https://doi.org/10.1117/1.JRS.16.044513

Chang, C.Y.-Y., Wen, J., Han, J., Kira, O., Levonne, J., Melkonian, J., Riha, S.J., Skovira, J., Ng, S., Gu, L., Wood, J.D., **Näthe, P.**, Sun, Y., 2021. Unpacking the drivers of diurnal dynamics of sun-induced chlorophyll fluorescence (SIF): Canopy structure, plant physiology, instrument configuration and retrieval methods. Remote Sens. Environ. 265, 112672. https://doi.org/10.1016/j.rse.2021.112672

9 References

Aasen, H., Bolten, A., 2018. Multi-temporal high-resolution imaging spectroscopy with hyperspectral 2D imagers – From theory to application. Remote Sens. Environ. 205, 374–389. https://doi.org/10.1016/j.rse.2017.10.043

Aasen, H., Honkavaara, E., Lucieer, A., Zarco-Tejada, P.J., 2018. Quantitative remote sensing at ultra-high resolution with UAV spectroscopy: A review of sensor technology, measurement procedures, and data correctionworkflows. Remote Sens. https://doi.org/10.3390/rs10071091

Aasen, H., Van Wittenberghe, S., Medina, N.S., Damm, A., Goulas, Y., Wieneke, S., Hueni, A., Malenovský, Z., Alonso, L., Pacheco-Labrador, J., Cendrero-Mateo, M.P., Tomelleri, E., Burkart, A., Cogliati, S., Rascher, U., Arthur, A. Mac, 2019. Sun-induced chlorophyll fluorescence II: Review of passive measurement setups, protocols, and their application at the leaf to canopy level. Remote Sens. https://doi.org/10.3390/rs11080956

Abdi, H., 2010. Partial least squares regression and projection on latent structure regression (PLS Regression). Wiley Interdiscip. Rev. Comput. Stat. 2, 97–106. https://doi.org/10.1002/wics.51

Acebron, K., Matsubara, S., Jedmowski, C., Emin, D., Muller, O., Rascher, U., 2021. Diurnal dynamics of nonphotochemical quenching in Arabidopsis npq mutants assessed by solar-induced fluorescence and reflectance measurements in the field. New Phytol. 229, 2104–2119. https://doi.org/10.1111/nph.16984

Adler-Golden, S.M., Matthew, M.W., Anderson, G.P., Felde, G.W., Gardner, J.A., 2002. Algorithm for de-shadowing spectral imagery 203. https://doi.org/10.1117/12.451691

Agapiou, A., Hadjimitsis, D., Sarris, A., Themistocleous, K., Papadavid, G., 2010. Hyperspectral ground truth data for the detection of buried architectural remains, in: Lecture Notes in Computer Science (Including Subseries Lecture Notes in Artificial Intelligence and Lecture Notes in Bioinformatics). pp. 318–331. https://doi.org/10.1007/978-3-642-16873-4_24

Agati, G., Mazzinghi, P., Fusi, F., Ambrosini, I., 1995. The F685/F730 Chlorophyll Fluorescence Ratio as a Tool in Plant Physiology: Response to Physiological and Environmental Factors*. J. Plant Physiol. https://doi.org/10.1016/S0176-1617(11)81882-1

Aghabozorgi, S., Seyed Shirkhorshidi, A., Ying Wah, T., 2015. Time-series clustering – A decade review. Inf. Syst. 53, 16–38. https://doi.org/https://doi.org/10.1016/j.is.2015.04.007

Al-Rawabdeh, A., Moussa, A., Foroutan, M., El-Sheimy, N., Habib, A., 2017. Time series UAV image-based point clouds for landslide progression evaluation applications. Sensors (Switzerland) 17.

https://doi.org/10.3390/s17102378

Alberton, B., Torres, R. da S., Cancian, L.F., Borges, B.D., Almeida, J., Mariano, G.C., Santos, J. dos, Morellato, L.P.C., 2017. Introducing digital cameras to monitor plant phenology in the tropics: applications for conservation. Perspect. Ecol. Conserv. 15, 82–90. https://doi.org/10.1016/J.PECON.2017.06.004

Alonso, L., Gómez-Chova, L., Vila-Francés, J., Amorós-López, J., Guanter, L., Calpe, J., Moreno, J., 2008. Improved fraunhofer line discrimination method for vegetation fluorescence quantification. IEEE Geosci. Remote Sens. Lett. 5, 620–624. https://doi.org/10.1109/LGRS.2008.2001180

Alonso, L., Van Wittenberghe, S., Amorós-López, J., Vila-Francés, J., Gómez-Chova, L., Moreno, J., 2017. Diurnal cycle relationships between passive fluorescence, PRI and NPQ of vegetation in a controlled stress experiment. Remote Sens. 9. https://doi.org/10.3390/rs9080770

Ariza, A., Robredo Irizar, M., Bayer, S., 2018. Empirical line model for the atmospheric correction of sentinel-2A MSI images in the Caribbean Islands. Eur. J. Remote Sens. 51, 765–776. https://doi.org/10.1080/22797254.2018.1482732

Bador, M., Naveau, P., Gilleland, E., Castellà, M., Arivelo, T., 2015. Spatial clustering of summer temperature maxima from the CNRM-CM5 climate model ensembles & E-OBS over Europe. Weather Clim. Extrem. 9, 17–24. https://doi.org/10.1016/j.wace.2015.05.003

Baetens, L., Desjardins, C., Hagolle, O., 2019. Validation of Copernicus Sentinel-2 Cloud Masks Obtained from MAJA, Sen2Cor, and FMask Processors Using Reference Cloud Masks Generated with a Supervised Active Learning Procedure. Remote Sens. 11, 433. https://doi.org/10.3390/rs11040433

Baeumker, M., Przybilla, Heinz-Jürgen, Bäumker, M., Przybilla, Heinz-Juergen, Manfred, B., 2020. RTK and PPK: GNSS-Technologies for direct georeferencing of UAV image flights, in: FIG Working Week 2020 Smart Surveyors for Land and Water Management Amsterdam, the Netherlands, 10–14 May.

Baldocchi, D., 2014. Measuring fluxes of trace gases and energy between ecosystems and the atmosphere - the state and future of the eddy covariance method. Glob. Chang. Biol. 20, 3600–3609. https://doi.org/10.1111/gcb.12649

Ball, C.P., Marks, A.A., Green, P.D., MacArthur, A., Maturilli, M., Fox, N.P., King, M.D., 2015. Hemispherical-Directional Reflectance (HDRF) of Windblown Snow-Covered Arctic Tundra at Large Solar Zenith Angles. IEEE Trans. Geosci. Remote Sens. 53, 5377–5387. https://doi.org/10.1109/TGRS.2015.2421733

Banerjee, A., Merugu, S., Dhillon, I.S., Ghosh, J., 2005. Clustering with Bregman Divergences. J. Mach. Learn. Res. 6, 1705–1749. https://doi.org/10.1007/s10994-005-5825-6

Barnes, R.A., Barnes, W.L., Lyu, C.-H., Gales, J.M., 2000. An Overview of the Visible and Infrared Scanner Radiometric Calibration Algorithm. J. Atmos. Ocean. Technol. 390–405.

Beer, C., Reichstein, M., Tomelleri, E., Ciais, P., Jung, M., Carvalhais, N., Rodenbeck, C., Arain, M.A., Baldocchi, D., Bonan, G.B., Bondeau, A., Cescatti, A., Lasslop, G., Lindroth, A., Lomas, M., Luyssaert, S., Margolis, H., Oleson, K.W., Roupsard, O., Veenendaal, E., Viovy, N., Williams, C., Woodward, F.I., Papale, D., 2010. Terrestrial Gross Carbon Dioxide Uptake: Global Distribution and Covariation with Climate. Science (80-.). 329, 834–838. https://doi.org/10.1126/science.1184984

Bendig, J., Malenovsky, Z., Gautam, D., Lucieer, A., 2019. Solar-Induced Chlorophyll Fluorescence Measured From an Unmanned Aircraft System: Sensor Etaloning and Platform Motion Correction. IEEE Trans. Geosci. Remote Sens. 1–8. https://doi.org/10.1109/TGRS.2019.2956194

Benoudjit, N., Melgani, F., Bouzgou, H., 2009. Multiple regression systems for spectrophotometric data analysis. Chemom. Intell. Lab. Syst. 95, 144–149. https://doi.org/10.1016/j.chemolab.2008.10.001

Berger, K., Machwitz, M., Kycko, M., Kefauver, S.C., Van Wittenberghe, S., Gerhards, M., Verrelst, J., Atzberger, C., van der Tol, C., Damm, A., Rascher, U., Herrmann, I., Paz, V.S., Fahrner, S., Pieruschka, R., Prikaziuk, E., Buchaillot, M.L., Halabuk, A., Celesti, M., Koren, G., Gormus, E.T., Rossini, M., Foerster, M., Siegmann, B., Abdelbaki, A., Tagliabue, G., Hank, T., Darvishzadeh, R., Aasen, H., Garcia, M., Pôças, I., Bandopadhyay, S., Sulis, M., Tomelleri, E., Rozenstein, O., Filchev, L., Stancile, G., Schlerf, M., 2022. Multi-sensor spectral synergies for crop stress detection and monitoring in the optical domain: A review. Remote Sens. Environ. https://doi.org/10.1016/j.rse.2022.113198

Berger, K., Verrelst, J., Féret, J.-B., Hank, T., Wocher, M., Mauser, W., Camps-Valls, G., 2020. Retrieval of aboveground crop nitrogen content with a hybrid machine learning method. Int. J. Appl. Earth Obs. Geoinf. 92, 102174. https://doi.org/10.1016/j.jag.2020.102174

Berk, A., Bernstein, L.S., Anderson, G.P., Acharya, P.K., Robertson, D.C., Chetwynd, J.H., Adler-Golden, S.M., 1998. MODTRAN cloud and multiple scattering upgrades with application to AVIRIS. Remote Sens. Environ. 65, 367–375. https://doi.org/10.1016/S0034-4257(98)00045-5

Berni, J.A.J., Zarco-Tejada, P.J., Suárez, L., Fereres, E., 2009. Thermal and narrowband multispectral remote sensing for vegetation monitoring from an unmanned aerial vehicle. IEEE Trans. Geosci.

Remote Sens. 47, 722–738. https://doi.org/10.1109/TGRS.2008.2010457

Bertolli, S.C., Mazzafera, P., Souza, G.M., 2013. Why is it so difficult to identify a single indicator of water stress in plants? A proposal for a multivariate analysis to assess emergent properties. plant Biol. 1–8. https://doi.org/10.1111/plb.12088

Biagioni, D.J., Astling, D.P., Graf, P., Davis, M.F., 2011. Orthogonal projection to latent structures solution properties for chemometrics and systems biology data. J. Chemom. 25, 514–525. https://doi.org/10.1002/cem.1398

Białek, A., Goodman, T., Woolliams, E., Brachmann, J.F., Schwarzmaier, T., Kuusk, J., Ansko, I., Vabson, V., Lau, I.C., MacLellan, C., Marty, S., Ondrusek, M., Servantes, W., Taylor, S., Dommelen, R. Van, Barnard, A., Vellucci, V., Banks, A.C., Fox, N., Vendt, R., Donlon, C., Casal, T., 2020. Results from verification of reference irradiance and radiance sources laboratory calibration experiment campaign. Remote Sens. 12. https://doi.org/10.3390/rs12142220

Biancolillo, A., Marini, F., 2018. Chemometric Methods for Spectroscopy-Based Pharmaceutical Analysis. Front. Chem. 6, 576. https://doi.org/10.3389/fchem.2018.00576

Biggar, S.F., Thome, K.J., Wisniewski, W., 2003. Vicarious radiometric calibration of EO-1 sensors by reference to high-reflectance ground targets. IEEE Trans. Geosci. Remote Sens. 41, 1174–1179. https://doi.org/10.1109/TGRS.2003.813211

Bioucas-Dias, J.M., Plaza, A., Camps-Valls, G., Scheunders, P., Nasrabadi, N., Chanussot, J., 2013. Hyperspectral Remote Sensing Data Analysis and Future Challenges. IEEE Geosci. Remote Sens. Mag. 1, 6–36. https://doi.org/10.1109/MGRS.2013.2244672

Biriukova, K., Celesti, M., Evdokimov, A., Pacheco-Labrador, J., Julitta, T., Migliavacca, M., Giardino, C., Miglietta, F., Colombo, R., Panigada, C., Rossini, M., 2020. Effects of varying solar-view geometry and canopy structure on solar-induced chlorophyll fluorescence and PRI. Int. J. Appl. Earth Obs. Geoinf. 89, 102069. https://doi.org/10.1016/j.jag.2020.102069

Blair, J., Nippert, J., Briggs, J., 2014. Grassland ecology, in: Ecology and the Environment. https://doi.org/10.1007/978-1-4614-7501-9_14

Bouvet, M., Thome, K., Berthelot, B., Bialek, A., Czapla-Myers, J., Fox, N.P., Goryl, P., Henry, P., Ma, L., Marcq, S., Meygret, A., Wenny, B.N., Woolliams, E.R., 2019. RadCalNet: A radiometric calibration network for earth observing imagers operating in the visible to shortwave infrared spectral range. Remote Sens. 11. https://doi.org/10.3390/rs11202401

Boyle, J., 2013. Biology must develop its own big-data systems. Nature.

https://doi.org/10.1038/499007a

Brault, J., Neckel, H., 1999. Announcement SPECTRAL ATLAS OF SOLAR ABSOLUTE DISK-AVERAGED AND DISK-CENTER INTENSITY FROM 3290 TO 12510 Å (Brault and Neckel, 1987) NOW AVAILABLE FROM HAMBURG OBSERVATORY ANONYMOUS FTP SITE. Sol. Phys. 184, 421–421. https://doi.org/10.1023/A:1017165208013

Buman, B., Hueni, A., Colombo, R., Cogliati, S., Celesti, M., Julitta, T., Burkart, A., Siegmann, B., Rascher, U., Drusch, M., Damm, A., 2022. Towards consistent assessments of in situ radiometric measurements for the validation of fluorescence satellite missions. Remote Sens. Environ. 274. https://doi.org/10.1016/j.rse.2022.112984

Burkart, A., Aasen, H., Alonso, L., Menz, G., Bareth, G., Rascher, U., 2015a. Angular dependency of hyperspectral measurements over wheat characterized by a novel UAV based goniometer. Remote Sens. 7, 725–746. https://doi.org/10.3390/rs70100725

Burkart, A., Cogliati, S., Schickling, A., Rascher, U., 2014. A novel UAV-Based ultra-light weight spectrometer for field spectroscopy. IEEE Sens. J. 14, 62–67. https://doi.org/10.1109/JSEN.2013.2279720

Burkart, A., Kennedy, M., Näthe, P., Julitta, T., 2022. Iterative design of a high light throughput cosine receptor fore optic for unattended proximal remote sensing. SPIE J. Appl. Remote Sens. 16, 1–9. https://doi.org/10.1117/1.JRS.16.044513

Burkart, A., Schickling, A., Mateo, M.P.C., Wrobel, T.J., Rossini, M., Cogliati, S., Julitta, T., Rascher, U., 2015b. A Method for Uncertainty Assessment of Passive Sun-Induced Chlorophyll Fluorescence Retrieval Using an Infrared Reference Light. IEEE Sens. J. 15. https://doi.org/10.1109/JSEN.2015.2422894

Burnett, A.C., Anderson, J., Davidson, K.J., Ely, K.S., Lamour, J., Li, Q., Morrison, B.D., Yang, D., Rogers, A., Serbin, S.P., 2021. A best-practice guide to predicting plant traits from leaf-level hyperspectral data using partial least squares regression. J. Exp. Bot. 72, 6175–6189. https://doi.org/10.1093/jxb/erab295

Caballero, I., Fernández, R., Escalante, O.M., Mamán, L., Navarro, G., 2020. New capabilities of Sentinel-2A/B satellites combined with in situ data for monitoring small harmful algal blooms in complex coastal waters. Sci. Rep. 10, 1–14. https://doi.org/10.1038/s41598-020-65600-1

Camino, C., Zarco-Tejada, P.J., Gonzalez-Dugo, V., 2018. Effects of heterogeneity within tree crowns on airborne-quantified SIF and the CWSI as indicators of water stress in the context of precision agriculture. Remote Sens. 10. https://doi.org/10.3390/rs10040604

Campbell, P.K.E., Huemmrich, K., Middleton, E., Ward, L., Julitta, T., Daughtry, C., Burkart, A., Russ, A., Kustas, W., 2019. Diurnal and Seasonal Variations in Chlorophyll Fluorescence Associated with Photosynthesis at Leaf and Canopy Scales. Remote Sens. 11, 488. https://doi.org/10.3390/rs11050488

Campbell, P.K.E., Middleton, E.M., Van Der Tol, C., Huemmrich, K.F., Cendrero-Mateo, M.P., Corp, L.A., Leifeld, J.K., 2014. DIURNAL AND PHENOLOGICAL CHANGES IN VEGETATION FLUORESCENCE AND REFLECTANCE , INDICATIVE OF VEGETATION PHOTOSYNTHETIC PROPERTIES AND FUNCTION, in: 5th International Workshop on Remote Sensing of Vegetation Fluorescence. PARIS (FRANCE), pp. 1–8.

Caporaso, N., Whitworth, M.B., Grebby, S., Fisk, I.D., 2018. Rapid prediction of single green coffee bean moisture and lipid content by hyperspectral imaging. J. Food Eng. 227, 18–29. https://doi.org/10.1016/j.jfoodeng.2018.01.009

Castro-Esau, K.L., Sánchez-Azofeifa, G.A., Rivard, B., 2006. Comparison of spectral indices obtained using multiple spectroradiometers. Remote Sens. Environ. 103, 276–288. https://doi.org/10.1016/j.rse.2005.01.019

Cavender-Bares, J., Gamon, J.A., Townsend, P.A., 2020. Remote Sensing of Plant Biodiversity. Springer Open. https://doi.org/https://doi.org/10.1007/978-3-030-33157-3

Cavender-Bares, J., Meireles, J., Couture, J., Kaproth, M., Kingdon, C., Singh, A., Serbin, S., Center, A., Zuniga, E., Pilz, G., Townsend, P., 2016. Associations of Leaf Spectra with Genetic and Phylogenetic Variation in Oaks: Prospects for Remote Detection of Biodiversity. Remote Sens. 8, 221. https://doi.org/10.3390/rs8030221

Cendrero-Mateo, M.P., Moran, M.S., Papuga, S.A., Thorp, K.R., Alonso, L., Moreno, J., Ponce-Campos, G., Rascher, U., Wang, G., 2016. Plant chlorophyll fluorescence: active and passive measurements at canopy and leaf scales with different nitrogen treatments. J. Exp. Bot. 67, 275–286. https://doi.org/10.1093/jxb/erv456

Cendrero-Mateo, M.P., Wieneke, S., Damm, A., Alonso, L., Pinto, F., Moreno, J., Guanter, L., Celesti, M., Rossini, M., Sabater, N., Cogliati, S., Julitta, T., Rascher, U., Goulas, Y., Aasen, H., Pacheco-Labrador, J., Arthur, A. Mac, 2019. Sun-induced chlorophyll fluorescence III: Benchmarking retrieval methods and sensor characteristics for proximal sensing. Remote Sens. 11. https://doi.org/10.3390/rs11080921

Chang, C.Y.-Y., Guanter, L., Frankenberg, C., Köhler, P., Gu, L., Magney, T.S., Grossmann, K., Sun, Y., 2020a. Systematic assessment of retrieval methods for canopy far-red solar-induced chlorophyll

fluorescence (SIF) using high-frequency automated field spectroscopy. J. Geophys. Res. Biogeosciences. https://doi.org/10.1029/2019jg005533

Chang, C.Y.-Y., Wen, J., Han, J., Kira, O., Levonne, J., Melkonian, J., Riha, S.J., Skovira, J., Ng, S., Gu, L., Wood, J.D., Näthe, P., Sun, Y., 2021. Unpacking the drivers of diurnal dynamics of sun-induced chlorophyll fluorescence (SIF): Canopy structure, plant physiology, instrument configuration and retrieval methods. Remote Sens. Environ. 265, 112672. https://doi.org/10.1016/j.rse.2021.112672

Chang, C.Y.-Y., Zhou, R., Kira, O., Marri, S., Skovira, J., Gu, L., Sun, Y., 2020b. An Unmanned Aerial System (UAS) for concurrent measurements of solar-induced chlorophyll fluorescence and hyperspectral reflectance toward improving crop monitoring. Agric. For. Meteorol. 294, 108145. https://doi.org/10.1016/j.agrformet.2020.108145

Chapman, J.W., Thompson, D.R., Helmlinger, M.C., Bue, B.D., Green, R.O., Eastwood, M.L., Geier, S., Olson-Duvall, W., Lundeen, S.R., 2019. Spectral and radiometric calibration of the Next Generation Airborne Visible Infrared Spectrometer (AVIRIS-NG). Remote Sens. 11. https://doi.org/10.3390/rs11182129

Cheng, Y., Gamon, J.A., Fuentes, D.A., Mao, Z., Sims, D.A., Qiu, H. lie, Claudio, H., Huete, A., Rahman, A.F., 2006. A multi-scale analysis of dynamic optical signals in a Southern California chaparral ecosystem: A comparison of field, AVIRIS and MODIS data. Remote Sens. Environ. 103, 369–378. https://doi.org/10.1016/j.rse.2005.06.013

Coccia, M., 2020a. How High Wind Speed Can Reduce Negative Effects of Confirmed Cases and Total Deaths of COVID-19 Infection in Society. SSRN Electron. J. https://doi.org/10.2139/ssrn.3603380

Coccia, M., 2020b. Factors determining the diffusion of COVID-19 and suggested strategy to prevent future accelerated viral infectivity similar to COVID. Sci. Total Environ. 729, 138474. https://doi.org/10.1016/j.scitotenv.2020.138474

Cogliati, S., Celesti, M., Cesana, I., Miglietta, F., Genesio, L., Julitta, T., Schuettemeyer, D., Drusch, M., Rascher, U., Jurado, P., Colombo, R., 2019. A Spectral Fitting Algorithm to Retrieve the Fluorescence Spectrum from Canopy Radiance. Remote Sens. 11, 1840. https://doi.org/10.3390/rs11161840

Cogliati, S., Rossini, M., Julitta, T., Meroni, M., Schickling, A., Burkart, A., Pinto, F., Rascher, U., Colombo, R., 2015a. Continuous and long-term measurements of reflectance and sun-induced chlorophyll fluorescence by using novel automated field spectroscopy systems. Remote Sens. Environ. 164, 270–281. https://doi.org/10.1016/j.rse.2015.03.027

Cogliati, S., Verhoef, W., Kraft, S., Sabater, N., Alonso, L., Vicent, J., Moreno, J., Drusch, M., Colombo, R., 2015b. Retrieval of sun-induced fluorescence using advanced spectral fitting methods. Remote Sens. Environ. 169, 344–357. https://doi.org/10.1016/J.RSE.2015.08.022

Congedo, L., 2021. Semi-Automatic Classification Plugin: A Python tool for the download and processing of remote sensing images in QGIS. J. Open Source Softw. 6, 3172. https://doi.org/10.21105/joss.03172

Cracknell, A.P., 2018. The development of remote sensing in the last 40 years. Int. J. Remote Sens. https://doi.org/10.1080/01431161.2018.1550919

Csavina, J., Roberti, J.A., Taylor, J.R., Loescher, H.W., 2017. Traceable measurements and calibration: A primer on uncertainty analysis. Ecosphere. https://doi.org/10.1002/ecs2.1683

D'Odorico, P., Gonsamo, A., Damm, A., Schaepman, M.E., 2013. Experimental evaluation of sentinel-2 spectral response functions for NDVI time-series continuity. IEEE Trans. Geosci. Remote Sens. 51, 1336–1348. https://doi.org/10.1109/TGRS.2012.2235447

Damm, A., Elber, J., Erler, A., Gioli, B., Hamdi, K., Hutjes, R., Kosvancova, M., Meroni, M., Miglietta, F., Moersch, A., Moreno, J., Schickling, A., Sonnenschein, R., Udelhoven, T., van der Linden, S., Hostert, P., Rascher, U., 2010a. Remote sensing of sun-induced fluorescence to improve modeling of diurnal courses of gross primary production (GPP). Glob. Chang. Biol. 16, 171–186. https://doi.org/10.1111/j.1365-2486.2009.01908.x

Damm, A., Erler, A., Hillen, W., Meroni, M., Schaepman, M.E., Verhoef, W., Rascher, U., 2011. Modeling the impact of spectral sensor configurations on the FLD retrieval accuracy of sun-induced chlorophyll fluorescence. Remote Sens. Environ. https://doi.org/10.1016/j.rse.2011.03.011

Damm, A., Guanter, L., Laurent, V.C.E., Schaepman, M.E., Schickling, A., Rascher, U., 2014. FLD-based retrieval of sun-induced chlorophyll fluorescence from medium spectral resolution airborne spectroscopy data. Remote Sens. Environ. 147, 256–266. https://doi.org/10.1016/j.rse.2014.03.009

Damm, A., Guanter, L., Verhoef, W., Schläpfer, D., Garbari, S., Schaepman, M.E., 2015. Impact of varying irradiance on vegetation indices and chlorophyll fluorescence derived from spectroscopy data. Remote Sens. Environ. https://doi.org/10.1016/j.rse.2014.09.031

Damm, A., Schickling, A., Schaepman, M., Rascher, U., 2010b. Deriving Sun-Induced Chlorophyll Fluorescence From Airborne Based Spectrometer Data. Hyperspectral Work. 2010, Frascati, IT 2010, 17–19.

Dash, J., Curran, & P.J., Curran, P.J., 2004. The MERIS terrestrial chlorophyll index. Int. J. Remote Sens. 25, 5403–5413. https://doi.org/10.1080/0143116042000274015

Daumard, F., Champagne, S., Fournier, A., Goulas, Y., Ounis, A., Hanocq, J.F., Moya, I., 2010. A field platform for continuous measurement of canopy fluorescence. IEEE Trans. Geosci. Remote Sens. 48, 3358–3368. https://doi.org/10.1109/TGRS.2010.2046420

Dayal, B.S., Macgregor, J.F., 1997. Improved PLS algorithms. J. Chemom. 11, 73–85. https://doi.org/10.1002/(sici)1099-128x(199701)11:1<73::aid-cem435>3.0.co;2-%23

De Jong, S., 1993. SIMPLS: An alternative approach to partial least squares regression. Chemom. Intell. Lab. Syst. 18, 251–263. https://doi.org/10.1016/0169-7439(93)85002-X

De Jong, S., Ter Braak, C.J.F., 1994. Comments on the PLS kernel algorithm. J. Chemom. 8, 169–174. https://doi.org/10.1002/cem.1180080208

Debella-Gilo, M., Gjertsen, A.K., 2021. Mapping Seasonal Agricultural Land Use Types Using Deep Learning on Sentinel-2 Image Time Series. Remote Sens. 13, 289. https://doi.org/10.3390/rs13020289

Dechant, B., Ryu, Y., Badgley, G., Köhler, P., Rascher, U., Migliavacca, M., Zhang, Y., Tagliabue, G., Guan, K., Rossini, M., Goulas, Y., Zeng, Y., Frankenberg, C., Berry, J.A., 2022. NIRVP: A robust structural proxy for sun-induced chlorophyll fluorescence and photosynthesis across scales. Remote Sens. Environ. 268, 112763. https://doi.org/10.1016/j.rse.2021.112763

Dechant, B., Ryu, Y., Badgley, G., Zeng, Y., Berry, J.A., Zhang, Y., Goulas, Y., Li, Z., Zhang, Q., Kang, M., Li, J., Moya, I., 2020. Canopy structure explains the relationship between photosynthesis and sun-induced chlorophyll fluorescence in crops. Remote Sens. Environ. 241. https://doi.org/10.1016/j.rse.2020.111733

Dray, S., 2008. On the number of principal components: A test of dimensionality based on measurements of similarity between matrices. Comput. Stat. Data Anal. 52, 2228–2237. https://doi.org/10.1016/j.csda.2007.07.015

Drolet, G., Wade, T., Nichol, C.J., MacLellan, C., Levula, J., Porcar-Castell, A., Nikinmaa, E., Vesala, T., 2014. A temperature-controlled spectrometer system for continuous and unattended measurements of canopy spectral radiance and reflectance. Int. J. Remote Sens. 35, 1769–1785. https://doi.org/10.1080/01431161.2014.882035

Drusch, M., Del Bello, U., Carlier, S., Colin, O., Fernandez, V., Gascon, F., Hoersch, B., Isola, C., Laberinti, P., Martimort, P., Meygret, A., Spoto, F., Sy, O., Marchese, F., Bargellini, P., 2012. Sentinel-2: ESA's

Optical High-Resolution Mission for GMES Operational Services. Remote Sens. Environ. 120, 25–36. https://doi.org/10.1016/j.rse.2011.11.026

Drusch, M., Moreno, J., Del Bello, U., Franco, R., Goulas, Y., Huth, A., Kraft, S., Middleton, E.M., Miglietta, F., Mohammed, G., Nedbal, L., Rascher, U., Schuttemeyer, D., Verhoef, W., 2017. The FLuorescence EXplorer Mission Concept-ESA's Earth Explorer 8. IEEE Trans. Geosci. Remote Sens. 55, 1273–1284. https://doi.org/10.1109/TGRS.2016.2621820

Du, S., Liu, L., Liu, X., Zhang, Xiao, Zhang, Xingying, Bi, Y., Zhang, L., 2018. Retrieval of global terrestrial solar-induced chlorophyll fluorescence from TanSat satellite. Sci. Bull. 63, 1502–1512. https://doi.org/10.1016/J.SCIB.2018.10.003

Duveiller, G., Cescatti, A., 2016. Spatially downscaling sun-induced chlorophyll fluorescence leads to an improved temporal correlation with gross primary productivity. Remote Sens. Environ. 182, 72–89. https://doi.org/10.1016/j.rse.2016.04.027

Ehn, M., Thornton, J.A., Kleist, E., Sipilä, M., Junninen, H., Pullinen, I., Springer, M., Rubach, F., Tillmann, R., Lee, B., Lopez-Hilfiker, F., Andres, S., Acir, I.H., Rissanen, M., Jokinen, T., Schobesberger, S., Kangasluoma, J., Kontkanen, J., Nieminen, T., Kurtén, T., Nielsen, L.B., Jørgensen, S., Kjaergaard, H.G., Canagaratna, M., Maso, M.D., Berndt, T., Petäjä, T., Wahner, A., Kerminen, V.M., Kulmala, M., Worsnop, D.R., Wildt, J., Mentel, T.F., 2014. A large source of low-volatility secondary organic aerosol. Nature. https://doi.org/10.1038/nature13032

Eick, C.F., Zeidat, N., Zhao, Z., 2004. Supervised clustering - Algorithms and benefits, in: Proceedings - International Conference on Tools with Artificial Intelligence, ICTAI. pp. 774–776. https://doi.org/10.1109/ICTAI.2004.111

Eitel, J.U.H., Keefe, R.F., Long, D.S., Davis, A.S., Vierling, L.A., 2010. Active Ground Optical Remote Sensing for Improved Monitoring of Seedling Stress in Nurseries. sensors 10, 2843–2850. https://doi.org/10.3390/s100402843

ESRI, 2021. World Imagery [basemap]. Scale not given. [WWW Document]. World Imag. URL https://www.arcgis.com/home/item.html?id=10df2279f9684e4a9f6a7f08febac2a9 (accessed 1.12.23).

Etzold, S., Sterck, F., Bose, A.K., Braun, S., Buchmann, N., Eugster, W., Gessler, A., Kahmen, A., Peters, R.L., Vitasse, Y., Walthert, L., Ziemińska, K., Zweifel, R., 2022. Number of growth days and not length of the growth period determines radial stem growth of temperate trees. Ecol. Lett. 25, 427–439. https://doi.org/10.1111/ele.13933

Farrance, I., Frenkel, R., 2012. Uncertainty of Measurement: A Review of the Rules for Calculating

Uncertainty Components through Functional Relationships, Clin Biochem Rev.

Fattorini, D., Regoli, F., 2020. Role of the chronic air pollution levels in the Covid-19 outbreak risk in Italy. Environ. Pollut. https://doi.org/10.1016/j.envpol.2020.114732

Feilhauer, H., Thonfeld, F., Faude, U., He, K.S., Rocchini, D., Schmidtlein, S., 2012. Assessing floristic composition with multispectral sensors-A comparison based: On monotemporal and multiseasonal field spectra. Int. J. Appl. Earth Obs. Geoinf. 21, 218–229. https://doi.org/10.1016/j.jag.2012.09.002

Fournier, A., Daumard, F., Champagne, S., Ounis, A., Goulas, Y., Moya, I., 2012. Effect of canopy structure on sun-induced chlorophyll fluorescence. ISPRS J. Photogramm. Remote Sens. 68, 112–120. https://doi.org/10.1016/j.isprsjprs.2012.01.003

Frankenberg, C., Berry, J., 2018. Solar Induced Chlorophyll Fluorescence: Origins, Relation to Photosynthesis and Retrieval, in: Comprehensive Remote Sensing. https://doi.org/10.1016/B978-0-12-409548-9.10632-3

Frankenberg, C., Köhler, P., Magney, T.S., Geier, S., Lawson, P., Schwochert, M., McDuffie, J., Drewry, D.T., Pavlick, R., Kuhnert, A., 2018. The Chlorophyll Fluorescence Imaging Spectrometer (CFIS), mapping far red fluorescence from aircraft. Remote Sens. Environ. 217, 523–536. https://doi.org/10.1016/j.rse.2018.08.032

Frontera, A., Cianfanelli, L., Vlachos, K., Landoni, G., Cremona, G., 2020. Severe air pollution links to higher mortality in COVID-19 patients: The “double-hit” hypothesis. J. Infect. https://doi.org/10.1016/j.jinf.2020.05.031

Fu, Y., Zhang, H., Dong, W., Yuan, W., 2014. Comparison of Phenology Models for Predicting the Onset of Growing Season over the Northern Hemisphere. PLoS One 9. https://doi.org/10.1371/journal.pone.0109544

Galvagno, M., Gamon, J., 2017. Integrating proximal and satellite optical data for the analysis of ecosystem carbon uptake and plant phenology at the European larch Specnet site, in: EGU. https://doi.org/10.13140/RG.2.2.16267.49443

Gamon, J.A., 2015. Reviews and Syntheses: Optical sampling of the flux tower footprint. Biogeosciences. https://doi.org/10.5194/bg-12-4509-2015

Gamon, J.A., Coburn, C., Flanagan, L.B., Huemmrich, K.F., Kiddle, C., Sanchez-Azofeifa, G.A., Thayer, D.R., Vescovo, L., Gianelle, D., Sims, D.A., Rahman, A.F., Pastorello, G.Z., 2010. SpecNet revisited: Bridging flux and remote sensing communities. Can. J. Remote Sens. 36, S376–S390.

https://doi.org/10.5589/m10-067

Gamon, J.A., Field, C.B., Hartley, A.E., Joel, G., Penuelas, J., Riccardo Valentini, A., 1995. RELATIONSHIPS BETWEEN NDVI, CANOPY STRUCTURE, AND PHOTOSYNTHESIS IN THREE CALIFORNIAN VEGETATION TYPES. Ecol. Appl. 5, 28–41.

Gamon, J.A., Kovalchuck, O., Wong, C.Y.S., Harris, A., Garrity, S.R., 2015. Monitoring seasonal and diurnal changes in photosynthetic pigments with automated PRI and NDVI sensors. Biogeosciences 12. https://doi.org/10.5194/bg-12-4149-2015

Gamon, J.A., Peñuelas, J., Field, C.B., 1992. A narrow-waveband spectral index that tracks diurnal changes in photosynthetic efficiency. Remote Sens. Environ. https://doi.org/10.1016/0034-4257(92)90059-S

Gamon, J.A., Rahman, A.F., Dungan, J.L., Schildhauer, M., Huemmrich, K.F., 2006. Spectral Network (SpecNet)—What is it and why do we need it? Remote Sens. Environ. 103, 227–235. https://doi.org/https://doi.org/10.1016/j.rse.2006.04.003

Gamon, J.A., Somers, B., Malenovský, Z., Middleton, E.M., Rascher, U., Schaepman, M.E., 2019. Assessing Vegetation Function with Imaging Spectroscopy. Surv. Geophys. 40, 489–513. https://doi.org/10.1007/s10712-019-09511-5

Gamon, J.A., Surfus, J.S., 1999. Assessing leaf pigment content and activity with a reflectometer. New Phytol. 143, 105–117. https://doi.org/10.1046/j.1469-8137.1999.00424.x

Gao, B.-C., Goetz, A.F.H., Wiscombe, W.J., 1993. CIRRUS CLOUD DETECTION FROM AIRBORNE IMAGING SPECTROMETER DATA USING THE 1.38 um WATER VAPOR BAND. Geophys. Res. Lett. 20, 301–304.

Gielen, B., Op de Beek, M., Loustau, D., Ceulemans, R., Jordan, A., Papale, D., 2017. Integrated Carbon Observation System (ICOS), in: Chabbi, A., Loescher, H.W. (Eds.), Terrestrial Ecosystem Research Infrastructures. CRC Press, Boca Raton, FL : CRC Press, 2017. https://doi.org/10.1201/9781315368252

Gilabert, M.A., Meliá, J., 1993. Solar angle and sky light effects on ground reflectance measurements in a citrus canopy. Remote Sens. Environ. 45, 281–293. https://doi.org/10.1016/0034-4257(93)90111-A

Giles, D.M., Sinyuk, A., Sorokin, M.G., Schafer, J.S., Smirnov, A., Slutsker, I., Eck, T.F., Holben, B.N., Lewis, J.R., Campbell, J.R., Welton, E.J., Korkin, S. V., Lyapustin, A.I., 2019. Advancements in the Aerosol Robotic Network (AERONET) Version 3 database - Automated near-real-time quality

control algorithm with improved cloud screening for Sun photometer aerosol optical depth (AOD) measurements. Atmos. Meas. Tech. 12, 169–209. https://doi.org/10.5194/amt-12-169-2019

Gitelson, A.A., Keydan, G.P., Merzlyak, M.N., 2006. Three-band model for noninvasive estimation of chlorophyll, carotenoids, and anthocyanin contents in higher plant leaves. Geophys. Res. Lett. 33. https://doi.org/10.1029/2006GL026457

Gkatzelis, G.I., Gilman, J.B., Brown, S.S., Eskes, H., Gomes, A.R., Lange, A.C., McDonald, B.C., Peischl, J., Petzold, A., Thompson, C.R., Kiendler-Scharr, A., 2021. The global impacts of COVID-19 lockdowns on urban air pollution. Elem. Sci. Anthr. 9. https://doi.org/10.1525/elementa.2021.00176

Gómez-Dans, J.L., Lewis, P.E., Disney, M., 2016. Efficient emulation of radiative transfer codes using gaussian processes and application to land surface parameter inferences. Remote Sens. 8, 1–32. https://doi.org/10.3390/rs8020119

Gorelick, N., Hancher, M., Dixon, M., Ilyushchenko, S., Thau, D., Moore, R., 2017. Google Earth Engine: Planetary-scale geospatial analysis for everyone. Remote Sens. Environ. 202, 18–27. https://doi.org/10.1016/j.rse.2017.06.031

Goulas, Y., Fournier, A., Daumard, F., Champagne, S., Ounis, A., Marloie, O., Moya, I., 2017. Gross Primary Production of a Wheat Canopy Relates Stronger to Far Red Than to Red Solar-Induced Chlorophyll Fluorescence. Remote Sens. 9, 97. https://doi.org/10.3390/rs9010097

Graf, L.V., Gorroño, J., Hueni, A., Walter, A., Aasen, H., 2023. Propagating Sentinel-2 Top-of-Atmosphere Radiometric Uncertainty into Land Surface Phenology Metrics Using a Monte Carlo. TechRxiv. Prepr. https://doi.org/10.36227/techrxiv.22179673.v1

Green, R.O., Eastwood, M.L., Sarture, C.M., Chrien, T.G., Aronsson, M., Chippendale, B.J., Faust, J.A., Pavri, B.E., Chovit, C.J., Solis, M., Olah, M.R., Williams, O., 1998. Imaging Spectroscopy and the Airborne Visible/Infrared Imaging Spectrometer (AVIRIS). Remote Sens. Environ. 65, 227–248.

Grolemund, G., Wickham, H., 2016. R for Data Science [WWW Document]. O'Reilly Media. URL http://r4ds.had.co.nz/ (accessed 2.10.18).

Grossmann, K., Frankenberg, C., Magney, T.S., Hurlock, S.C., Seibt, U., Stutz, J., 2018. PhotoSpec: A new instrument to measure spatially distributed red and far-red Solar-Induced Chlorophyll Fluorescence. Remote Sens. Environ. 216, 311–327. https://doi.org/10.1016/j.rse.2018.07.002

Gu, L., Pallardy, S.G., Yang, B., Hosman, K.P., Mao, J., Ricciuto, D., Shi, X., Sun, Y., 2016. Testing a land model in ecosystem functional space via a comparison of observed and modeled ecosystem flux responses to precipitation regimes and associated stresses in a Central U.S. forest. J. Geophys.

Res. Biogeosciences 121, 1884–1902. https://doi.org/10.1002/2015JG003302

Gu, L., Wood, J.D., Chang, C.Y. -Y., Sun, Y., Riggs, J.S., 2019. Advancing Terrestrial Ecosystem Science With a Novel Automated Measurement System for Sun-Induced Chlorophyll Fluorescence for Integration With Eddy Covariance Flux Networks. J. Geophys. Res. Biogeosciences 124, 127–146. https://doi.org/10.1029/2018JG004742

Guanter, L., Frankenberg, C., Dudhia, A., Lewis, P.E., Gómez-Dans, J., Kuze, A., Suto, H., Grainger, R.G., 2012. Retrieval and global assessment of terrestrial chlorophyll fluorescence from GOSAT space measurements. Remote Sens. Environ. 121, 236–251. https://doi.org/10.1016/j.rse.2012.02.006

Guanter, L., Rossini, M., Colombo, R., Meroni, M., Frankenberg, C., Lee, J.-E., Joiner, J., 2013. Using field spectroscopy to assess the potential of statistical approaches for the retrieval of sun-induced chlorophyll fluorescence from ground and space. Remote Sens. Environ. 133, 52–61. https://doi.org/10.1016/j.rse.2013.01.017

Guanter, L., Zhang, Y., Jung, M., Joiner, J., Voigt, M., Berry, J.A., Frankenberg, C., Huete, A.R., Zarco-Tejada, P., Lee, J.-E., Moran, M.S., Ponce-Campos, G., Beer, C., Camps-Valls, G., Buchmann, N., Gianelle, D., Klumpp, K., Cescatti, A., Baker, J.M., Griffis, T.J., 2014. Global and time-resolved monitoring of crop photosynthesis with chlorophyll fluorescence. Proc. Natl. Acad. Sci. 111. https://doi.org/10.1073/pnas.1320008111

Guo, Y., Senthilnath, J., Wu, W., Zhang, X., Zeng, Z., Huang, H., 2019. Radiometric calibration for multispectral camera of different imaging conditions mounted on a UAV platform. Sustain. 11. https://doi.org/10.3390/su11040978

Guyet, T., Nicolas, H., 2016. Long term analysis of time series of satellite images. Pattern Recognit. Lett. 70, 17–23. https://doi.org/10.1016/j.patrec.2015.11.005

Haboudane, D., Miller, J.R., Tremblay, N., Zarco-Tejada, P.J., Dextraze, L., 2002. Integrated narrow-band vegetation indices for prediction of crop chlorophyll content for application to precision agriculture. Remote Sens. Environ. 81, 416–426.

Hakala, T., Honkavaara, E., Saari, H., Mäkynen, J., Kaivosoja, J., Pesonen, L., Pölönen, I., 2013. SPECTRAL IMAGING FROM UAVS UNDER VARYING ILLUMINATION CONDITIONS. Int. Arch. Photogramm. Remote Sens. Spat. Inf. Sci. XL-1/W2, 189–194. https://doi.org/10.5194/isprsarchives-xl-1-w2-189-2013

Hakala, T., Markelin, L., Honkavaara, E., Scott, B., Theocharous, T., Nevalainen, O., Näsi, R., Suomalainen, J., Viljanen, N., Greenwell, C., Fox, N., 2018. Direct reflectance measurements from drones: Sensor absolute radiometric calibration and system tests for forest reflectance

characterization. Sensors (Switzerland) 18. https://doi.org/10.3390/s18051417

Hall, F.G., Hilker, T., Coops, N.C., Lyapustin, A., Huemmrich, K.F., Hall, N.-L., Hilker, F.G.;, Coops, T.;, Lyapustin, N.C.;, Huemmrich, A.;, Middleton, K.F.;, Margolis, E.;, Drolet, H.;, Black, G., Andrew, T., 2008. Multi-angle remote sensing of forest light use efficiency by observing PRI variation with canopy shadow fraction. Remote Sens. Environ. 112, 3201–3211.

Hank, T.B., Berger, K., Bach, H., Clevers, J.G.P.W., Gitelson, A., Zarco-Tejada, P., Mauser, W., 2019. Spaceborne Imaging Spectroscopy for Sustainable Agriculture: Contributions and Challenges. Surv. Geophys. 40, 515–551. https://doi.org/10.1007/s10712-018-9492-0

Harris, A., Gamon, J.A., Pastorello, G.Z., Wong, C.Y.S., 2014. Retrieval of the photochemical reflectance index for assessing xanthophyll cycle activity: A comparison of near-surface optical sensors. Biogeosciences 11, 6277–6292. https://doi.org/10.5194/bg-11-6277-2014

He, L., Chen, J.M., Liu, J., Zheng, T., Wang, R., Joiner, J., Chou, S., Chen, B., Liu, Y., Liu, R., Rogers, C., 2019. Diverse photosynthetic capacity of global ecosystems mapped by satellite chlorophyll fluorescence measurements. Remote Sens. Environ. 232, 111344. https://doi.org/10.1016/j.rse.2019.111344

He, X., Xu, X., Zheng, Z., 2019. Optimal band analysis of a space-based multispectral sensor for Urban Air Pollutant Detection. Atmosphere (Basel). 10. https://doi.org/10.3390/atmos10100631

Herrmann, I., Karnieli, A., Bonfil, D.J., Cohen, Y., Alchanatis, V., 2010. SWIR-based spectral indices for assessing nitrogen content in potato fields. Int. J. Remote Sens. 31, 5127–5143. https://doi.org/10.1080/01431160903283892

Honkavaara, E., Khoramshahi, E., 2018. Radiometric Correction of Close-Range Spectral Image Blocks Captured Using an Unmanned Aerial Vehicle with a Radiometric Block Adjustment. Remote Sens. 10, 256. https://doi.org/10.3390/rs10020256

Honkavaara, E., Saari, H., Kaivosoja, J., Pölönen, I., Hakala, T., Litkey, P., Mäkynen, J., Pesonen, L., 2013. Processing and Assessment of Spectrometric, Stereoscopic Imagery Collected Using a Lightweight UAV Spectral Camera for Precision Agriculture. Remote Sens. 5, 5006–5039. https://doi.org/10.3390/rs5105006

Hosseiny, B., Mahdianpari, M., Hemati, M., Radman, A., Mohammadimanesh, F., Chanussot, J., 2024. Beyond Supervised Learning in Remote Sensing: A Systematic Review of Deep Learning Approaches. IEEE J. Sel. Top. Appl. Earth Obs. Remote Sens. 17, 1035–1052. https://doi.org/10.1109/JSTARS.2023.3316733

Hothorn, T., Hornik, K., Zeileis, A., 2006. Unbiased recursive partitioning: A conditional inference framework. J. Comput. Graph. Stat. 15, 651–674. https://doi.org/10.1198/106186006X133933

Hueni, A., Bialek, A., 2017. Cause, Effect, and Correction of Field Spectroradiometer Interchannel Radiometric Steps. IEEE J. Sel. Top. Appl. Earth Obs. Remote Sens. 10, 1542–1551. https://doi.org/10.1109/JSTARS.2016.2625043

Hueni, A., Damm, A., Kneubuehler, M., Schlapfer, D., Schaepman, M.E., 2017. Field and Airborne Spectroscopy Cross Validation -Some Considerations. IEEE J. Sel. Top. Appl. Earth Obs. Remote Sens. 10, 1117–1135. https://doi.org/10.1109/JSTARS.2016.2593984

Hueni, A., Mason, K., Trim, S.A., 2023. Uncertainty Support in the Spectral Information System SPECCHIO. IEEE J. Sel. Top. Appl. Earth Obs. Remote Sens. https://doi.org/10.1109/JSTARS.2023.3251894

Hueni, A., Nieke, J., Schopfer, J., Kneubühler, M., Itten, K.I., 2009. The spectral database SPECCHIO for improved long-term usability and data sharing. Comput. Geosci. 35, 557–565. https://doi.org/10.1016/J.CAGEO.2008.03.015

Humphrey, V., Berg, A., Ciais, P., Gentine, P., Jung, M., Reichstein, M., Seneviratne, S.I., Frankenberg, C., 2021. Soil moisture–atmosphere feedback dominates land carbon uptake variability. Nature 592, 65–69. https://doi.org/10.1038/s41586-021-03325-5

Hundt, P.M., Müller, M., Mangold, M., Tuzson, B., Scheidegger, P., Looser, H., Hüglin, C., Emmenegger, L., 2018. Mid-IR spectrometer for mobile, real-time urban NO2 measurements. Atmos. Meas. Tech. 11, 2669–2681. https://doi.org/10.5194/amt-11-2669-2018

Imran, H.A., Gianelle, D., Scotton, M., Rocchini, D., Dalponte, M., Macolino, S., Sakowska, K., Pornaro, C., Vescovo, L., 2021. Potential and Limitations of Grasslands α-Diversity Prediction Using Fine-Scale Hyperspectral Imagery. Remote Sens. 13, 2649. https://doi.org/10.3390/rs13142649

Inamdar, D., Kalacska, M., Leblanc, G., Arroyo-Mora, J.P., 2020. Characterizing and mitigating sensor generated spatial correlations in airborne hyperspectral imaging data. Remote Sens. 12. https://doi.org/10.3390/rs12040641

Ismael, K., Duleba, S., 2021. Investigation of the relationship between the perceived public transport service quality and satisfaction: A pls-sem technique. Sustain. 13. https://doi.org/10.3390/su132313018

Jansen, M., Gilmer, F., Biskup, B., Nagel, K.A., Rascher, U., Fischbach, A., Briem, S., Dreissen, G., Tittmann, S., Braun, S., De Jaeger, I., Metzlaff, M., Schurr, U., Scharr, H., Walter, A., 2009.

Simultaneous phenotyping of leaf growth and chlorophyll fluorescence via Growscreen Fluoro allows detection of stress tolerance in Arabidopsis thaliana and other rosette plants. Funct. Plant Biol. https://doi.org/10.1071/FP09095

JCGM, 2020. JCGM GUM-6:2020 Guide to the expression of uncertainty in measurement-Part 6: Developing and using measurement models. Geneva, Switzerland.

JCGM, 2008. JCGM GUM-100:2008 Evaluation of measurement data — Guide to the expression of uncertainty in measurement. Geneva, Switzerland.

Jenal, A., Weber, I., Kneer, C., Bongartz, J., 2015. Der Tragschrauber als Sensorplattform für die Fernerkundung, in: Dreiländertagung Der DGPF, Der OVG Und Der SGPF in Bern, Schweiz – Publikationen Der DGPF, Band 25.

Jiang, G., Zhou, S., Cui, S., Chen, T., Wang, J., Chen, X., Liao, S., Zhou, K., 2020. Exploring the Potential of HySpex Hyperspectral Imagery for Extraction of Copper Content. Sensors 20, 6325. https://doi.org/10.3390/s20216325

Jiang, Z., Huete, A.R., Chen, J., Chen, Y., Li, J., Yan, G., Zhang, X., 2006. Analysis of NDVI and scaled difference vegetation index retrievals of vegetation fraction. Remote Sens. Environ. 101, 366–378. https://doi.org/10.1016/j.rse.2006.01.003

Jin, J., Wang, Q., 2019. Evaluation of informative bands used in different PLS regressions for estimating leaf biochemical contents from hyperspectral reflectance. Remote Sens. 11. https://doi.org/10.3390/rs11020197

Joiner, J., Yoshida, Y., Guanter, L., Middleton, E.M., 2016. New methods for the retrieval of chlorophyll red fluorescence from hyperspectral satellite instruments: simulations and application to GOME-2 and SCIAMACHY. Atmos. Meas. Tech 9, 3939–3967. https://doi.org/10.5194/amt-9-3939-2016

Joiner, J., Yoshida, Y., Zhang, Y., Duveiller, G., Jung, M., Lyapustin, A., Wang, Y., Tucker, C.J., 2018. Estimation of Terrestrial Global Gross Primary Production (GPP) with Satellite Data-Driven Models and Eddy Covariance Flux Data. Remote Sens. 10, 1346. https://doi.org/10.3390/rs10091346

Julitta, T., Burkart, A., Rossini, M., Schickling, A., Colombo, R., Rascher, U., Cogliati, S.M., Migliavacca, M., 2017. FLoX: A System for Automatic Long Term Measurements of Top of Canopy Sun Induced Chlorophyll Fluorescence, in: Remote Sensing of Fluorescence, Photosynthesis and Vegetation Status. ESA-ESRIN, Frascati RM, Italy.

Julitta, T., Corp, L.A., Rossini, M., Burkart, A., Cogliati, S., Davies, N., Hom, M., Mac Arthur, A.,

Middleton, E.M., Rascher, U., Schickling, A., Colombo, R., 2016. Comparison of sun-induced chlorophyll fluorescence estimates obtained from four portable field spectroradiometers. Remote Sens. 8. https://doi.org/10.3390/rs8020122

Jung, M., Koirala, S., Weber, U., Ichii, K., Gans, F., Camps-Valls, G., Papale, D., Schwalm, C., Tramontana, G., Reichstein, M., 2019. The FLUXCOM ensemble of global land-atmosphere energy fluxes. Sci. Data 6, 74. https://doi.org/10.1038/s41597-019-0076-8

Kanniah, K.D., Beringer, J., North, P., Hutley, L., 2012. Control of atmospheric particles on diffuse radiation and terrestrial plant productivity: A review. Prog. Phys. Geogr. https://doi.org/10.1177/0309133311434244

Karpouzli, E., Malthus, T., 2003. The empirical line method for the atmospheric correction of IKONOS imagery. Int. J. Remote Sens. 24, 1143–1150. https://doi.org/10.1080/0143116021000026779

Kaskaoutis, D.G., Kambezidis, H.D., Kumar Kharol, S., Badarinath, K.V.S., 2008. The diffuse-to-global spectral irradiance ratio as a cloud-screening technique for radiometric data. J. Atmos. Solar-Terrestrial Phys. https://doi.org/10.1016/j.jastp.2008.04.013

Keller, S., Maier, P.M., Riese, F.M., Norra, S., Holbach, A., Börsig, N., Wilhelms, A., Moldaenke, C., Zaake, A., Hinz, S., 2018. Hyperspectral data and machine learning for estimating CDOM, chlorophyll a, diatoms, green algae and turbidity. Int. J. Environ. Res. Public Health 15. https://doi.org/10.3390/ijerph15091881

Kepler, J., 1604. Ad Vitellionem Paralipomena, Quibus Astronomiae Pars Optica Traditvr : Potißimum De Artificiosa Observatione Et Aestimatione Diametrorvm deliquiorumq[ue] Solis & Lunae ; Cvm Exemplis Insignivm Eclipsivm ... Tractatum luculentum de modo visionis, & humorum. Claude de Marne, Johann Aubry Erben, Francofurti: Marnius; Aubrius.

Kim, M., Sankararao, B., Kang, O., Kim, J., Yoo, C., 2012. Monitoring and prediction of indoor air quality (IAQ) in subway or metro systems using season dependent models, in: Energy and Buildings. pp. 48–55. https://doi.org/10.1016/j.enbuild.2011.10.047

Kimes, D.S., Kirchner, J.A., Newcomb, W.W., 1983. Spectral radiance errors in remote sensing ground studies due to nearby objects. Appl. Opt. 22.

Klein, J., Brauers, J., Aach, T., 2011. Methods for spectral characterization of multispectral cameras, in: Electronic Imaging: Digital Photography VII. SPIE, San Francisco, CA, USA.

Kneer, C., Jenal, A., Weber, I., Bongartz, J., 2016. Ein adaptives und kompaktes Fernerkundungssystem für UL-Fluggeräte-Konzept und Anwendungen, in: Dreiländertagung Der DGPF, Der OVG Und Der

SGPF in Bern, Schweiz – Publikationen Der DGPF, Band 25.

Köhler, P., Behrenfeld, M.J., Landgraf, J., Joiner, J., Magney, T.S., Frankenberg, C., 2020. Global Retrievals of Solar-Induced Chlorophyll Fluorescence at Red Wavelengths With TROPOMI. Geophys. Res. Lett. 47, 1–10. https://doi.org/10.1029/2020GL087541

Köhler, P., Guanter, L., Joiner, J., 2015. A linear method for the retrieval of sun-induced chlorophyll fluorescence from GOME-2 and SCIAMACHY data. Atmos. Meas. Tech. 8, 2589–2608. https://doi.org/10.5194/amt-8-2589-2015

Kokhanovsky, A., Di Mauro, B., Garzonio, R., Colombo, R., 2021. Retrieval of Dust Properties From Spectral Snow Reflectance Measurements. Front. Environ. Sci. 9. https://doi.org/10.3389/fenvs.2021.644551

Krämer, J., Siegmann, B., Kraska, T., Muller, O., Rascher, U., 2021. The potential of spatial aggregation to extract remotely sensed sun-induced fluorescence (SIF) of small-sized experimental plots for applications in crop phenotyping. Int. J. Appl. Earth Obs. Geoinf. 104, 102565. https://doi.org/10.1016/j.jag.2021.102565

Kucheryavskiy, S., 2020. mdatools – R package for chemometrics. Chemom. Intell. Lab. Syst. 198. https://doi.org/10.1016/j.chemolab.2020.103937

Kuester, M., Thome, K., Krause, K., Canham, K., Whittington, E., 2001. Comparison of surface reflectance measurements from three ASD FieldSpec FR spectroradiometers and one ASD FieldSpec VNIR spectroradiometer, in: International Geoscience and Remote Sensing Symposium (IGARSS). pp. 72–74. https://doi.org/10.1109/igarss.2001.976060

Lama, G.F.C., Crimaldi, M., De Vivo, A., Chirico, G.B., Sarghini, F., 2021a. Eco-hydrodynamic characterization of vegetated flows derived by UAV-based imagery, in: 2021 IEEE International Workshop on Metrology for Agriculture and Forestry (MetroAgriFor). pp. 273–278. https://doi.org/10.1109/MetroAgriFor52389.2021.9628749

Lama, G.F.C., Rillo Migliorini Giovannini, M., Errico, A., Mirzaei, S., Chirico, G.B., Preti, F., 2021b. The impacts of Nature Based Solutions (NBS) on vegetated flows' dynamics in urban areas, in: 2021 IEEE International Workshop on Metrology for Agriculture and Forestry (MetroAgriFor). pp. 58–63. https://doi.org/10.1109/MetroAgriFor52389.2021.9628438

Lense, G.H.E., Lämmle, L., Ayer, J.E.B., Lama, G.F.C., Rubira, F.G., Mincato, R.L., 2023. Modeling of Soil Loss by Water Erosion and Its Impacts on the Cantareira System, Brazil. Water (Switzerland) 15. https://doi.org/10.3390/w15081490

Li, Y., Chen, J., Ma, Q., Zhang, H.K., Liu, J., 2018. Evaluation of Sentinel-2A Surface Reflectance Derived Using Sen2Cor in North America. IEEE J. Sel. Top. Appl. Earth Obs. Remote Sens. 11, 1997–2021. https://doi.org/10.1109/JSTARS.2018.2835823

Linkosalmi, M., Tuovinen, J.-P., Nevalainen, O., Peltoniemi, M., Taniş, C.M., Arslan, A.N., Rainne, J., Lohila, A., Laurila, T., Aurela, M., 2022. Tracking vegetation phenology of pristine northern boreal peatlands by combining digital photography with CO2 flux and remote sensing data. Biogeosciences Discuss. Prepr. https://doi.org/10.5194/bg-2022-58

Lipfert, F.W., Wyzga, R.E., 2021. Covid-19 and the environment, review and analysis. Environ. - MDPI. https://doi.org/10.3390/environments8050042

Liu, H.Q., Huete, A., 1995. A feedback based modification of the NDVI to minimize canopy background and atmospheric noise. IEEE Trans. Geosci. Remote Sens. 33, 457–465. https://doi.org/10.1109/tgrs.1995.8746027

Liu, L., Liu, X., Hu, J., 2015. Effects of spectral resolution and SNR on the vegetation solar-induced fluorescence retrieval using FLD-based methods at canopy level. Eur. J. Remote Sens. 48, 743–762. https://doi.org/10.5721/EuJRS20154841

Liu, X., Guanter, L., Liu, L., Damm, A., Malenovský, Z., Rascher, U., Peng, D., Du, S., Gastellu-Etchegorry, J.P., 2019a. Downscaling of solar-induced chlorophyll fluorescence from canopy level to photosystem level using a random forest model. Remote Sens. Environ. 231. https://doi.org/10.1016/j.rse.2018.05.035

Liu, X., Guo, J., Hu, J., Liu, L., 2019b. Atmospheric Correction for Tower-Based Solar-Induced Chlorophyll Fluorescence Observations at O2-A Band. Remote Sens. 11, 355. https://doi.org/10.3390/rs11030355

Liu, X., Hou, Z., Shi, Z., Bo, Y., Cheng, J., 2017. A shadow identification method using vegetation indices derived from hyperspectral data. Int. J. Remote Sens. 38, 5357–5373. https://doi.org/10.1080/01431161.2017.1338785

Liu, X., Liu, L., 2018. Influence of the canopy BRDF characteristics and illumination conditions on the retrieval of solar-induced chlorophyll fluorescence. Int. J. Remote Sens. https://doi.org/10.1080/01431161.2017.1404165

Liu, X., Liu, L., Zhang, S., Zhou, X., 2015. New spectral fitting method for full-spectrum solar-induced chlorophyll fluorescence retrieval based on principal components analysis. Remote Sens. 7, 10626–10645. https://doi.org/10.3390/rs70810626

Ma, H., Liang, S., Xiong, C., Wang, Q., Jia, A., Li, B., 2022. Global land surface 250 m 8 d fraction of absorbed photosynthetically active radiation (FAPAR) product from 2000 to 2021. Earth Syst. Sci. Data 14, 5333–5347. https://doi.org/10.5194/essd-14-5333-2022

Ma, X., Mahecha, M.D., Migliavacca, M., van der Plas, F., Benavides, R., Ratcliffe, S., Kattge, J., Richter, R., Musavi, T., Baeten, L., Barnoaiea, I., Bohn, F.J., Bouriaud, O., Bussotti, F., Coppi, A., Domisch, T., Huth, A., Jaroszewicz, B., Joswig, J., Pabon-Moreno, D.E., Papale, D., Selvi, F., Laurin, G.V., Valladares, F., Reichstein, M., Wirth, C., 2019. Inferring plant functional diversity from space: the potential of Sentinel-2. Remote Sens. Environ. 233, 111368. https://doi.org/10.1016/j.rse.2019.111368

Mac Arthur, A.A., MacLellan, C., Malthus, T.J., 2007a. Determining the FOV and directional response field spectroradiometers. Proc. 5th EARSeL Work. Imaging Spectrosc. Innov. Environ. Res. 1–8.

Mac Arthur, A.A., MacLellan, C., Malthus, T.J., 2007b. The implications of non-uniformity in fields-of-view of commonly used field spectroradiometers, in: International Geoscience and Remote Sensing Symposium (IGARSS). pp. 2890–2893. https://doi.org/10.1109/IGARSS.2007.4423447

Mac Arthur, A.A., Robinson, I., Rossini, M., Davis, N., MacDonald, K., 2014. A dual-field-of-view spectrometer system for reflectance and fluorescence measurements (Piccolo Doppio) and correction of etaloning, in: Proceedings of the Fifth International Workshop on Remote Sensing of Vegetation Fluorescence. EuropeanSpace Agenccy, Fifth International Workshop on Remote Sensing of Vegetation Fluorescence, Paris, 22–24 April.

Madin, J., Bowers, S., Schildhauer, M., Krivov, S., Pennington, D., Villa, F., 2007. An ontology for describing and synthesizing ecological observation data. Ecol. Inform. https://doi.org/10.1016/j.ecoinf.2007.05.004

Magney, T.S., Bowling, D.R., Logan, B.A., Grossmann, K., Stutz, J., Blanken, P.D., Burns, S.P., Cheng, R., Garcia, M.A., Köhler, P., Lopez, S., Parazoo, N.C., Raczka, B., Schimel, D., Frankenberg, C., 2019a. Mechanistic evidence for tracking the seasonality of photosynthesis with solar-induced fluorescence. Proc. Natl. Acad. Sci. U. S. A. https://doi.org/10.1073/pnas.1900278116

Magney, T.S., Frankenberg, C., Fisher, J.B., Sun, Y., North, G.B., Davis, T.S., Kornfeld, A., Siebke, K., 2017. Connecting active to passive fluorescence with photosynthesis: a method for evaluating remote sensing measurements of Chl fluorescence. New Phytol. https://doi.org/10.1111/nph.14662

Magney, T.S., Frankenberg, C., Köhler, P., North, G., Davis, T.S., Dold, C., Dutta, D., Fisher, J.B., Grossmann, K., Harrington, A., Hatfield, J., Stutz, J., Sun, Y., Porcar-Castell, A., 2019b. Disentangling Changes in the Spectral Shape of Chlorophyll Fluorescence: Implications for

Remote Sensing of Photosynthesis. J. Geophys. Res. Biogeosciences 124, 1491–1507. https://doi.org/10.1029/2019JG005029

Maier, P.M., Keller, S., Hinz, S., 2021. Deep learning with WASI simulation data for estimating chlorophyll-a concentration of inland water bodies. Remote Sens. 13, 1–27. https://doi.org/10.3390/rs13040718

Main, R., Cho, M.A., Mathieu, R., O'Kennedy, M.M., Ramoelo, A., Koch, S., 2011. An investigation into robust spectral indices for leaf chlorophyll estimation. ISPRS J. Photogramm. Remote Sens. 66, 751–761. https://doi.org/10.1016/j.isprsjprs.2011.08.001

Malenovský, Z., Ufer, C., Lhotáková, Z., Clevers, J.G.P.W., Schaepman, M.E., Albrechtová, J., Cudlín, P., 2006. A NEW HYPERSPECTRAL INDEX FOR CHLOROPHYLL ESTIMATION OF A FOREST CANOPY: AREA UNDER CURVE NORMALISED TO MAXIMAL BAND DEPTH BETWEEN 650-725 NM, EARSeL eProceedings.

Mamaghani, B., Salvaggio, C., 2019. Multispectral sensor calibration and characterization for sUAS remote sensing. Sensors (Switzerland) 19. https://doi.org/10.3390/s19204453

Mardia, K. V., Kent, J.T. (John T.., Bibby, J.M. (John M.., 1979. Multivariate analysis, in: Birnbaum, Z.W., Lukacs, E. (Eds.), Probability and Mathematical Statistics. Academic Press, London, GB, p. 521.

Martini, D., Pacheco-Labrador, J., Perez-Priego, O., van der Tol, C., El-Madany, T.S., Julitta, T., Rossini, M., Reichstein, M., Christiansen, R., Rascher, U., Moreno, G., Pilar Martín, M., Yang, P., Carrara, A., Guan, J., González-Cascón, R., Migliavacca, M., 2019. Nitrogen and phosphorus effect on sun-induced fluorescence and gross primary productivity in mediterranean grassland. Remote Sens. 11, 2562. https://doi.org/10.3390/rs11212562

Martini, D., Sakowska, K., Wohlfahrt, G., Pacheco-Labrador, J., van der Tol, C., Porcar-Castell, A., Magney, T.S., Carrara, A., Colombo, R., El-Madany, T.S., Gonzalez-Cascon, R., Martín, M.P., Julitta, T., Moreno, G., Rascher, U., Reichstein, M., Rossini, M., Migliavacca, M., 2022. Heatwave breaks down the linearity between sun-induced fluorescence and gross primary production. New Phytol. https://doi.org/10.1111/nph.17920

Mateo-Sanchis, A., Piles, M., Amorós-López, J., Muñoz-Marí, J., Adsuara, J.E., Moreno-Martínez, Á., Camps-Valls, G., 2021. Learning main drivers of crop progress and failure in Europe with interpretable machine learning. Int. J. Appl. Earth Obs. Geoinf. 104, 102574. https://doi.org/10.1016/j.jag.2021.102574

Matheron, G., 1963. Principles of geostatistics. Econ. Geol. https://doi.org/10.2113/gsecongeo.58.8.1246

Meacham-Hensold, K., Montes, C.M., Wu, J., Guan, K., Fu, P., Ainsworth, E.A., Pederson, T., Moore, C.E., Brown, K.L., Raines, C., Bernacchi, C.J., 2019. High-throughput field phenotyping using hyperspectral reflectance and partial least squares regression (PLSR) reveals genetic modifications to photosynthetic capacity. Remote Sens. Environ. 231, 111176. https://doi.org/10.1016/j.rse.2019.04.029

Meroni, M., Barducci, A., Cogliati, S., Castagnoli, F., Rossini, M., Busetto, L., Migliavacca, M., Cremonese, E., Galvagno, M., Colombo, R., Di Cella, U.M., 2011. The hyperspectral irradiometer, a new instrument for long-term and unattended field spectroscopy measurements. Rev. Sci. Instrum. 82. https://doi.org/10.1063/1.3574360

Meroni, M., Busetto, L., Colombo, R., Guanter, L., Moreno, J., Verhoef, W., 2010. Performance of Spectral Fitting Methods for vegetation fluorescence quantification. Remote Sens. Environ. 114, 363–374. https://doi.org/10.1016/j.rse.2009.09.010

Meroni, M., Rossini, M., Guanter, L., Alonso, L., Rascher, U., Colombo, R., Moreno, J., 2009. Remote sensing of solar-induced chlorophyll fluorescence: Review of methods and applications. Remote Sens. Environ. 113, 2037–2051. https://doi.org/10.1016/j.rse.2009.05.003

Metzger, S., Ayres, E., Durden, D., Florian, C., Lee, R., Lunch, C., Luo, H., Pingintha-Durden, N., Roberti, J.A., SanClements, M., Sturtevant, C., Xu, K., Zulueta, R.C., 2019. From neon field sites to data portal: A community resource for surface-atmosphere research comes online. Bull. Am. Meteorol. Soc. 100, 2305–2325. https://doi.org/10.1175/BAMS-D-17-0307.1

Mevik, B.H., Wehrens, R., 2007. The pls package: Principal component and partial least squares regression in R. J. Stat. Softw. 18, 1–23. https://doi.org/10.18637/jss.v018.i02

Middleton, E.M., Rascher, U., Corp, L.A., Huemmrich, K.F., Cook, B.D., Noormets, A., Schickling, A., Pinto, F., Alonso, L., Damm, A., Guanter, L., Colombo, R., Campbell, P.K.E., Landis, D.R., Zhang, Q., Rossini, M., Schuettemeyer, D., Bianchi, R., 2017. The 2013 FLEX-US airborne campaign at the parker tract loblolly pine plantation in North Carolina, USA. Remote Sens. https://doi.org/10.3390/rs9060612

Migliavacca, M., Perez-Priego, O., Rossini, M., El-Madany, T.S., Moreno, G., van der Tol, C., Rascher, U., Berninger, A., Bessenbacher, V., Burkart, A., Carrara, A., Fava, F., Guan, J.H., Hammer, T.W., Henkel, K., Juarez-Alcalde, E., Julitta, T., Kolle, O., Martín, M.P., Musavi, T., Pacheco-Labrador, J., Pérez-Burgueño, A., Wutzler, T., Zaehle, S., Reichstein, M., 2017. Plant functional traits and canopy structure control the relationship between photosynthetic CO2 uptake and far-red sun-induced fluorescence in a Mediterranean grassland under different nutrient availability. New Phytol. 214, 1078–1091. https://doi.org/10.1111/nph.14437

Mihai, L., Mac Arthur, A.A., Hueni, A., Robinson, I., Sporea, D., 2018. Optimized spectrometers characterization procedure for near ground support of ESA FLEX observations: Part 1 spectral calibration and characterisation. Remote Sens. https://doi.org/10.3390/rs10020289

Milton, E.J., 1987. Principles of field spectroscopy. Int. J. Remote Sens. 8, 1807–1827. https://doi.org/10.1080/01431168708954818

Milton, E.J., Schaepman, M.E., Anderson, K., Fox, N., 2009. Progress in field spectroscopy. Remote Sens. Environ. 113, S92–S109. https://doi.org/10.1016/j.rse.2007.08.001

Mohammad, L., Bandyopadhyay, J., Sk, R., Mondal, I., Nguyen, T.T., Lama, G.F.C., Anh, D.T., 2023. Estimation of agricultural burned affected area using NDVI and dNBR satellite-based empirical models. J. Environ. Manage. 343, 118226. https://doi.org/https://doi.org/10.1016/j.jenvman.2023.118226

Mohammed, G.H., Colombo, R., Middleton, E.M., Rascher, U., van der Tol, C., Nedbal, L., Goulas, Y., Pérez-Priego, O., Damm, A., Meroni, M., Joiner, J., Cogliati, S., Verhoef, W., Malenovský, Z., Gastellu-Etchegorry, J.P., Miller, J.R., Guanter, L., Moreno, J., Moya, I., Berry, J.A., Frankenberg, C., Zarco-Tejada, P.J., 2019. Remote sensing of solar-induced chlorophyll fluorescence (SIF) in vegetation: 50 years of progress. Remote Sens. Environ. 231. https://doi.org/10.1016/j.rse.2019.04.030

Moharana, S., Dutta, S., 2014. Hyperspectral remote sensing of paddy crop using in-situ measurement and clustering technique, in: International Archives of the Photogrammetry, Remote Sensing and Spatial Information Sciences - ISPRS Archives. International Society for Photogrammetry and Remote Sensing, pp. 845–851. https://doi.org/10.5194/isprsarchives-XL-8-845-2014

Mou, L., Ghamisi, P., Zhu, X.X., 2017. Deep recurrent neural networks for hyperspectral image classification. IEEE Trans. Geosci. Remote Sens. 55, 3639–3655. https://doi.org/10.1109/TGRS.2016.2636241

Muhammad, S., Long, X., Salman, M., 2020. COVID-19 pandemic and environmental pollution: A blessing in disguise? Sci. Total Environ. 728, 138820. https://doi.org/10.1016/j.scitotenv.2020.138820

Mulla, D.J., 2013. Twenty five years of remote sensing in precision agriculture: Key advances and remaining knowledge gaps. Biosyst. Eng. 114, 358–371. https://doi.org/10.1016/j.biosystemseng.2012.08.009

Murphy, J.M., Maggioni, M., 2019. Unsupervised Clustering and Active Learning of Hyperspectral Images with Nonlinear Diffusion. IEEE Trans. Geosci. Remote Sens. 57, 1829–1845.

https://doi.org/10.1109/TGRS.2018.2869723

Musavi, T., Migliavacca, M., van de Weg, M.J., Kattge, J., Wohlfahrt, G., van Bodegom, P.M., Reichstein, M., Bahn, M., Carrara, A., Domingues, T.F., Gavazzi, M., Gianelle, D., Gimeno, C., Granier, A., Gruening, C., Havránková, K., Herbst, M., Hrynkiw, C., Kalhori, A., Kaminski, T., Klumpp, K., Kolari, P., Longdoz, B., Minerbi, S., Montagnani, L., Moors, E., Oechel, W.C., Reich, P.B., Rohatyn, S., Rossi, A., Rotenberg, E., Varlagin, A., Wilkinson, M., Wirth, C., Mahecha, M.D., 2016. Potential and limitations of inferring ecosystem photosynthetic capacity from leaf functional traits. Ecol. Evol. 6, 7352–7366. https://doi.org/10.1002/ece3.2479

Naethe, P., Asgari, M., Kneer, C., Knieps, M., Jenal, A., Weber, I., Moelter, T., Dzunic, F., Deffert, P., Rommel, E., Delaney, M., Baschek, B., Rock, G., Bongartz, J., Burkart, A., 2023. Calibration and Validation from Ground to Airborne and Satellite Level: Joint Application of Time-Synchronous Field Spectroscopy, Drone, Aircraft and Sentinel-2 Imaging. PFG – J. Photogramm. Remote Sens. Geoinf. Sci. https://doi.org/10.1007/s41064-022-00231-x

Naethe, P., De Sanctis, A., Burkart, A., Campbell, P.K.E., Colombo, R., Di Mauro, B., Damm, A., El-Madany, T., Fava, F., Gamon, J.A., Huemmrich, K.F., Migliavacca, M., Paul-Limoges, E., Rascher, U., Rossini, M., Schüttemeyer, D., Tagliabue, G., Zhang, Y., Julitta, T., 2024. Towards a standardized, ground-based network of hyperspectral measurements: Combining time series from autonomous field spectrometers with Sentinel-2. Remote Sens. Environ. 303, 114013. https://doi.org/10.1016/j.rse.2024.114013

Naethe, P., Delaney, M., Julitta, T., 2020. Changes of NOx in urban air detected with monitoring VIS-NIR field spectrometer during the coronavirus pandemic: A case study in Germany. Sci. Total Environ. 748, 141286. https://doi.org/10.1016/j.scitotenv.2020.141286

Naethe, P., Julitta, T., Chang, C.Y.Y., Burkart, A., Migliavacca, M., Guanter, L., Rascher, U., 2022. A precise method unaffected by atmospheric reabsorption for ground-based retrieval of red and far-red sun-induced chlorophyll fluorescence. Agric. For. Meteorol. 325. https://doi.org/10.1016/j.agrformet.2022.109152

Nagai, S., Nasahara, K.N., Akitsu, T.K., Saitoh, T.M., Muraoka, H., 2020. Importance of the Collection of Abundant Ground-Truth Data for Accurate Detection of Spatial and Temporal Variability of Vegetation by Satellite Remote Sensing, in: Biogeochemical Cycles: Ecological Drivers and Environmental Impact. wiley, pp. 223–244. https://doi.org/10.1002/9781119413332.ch11

Nichol, C.J., Drolet, G., Porcar-Castell, A., Wade, T., Sabater, N., Middleton, E.M., MacLellan, C., Levula, J., Mammarella, I., Vesala, T., Atherton, J., 2019. Diurnal and seasonal solar induced chlorophyll fluorescence and photosynthesis in a boreal scots pine canopy. Remote Sens. 11.

https://doi.org/10.3390/rs11030273

Niinemets, Ü., 2010. Responses of forest trees to single and multiple environmental stresses from seedlings to mature plants: Past stress history, stress interactions, tolerance and acclimation. For. Ecol. Manage. 260, 1623–1639. https://doi.org/10.1016/j.foreco.2010.07.054

Nock, R., Magdalou, B., Briys, E., Nielsen, F., 2013. Matrix Information Geometry. pp. 373–402. https://doi.org/10.1007/978-3-642-30232-9

Norton, A.J., Rayner, P.J., Koffi, E.N., Scholze, M., Silver, J.D., Wang, Y.-P., 2019. Estimating global gross primary productivity using chlorophyll fluorescence and a data assimilation system with the BETHY-SCOPE model. Biogeosciences Discuss. 1–45. https://doi.org/10.5194/bg-2019-83

Ogen, Y., 2020. Assessing nitrogen dioxide (NO2) levels as a contributing factor to coronavirus (COVID-19) fatality. Sci. Total Environ. 726, 138605. https://doi.org/10.1016/j.scitotenv.2020.138605

Olsson, P.-O., Vivekar, A., Adler, K., Garcia Millan, V.E., Koc, A., Alamrani, M., Eklundh, L., 2021. Radiometric Correction of Multispectral UAS Images: Evaluating the Accuracy of the Parrot Sequoia Camera and Sunshine Sensor. Remote Sens. 13, 577. https://doi.org/10.3390/rs13040577

Origo, N., Gorroño, J., Ryder, J., Nightingale, J., Bialek, A., 2020. Fiducial Reference Measurements for validation of Sentinel-2 and Proba-V surface reflectance products. Remote Sens. Environ. 241. https://doi.org/10.1016/j.rse.2020.111690

Oxoli, D., Brovelli, M.A., Frizzi, D., Martinati, S., 2020. Detection of land cover displacements through time-series analysis of multispectral satellite imagery: Application to desert, in: International Archives of the Photogrammetry, Remote Sensing and Spatial Information Sciences - ISPRS Archives. International Society for Photogrammetry and Remote Sensing, pp. 739–744. https://doi.org/10.5194/isprs-archives-XLIII-B3-2020-739-2020

Pacheco-Labrador, J., Hueni, A., Mihai, L., Sakowska, K., Julitta, T., Kuusk, J., Sporea, D., Alonso, L., Burkart, A., Cendrero-Mateo, M.P., Aasen, H., Goulas, Y., Mac Arthur, A. Mac, Pacheco-Labrador, J., Hueni, A., Mihai, L., Sakowska, K., Julitta, T., Kuusk, J., Sporea, D., Alonso, L., Burkart, A., Cendrero-Mateo, M.P., Aasen, H., Goulas, Y., Mac Arthur, A.A., 2019a. Sun-Induced Chlorophyll Fluorescence I: Instrumental Considerations for Proximal Spectroradiometers. Remote Sens. 11, 960. https://doi.org/10.3390/rs11080960

Pacheco-Labrador, J., Martin, M.P., 2014. Nonlinear response in a field portable spectroradiometer: Characterization and effects on output reflectance. IEEE Trans. Geosci. Remote Sens. 52, 920–928. https://doi.org/10.1109/TGRS.2013.2245671

Pacheco-Labrador, J., Martín, M.P., 2015. Characterization of a field spectroradiometer for unattended vegetation monitoring. Key sensor models and impacts on reflectance. Sensors (Switzerland) 15, 4154–4175. https://doi.org/10.3390/s150204154

Pacheco-Labrador, J., Martïn, M.P., Riaïo, D., Hilker, T., Carrara, A., 2016. New approaches in multi-angular proximal sensing of vegetation: Accounting for spatial heterogeneity and diffuse radiation in directional reflectance distribution models. Remote Sens. Environ. https://doi.org/10.1016/j.rse.2016.10.051

Pacheco-Labrador, J., Perez-Priego, O., El-Madany, T.S., Julitta, T., Rossini, M., Guan, J., Moreno, G., Carvalhais, N., Martín, M.P., Gonzalez-Cascon, R., Kolle, O., Reischtein, M., van der Tol, C., Carrara, A., Martini, D., Hammer, T.W., Moossen, H., Migliavacca, M., 2019b. Multiple-constraint inversion of SCOPE. Evaluating the potential of GPP and SIF for the retrieval of plant functional traits. Remote Sens. Environ. 234. https://doi.org/10.1016/j.rse.2019.111362

Painter, T.H., Dozier, J., 2004. Measurements of the hemispherical-directional reflectance of snow at fine spectral and angular resolution. J. Geophys. Res. Atmos. 109. https://doi.org/10.1029/2003JD004458

Park, H.-J., Park, J.-S., Kim, S.-W., Chong, H., Lee, H., Kim, H., Ahn, J.-Y., Kim, D.-G., Kim, J., Park, S.S., 2019. Retrieval of NO2 Column Amounts from Ground-Based Hyperspectral Imaging Sensor Measurements. Remote Sens. 11, 3005. https://doi.org/10.3390/rs11243005

Peano, D., Hemming, D., Materia, S., Delire, C., Fan, Y., Joetzjer, E., Lee, H., Nabel, J.E.M.S., Park, T., Peylin, P., Wärlind, D., Wiltshire, A., Zaehle, S., 2021. Plant phenology evaluation of CRESCENDO land surface models-Part 1: Start and end of the growing season. Biogeosciences 18, 2405–2428. https://doi.org/10.5194/bg-18-2405-2021

Peddle, D.R., White, H.P., Soffer, R.J., Miller, J.R., Ledrew, E.F., 2001. Reflectance processing of remote sensing spectroradiometer data. Comput. Geosci. 27, 203–213.

Peine, J.D., Jacobs, B.L., Franzreb, K.E., Stevens, M.R., 2011. Ecosystem Management. Berksh. Encycl. Sustain. 5/10 Ecosyst. Manag. Sustain.

Peltoniemi, M., Aurela, M., Böttcher, K., Kolari, P., Loehr, J., Karhu, J., 2018. Webcam network and image database for studies of phenological changes of vegetation and snow cover in Finland , image time series from 2014 to 2016 173–184.

Peng, H., Cendrero-Mateo, M.P., Bendig, J., Siegmann, B., Acebron, K., Kneer, C., Kataja, K., Muller, O., Rascher, U., 2022. HyScreen: A Ground-Based Imaging System for High-Resolution Red and Far-Red Solar-Induced Chlorophyll Fluorescence. Sensors 22. https://doi.org/10.3390/s22239443

Pérez-Harguindeguy, N., Díaz, S., Garnier, E., Lavorel, S., Poorter, H., Jaureguiberry, P., Bret-Harte, M.S., Cornwell, W.K., Craine, J.M., Gurvich, D.E., Urcelay, C., Veneklaas, E.J., Reich, P.B., Poorter, L., Wright, I.J., Ray, P., Enrico, L., Pausas, J.G., De Vos, A.C., Buchmann, N., Funes, G., Quétier, F., Hodgson, J.G., Thompson, K., Morgan, H.D., Ter Steege, H., Van Der Heijden, M.G.A., Sack, L., Blonder, B., Poschlod, P., Vaieretti, M. V., Conti, G., Staver, A.C., Aquino, S., Cornelissen, J.H.C., 2013. New handbook for standardised measurement of plant functional traits worldwide. Aust. J. Bot. https://doi.org/10.1071/BT12225

Perez-Priego, O., Guan, J., Rossini, M., Fava, F., Wutzler, T., Moreno, G., Carvalhais, N., Carrara, A., Kolle, O., Julitta, T., Schrumpf, M., Reichstein, M., Migliavacca, M., 2015. Sun-induced chlorophyll fluorescence and photochemical reflectance index improve remote-sensing gross primary production estimates under varying nutrient availability in a typical Mediterranean savanna ecosystem. Biogeosciences. https://doi.org/10.5194/bg-12-6351-2015

Petitjean, F., Weber, J., 2014. Efficient satellite image time series analysis under time warping. IEEE Geosci. Remote Sens. Lett. 11, 1143–1147. https://doi.org/10.1109/LGRS.2013.2288358

Picard, G., Dumont, M., Lamare, M., Tuzet, F., Larue, F., Pirazzini, R., Arnaud, L., 2020. Spectral albedo measurements over snow-covered slopes: Theory and slope effect corrections. Cryosphere 14, 1497–1517. https://doi.org/10.5194/tc-14-1497-2020

Picard, G., Libois, Q., Arnaud, L., Verin, G., Dumont, M., 2016. Development and calibration of an automatic spectral albedometer to estimate near-surface snow SSA time series. Cryosphere 10, 1297–1316. https://doi.org/10.5194/tc-10-1297-2016

Pieruschka, R., Albrecht, H., Muller, O., Berry, J.A., Klimov, D., Kolber, Z.S., Malenovský, Z., Rascher, U., 2014. Daily and seasonal dynamics of remotely sensed photosynthetic efficiency in tree canopies. Mol. Hum. Reprod. 34. https://doi.org/10.1093/treephys/tpu035

Pinter, P.J., Jackson, R.D., Idso, S.B., Reginato, R.J., 1983. Diurnal Patterns of Wheat Spectral Reflectances. IEEE Trans. Geosci. Remote Sens. https://doi.org/10.1109/TGRS.1983.350484

Pirone, D., Cimorelli, L., Del Giudice, G., Pianese, D., 2023. Short-term rainfall forecasting using cumulative precipitation fields from station data: a probabilistic machine learning approach. J. Hydrol. 617, 128949. https://doi.org/https://doi.org/10.1016/j.jhydrol.2022.128949

Plascyk, J.A., Gabriel, F.C., 1975. The Fraunhofer Line Discriminator MKII-An Airborne Instrument for Precise and Standardized Ecological Luminescence Measurement. IEEE Trans. Instrum. Meas. 24, 306–313. https://doi.org/10.1109/TIM.1975.4314448

Pompilio, L., Marinangeli, L., Amitrano, L., Pacci, G., D'Andrea, S., Iacullo, S., Monaco, E., 2018.

Application of the empirical line method (ELM) to calibrate the airborne Daedalus-CZCS scanner. Eur. J. Remote Sens. 51, 33–46. https://doi.org/10.1080/22797254.2017.1399087

Pompilio, L., Pepe, M., Pedrazzi, G., Marinangeli, L., 2014. Informational clustering of hyperspectral data. IEEE J. Sel. Top. Appl. Earth Obs. Remote Sens. 7, 2209–2223. https://doi.org/10.1109/JSTARS.2013.2294053

Porcar-Castell, A., Mac Arthur, A., Rossini, M., Eklundh, L., Pacheco-Labrador, J., Anderson, K., Balzarolo, M., Martín, M.P., Jin, H., Tomelleri, E., Cerasoli, S., Sakowska, K., Hueni, A., Julitta, T., Nichol, C.J., Vescovo, L., 2015. EUROSPEC: At the interface between remote-sensing and ecosystem CO2flux measurements in Europe. Biogeosciences 12, 6103–6124. https://doi.org/10.5194/bg-12-6103-2015

Porcar-Castell, A., Tyystjärvi, E., Atherton, J., Van Der Tol, C., Flexas, J., Pfündel, E.E., Moreno, J., Frankenberg, C., Berry, J.A., 2014. Linking chlorophyll a fluorescence to photosynthesis for remote sensing applications: Mechanisms and challenges. J. Exp. Bot. https://doi.org/10.1093/jxb/eru191

R Core Team, 2017. R: A Language and Environment for Statistical Computing. R Foundation for Statistical Computing, Vienna, Austria.

Rahman, A.F., Gamon, J.A., Fuentes, D.A., Roberts, D.A., Prentiss, D., 2001. Modeling spatially distributed ecosystem flux of boreal forest using hyperspectral indices from AVIRIS imagery. J. Geophys. Res. Atmos. 106, 33579–33591. https://doi.org/10.1029/2001JD900157

Rascher, U., Agati, G., Alonso, L., Cecchi, G., Champagne, S., Colombo, R., Damm, A., Daumard, F., de Miguel, E., Fernandez, G., Franch, B., Franke, J., Gerbig, C., Gioli, B., Gómez, J.A., Goulas, Y., Guanter, L., Gutiérrez-de-la-Cámara, Ó., Hamdi, K., Hostert, P., Jiménez, M., Kosvancova, M., Lognoli, D., Meroni, M., Miglietta, F., Moersch, A., Moreno, J., Moya, I., Neininger, B., Okujeni, A., Ounis, A., Palombi, L., Raimondi, V., Schickling, A., Sobrino, J.A., Stellmes, M., Toci, G., Toscano, P., Udelhoven, T., van der Linden, S., Zaldei, A., 2009. CEFLES2: the remote sensing component to quantify photosynthetic efficiency from the leaf to the region by measuring sun-induced fluorescence in the oxygen absorption bands. Biogeosciences 6, 1181–1198. https://doi.org/10.5194/bg-6-1181-2009

Rascher, U., Alonso, L., Burkart, A., Cilia, C., Cogliati, S., Colombo, R., Damm, A., Drusch, M., Guanter, L., Hanus, J., Hyv??rinen, T., Julitta, T., Jussila, J., Kataja, K., Kokkalis, P., Kraft, S., Kraska, T., Matveeva, M., Moreno, J., Muller, O., Panigada, C., Pikl, M., Pinto, F., Prey, L., Pude, R., Rossini, M., Schickling, A., Schurr, U., Sch??ttemeyer, D., Verrelst, J., Zemek, F., 2015. Sun-induced fluorescence - a new probe of photosynthesis: First maps from the imaging spectrometer

HyPlant. Glob. Chang. Biol. 21, 4673–4684. https://doi.org/10.1111/gcb.13017

Rascher, U., Damm, A., van der Linden, S., Okujeni, A., Pieruschka, R., Schickling, A., Hostert, P., 2010. Sensing of Photosynthetic Activity of Crops, in: Precision Crop Protection - the Challenge and Use of Heterogeneity. Springer Netherlands, Dordrecht, pp. 87–99. https://doi.org/10.1007/978-90-481-9277-9_6

Rascher, U., Pieruschka, R., 2008. Spatio-temporal variations of photosynthesis: the potential of optical remote sensing to better understand and scale light use efficiency and stresses of plant ecosystems. Precis. Agric. 9, 355–366. https://doi.org/10.1007/s11119-008-9074-0

Rautiainen, M., Lukeš, P., Homolová, L., Hovi, A., Pisek, J., Mõttus, M., 2018. Spectral properties of coniferous forests: A review of in situ and laboratory measurements. Remote Sens. https://doi.org/10.3390/rs10020207

Rejichi, S., Chaabane, F., 2015. Satellite image time series classification and analysis using an adapted graph labeling, in: 2015 8th International Workshop on the Analysis of Multitemporal Remote Sensing Images, Multi-Temp 2015. Institute of Electrical and Electronics Engineers Inc. https://doi.org/10.1109/Multi-Temp.2015.7245747

Richter, R., Schläpfer, D., 2002. Geo-atmospheric processing of airborne imaging spectrometry data Part 2: atmospheric / topographic correction. Int. J. Remote Sens. 23. https://doi.org/https://doi.org/10.1080/01431160110115834

Rivera-Caicedo, J.P., Verrelst, J., Munoz-Mari, J., Moreno, J., Camps-Valls, G., 2014. Toward a semiautomatic machine learning retrieval of biophysical parameters. IEEE J. Sel. Top. Appl. Earth Obs. Remote Sens. 7, 1249–1259. https://doi.org/10.1109/JSTARS.2014.2298752

Rivera, J., Verrelst, J., Gómez-Dans, J., Muñoz-Marí, J., Moreno, J., Camps-Valls, G., 2015. An Emulator Toolbox to Approximate Radiative Transfer Models with Statistical Learning. Remote Sens. 7, 9347–9370. https://doi.org/10.3390/rs70709347

Roberts, D.A., Numata, I., Holmes, K., Batista, G., Krug, T., Monteiro, A., Powell, B., Chadwick, O.A., 2002. Large area mapping of land-cover change in Rondônia using multitemporal spectral mixture analysis and decision tree classifiers. J. Geophys. Res. Atmos. 107, LBA 40-1-LBA 40-18. https://doi.org/10.1029/2001JD000374

Rollin, E.M., Emery, D.R., Milton, E.J., 2000. Reference panel anisotropy and diffuse radiation - some implications for field spectroscopy. Int. J. Remote Sens. 21, 2799–2810. https://doi.org/10.1080/01431160050121258

Rommel, E., Giese, L., Fricke, K., Kathöfer, F., Heuner, M., Mölter, T., Deffert, P., Asgari, M., Näthe, P., Dzunic, F., Rock, G., Bongartz, J., Burkart, A., Quick, I., Schröder, U., Baschek, B., 2022. Very High-Resolution Imagery and Machine Learning for Detailed Mapping of Riparian Vegetation and Substrate Types. Remote Sens. 14, 954. https://doi.org/10.3390/rs14040954

Rossini, M., Meroni, M., Migliavacca, M., Manca, G., Cogliati, S., Busetto, L., Picchi, V., Cescatti, A., Seufert, G., Colombo, R., 2010. High resolution field spectroscopy measurements for estimating gross ecosystem production in a rice field. Agric. For. Meteorol. 150, 1283–1296. https://doi.org/10.1016/j.agrformet.2010.05.011

Rossini, M., Nedbal, L., Guanter, L., Ac, A., Alonso, L., Burkart, A., Cogliati, S., Colombo, R., Damm, A., Drusch, M., Hanus, J., Janoutova, R., Julitta, T., Kokkalis, P., Moreno, J., Novotny, J., Panigada, C., Pinto, F., Schickling, A., Sch??ttemeyer, D., Zemek, F., Rascher, U., 2015. Red and far red Sun-induced chlorophyll fluorescence as a measure of plant photosynthesis. Geophys. Res. Lett. 42, 1632–1639. https://doi.org/10.1002/2014GL062943

Roth, L., Hund, A., Aasen, H., 2018. PhenoFly Planning Tool : flight planning for high - resolution optical remote sensing with unmanned areal systems. Plant Methods. https://doi.org/10.1186/s13007-018-0376-6

Sabater, N., Vicent, J., Alonso, L., Cogliati, S., Verrelst, J., Moreno, J., 2017. Impact of atmospheric inversion effects on solar-induced chlorophyll fluorescence: Exploitation of the apparent reflectance as a quality indicator. Remote Sens. 9. https://doi.org/10.3390/rs9060622

Sabater, N., Vicent, J., Alonso, L., Verrelst, J., Middleton, E., Porcar-Castell, A., Moreno, J., 2018. Compensation of Oxygen Transmittance Effects for Proximal Sensing Retrieval of Canopy–Leaving Sun–Induced Chlorophyll Fluorescence. Remote Sens. 10, 1551. https://doi.org/10.3390/rs10101551

Schaepman-Strub, G., Schaepman, M.E., Martonchik, J., Painter, T., Dangel, S., 2008. Radiometry and Reflectance: From Terminology Concepts to Measured Quantities, in: Warner, T.A., Nellis, M.D., Foody, G.M. (Eds.), The SAGE Handbook of Remote Sensing. Sage, pp. 215–228. https://doi.org/10.4135/9780857021052.n15

Schaepman, M.E., Dangel, S., 2000. Solid laboratory calibration of a nonimaging spectroradiometer. Appl. Opt. 39, 3754–3764. https://doi.org/10.1364/AO.39.003754

Schläpfer, D., Popp, C., Richter, R., 2020a. Drone data atmospheric correction concept for multi-and hyperspectral imagery-The droacor model, in: International Archives of the Photogrammetry, Remote Sensing and Spatial Information Sciences - ISPRS Archives. International Society for

Photogrammetry and Remote Sensing, pp. 473–478. https://doi.org/10.5194/isprs-archives-XLIII-B3-2020-473-2020

Schläpfer, D., Richter, R., 2002. Geo-atmospheric processing of airborne imaging spectrometry data Part 1: parametric orthorectification. Int. J. Remote Sens. 23. https://doi.org/10.1080/01431160110115825

Schläpfer, D., Richter, R., Reinartz, P., 2020b. Elevation-dependent removal of cirrus clouds in satellite imagery. Remote Sens. 12. https://doi.org/10.3390/rs12030494

Schlesinger, W.H., Bernhardt, E.S., Schlesinger, W.H., Bernhardt, E.S., 2013. The Biosphere: The Carbon Cycle of Terrestrial Ecosystems, in: Biogeochemistry. Academic Press, pp. 135–172. https://doi.org/10.1016/B978-0-12-385874-0.00005-4

Schmidtlein, S., Zimmermann, ;, Schüpferling, ;, Weiß, &, 2007. Mapping the floristic continuum: Ordination space position estimated from imaging spectroscopy. J. Veg. Sci. 18, 131–140.

Schmitt, M., Zhu, X.X., 2016. Data Fusion and Remote Sensing: An ever-growing relationship. IEEE Geosci. Remote Sens. Mag. https://doi.org/10.1109/MGRS.2016.2561021

Schneider, P., Castell, N., Vogt, M., Dauge, F.R., Lahoz, W.A., Bartonova, A., 2017. Mapping urban air quality in near real-time using observations from low-cost sensors and model information. Environ. Int. 106, 234–247. https://doi.org/10.1016/j.envint.2017.05.005

Scodellaro, R., Cesana, I., D'Alfonso, L., Bouzin, M., Collini, M., Chirico, G., Colombo, R., Miglietta, F., Celesti, M., Schuettemeyer, D., Cogliati, S., Sironi, L., 2022. A novel hybrid machine learning phasor-based approach to retrieve a full set of solar-induced fluorescence metrics and biophysical parameters. Remote Sens. Environ. 280. https://doi.org/10.1016/j.rse.2022.113196

Sefrin, O., Riese, F.M., Keller, S., 2021. Deep learning for land cover change detection. Remote Sens. 13, 1–27. https://doi.org/10.3390/rs13010078

Seidl, R., Thom, D., Kautz, M., Martin-Benito, D., Peltoniemi, M., Vacchiano, G., Wild, J., Ascoli, D., Petr, M., Honkaniemi, J., Lexer, M.J., Trotsiuk, V., Mairota, P., Svoboda, M., Fabrika, M., Nagel, T.A., Reyer, C.P.O., 2017. Forest disturbances under climate change. Nat. Clim. Chang. 7, 395–402. https://doi.org/10.1038/nclimate3303

Serbin, S.P., Dillaway, D.N., Kruger, E.L., Townsend, P.A., 2012. Leaf optical properties reflect variation in photosynthetic metabolism and its sensitivity to temperature. J. Exp. Bot. 63, 489–502. https://doi.org/10.1093/jxb/err294

Serbin, S.P., Townsend, P.A., 2020. Scaling functional traits from leaves to canopies, in: Remote Sensing

of Plant Biodiversity. Springer International Publishing, pp. 43–82. https://doi.org/10.1007/978-3-030-33157-3_3

Serbin, S.P., Wu, J., Ely, K.S., Kruger, E.L., Townsend, P.A., Meng, R., Wolfe, B.T., Chlus, A., Wang, Z., Rogers, A., 2019. From the Arctic to the tropics: multibiome prediction of leaf mass per area using leaf reflectance. New Phytol. 224, 1557–1568. https://doi.org/10.1111/nph.16123

Shahtahmassebi, A., Yang, N., Wang, K., Moore, N., Shen, Z., 2013. Review of shadow detection and de-shadowing methods in remote sensing. Chinese Geogr. Sci. 23, 403–420. https://doi.org/10.1007/s11769-013-0613-x

Shi, P., Castaldi, F., Van Wesemael, B., Oost, K. Van, 2020. Large-Scale, High-Resolution Mapping of Soil Aggregate Stability in Croplands Using APEX Hyperspectral Imagery. Remote Sens. 12. https://doi.org/10.3390/rs12040666

Siegmann, B., Alonso, L., Celesti, M., Cogliati, S., Colombo, R., Damm, A., Douglas, S., Guanter, L., Hanuš, J., Kataja, K., Kraska, T., Matveeva, M., Moreno, J., Muller, O., Pikl, M., Pinto, F., Quirós Vargas, J., Rademske, P., Rodriguez-Morene, F., Sabater, N., Schickling, A., Schüttemeyer, D., Zemek, F., Rascher, U., 2019. The High-Performance Airborne Imaging Spectrometer HyPlant—From Raw Images to Top-of-Canopy Reflectance and Fluorescence Products: Introduction of an Automatized Processing Chain. Remote Sens. 11, 2760. https://doi.org/10.3390/rs11232760

Siegmann, B., Cendrero-Mateo, M.P., Cogliati, S., Damm, A., Gamon, J., Herrera, D., Jedmowski, C., Junker-Frohn, L.V., Kraska, T., Muller, O., Rademske, P., van der Tol, C., Quiros-Vargas, J., Yang, P., Rascher, U., 2021. Downscaling of far-red solar-induced chlorophyll fluorescence of different crops from canopy to leaf level using a diurnal data set acquired by the airborne imaging spectrometer HyPlant. Remote Sens. Environ. 264. https://doi.org/10.1016/j.rse.2021.112609

Siegmann, B., Jarmer, T., 2015. Comparison of different regression models and validation techniques for the assessment of wheat leaf area index from hyperspectral data. Int. J. Remote Sens. 36, 4519–4534. https://doi.org/10.1080/01431161.2015.1084438

Singh, A., Serbin, S.P., McNeil, B.E., Kingdon, C.C., Townsend, P.A., 2015. Imaging spectroscopy algorithms for mapping canopy foliar chemical and morphological traits and their uncertainties. Ecol. Appl. 25, 2180–2197. https://doi.org/10.1890/14-2098.1

Sirignano, C., Neubert, R.E.M., Rödenbeck, C., J. Meijer, H.A., 2010. Atmospheric oxygen and carbon dioxide observations from two European coastal stations 2000-2005: Continental influence, trend changes and APO climatology. Atmos. Chem. Phys. 10, 1599–1615. https://doi.org/10.5194/acp-10-1599-2010

Slater, P.N., Biggar, S.F., Holm, R.G., Jackson, R.D., Mao, Y., Palmer, J.M., Yuan, B., 1987. Reflectance- and Radiance-Based Methods for the In-Flight Absolute Calibration of Multispectral Sensors. Remote Sens. Environ. 22, 11–37.

Smith, G., Thomson, A., Möller, I., Kromkamp, J., 2003. Hyperspectral imaging for mapping sediment characteristics, in: Habermeyer M., M.A.. H.S. (Ed.), 3rd EARSeL Workshop on Imaging Spectroscopy, 13-16th May 2003. Herrsching, pp. 439–446.

Soudani, K., François, C., 2014. Remote sensing: A green illusion. Nature. https://doi.org/10.1038/nature13052

Spyrakos, E., O'Donnell, R., Hunter, P.D., Miller, C., Scott, M., Simis, S.G.H., Neil, C., Barbosa, C.C.F., Binding, C.E., Bradt, S., Bresciani, M., Dall'Olmo, G., Giardino, C., Gitelson, A.A., Kutser, T., Li, L., Matsushita, B., Martinez-Vicente, V., Matthews, M.W., Ogashawara, I., Ruiz-Verdú, A., Schalles, J.F., Tebbs, E., Zhang, Y., Tyler, A.N., 2018. Optical types of inland and coastal waters. Limnol. Oceanogr. 63, 846–870. https://doi.org/10.1002/lno.10674

Stow, D., Nichol, C.J., Wade, T., Assmann, J.J., Simpson, G., Helfter, C., 2019. Illumination geometry and flying height influence surface reflectance and ndvi derived from multispectral UAS imagery. Drones 3, 1–28. https://doi.org/10.3390/drones3030055

Sun, Y., Frankenberg, C., Jung, M., Joiner, J., Guanter, L., Köhler, P., Magney, T., 2018. Overview of Solar-Induced chlorophyll Fluorescence (SIF) from the Orbiting Carbon Observatory-2: Retrieval, cross-mission comparison, and global monitoring for GPP. Remote Sens. Environ. 209, 808–823. https://doi.org/10.1016/j.rse.2018.02.016

Sun, Y., Geng, Q., Du, Y., Yang, X., Zhai, H., 2017. Induction of cyclic electron flow around photosystem I during heat stress in grape leaves. Plant Sci. https://doi.org/10.1016/j.plantsci.2016.12.004

Tagliabue, G., Panigada, C., Dechant, B., Baret, F., Cogliati, S., Colombo, R., Migliavacca, M., Rademske, P., Schickling, A., Schüttemeyer, D., Verrelst, J., Rascher, U., Ryu, Y., Rossini, M., 2019. Exploring the spatial relationship between airborne-derived red and far-red sun-induced fluorescence and process-based GPP estimates in a forest ecosystem. Remote Sens. Environ. 231, 111272. https://doi.org/10.1016/j.rse.2019.111272

Therneau, T.M., Atkinson, E.J., 2019. rpart: Recursive Partitioning and Regression Trees. [WWW Document]. R Packag. version 4.1-13. URL https://cran.r-project.org/package=rpart (accessed 5.28.20).

Thuillier, G., Floyd, L., Woods, T.N., Cebula, R., Hilsenrath, E., Hersé, M., Labs, D., 2004. Solar irradiance reference spectra for two solar active levels. Adv. Sp. Res. 34, 256–261.

https://doi.org/10.1016/j.asr.2002.12.004

Trim, S.A., Mason, K., Hueni, A., 2021. Spectroradiometer spectral calibration, ISRF shapes, and related uncertainties. Appl. Opt. 60, 5405. https://doi.org/10.1364/ao.425676

Tucker, C.J., 1979. Red and photographic infrared linear combinations for monitoring vegetation. Remote Sens. Environ. 8, 127–150. https://doi.org/10.1016/0034-4257(79)90013-0

Turner, D., Lucieer, A., De Jong, S.M., 2015. Time Series Analysis of Landslide Dynamics Using an Unmanned Aerial Vehicle (UAV). Remote Sens. 7, 1736–1757. https://doi.org/10.3390/rs70201736

Ustin, S.L., Roberts, D.A., Gamon, J.A., Asner, G.P., Green, R.O., 2004. Using Imaging Spectroscopy to Study Ecosystem Processes and Properties, BioScience.

van der Tol, C., Julitta, T., Yang, P., Sabater, N., Reiter, I., Tudoroiu, M., Schuettemeyer, D., Drusch, M., 2023. Retrieval of chlorophyll fluorescence from a large distance using oxygen absorption bands. Remote Sens. Environ. 284. https://doi.org/10.1016/j.rse.2022.113304

van der Tol, C., Rossini, M., Cogliati, S., Verhoef, W., Colombo, R., Rascher, U., Mohammed, G., 2016. A model and measurement comparison of diurnal cycles of sun-induced chlorophyll fluorescence of crops. Remote Sens. Environ. 186. https://doi.org/10.1016/j.rse.2016.09.021

van der Tol, C., Verhoef, W., Timmermans, J., Verhoef, A., Su, Z., 2009. An integrated model of soil-canopy spectral radiances, photosynthesis, fluorescence, temperature and energy balance. Biogeosciences 6, 3109–3129.

Van Wittenberghe, S., Alonso, L., Verrelst, J., Moreno, J., Samson, R., 2015. Bidirectional sun-induced chlorophyll fluorescence emission is influenced by leaf structure and light scattering properties — A bottom-up approach. Remote Sens. Environ. 158, 169–179. https://doi.org/10.1016/j.rse.2014.11.012

Van Wittenberghe, S., Sabater, N., Cendrero-Mateo, M.P., Tenjo, C., Moncholi, A., Alonso, L., Moreno, J., 2021. Towards the quantitative and physically-based interpretation of solar-induced vegetation fluorescence retrieved from global imaging. Photosynthetica. https://doi.org/10.32615/ps.2021.034

Vanderbilt, V.C., Ambrosia, V.G., Ustin, S.L., 1998. Diurnal Reflectance Changes in Vegetation Observed with AVIRIS, in: Green, R.O. (Ed.), Summaries of the Seventh JPL Airborne Earth Science Workshop January 12-16, 1998. Jet Propulsion Lab., California Inst. of Tech.; Pasadena, CA United States, pp. 399–408.

Vargas, J.Q., Bendig, J., Mac Arthur, A.A., Burkart, A., Julitta, T., Maseyk, K., Thomas, R., Siegmann, B., Rossini, M., Celesti, M., Schüttemeyer, D., Kraska, T., Muller, O., Rascher, U., 2020. Unmanned aerial systems (UAS)-based methods for solar induced chlorophyll fluorescence (SIF) retrieval with non-imaging spectrometers: State of the art. Remote Sens. 12. https://doi.org/10.3390/rs12101624

Verhoef, W., van der Tol, C., Middleton, E.M., 2018. Hyperspectral radiative transfer modeling to explore the combined retrieval of biophysical parameters and canopy fluorescence from FLEX – Sentinel-3 tandem mission multi-sensor data. Remote Sens. Environ. 204, 942–963. https://doi.org/10.1016/J.RSE.2017.08.006

Verrelst, J., Muñoz, J., Alonso, L., Delegido, J., Rivera, J.P., Camps-Valls, G., Moreno, J., 2012. Machine learning regression algorithms for biophysical parameter retrieval: Opportunities for Sentinel-2 and -3. Remote Sens. Environ. 118, 127–139. https://doi.org/10.1016/j.rse.2011.11.002

Verrelst, J., Rivera Caicedo, J., Muñoz-Marí, J., Camps-Valls, G., Moreno, J., 2017. SCOPE-Based Emulators for Fast Generation of Synthetic Canopy Reflectance and Sun-Induced Fluorescence Spectra. Remote Sens. 9, 927. https://doi.org/10.3390/rs9090927

Verrelst, J., Rivera, J.P., van der Tol, C., Magnani, F., Mohammed, G., Moreno, J., 2015. Global sensitivity analysis of the SCOPE model: What drives simulated canopy-leaving sun-induced fluorescence? Remote Sens. Environ. 166, 8–21. https://doi.org/10.1016/j.rse.2015.06.002

Verrelst, J., Sabater, N., Rivera, J.P., Muñoz-Marí, J., Vicent, J., Camps-Valls, G., Moreno, J., 2016a. Emulation of leaf, canopy and atmosphere radiative transfer models for fast global sensitivity analysis. Remote Sens. 8, 1–27. https://doi.org/10.3390/rs8080673

Verrelst, J., van der Tol, C., Magnani, F., Sabater, N., Rivera, J.P., Mohammed, G., Moreno, J., 2016b. Evaluating the predictive power of sun-induced chlorophyll fluorescence to estimate net photosynthesis of vegetation canopies: A SCOPE modeling study. Remote Sens. Environ. 176, 139–151. https://doi.org/10.1016/J.RSE.2016.01.018

Viana, M., Rivas, I., Reche, C., Fonseca, A.S., Pérez, N., Querol, X., Alastuey, A., Álvarez-Pedrerol, M., Sunyer, J., 2015. Field comparison of portable and stationary instruments for outdoor urban air exposure assessments. Atmos. Environ. 123, 220–228. https://doi.org/10.1016/j.atmosenv.2015.10.076

Vicent, J., Sabater, N., Tenjo, C., Acarreta, J.R., Manzano, M., Rivera, J.P., Jurado, P., Franco, R., Alonso, L., Verrelst, J., Moreno, J., 2016. FLEX End-to-End Mission Performance Simulator. IEEE Trans. Geosci. Remote Sens. 54, 4215–4223. https://doi.org/10.1109/TGRS.2016.2538300

Vincini, M., Calegari, F., Casa, R., 2016. Sensitivity of leaf chlorophyll empirical estimators obtained at Sentinel-2 spectral resolution for different canopy structures. Precis. Agric. 17, 313–331. https://doi.org/10.1007/s11119-015-9424-7

Viscarra Rossel, R.A., Behrens, T., Ben-Dor, E., Brown, D.J., Demattê, J.A.M., Shepherd, K.D., Shi, Z., Stenberg, B., Stevens, A., Adamchuk, V., Aïchi, H., Barthès, B.G., Bartholomeus, H.M., Bayer, A.D., Bernoux, M., Böttcher, K., Brodský, L., Du, C.W., Chappell, A., Fouad, Y., Genot, V., Gomez, C., Grunwald, S., Gubler, A., Guerrero, C., Hedley, C.B., Knadel, M., Morrás, H.J.M., Nocita, M., Ramirez-Lopez, L., Roudier, P., Campos, E.M.R., Sanborn, P., Sellitto, V.M., Sudduth, K.A., Rawlins, B.G., Walter, C., Winowiecki, L.A., Hong, S.Y., Ji, W., 2016. A global spectral library to characterize the world's soil. Earth-Science Rev. https://doi.org/10.1016/j.earscirev.2016.01.012

Vogtli, M., Schlapfer, D., Richter, R., Hueni, A., Schaepman, M.E., Kneubuhler, M., 2021. About the Transferability of Topographic Correction Methods from Spaceborne to Airborne Optical Data. IEEE J. Sel. Top. Appl. Earth Obs. Remote Sens. 14, 1348–1362. https://doi.org/10.1109/JSTARS.2020.3039327

Von Bueren, S.K., Burkart, A., Hueni, A., Rascher, U., Tuohy, M.P., Yule, I.J., 2015. Deploying four optical UAV-based sensors over grassland: Challenges and limitations. Biogeosciences 12, 163–175. https://doi.org/10.5194/bg-12-163-2015

Wagner, A., Hilgert, S., Kattenborn, T., Fuchs, S., 2018. Proximal VIS-NIR spectrometry to retrieve substance concentrations in surface waters using partial least squares modelling. Water Sci. Technol. Water Supply. https://doi.org/10.2166/ws.2018.177

Wallace, C.S., Dale, M.B., 2005. Hierarchical clusters of vegetation types. Community Ecol. 6, 57–74. https://doi.org/10.1556/ComEc.6.2005.1.7

Wang, B., Jia, K., Liang, S., Xie, X., Wei, X., Zhao, X., Yao, Y., Zhang, X., 2018. Assessment of Sentinel-2 MSI spectral band reflectances for estimating fractional vegetation cover. Remote Sens. 10. https://doi.org/10.3390/rs10121927

Wang, C., Myint, S.W., 2015. A Simplified Empirical Line Method of Radiometric Calibration for Small Unmanned Aircraft Systems-Based Remote Sensing. IEEE J. Sel. Top. Appl. Earth Obs. Remote Sens. 8, 1876–1885. https://doi.org/10.1109/JSTARS.2015.2422716

Wang, N., Suomalainen, J., Bartholomeus, H., Kooistra, L., Masiliūnas, D., Clevers, J.G.P.W., 2021. Diurnal variation of sun-induced chlorophyll fluorescence of agricultural crops observed from a point-based spectrometer on a UAV. Int. J. Appl. Earth Obs. Geoinf. 96, 102276. https://doi.org/10.1016/j.jag.2020.102276

Wang, R., Bowling, D.R., Gamon, J.A., Smith, K.R., Yu, R., Hmimina, G., Ueyama, M., Noormets, A., Kolb, T.E., Richardson, A.D., Bourque, C.P.A., Bracho, R., Blanken, P.D., Black, T.A., Arain, M.A., 2023a. Snow-corrected vegetation indices for improved gross primary productivity assessment in North American evergreen forests. Agric. For. Meteorol. 340, 109600. https://doi.org/https://doi.org/10.1016/j.agrformet.2023.109600

Wang, R., Springer, K.R., Gamon, J.A., 2023b. Confounding effects of snow cover on remotely sensed vegetation indices of evergreen and deciduous trees: An experimental study. Glob. Chang. Biol. https://doi.org/10.1111/gcb.16916

Wang, Y., Yuan, Y., Wang, Q., Liu, C.G., Zhi, Q., Cao, J., 2020. Changes in air quality related to the control of coronavirus in China: Implications for traffic and industrial emissions. Sci. Total Environ. 731, 139133. https://doi.org/10.1016/j.scitotenv.2020.139133

Weber, I., Jenal, A., Kneer, C., Bongartz, J., 2015a. Gyrocopter-based remote sensing platform, in: International Archives of the Photogrammetry, Remote Sensing and Spatial Information Sciences - ISPRS Archives. International Society for Photogrammetry and Remote Sensing, pp. 1333–1337. https://doi.org/10.5194/isprsarchives-XL-7-W3-1333-2015

Weber, I., Jenal, A., Kneer, C., Bongartz, J., 2015b. PANTIR-a dual camera setup for precise georeferencing and mosaicing of thermal aerial images, in: International Archives of the Photogrammetry, Remote Sensing and Spatial Information Sciences - ISPRS Archives. International Society for Photogrammetry and Remote Sensing, pp. 269–272. https://doi.org/10.5194/isprsarchives-XL-3-W2-269-2015

Wemett, B.D., Riek, J.K., Leathers, R.A., 2009. Dynamic thresholding for hyperspectral shadow detection using Levenberg-Marquardt minimization on multiple Gaussian illumination distributions 7334, 733411. https://doi.org/10.1117/12.817826

Wen, J., Köhler, P., Duveiller, G., Parazoo, N.C., Magney, T.S., Hooker, G., Yu, L., Chang, C.Y., Sun, Y., 2020. A framework for harmonizing multiple satellite instruments to generate a long-term global high spatial-resolution solar-induced chlorophyll fluorescence (SIF). Remote Sens. Environ. 239. https://doi.org/10.1016/j.rse.2020.111644

Westoby, M.J., Brasington, J., Glasser, N.F., Hambrey, M.J., Reynolds, J.M., 2012. “Structure-from-Motion” photogrammetry: A low-cost, effective tool for geoscience applications. Geomorphology 179, 300–314. https://doi.org/10.1016/j.geomorph.2012.08.021

Wickham, H., Averick, M., Bryan, J., Chang, W., McGowan, L., François, R., Grolemund, G., Hayes, A., Henry, L., Hester, J., Kuhn, M., Pedersen, T., Miller, E., Bache, S., Müller, K., Ooms, J., Robinson,

D., Seidel, D., Spinu, V., Takahashi, K., Vaughan, D., Wilke, C., Woo, K., Yutani, H., 2019. Welcome to the Tidyverse. J. Open Source Softw. 4, 1686. https://doi.org/10.21105/joss.01686

Wieneke, S., Ahrends, H., Damm, A., Pinto, F., Stadler, A., Rossini, M., Rascher, U., 2016. Airborne based spectroscopy of red and far-red sun-induced chlorophyll fluorescence: Implications for improved estimates of gross primary productivity. Remote Sens. Environ. 184, 654–667. https://doi.org/10.1016/j.rse.2016.07.025

Wieneke, S., Burkart, A., Cendrero-Mateo, M.P., Julitta, T., Rossini, M., Schickling, A., Schmidt, M., Rascher, U., 2018. Linking photosynthesis and sun-induced fluorescence at sub-daily to seasonal scales. Remote Sens. Environ. 219, 247–258. https://doi.org/10.1016/j.rse.2018.10.019

Wiklund, S.S., 2007. Spectroscopic data and multivariate analysis : tools to study genetic perturbations in poplar trees. Department of Chemistry Research Group for Chemometrics, Umeå.

Wilson, G., Aruliah, D.A., Brown, C.T., Chue Hong, N.P., Davis, M., Guy, R.T., Haddock, S.H.D., Huff, K.D., Mitchell, I.M., Plumbley, M.D., Waugh, B., White, E.P., Wilson, P., 2014. Best Practices for Scientific Computing. PLoS Biol. 12. https://doi.org/10.1371/journal.pbio.1001745

Wingate, L., Cremonese, E., Migliavacca, M., Brown, T., Peichl, M., Gielen, B., D'Odorico, P., Hortnagl, L., 2015. Phenocamera: automated phenology monitoring.

Wohlfahrt, G., Gerdel, K., Migliavacca, M., Rotenberg, E., Tatarinov, F., Müller, J., Hammerle, A., Julitta, T., Spielmann, F.M., Yakir, D., 2018. Sun-induced fluorescence and gross primary productivity during a heat wave. Sci. Rep. 8, 14169. https://doi.org/10.1038/s41598-018-32602-z

Yang, K., Ryu, Y., Dechant, B., Berry, J.A., Hwang, Y., Jiang, C., Kang, M., Kim, J., Kimm, H., Kornfeld, A., Yang, X., 2018. Sun-induced chlorophyll fluorescence is more strongly related to absorbed light than to photosynthesis at half-hourly resolution in a rice paddy. Remote Sens. Environ. 216, 658–673. https://doi.org/10.1016/j.rse.2018.07.008

Yang, P., Prikaziuk, E., Verhoef, W., Van Der Tol, C., 2021. SCOPE 2.0: A model to simulate vegetated land surface fluxes and satellite signals. Geosci. Model Dev. 14, 4697–4712. https://doi.org/10.5194/gmd-14-4697-2021

Yang, P., van der Tol, C., Campbell, P.K.E., Middleton, E.M., 2020. Fluorescence Correction Vegetation Index (FCVI): A physically based reflectance index to separate physiological and non-physiological information in far-red sun-induced chlorophyll fluorescence. Remote Sens. Environ. 240. https://doi.org/10.1016/j.rse.2020.111676

Yang, P., van der Tol, C., Verhoef, W., Damm, A., Schickling, A., Kraska, T., Muller, O., Rascher, U., 2019.

Using reflectance to explain vegetation biochemical and structural effects on sun-induced chlorophyll fluorescence. Remote Sens. Environ. 231. https://doi.org/10.1016/j.rse.2018.11.039

Yang, X., Shi, H., Stovall, A., Guan, K., Miao, G., Zhang, Yongguang, Zhang, Yao, Xiao, X., Ryu, Y., Lee, J.E., 2018. FluoSpec 2—an automated field spectroscopy system to monitor canopy solar-induced fluorescence. Sensors (Switzerland) 18. https://doi.org/10.3390/s18072063

Yang, X., Tang, J., Mustard, J.F., Lee, J.E., Rossini, M., Joiner, J., Munger, J.W., Kornfeld, A., Richardson, A.D., 2015. Solar-induced chlorophyll fluorescence that correlates with canopy photosynthesis on diurnal and seasonal scales in a temperate deciduous forest. Geophys. Res. Lett. https://doi.org/10.1002/2015GL063201

Yao, Xinfeng, Yao, Xia, Jia, W., Tian, Y., Ni, J., Cao, W., Zhu, Y., 2013. Comparison and intercalibration of vegetation indices from different sensors for monitoring above-ground plant nitrogen uptake in winter wheat. Sensors (Switzerland) 13, 3109–3130. https://doi.org/10.3390/s130303109

Zagajewski, B., Tømmervik, H., Bjerke, J.W., Raczko, E., Bochenek, Z., Klos, A., Jarocińska, A., Lavender, S., Ziólkowski, D., 2017. Intraspecific differences in spectral reflectance curves as indicators of reduced vitality in high-arctic plants. Remote Sens. 9. https://doi.org/10.3390/rs9121289

Zarco-Tejada, P.J., González-Dugo, M. V, Fereres, E., 2016. Seasonal stability of chlorophyll fluorescence quantified from airborne hyperspectral imagery as an indicator of net photosynthesis in the context of precision agriculture. Remote Sens. Environ. 179, 89–103. https://doi.org/10.1016/j.rse.2016.03.024

Zhang, Yongguang, Zhang, Q., Liu, L., Zhang, Yangjian, Wang, Shaoqiang, Ju, W., Zhou, G., Zhou, L., Tang, J., Zhu, X., Wang, F., Huang, Y., Zhang, Z., Qiu, B., Zhang, X., Wang, Songhan, Huang, C., Tang, X., Zhang, J., 2021. ChinaSpec: A Network for Long-Term Ground-Based Measurements of Solar-Induced Fluorescence in China. J. Geophys. Res. Biogeosciences 126. https://doi.org/10.1029/2020JG006042

Zhao, Y., Yuan, Y., Wang, Q., 2019. Fast spectral clustering for unsupervised hyperspectral image classification. Remote Sens. 11. https://doi.org/10.3390/rs11040399

Zheng, K., Zheng, C., Zhang, Y., Wang, Y., Tittel, F.K., 2018. Review of Incoherent Broadband Cavity-Enhanced Absorption Spectroscopy (IBBCEAS) for Gas Sensing. Sensors (Basel). https://doi.org/10.3390/s18113646